NASA Reference Publication 1218

July 1989

Airfoil Self-Noise and Prediction

Thomas F. Brooks,
D. Stuart Pope,
and Michael A. Marcolini

(NASA-RP-1218) AIRFOIL SELF-NOISE AND PREDICTION (NASA. Langley Research Center) 145 p CSCL 20A

N89-25673

Unclas
H1/71 0197717

NASA

NASA
Reference
Publication
1218

1989

Airfoil Self-Noise and Prediction

Thomas F. Brooks
Langley Research Center
Hampton, Virginia

D. Stuart Pope
PRC Kentron, Inc.
Aerospace Technologies Division
Hampton, Virginia

Michael A. Marcolini
Langley Research Center
Hampton, Virginia

NASA
National Aeronautics and
Space Administration
Office of Management
Scientific and Technical
Information Division

Contents

Symbols

A	spectral shape function for TBL–TE noise, eqs. (35) and (36)
a, a_0	parameters of shape function A, eqs. (37) and (38)
B	spectral shape function for separation noise, eqs. (41) and (42)
b, b_0	parameters of shape function B, eqs. (43) and (44)
c	chord length, m
c_o	medium speed of sound, m/s
$\overline{D}_h$	directivity function for TE noise (high-frequency limit), eq. (B1)
$\overline{D}_\ell$	directivity function for translating dipole (low-frequency limit), eq. (B2)
$F(\mathrm{St})$	universal spectral shape function, eq. (18)
f	frequency, Hz
G_1	spectral shape function for LBL–VS noise, eq. (57)
G_2	R_c-dependence for LBL–VS noise peak amplitude, eq. (58)
G_3	angle dependence for G_2 function, eq. (60)
G_4	peak level function for G_5, eq. (74)
G_5	spectral shape function for TE bluntness noise, eqs. (75)–(82)
$G_{ij}(f)$	cross-spectrum between microphone Mi and Mj, Pa^2/Hz
H	tunnel height, m
h	TE thickness (degree of bluntness), m
$K, K_1, \Delta K_1, K_2$	constants, defined by eqs. (18), (47), (48), and (49)
L	span, m
L'	sectional lift of blade, lift per unit span
$\mathcal{L}$	turbulence correlation scale, m
ℓ	spanwise extent of tip vortex at TE, m
M	Mach number, U/c_o
M_{max}	maximum Mach number in tip vortex formation region
R_c	Reynolds number based on chord length, cU/ν
$R_{ij}(\tau)$	cross-correlation between microphones Mi and Mj, Pa^2
r	distance from source to observer, m
$S(f)$	spectrum of self-noise, Pa^2/Hz
St, St_1, $\overline{\mathrm{St}}_1$, St_2	Strouhal numbers defined for TBL–TE and separation noise scaling, section 5.1.
St$'$, St'_1	Strouhal numbers defined for LBL-VS noise scaling, section 5.2.
St$''$	Strouhal number defined for tip vortex formation noise, section 5.3.
St$'''$	Strouhal number defined for TE-bluntness–vortex-shedding noise, section 5.4.
t	time, s
U	free-stream velocity, m/s
U_c	convection velocity, m/s
x	streamwise axis, see fig. B3, m
y	lateral axis, m
z	vertical axis, m
α_{TIP}	angle of attack of airfoil tip to oncoming flow, deg
α'_{TIP}	corrected angle of attack of airfoil tip, eq. (66), deg
α_t	airfoil angle of attack referenced to tunnel streamwise axis, deg
α_*	effective aerodynamic angle of attack, corrected for open wind tunnel effects, deg
δ	boundary-layer thickness, m
δ^*	boundary-layer displacement thickness, m

Γ	tip vortex strength, m^2/s
Θ	angle from source streamwise axis x to observer, see fig. B3, deg
θ	boundary-layer momentum thickness, m
ν	kinematic viscosity of medium, m^2/s
τ	time delay, s
Φ	angle from source lateral axis y to observer, see fig. B3, deg
ϕ	cross-spectral phase angle, deg
Ψ	angle parameter related to surface slope at TE, section 5.4, deg

Subscripts:

avg	average
e	retarded coordinate
p	pressure side of airfoil
s	suction side of airfoil
TIP	tip of blade
TOT	total
α	angle dependent
0	for δ_0, δ_0^*, and θ_0 is for airfoil at zero angle of attack, reference value
1/3	1/3-octave spectral presentation

Abbreviations:

BL	boundary layer
LBL	laminar boundary layer
LE	leading edge of airfoil blade
LHS	left-hand side
Mi	microphone number i for $i = 1$ through 9, see fig. 4
OASPL	overall sound pressure level, dB
RHS	right-hand side
SPL	sound pressure level, spectrum, dB (re 2×10^{-5} Pa)
TBL	turbulent boundary layer
TE	trailing edge of airfoil blade
UTRC	United Technologies Research Center
VS	vortex shedding
2D	two-dimensional
3D	three-dimensional

Summary

An overall prediction method has been developed for the self-generated noise of an airfoil blade encountering smooth flow. Prediction methods for individual self-noise mechanisms are semiempirical and are based on previous theoretical studies and the most comprehensive self-noise data set available. The specially processed data set, most of which is newly presented in this report, is from a series of aerodynamic and acoustic tests of two- and three-dimensional airfoil blade sections conducted in an anechoic wind tunnel. Five self-noise mechanisms due to specific boundary-layer phenomena have been identified and modeled: boundary-layer turbulence passing the trailing edge, separated-boundary-layer and stalled-airfoil flow, vortex shedding due to laminar-boundary-layer instabilities, vortex shedding from blunt trailing edges, and the turbulent vortex flow existing near the tips of lifting blades. The data base, with which the predictions are matched, is from seven NACA 0012 airfoil blade sections of different sizes (chord lengths from 2.5 to 61 cm) tested at wind tunnel speeds up to Mach 0.21 (Reynolds number based on chord up to 3×10^6) and at angles of attack from 0° to 25.2°. The predictions are compared successfully with published data from three self-noise studies of different airfoil shapes, which were tested up to Mach and Reynolds numbers of 0.5 and 4.6×10^6, respectively. An application of the prediction method is reported for a large-scale-model helicopter rotor and the predictions compared well with data from a broadband noise test of the rotor, conducted in a large anechoic wind tunnel. A computer code of the methods is given for the predictions of 1/3-octave formatted spectra.

1. Introduction

Airfoil self-noise is due to the interaction between an airfoil blade and the turbulence produced in its own boundary layer and near wake. It is the total noise produced when an airfoil encounters smooth nonturbulent inflow. Over the last decade, research has been conducted at and supported by NASA Langley Research Center to develop fundamental understanding, as well as prediction capability, of the various self-noise mechanisms. The interest has been motivated by its importance to broadband helicopter rotor, wind turbine, and airframe noises. The present paper is the cumulative result of a series of aerodynamic and acoustic wind tunnel tests of airfoil sections, which has produced a comprehensive data base. A correspondingly extensive semi-empirical scaling effort has produced predictive capability for five self-noise mechanisms.

1.1. Noise Sources and Background

Previous research efforts (prior to 1983) for the broadband noise mechanisms are reviewed in some detail by Brooks and Schlinker (ref. 1). In figure 1, the subsonic flow conditions for five self-noise mechanisms of concern here are illustrated. At high Reynolds number R_c (based on chord length), turbulent boundary layers (TBL) develop over most of the airfoil. Noise is produced as this turbulence passes over the trailing edge (TE). At low R_c, largely laminar boundary layers (LBL) develop, whose instabilities result in vortex shedding (VS) and associated noise from the TE. For nonzero angles of attack, the flow can separate near the TE on the suction side of the airfoil to produce TE noise due to the shed turbulent vorticity. At very high angles of attack, the separated flow near the TE gives way to large-scale separation (deep stall) causing the airfoil to radiate low-frequency noise similar to that of a bluff body in flow. Another noise source is vortex shedding occurring in the small separated flow region aft of a blunt TE. The remaining source considered here is due to the formation of the tip vortex, containing highly turbulent flow, occurring near the tips of lifting blades or wings.

1.1.1. Turbulent-Boundary-Layer–Trailing-Edge (TBL–TE) Noise

Using measured surface pressures, Brooks and Hodgson (ref. 2) demonstrated that if sufficient information is known about the TBL convecting surface pressure field passing the TE, then TBL–TE noise can be accurately predicted. Schlinker and Amiet (ref. 3) employed a generalized empirical description of surface pressure to predict measured noise. However, the lack of agreement for many cases indicated

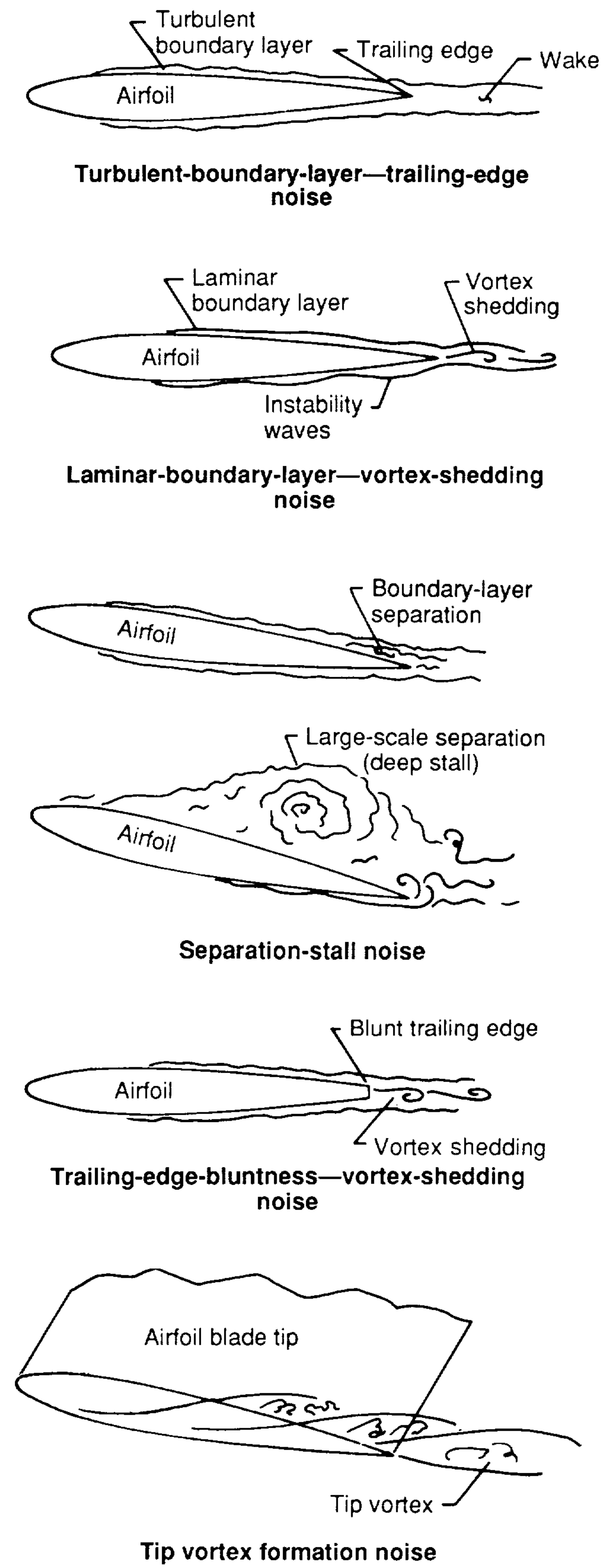

Figure 1. Flow conditions producing airfoil blade self-noise.

a need for a more accurate pressure description than was available. Langley supported a research effort (ref. 4) to model the turbulence within boundary layers as a sum of discrete "hairpin" vortex elements. In a parallel and follow-up effort, the present authors matched measured and calculated mean boundary-layer characteristics to prescribed distributions of the discrete vortex elements so that associated surface pressure could be determined. The use of the model to predict TBL–TE noise proved disappointing because of its inability to show correct trends with angle of attack or velocity. The results showed that to successfully describe the surface pressure, the history of the turbulence must be accounted for in addition to the mean TBL characteristics. This level of turbulence modeling has not been attempted to date.

A simpler approach to the TBL–TE noise problem is based on the Ffowcs Williams and Hall (ref. 5) edge-scatter formulation. In reference 3, the noise data were normalized by employing the edge-scatter model with the mean TBL thickness δ used as a required length scale. When δ was unknown, simple flat plate theory was used to estimate δ. Spectral data initially differing by 40 dB collapsed to within 7 dB, consistent with the results of the approach discussed above using surface pressure models. The extent of agreement between data sets was largely due to the correct scaling of the velocity dependence, which is the most sensitive parameter in the scaling approach. The dependence of the overall sound pressure level on velocity to the fifth power had been verified in a number of studies. The extent to which the normalized data deviation was due to uncertainty in δ was addressed by Brooks and Marcolini (ref. 6) in a forerunner to the present report. For large R_c and small angles of attack, which matched the conditions of reference 3, the use of measured TBL thicknesses δ, displacement thicknesses δ^*, or momentum thicknesses θ in the normalization produced the same degree of deviation within the TBL–TE noise data. Subsequently, normalizations based on boundary-layer maximum shear stress measurements and, alternately, profile shape factors were also examined. Of particular concern in reference 6 was that when an array of model sizes, rather than just large models, was tested at various angles of attack, the normalized spectrum deviations increased to 10 or even 20 dB. These large deviations indicate a lack of fidelity of the spectrum normalization and any subsequent prediction methods based on curve fits. They also reinforce the conclusion from the aforementioned surface pressure modeling effort that knowledge of the mean TBL characteristics alone is insufficient to define the turbulence structure. The conditions under which the turbulence evolves were found to be important. The normalized data appeared to be directly influenced by factors such as Reynolds number and angle of attack, which in previous analyses were assumed to be of pertinence only through their effect on TBL thickness δ (refs. 3 and 7).

Several prediction schemes for TBL–TE noise have been used previously for helicopter rotor noise (refs. 3 and 8) and for wind turbines (refs. 9 and 10). These schemes have all evolved from scaling law equations which were fitted to the normalized data of reference 3 and, thus, are limited by the same concerns of generality discussed above.

1.1.2. Separation-Stall Noise

Assessments of the separated flow noise mechanism for airfoils at moderate to high angles of attack have been very limited (ref. 1). The relative importance of airfoil stall noise was illustrated in the data of Fink and Bailey (ref. 11) in an airframe noise study. At stall, noise increased by more than 10 dB relative to TBL–TE noise, emitted at low angles of attack. Paterson et al. (ref. 12) found evidence through surface to far field cross-correlations that for mildly separated flow the dominant noise is emitted from the TE, whereas for deep stall the noise radiated from the chord as a whole. This finding is consistent with the conclusions of reference 11.

No predictive methods are known to have been developed. A successful method would have to account for the gradual introduction of separated flow noise as airfoil angle of attack is increased. Beyond limiting angles, deep stall noise would be the only major contributing source.

1.1.3. Laminar-Boundary-Layer–Vortex-Shedding (LBL–VS) Noise

When a LBL exists over most of at least one side of an airfoil, vortex shedding noise can occur. The vortex shedding is apparently coupled to acoustically excited aerodynamic feedback loops (refs. 13, 14, and 15). In references 14 and 15, the feedback loop is taken between the airfoil TE and an upstream "source" point on the surface, where Tollmien-Schlichting instability waves originate in the LBL. The resulting noise spectrum is composed of quasi-tones related to the shedding rates at the TE. The gross trend of the frequency dependence was found by Paterson et al. (ref. 16) by scaling on a Strouhal number basis with the LBL thickness at the TE being the relevant length scale. Simple flat plate LBL theory was used to determine the boundary-layer thicknesses δ in the frequency comparisons. The use of measured values of δ in reference 6 verified the general Strouhal dependence. Additionally, for zero angle of attack, Brooks and Marcolini (ref. 6) found that overall levels of LBL–VS noise could be normalized so that the transition from LBL–VS noise to TBL–TE noise is a unique function of R_c.

There have been no LBL–VS noise prediction methods proposed, because most studies have emphasized the examination of the rather erratic frequency dependence of the individual quasi-tones in attempts to explain the basic mechanism. However, the scaling successes described above in references 6 and 16 can offer initial scaling guidance for the development of predictions in spite of the general complexity of the mechanism.

1.1.4. Tip Vortex Formation Noise

The tip noise source has been identified with the turbulence in the local separated flow associated with formation of the tip vortex (ref. 17). The flow over the blade tip consists of a vortex with a thick viscous turbulent core. The mechanism for noise production is taken to be TE noise due to the passage of the turbulence over the TE of the tip region. George and Chou (ref. 8) proposed a prediction model based on spectral data from delta wing studies (assumed to approximate the tip vortex flow of interest), mean flow studies of several tip shapes, and TE noise analysis.

Brooks and Marcolini (ref. 18) conducted an experimental study to isolate tip noise in a quantitative manner. The data were obtained by comparing sets of two- and three-dimensional test results for different model sizes, angles of attack, and tunnel flow velocities. From data scaling, a quantitative prediction method was proposed which had basic consistency with the method of reference 8.

1.1.5. Trailing-Edge-Bluntness–Vortex-Shedding Noise

Noise due to vortex shedding from blunt trailing edges was established by Brooks and Hodgson (ref. 2) to be an important airfoil self-noise source. Other studies of bluntness effects, as reviewed by Blake (ref. 19) and Brooks and Schlinker (ref. 1), were only aerodynamic in scope and dealt with TE thicknesses that were large compared with the boundary-layer displacement thicknesses. For rotor blade and wing designs, the bluntness is likely to be small compared with boundary-layer thicknesses.

Grosveld (ref. 9) used the data of reference 2 to obtain a scaling law for TE bluntness noise. He found that the scaling model could explain the spectral behavior of high-frequency broadband noise of wind turbines. Chou and George (ref. 20) followed suit with an alternative scaling of the data of reference 2 to model the noise. For both modeling techniques neither the functional dependence of the noise on boundary-layer thickness (as compared with the TE bluntness) nor the specifics of the blunted TE shape were incorporated. A more general model is needed.

1.2. Overview of Report

The purpose of this report is to document the development of a self-noise prediction method and to verify its accuracy for a range of applications. The tests producing the data base for the scaling effort are described in section 2. In section 3, the measured boundary-layer thickness and integral parameter data, used to normalize airfoil noise data, are documented. The acoustic measurements are reported in section 4, where a special correlation editing procedure is used to extract clean self-noise spectra from data containing extraneous test rig noise. In section 5, the scaling laws are developed for the five self-noise mechanisms. For each, the data are first normalized by fundamental techniques and then examined for dependences on parameters such as Reynolds number, Mach number, and geometry. The resulting prediction methods are delineated with specific calculation procedures and results are compared with the original data base. The predictions are compared in section 6 with self-noise data from three studies reported in the literature. In appendix A, the data processing technique is detailed; in appendix B, the noise directivity functions are defined; and in appendix C, an application of the prediction methods is reported for a helicopter rotor broadband noise study. In appendix D, a computer code of the prediction method is given.

2. Description of Experiments

The details of the measurements and test facility have been reported in reference 6 for the sharp TE two-dimensional (2D) airfoil model tests, in reference 18 for corresponding three-dimensional (3D) tests, and in reference 2 for the blunt TE 2D airfoil model test. Specific information applicable to this report is presented here.

2.1. Models and Facility

The models were tested in the low-turbulence potential core of a free jet located in an anechoic chamber. The jet was provided by a vertically mounted nozzle with a rectangular exit with dimensions of 30.48 × 45.72 cm. The 2D sharp TE models are shown in figure 2. The models, all of 45.72-cm span, were NACA 0012 airfoils with chord lengths of 2.54, 5.08, 10.16, 15.24, 22.86, and 30.48 cm. The models were made with very sharp TE, less than 0.05 mm thick, without beveling the edge. The slope of the surface near the uncusped TE corresponded to the required 7° off the chord line. The sharp TE 3D models, shown in figure 3, all had spans of 30.48 cm and chord lengths that were the same as the five largest 2D models. The 3D models had rounded tips, defined by rotating the NACA 0012 shape about the chord line at 30.48-cm span. An NACA 0012 model of pertinence to the present paper, which is not shown here, is the blunt-TE airfoil of reference 2, with a chord length of 60.96 cm. Details of the blunt TE of this large model are given in section 5.

The cylindrical hubs, shown attached to the models, provided support and flush-mounting on the side plates of the test rig. At a geometric tunnel angle of attack α_t of 0°, the TE of all models was located 61.0 cm above the nozzle exit. The tunnel angle α_t is referenced to the undisturbed tunnel streamline direction. In figure 4, an acoustic test configuration for a 3D model is shown. A 3D setup is shown so that the model can be seen fitted to the side plate. The side plates (152.4 × 30.0 × 1 cm) were reinforced and flush mounted on the nozzle lips. For the 2D configurations, an additional side plate was used.

2.2. Instrumentation

For all of the acoustic testing, eight 1.27-cm-diameter (1/2-in.) free-field-response microphones were mounted in the plane perpendicular to the 2D model midspan. One microphone was offset from this midspan plane. In figure 4, seven of these are shown with the identification numbers indicated. Microphones M1 and M2 were perpendicular to the chord line at the TE for $\alpha_t = 0°$. The other microphones shown were at radii of 122 cm from the TE, as with M1 and M2, but were positioned 30° forward (M4 and M7) and 30° aft (M5 and M8). The data acquisition and processing approaches are described in appendix A.

For the aerodynamic tests the microphones to the right in figure 4 were removed and replaced by a large three-axis computer-controlled traverse rig used to position hot-wire probes. The miniature probes included both cross-wire and single-wire configurations. In figure 5, a cross-wire probe is shown mounted on the variable-angle arm of the traverse rig. Again, for clarity, a 3D airfoil model is shown. The probes were used to survey the flow fields about the models, especially in the boundary-layer and near-wake region just downstream of the trailing edge.

2.3. Test Conditions

The models were tested at free-stream velocities U up to 71.3 m/s, corresponding to Mach numbers up to 0.208 and Reynolds numbers, based on a 30.48-cm-chord model, up to 1.5×10^6. The tunnel angles of attack α_t were 0°, 5.4°, 10.8°, 14.4°, 19.8°, and 25.2°. The larger angles were not attempted for the larger models to avoid large uncorrectable tunnel flow deflections. For the 22.86-cm- and 30.48-cm-chord models, α_t was limited to 19.8° and 14.4°, respectively.

For the untripped BL cases (natural BL development), the surfaces were smooth and clean. For the tripped BL cases, BL transition was achieved by a random distribution of grit in strips from the leading edge (LE) to 20 percent chord. This tripping is considered heavy because the chordwise extent of the strip produced thicker than normal BL thicknesses. It was used to establish a well-developed TBL even for the smaller models and at the same time retain geometric similarity. The commercial grit number was No. 60 (nominal particle diameter of 0.29 mm) with an application density of about 380 particles/cm^2. An exception was the 2.54-cm-chord airfoil which had a strip at 30 percent chord of No. 100 grit with a density of about 690 particles/cm^2.

2.4. Wind Tunnel Corrections

The testing of airfoil models in a finite-size open wind tunnel causes flow curvature and downwash deflection of the incident flow that do not occur in free air. This effectively reduces the angle of attack, more so for the larger models. Brooks, Marcolini, and Pope (ref. 21) used lifting surface theory to develop the 2D open wind tunnel corrections to angle of attack and camber. Of interest here is a corrected angle of attack α_* representing the angle in free air required to give the same lift as α_t would give in the tunnel. One has from reference 21, upon ignoring

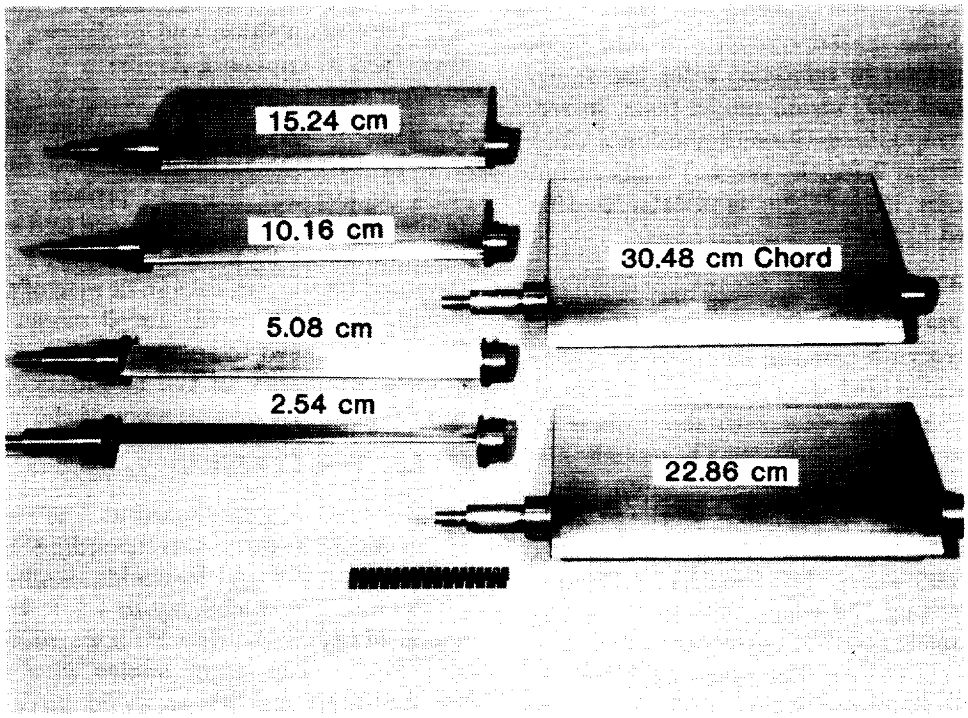

L-82-4573

Figure 2. Two-dimensional NACA 0012 airfoil blade models.

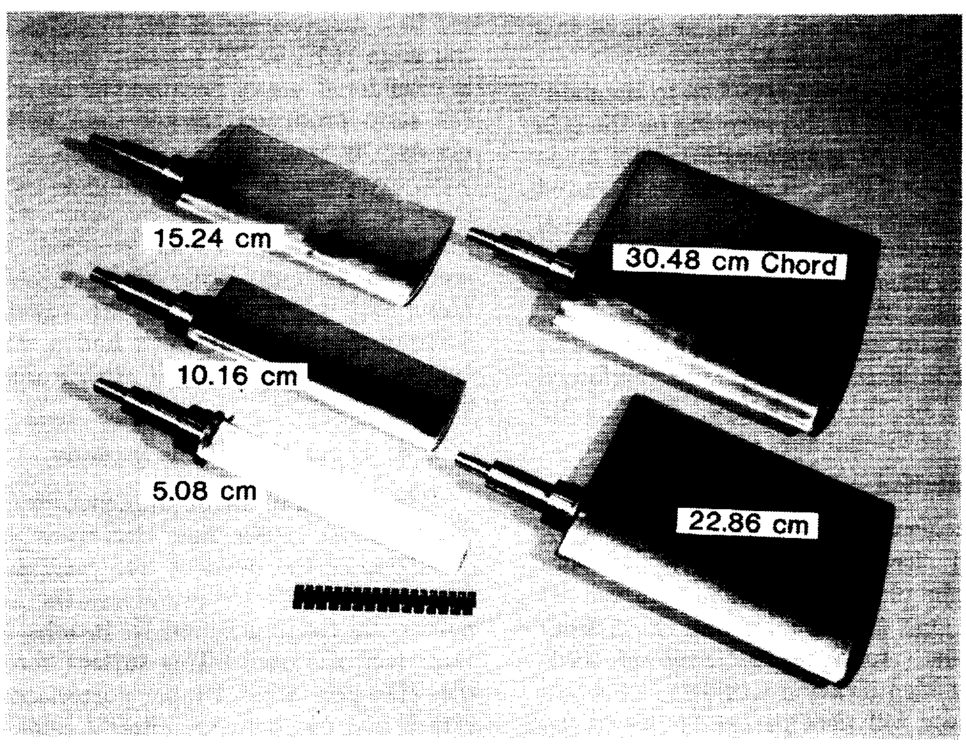

L-82-4570

Figure 3. Three-dimensional NACA 0012 airfoil blade models.

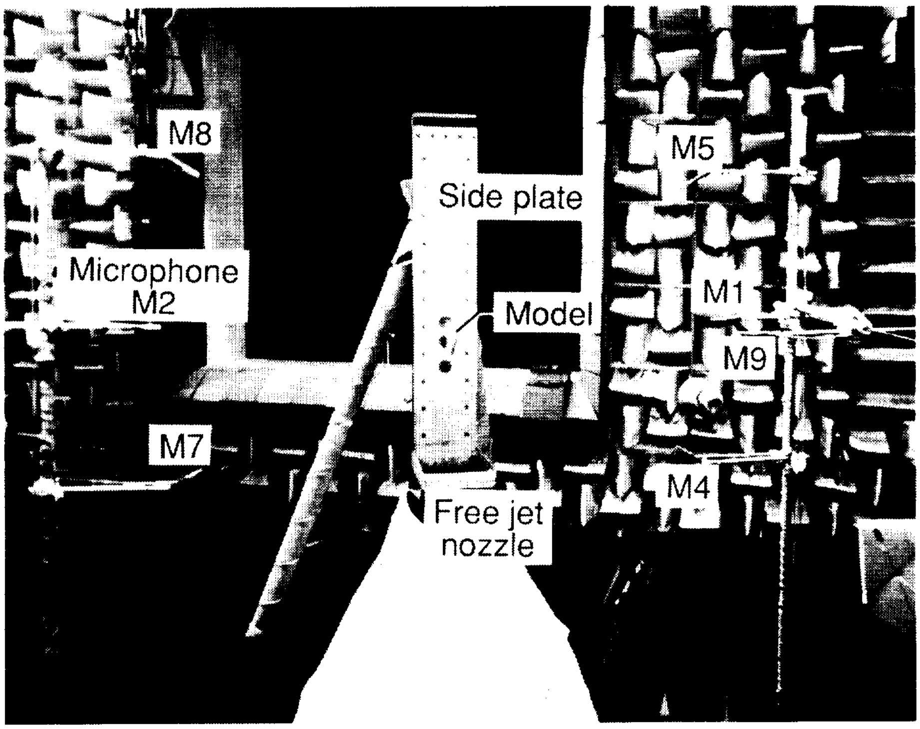

L-89-42

Figure 4. Test setup for acoustic tests of a 3D model airfoil.

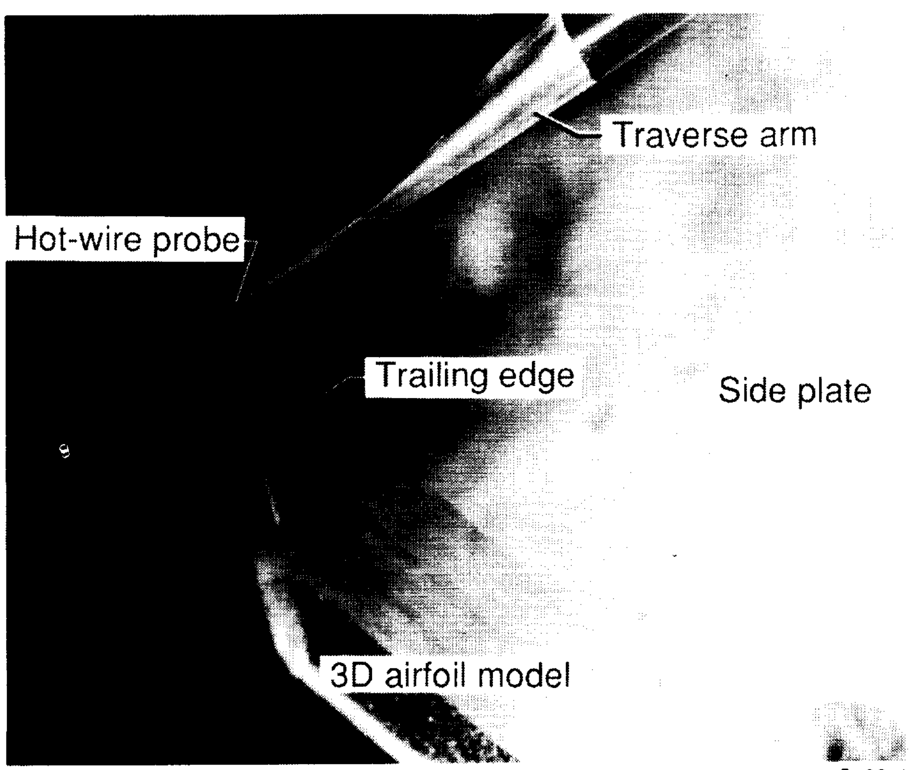

L-89-43

Figure 5. Tip survey using hot-wire probe.

small camber effects,

$$\alpha_* = \alpha_t/\zeta \tag{1}$$

where

$$\zeta = (1+2\sigma)^2 + \sqrt{12\sigma}$$

and

$$\sigma = (\pi^2/48)(c/H)^2$$

The term c is the airfoil chord and H is the tunnel height or vertical open jet dimension for a horizontally aligned airfoil. For the present 2D configurations, α_*/α_t equals 0.88, 0.78, 0.62, 0.50, 0.37, and 0.28 for the models with chord lengths of 2.54, 5.08, 10.16, 15.24, 22.86, and 30.48 cm, respectively.

3. Boundary-Layer Parameters at the Trailing Edge

The purpose of this section is to present measured boundary-layer thicknesses from reference 21 and to document corresponding curve fit scaling equations to be employed in the normalization of the airfoil self-noise data.

The data presented are the result of hot-wire probe measurements made in the boundary-layer/near-wake region of the sharp TE of the 2D airfoil models. The probes were traversed perpendicular to the model chord lines downstream of the TE. These measurements were made at 0.64 mm from the TE for the 2.54-cm-chord airfoil and at 1.3 mm for the other airfoils. The integral BL parameters—displacement thickness δ^* and momentum thickness θ—were calculated from mean velocity profiles with the BL/near-wake thickness δ specified. The thickness δ is that distance from the airfoil surface where the mean velocity reaches 99 percent of the potential flow stream velocity. The values of δ were chosen by carefully examining the respective turbulent velocity and Reynolds stress distributions as well as the mean profiles. For all cases, the estimated accuracy of δ is within ±5 percent for the turbulent-boundary-layer (TBL) flow and ±10 percent for the laminar and transitional flows, whereas the error range for the integral thicknesses δ^* and θ is less (ref. 21).

3.1. Scaled Data

The thicknesses δ and integral properties δ^* and θ at the TE of the sharp TE 2D airfoil models at $\alpha_t = 0°$ are given in figure 6 for both the artificially tripped and the untripped boundary-layer conditions. The subscript 0 for the thicknesses indicates that the airfoil is at zero angle of attack. The parameters are normalized by the chord length c and are given as a function of Reynolds number based on the chord R_c. As R_c increases, the thicknesses decrease for both the tripped and the untripped boundary layers. The tripped boundary layers are almost uniformly thicker than the corresponding untripped boundary layers. One should refer to reference 21 for details of the boundary-layer character for the cases of figure 6. In general, however, one can say that the tripped boundary layers are fully turbulent for even the lowest R_c. The untripped boundary layers are laminar or transitional at low R_c and become fully turbulent for high R_c. In figure 6, the boundary-layer thickness data are approximated by curve fits whose equations are specified in the following section.

Angle-of-attack effects on the thickness parameters are given at free-stream velocities of 71.3 and 39.6 m/s for the untripped and tripped BL airfoils in figures 7 and 8. The parameters are normalized by those measured for the corresponding cases at zero angle of attack, given in figure 6. The data are plotted against the corrected angle α_* of equation (1). The collapse of the data is much improved over that when α_t is used (ref. 21). In general, the data show that for increasing α_* (or α_t) the thicknesses increase on the suction side because of the increasing severity of the adverse pressure gradient. The converse is true for the pressure side, where the pressure gradient becomes increasingly favorable. Also included in figures 7 and 8 are curve fits to the data. For the pressure side of the airfoils, the curves are the same for the tripped and untripped cases. The suction side curves differ, reflecting differences in the angle dependence of where the TE boundary layer separates and finally stalls the airfoil.

In reference 21, the data are discussed and compared with flat plate experimental results and results from boundary-layer prediction codes.

3.2. Calculation Procedures

The boundary-layer thickness parameters at the TE of a symmetric NACA 0012 airfoil at zero angle of attack are approximated by the curve fits to the data of figure 6. The expressions for the curve fits for boundary-layer thickness δ, displacement thickness δ^*, and momentum thickness θ are, for the *heavily tripped boundary layer*,

$$\delta_0/c = 10^{[1.892-0.9045 \log R_c+0.0596(\log R_c)^2]} \tag{2}$$

$$\delta_0^*/c = \begin{cases} 0.0601 R_c^{-0.114} & (R_c \leq 0.3 \times 10^6) \\ 10^{[3.411-1.5397 \log R_c+0.1059(\log R_c)^2]} & (R_c > 0.3 \times 10^6) \end{cases} \tag{3}$$

$$\theta_0/c = \begin{cases} 0.0723 R_c^{-0.1765} & (R_c \leq 0.3 \times 10^6) \\ 10^{[0.5578-0.7079 \log R_c+0.0404(\log R_c)^2]} & (R_c > 0.3 \times 10^6) \end{cases} \tag{4}$$

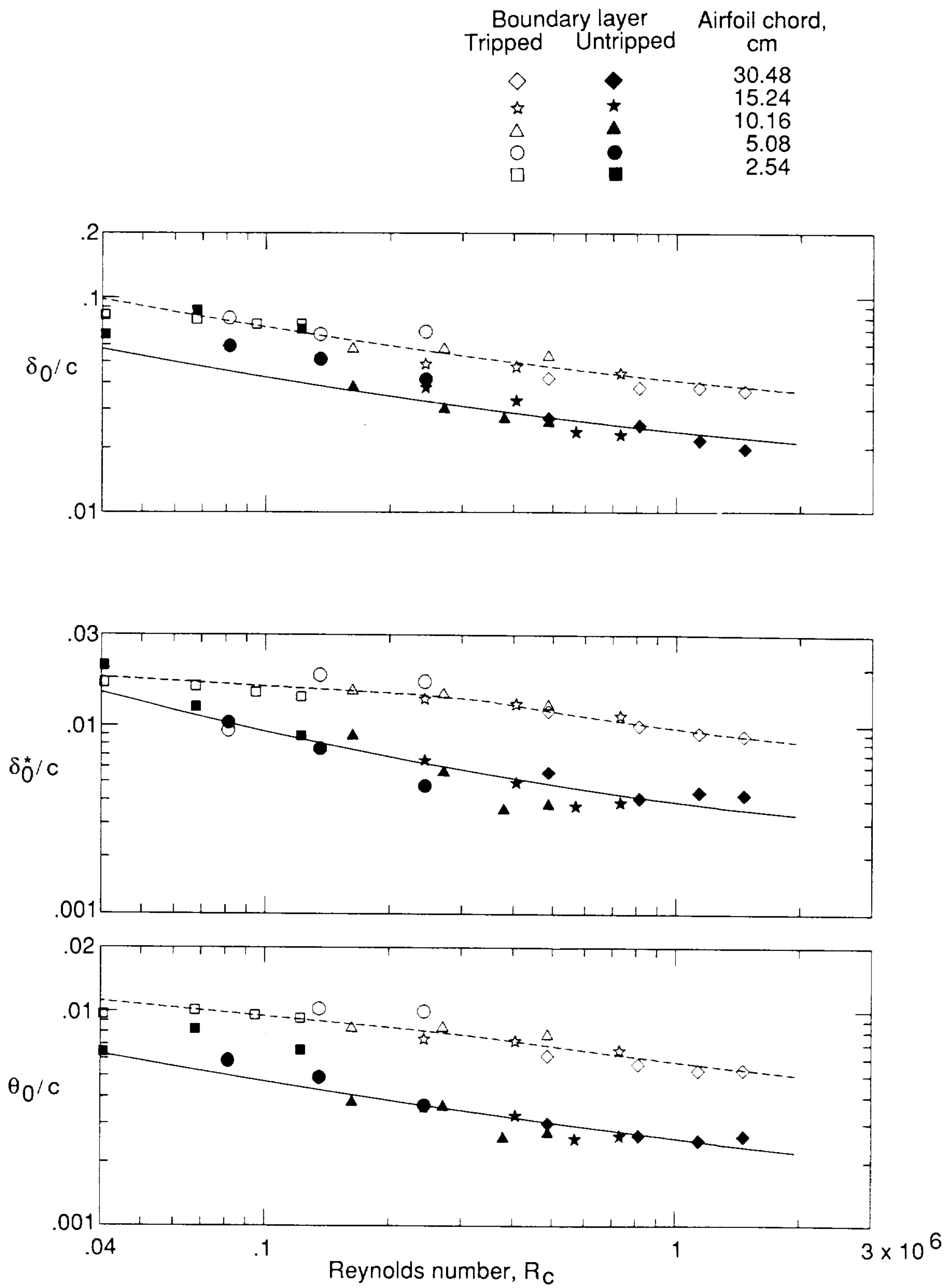

Figure 6. Boundary-layer thicknesses at the trailing edge of 2D airfoil models at angle of attack of zero. Solid lines are for untripped BL and broken lines are for tripped BL.

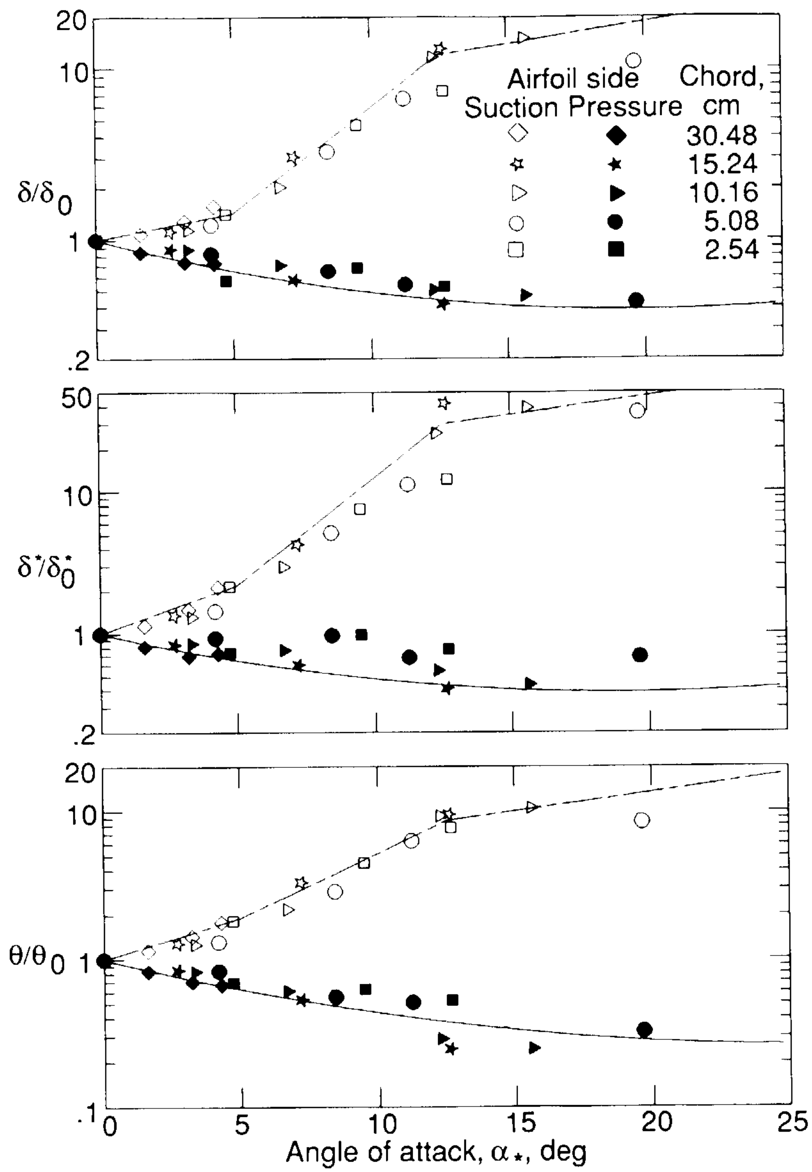

(a) $U = 71.3$ m/s.

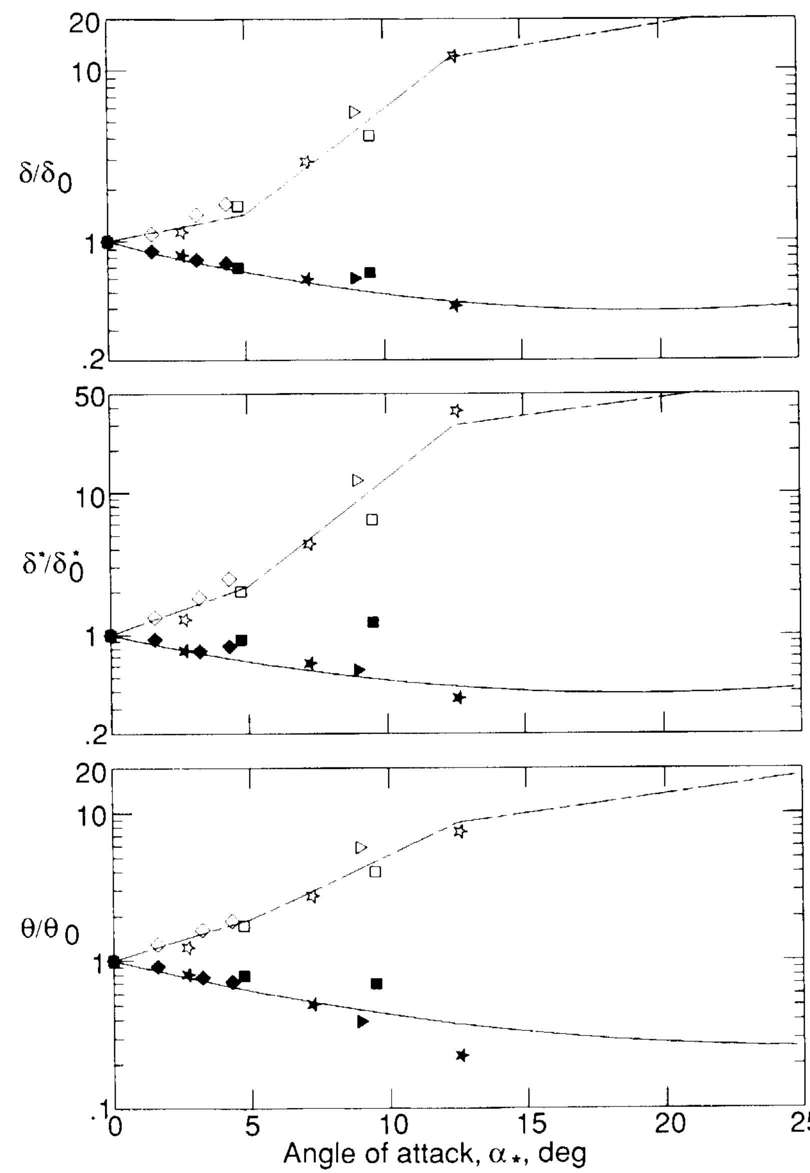

(b) $U = 39.6$ m/s.

Figure 7. Tripped BL thicknesses at the TE versus corrected angle of attack. Solid lines are for pressure side of airfoil and broken lines are for suction side.

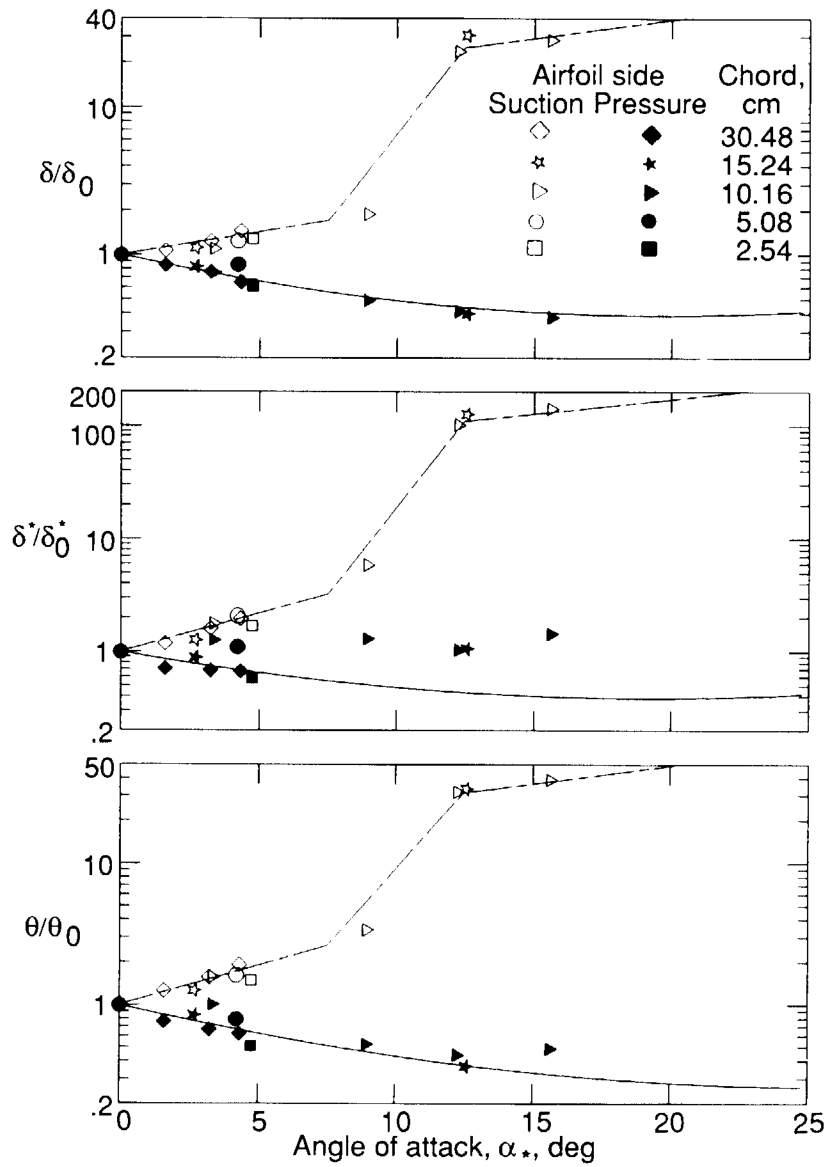

(a) U = 71.3 m/s.

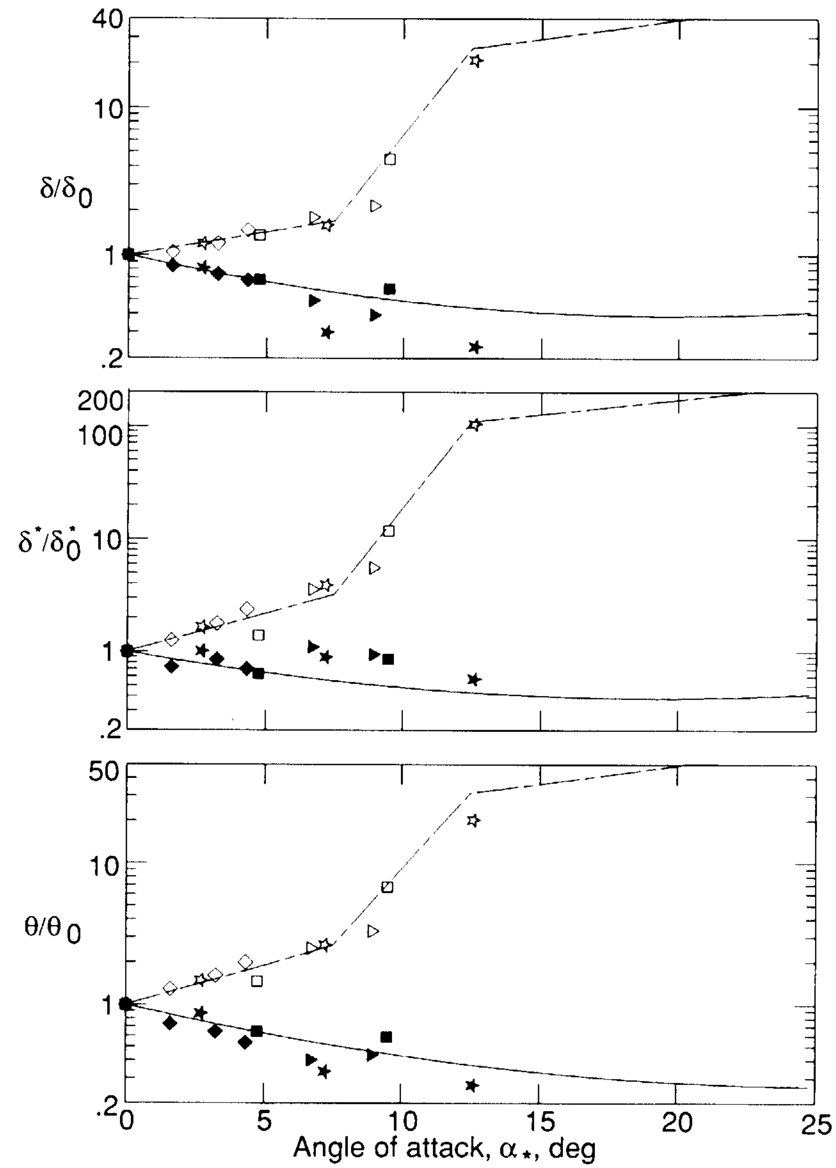

(b) U = 39.6 m/s.

Figure 8. Untripped BL thicknesses at the TE versus corrected angle of attack. Solid lines are for pressure side of airfoil and broken lines are for suction side.

where the zero subscripts indicate zero angle of attack, zero lift on these symmetric airfoils. For the *untripped* (natural transition) *boundary layers,*

$$\delta_0/c = 10^{[1.6569-0.9045\ \log\ R_c+0.0596(\log\ R_c)^2]} \tag{5}$$

$$\delta_0^*/c = 10^{[3.0187-1.5397\ \log\ R_c+0.1059(\log\ R_c)^2]} \tag{6}$$

$$\theta_0/c = 10^{[0.2021-0.7079\ \log\ R_c+0.0404(\log\ R_c)^2]} \tag{7}$$

The boundary-layer thicknesses for the airfoils at nonzero angle of attack, in terms of the zero-angle-of-attack thicknesses and the corrected angles α_*, are given in figures 7 and 8. The expressions for the curve fits for the *pressure side, for both the tripped and the untripped boundary layers,* are

$$\frac{\delta_p}{\delta_0} = 10^{[-0.04175\alpha_*+0.00106\alpha_*^2]} \tag{8}$$

$$\frac{\delta_p^*}{\delta_0^*} = 10^{[-0.0432\alpha_*+0.00113\alpha_*^2]} \tag{9}$$

$$\frac{\theta_p}{\theta_0} = 10^{[-0.04508\alpha_*+0.000873\alpha_*^2]} \tag{10}$$

For the suction side, the parametric behavior of the thicknesses depends on whether the boundary layers are attached, separated near the trailing edge, or separated a sufficient distance upstream to produce stall. For the *suction side for the tripped boundary layers* (fig. 7),

$$\frac{\delta_s}{\delta_0} = \begin{cases} 10^{0.0311\alpha_*} & (0^\circ \leq \alpha_* \leq 5^\circ) \\ 0.3468(10^{0.1231\alpha_*}) & (5^\circ < \alpha_* \leq 12.5^\circ) \\ 5.718(10^{0.0258\alpha_*}) & (12.5^\circ < \alpha_* \leq 25^\circ) \end{cases} \tag{11}$$

$$\frac{\delta_s^*}{\delta_0^*} = \begin{cases} 10^{0.0679\alpha_*} & (0^\circ \leq \alpha_* \leq 5^\circ) \\ 0.381(10^{0.1516\alpha_*}) & (5^\circ < \alpha_* \leq 12.5^\circ) \\ 14.296(10^{0.0258\alpha_*}) & (12.5^\circ < \alpha_* \leq 25^\circ) \end{cases} \tag{12}$$

$$\frac{\theta_s}{\theta_0} = \begin{cases} 10^{0.0559\alpha_*} & (0^\circ \leq \alpha_* \leq 5^\circ) \\ 0.6984(10^{0.0869\alpha_*}) & (5^\circ < \alpha_* \leq 12.5^\circ) \\ 4.0846(10^{0.0258\alpha_*}) & (12.5^\circ < \alpha_* \leq 25^\circ) \end{cases} \tag{13}$$

For the *suction side for the untripped boundary layers* (fig. 8),

$$\frac{\delta_s}{\delta_0} = \begin{cases} 10^{0.03114\alpha_*} & (0^\circ \leq \alpha_* \leq 7.5^\circ) \\ 0.0303(10^{0.2336\alpha_*}) & (7.5^\circ < \alpha_* \leq 12.5^\circ) \\ 12(10^{0.0258\alpha_*}) & (12.5^\circ < \alpha_* \leq 25^\circ) \end{cases} \tag{14}$$

$$\frac{\delta_s^*}{\delta_0^*} = \begin{cases} 10^{0.0679\alpha_*} & (0^\circ \leq \alpha_* \leq 7.5^\circ) \\ 0.0162(10^{0.3066\alpha_*}) & (7.5^\circ < \alpha_* \leq 12.5^\circ) \\ 52.42(10^{0.0258\alpha_*}) & (12.5^\circ < \alpha_* \leq 25^\circ) \end{cases} \tag{15}$$

$$\frac{\theta_s}{\theta_0} = \begin{cases} 10^{0.0559\alpha_*} & (0^\circ \leq \alpha_* \leq 7.5^\circ) \\ 0.0633(10^{0.2157\alpha_*}) & (7.5^\circ < \alpha_* \leq 12.5^\circ) \\ 14.977(10^{0.0258\alpha_*}) & (12.5^\circ < \alpha_* \leq 25^\circ) \end{cases} \tag{16}$$

4. Acoustic Measurements

The aim of the acoustic measurements was to determine spectra for self-noise from airfoils encountering smooth airflow. This task is complicated by the unavoidable presence of extraneous tunnel test rig noise. In this section, cross-correlations between microphones are examined to identify the self-noise emitted from the TE in the presence of other sources. Then, the spectra of self-noise are determined by performing Fourier transforms of cross-correlation data which have been processed and edited to eliminate the extraneous contributions. The results are presented as 1/3-octave spectra, which then form the data base from which the self-noise scaling prediction equations are developed.

4.1. Source Identification

The upper curves in figure 9 are the cross-correlations, $R_{12}(\tau) = \langle p_1(t)p_2(t+\tau)\rangle$, between the sound pressure signals p_1 and p_2 of microphones M1 and M2 identified in figure 4. Presented are cross-correlations both with and without the tripped 30.48-cm-chord airfoil mounted in the test rig. Because the microphones were on opposite sides of, and at equal distance from, the airfoil, a negative correlation peak occurs at a signal delay time τ of 0. This correlation is consistent with a broadband noise source of dipole character, whose phase is reversed on opposing sides. When the airfoil is removed, the strong negative peak disappears leaving the contribution from the test rig alone. The most coherent parts of this noise are from the lips of the nozzle and are, as with the airfoil noise, of a dipole character. The microphone time delays predicted for these sources are indicated by arrows. The predictions account for the effect of refraction of sound by the free-jet shear layer (refs. 22 and 23), as well as the geometric relationship between the microphones and the hardware and the speed of sound.

The lower curves in figure 9 are the cross-correlations, $R_{45}(\tau)$, between microphones M4 and M5. The predicted delay times again appear to correctly identify the correlation peaks associated with the noise emission locations. The peaks are positive for $R_{45}(\tau)$ because both microphones are on the same side of the dipoles' directional lobes. The noise field is dominated by TE noise. Any contribution to the noise field from the LE would appear where indicated in the figure. As is subsequently shown, there are contributions in many cases. For such cases the negative correlation peak for $R_{12}(\tau)$ would be the sum of the TE and LE correlation peaks brought together at $\tau = 0$ and inverted in sign.

In figure 10, the cross-correlations $R_{45}(\tau)$ are shown for tripped BL airfoils of various sizes. The TE noise correlation peaks are at $\tau_{TE} = -0.11$ ms for all cases because at $\alpha_t = 0°$, the TE location of all models is the same. The LE location changes with chord size, as is indicated by the change in the predicted LE noise correlation peak delay times.

For the larger airfoils in figure 10, the TE contribution dominates the noise field. As the chord length decreases, the LE noise peaks increase to become readily identifiable in the correlation. For the smallest chord the LE contribution is even somewhat more than that of the TE. Note the extraneous, but inconsequential, source of discrete low-frequency noise contributing to the 22.86-cm-chord correlation, which can be readily edited in a spectral format.

It is shown in reference 6 that the LE and TE sources are uncorrelated. The origin of LE noise appears to be inflow turbulence to the LE from the TBL of the test rig side plates. This should be the case even though the spanwise extent of this TBL is small compared with the portion of the models that encounter uniform low-turbulence flow from the nozzle. Inflow turbulence can be a very efficient noise mechanism (ref. 24); however its full efficiency can be obtained only when the LE of the model is relatively sharp compared with the scale of the turbulence. The LE noise contributions diminish for the large chord because of the proportional increase in LE radius with chord. When this radius increases to a size that is large compared with the turbulent scale in the side plate TBL, then the sectional lift fluctuations associated with inflow turbulence noise are not developed.

4.2. Correlation Editing and Spectral Determination

The cross-spectrum between microphones M1 and M2, denoted $G_{12}(f)$, is the Fourier transform of $R_{12}(\tau)$. If the contributions from the LE, nozzle lips, and any other coherent extraneous source locations were removed, $G_{12}(f)$ would equal the autospectrum of the airfoil TE self-noise, $S(f)$. Actually the relationship would be $G_{12}(f) = S(f)\exp[i(2\pi f\tau_{TE} \pm \pi)]$, where $i = \sqrt{-1}$ and τ_{TE} is the delay time of the TE correlation peak. This approach is formalized in reference 2.

In reference 6, the spectra were found from $G_{12}(f)$ determined with the models of the test rig after a point-by-point vectorial subtraction of $G_{12}(f)$ determined with the airfoil removed. This was equivalent to subtracting corresponding $R_{12}(\tau)$ results, such as those of figure 9, and then taking the Fourier transform. This resulted in "corrected" spectra which were devoid of at least a portion of the background test rig noise, primarily emitted from the nozzle lips. The spectra still were contaminated by the LE noise due to the inflow turbulence.

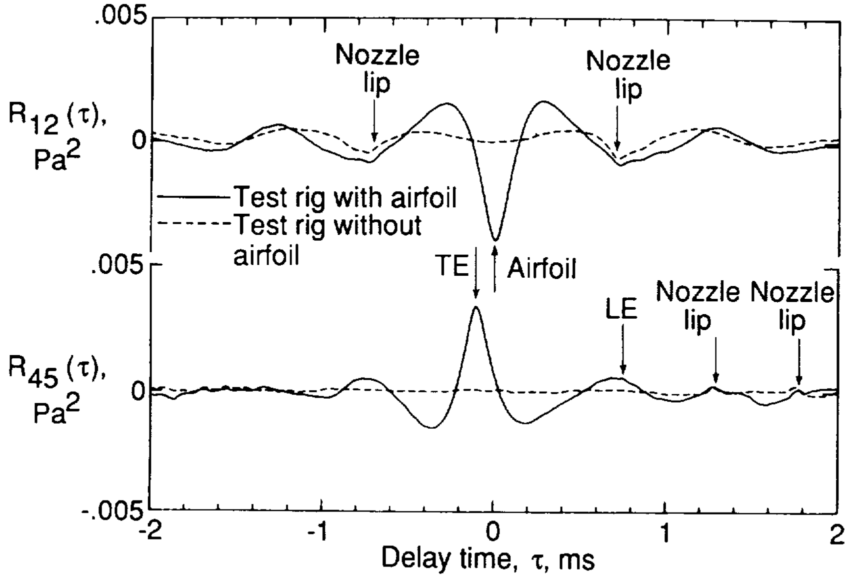

Figure 9. Cross-correlations for two microphone pairs with and without airfoil mounted in test rig. $c = 30.48$ cm; BL tripped; $\alpha_t = 0°$; $U = 71.3$ m/s. Arrows indicate predicted values of τ. (From ref. 6.)

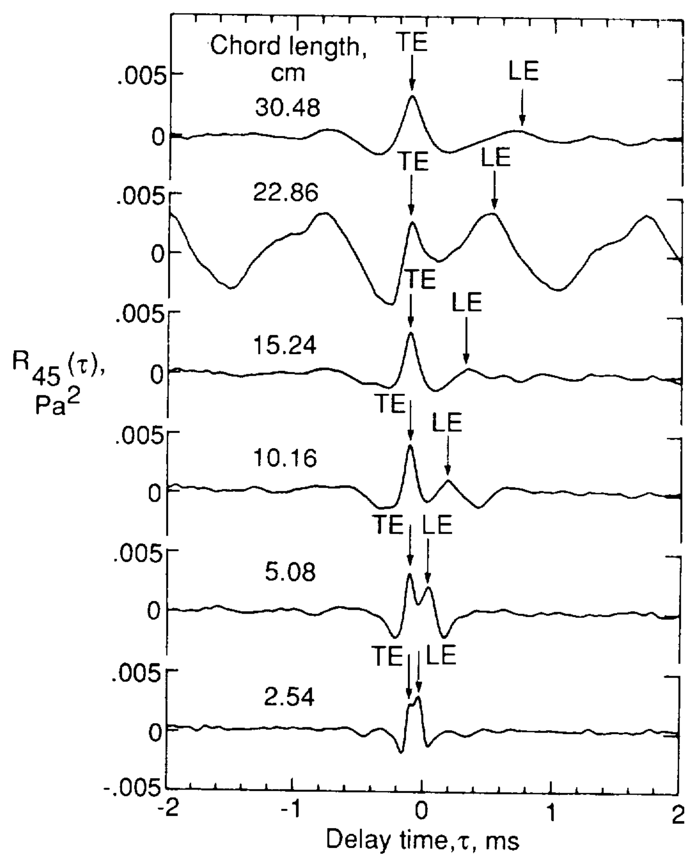

Figure 10. Cross-correlations between microphones M4 and M5 for tripped BL airfoils of various chord sizes. $U = 71.3$ m/s. Arrows indicate predicted values of τ. (From ref. 6.)

In the present paper, most spectra presented were obtained by taking the Fourier transform of microphone-pair cross-correlations which had been edited to eliminate LE noise (see details in appendix A). The microphone pairs used included M4 and M5, M4 and M8, and M4 and M2. These pairs produced correlations where the TE and LE noise peaks were generally separated and readily identifiable. Referring to figure 10 for $R_{45}(\tau)$, the approach was to employ only the left-hand side (LHS) of the TE noise peak. The LHS was "folded" about τ at the peak (τ_{TE}) to produce a nearly symmetrical correlation. Care was taken in the processing to maintain the actual shapes near the very peak, to avoid to the extent possible the artificial introduction of high-frequency noise in the resulting spectra. Cross-spectra were then determined which were equated to the spectra of TE self-noise.

The data processing was straightforward for the larger chord airfoils because the LE and TE peaks were sufficiently separated from one another that the influence of the LE did not significantly impact the TE noise correlation shapes. For many of the smaller airfoils, such as those with chord lengths of 2.54, 5.08, and 10.16 cm shown in figure 10, the closeness of the LE contribution distorted the TE noise correlation. A processing procedure was developed to effectively "separate" the TE and LE peaks to a sufficient distance from one another, within the correlation presentation, so that the correlation folding of the LHS about τ_{TE} produced a more accurate presentation of the TE noise correlation shape. The separation processing employed symmetry assumptions for the TE and LE noise correlations to allow manipulation of the correlation records. This processing represented a contamination removal method used for about one-quarter of the spectra presented for the three smallest airfoil chord lengths. Each case was treated individually to determine whether correlation folding alone, folding after the separation processing, or not folding at all produced spectra containing the least apparent error. In appendix A, details of the editing and Fourier transform procedures, as well as the separation processing, are given.

4.3. Self-Noise Spectra

The self-noise spectra for the 2D NACA 0012 airfoil models with sharp TE are presented in a 1/3-octave format in figures 11 to 74. Figures 11 to 43 are for airfoils where the boundary layers have been tripped and figures 44 to 74 are for smooth surface airfoils where the boundary layers are untripped (natural transition). Each figure contains spectra for a model at a specific angle of attack for various tunnel speeds. Note that the spectra are truncated at upper and lower frequencies. This editing of the spectra was done because, as described in appendix A, a review of the narrow-band amplitude and phase for all cases revealed regions where extraneous noise affected the spectra in a significant way (2 dB or more). These regions were removed from the 1/3-octave presentations.

The spectra levels have been corrected for shear layer diffraction and TE noise directivity effects, as detailed in appendix B. The noise should be that for an observer positioned perpendicular to, and 1.22 m from, the TE and the model midspan. In terms of the directivity definitions of appendix B, $r_e = 1.22$ m, $\Theta_e = 90°$, and $\Phi_e = 90°$. In section 5 (beginning on p. 51), the character and parametric behavior of the self-noise, as well as the predictions which are compared with the data, are discussed.

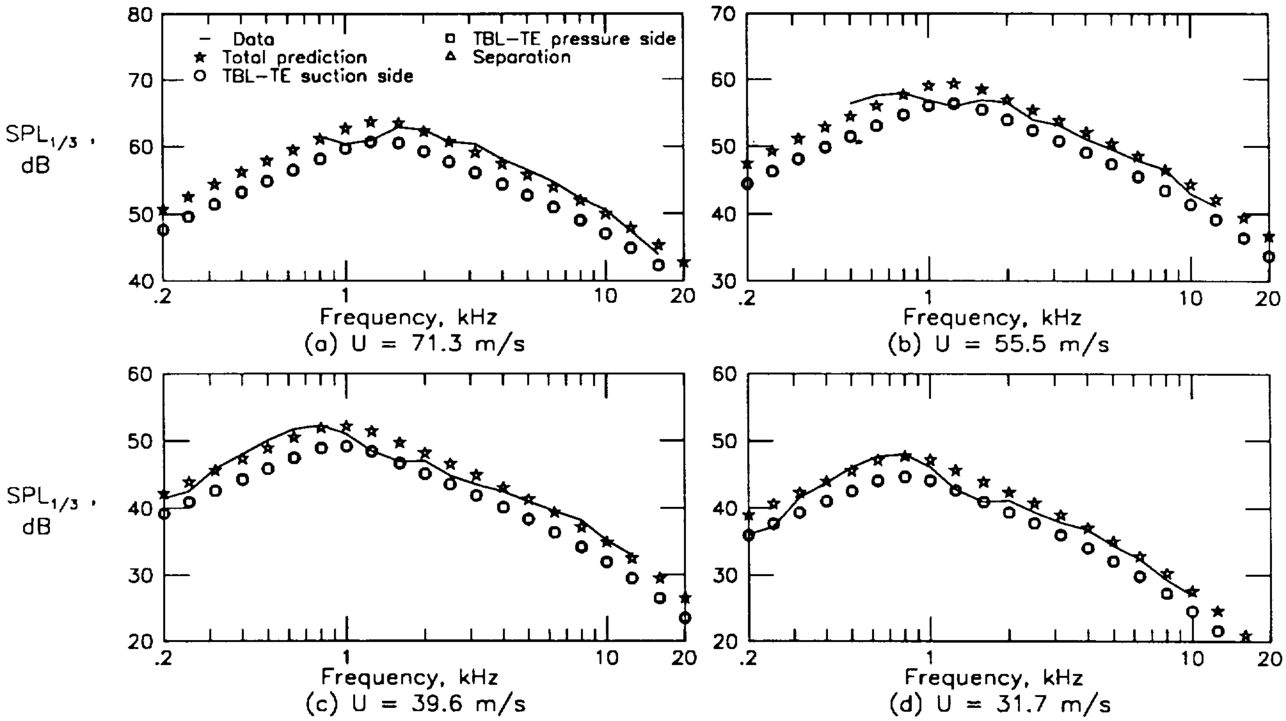

Figure 11. Self-noise spectra for 30.48-cm-chord airfoil with tripped BL at $\alpha_t = 0°$ ($\alpha_* = 0°$).

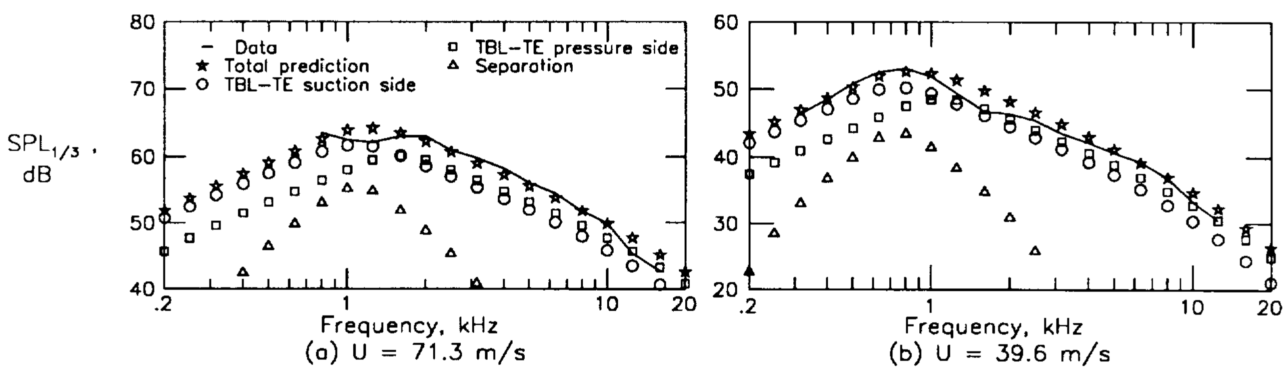

Figure 12. Self-noise spectra for 30.48-cm-chord airfoil with tripped BL at $\alpha_t = 5.4°$ ($\alpha_* = 1.5°$).

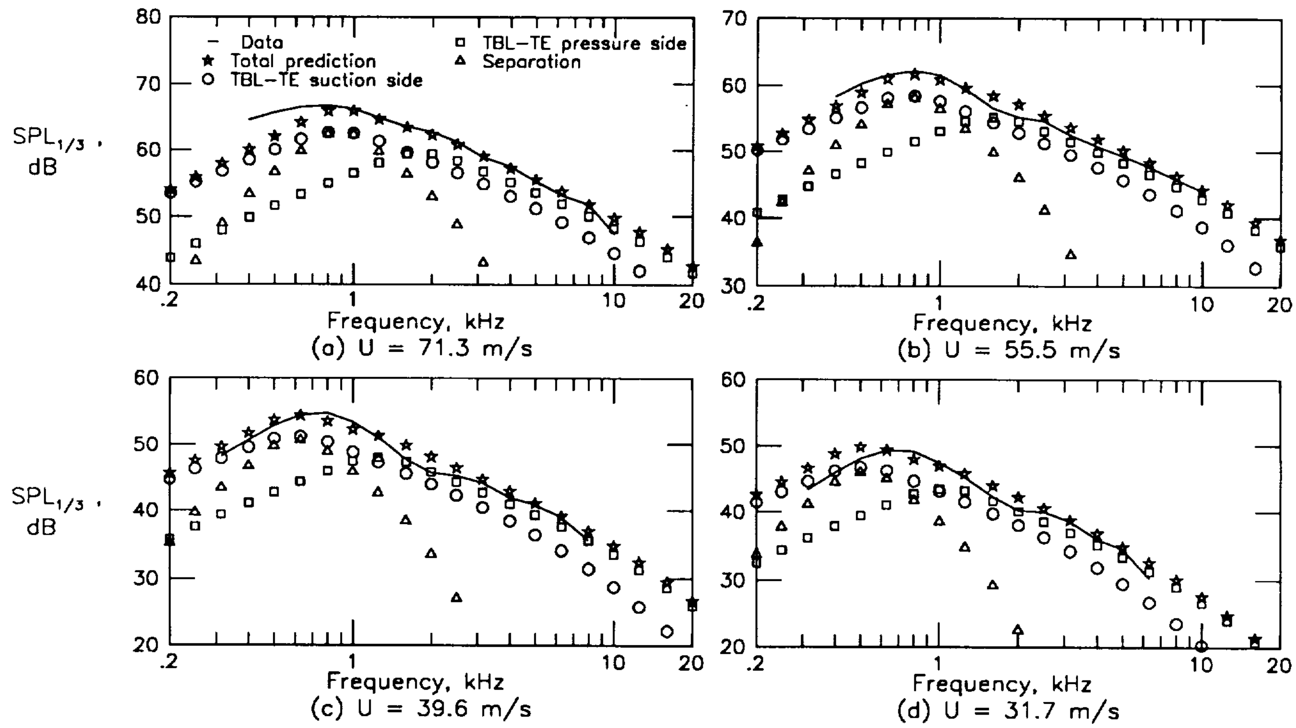

Figure 13. Self-noise spectra for 30.48-cm-chord airfoil with tripped BL at $\alpha_t = 10.8°$ ($\alpha_* = 3.0°$).

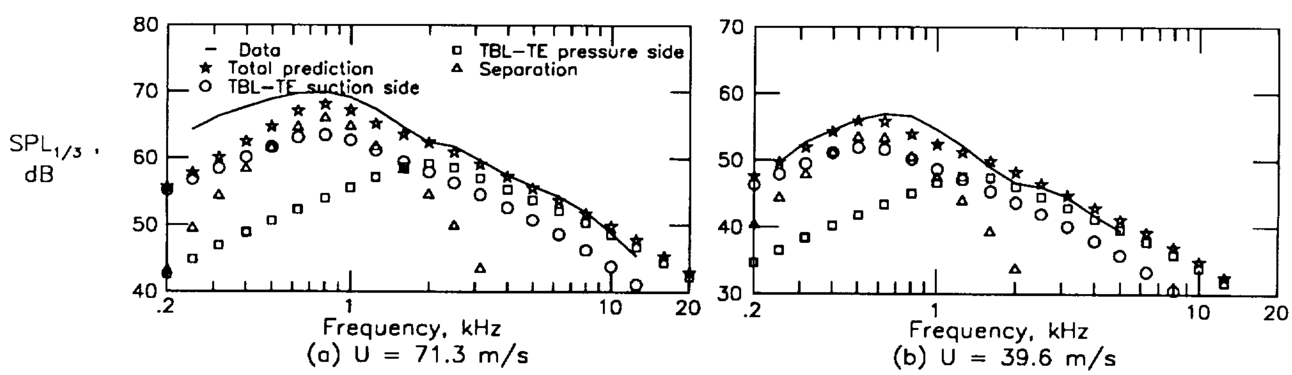

Figure 14. Self-noise spectra for 30.48-cm-chord airfoil with tripped BL at $\alpha_t = 14.4°$ ($\alpha_* = 4.0°$).

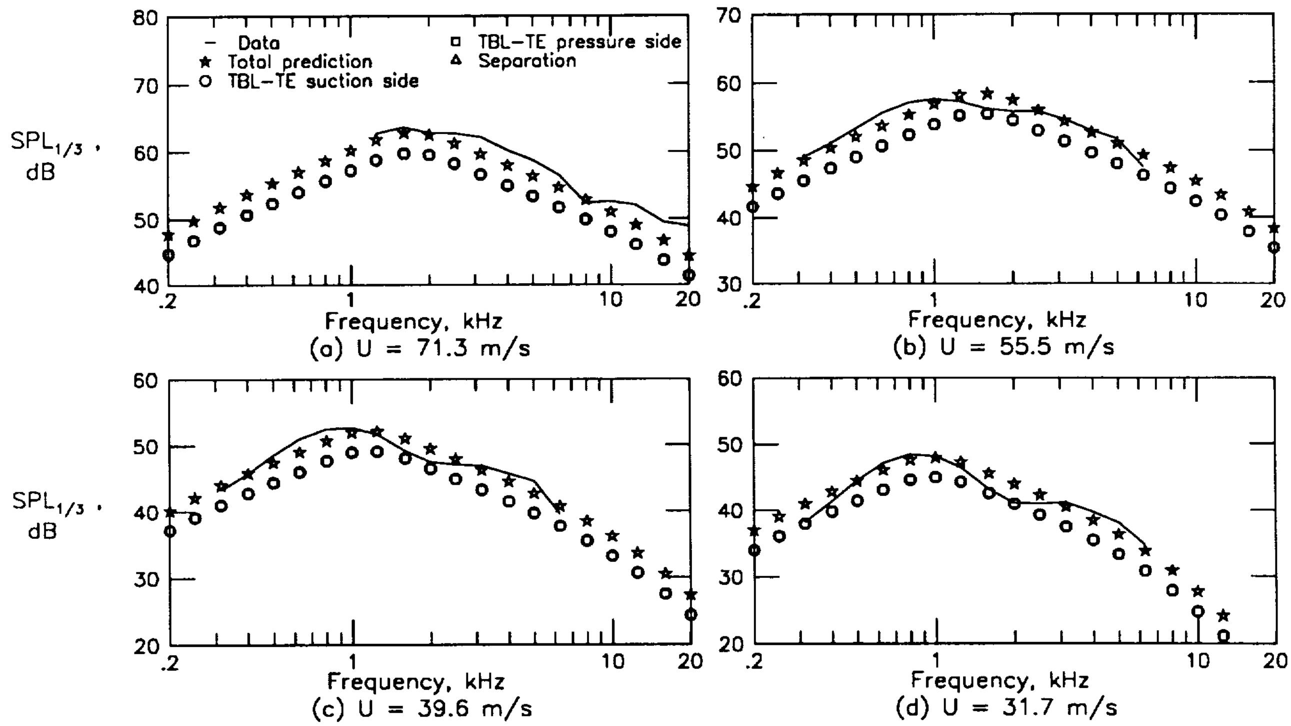

Figure 15. Self-noise spectra for 22.86-cm-chord airfoil with tripped BL at $\alpha_t = 0°$ ($\alpha_* = 0°$).

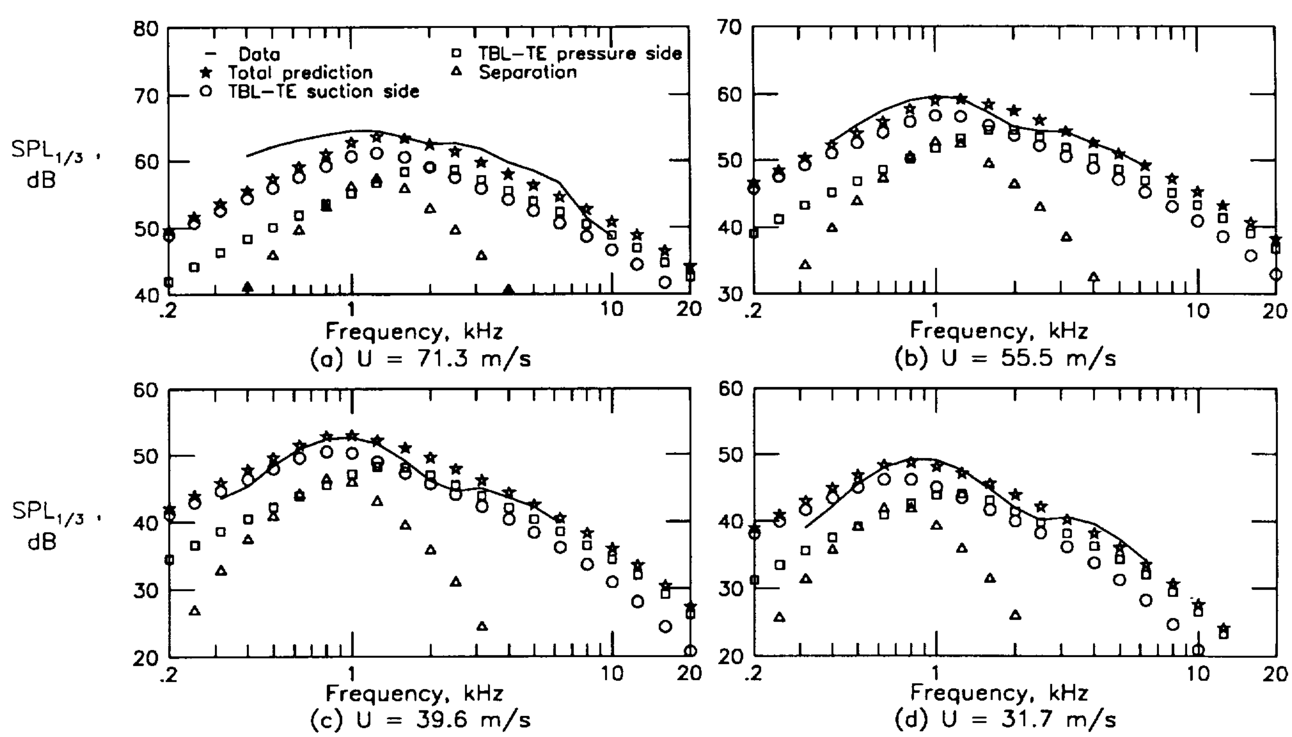

Figure 16. Self-noise spectra for 22.86-cm-chord airfoil with tripped BL at $\alpha_t = 5.4°$ ($\alpha_* = 2.0°$).

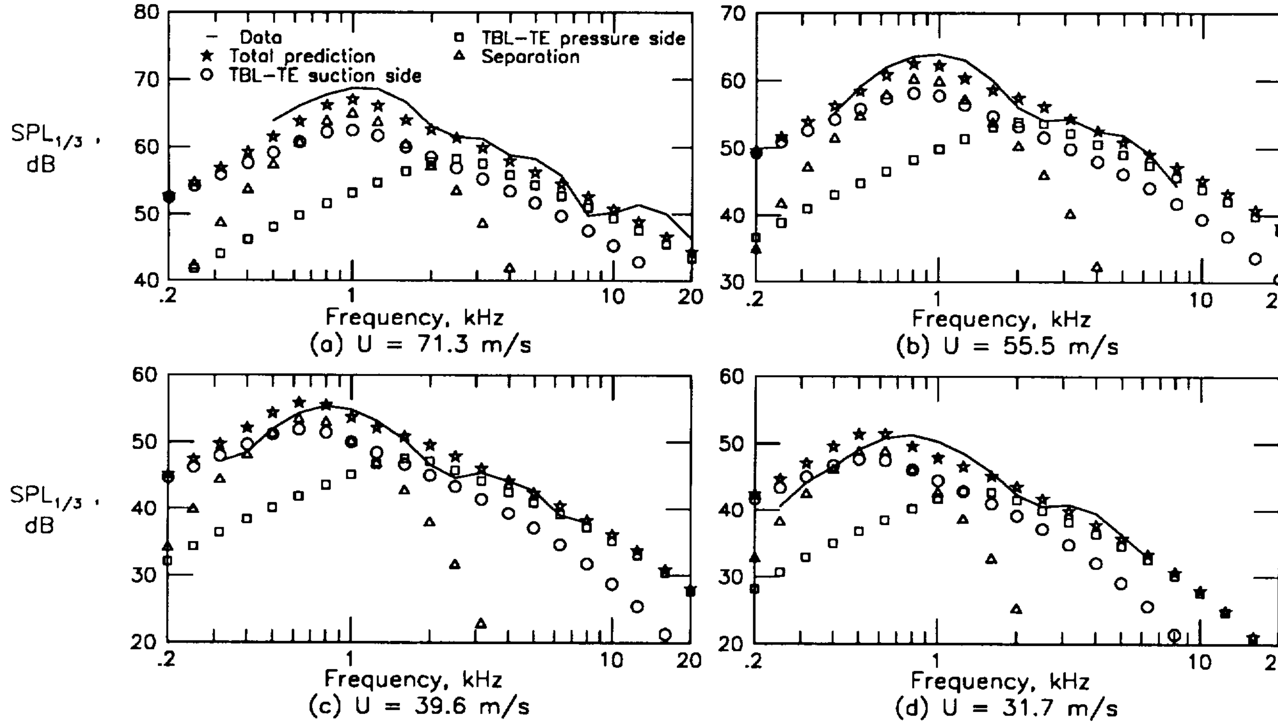

Figure 17. Self-noise spectra for 22.86-cm-chord airfoil with tripped BL at $\alpha_t = 10.8°$ ($\alpha_* = 4.0°$).

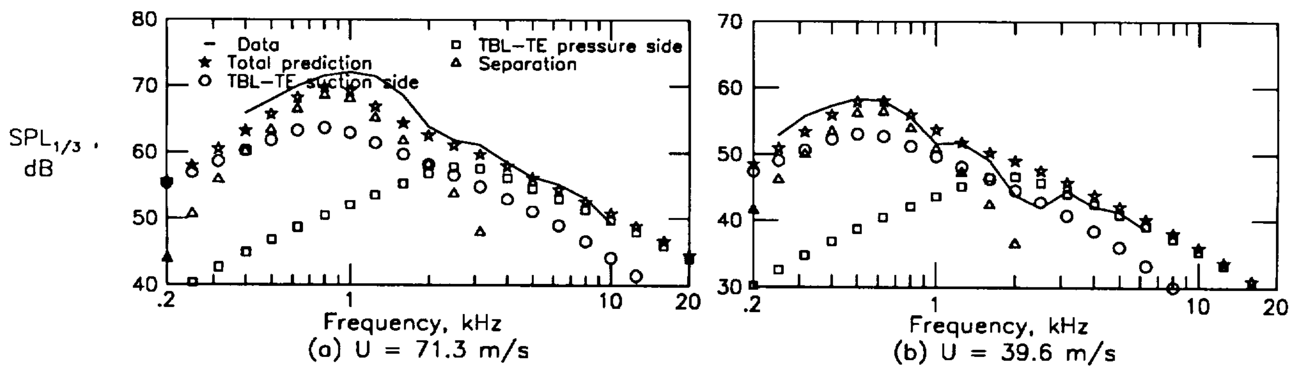

Figure 18. Self-noise spectra for 22.86-cm-chord airfoil with tripped BL at $\alpha_t = 14.4°$ ($\alpha_* = 5.3°$).

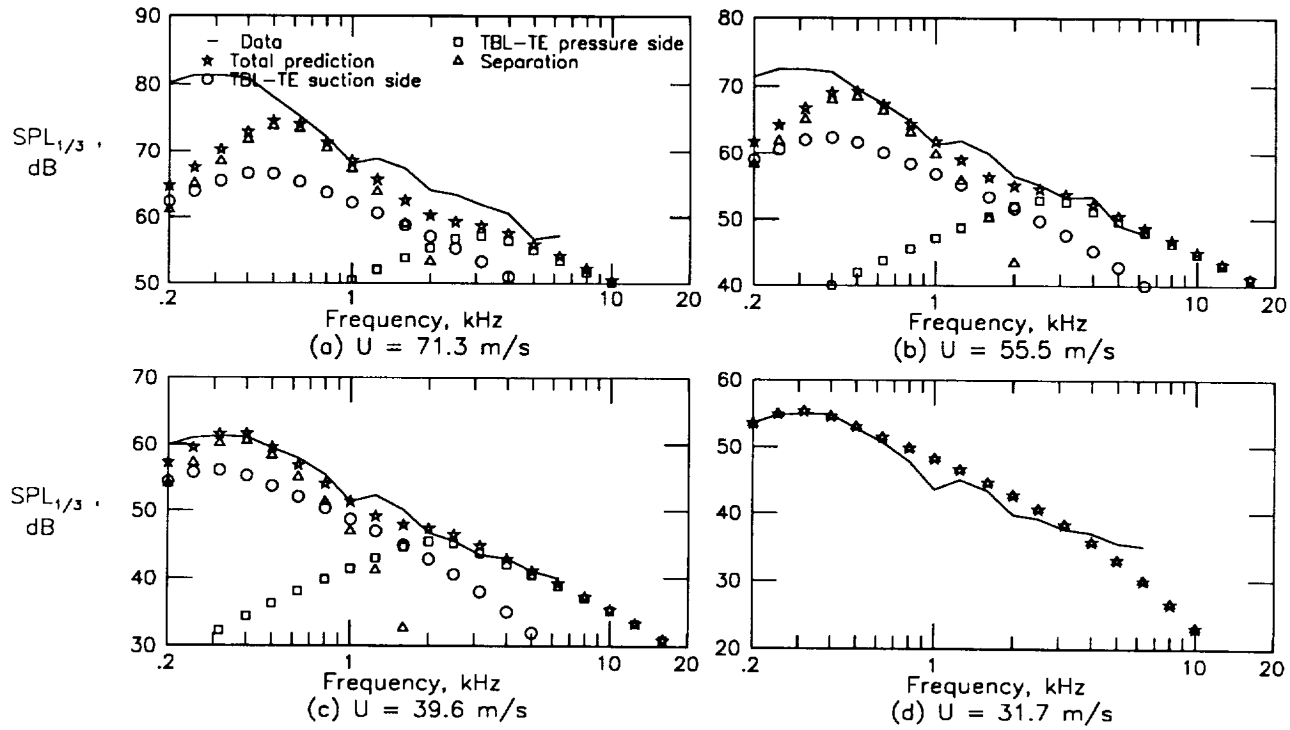

Figure 19. Self-noise spectra for 22.86-cm-chord airfoil with tripped BL at $\alpha_t = 19.8°$ ($\alpha_* = 7.3°$).

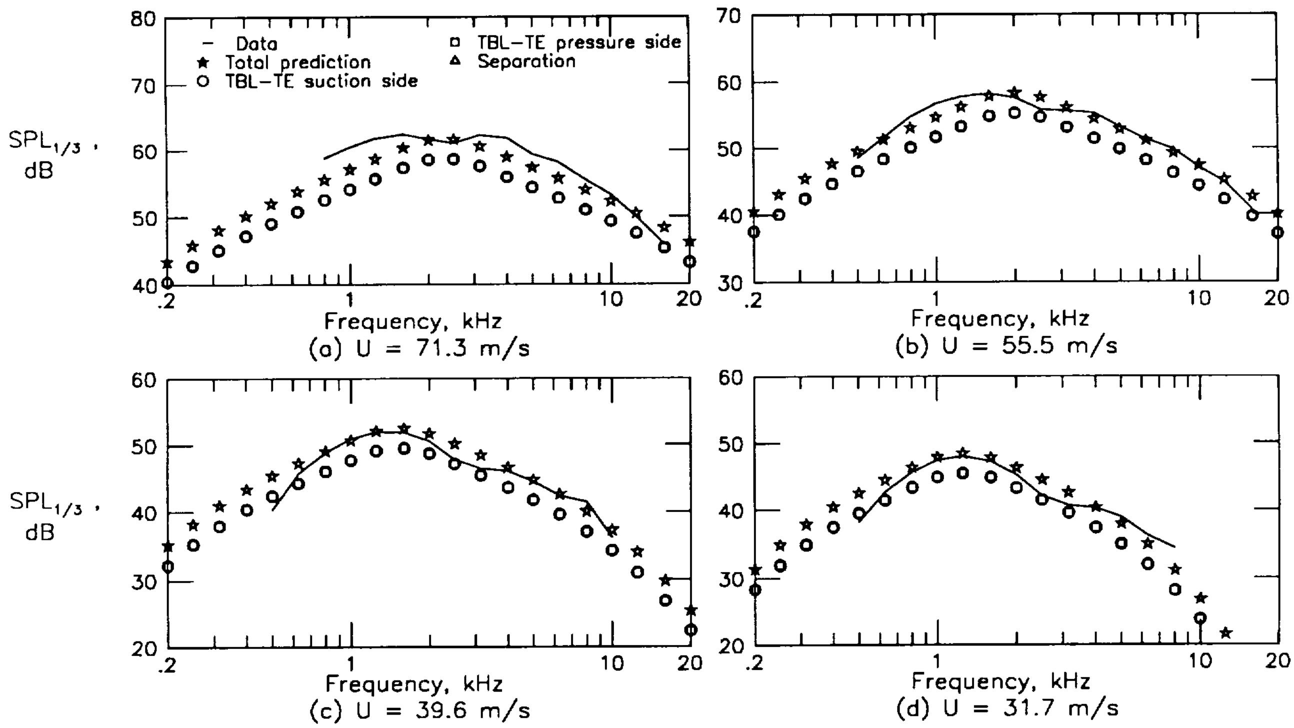

Figure 20. Self-noise spectra for 15.24-cm-chord airfoil with tripped BL at $\alpha_t = 0°$ ($\alpha_* = 0°$).

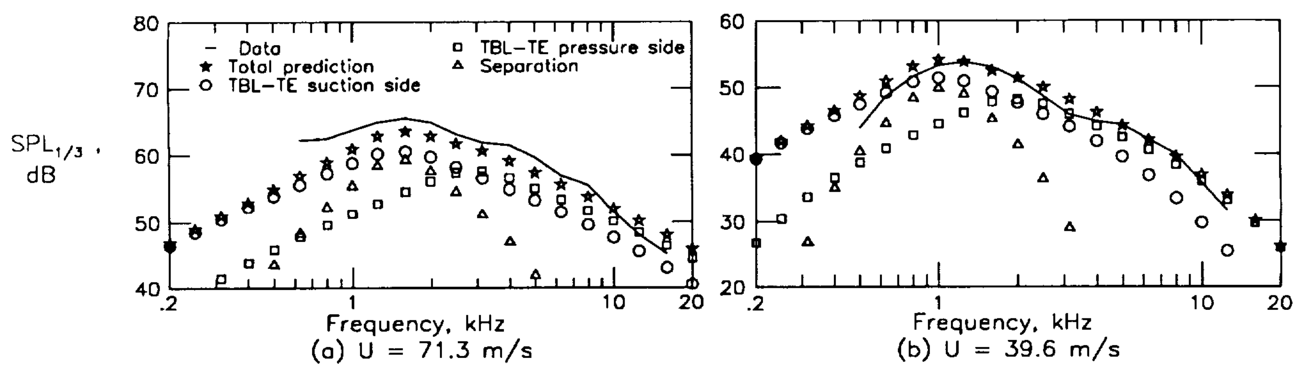

Figure 21. Self-noise spectra for 15.24-cm-chord airfoil with tripped BL at $\alpha_t = 5.4°$ ($\alpha_* = 2.7°$).

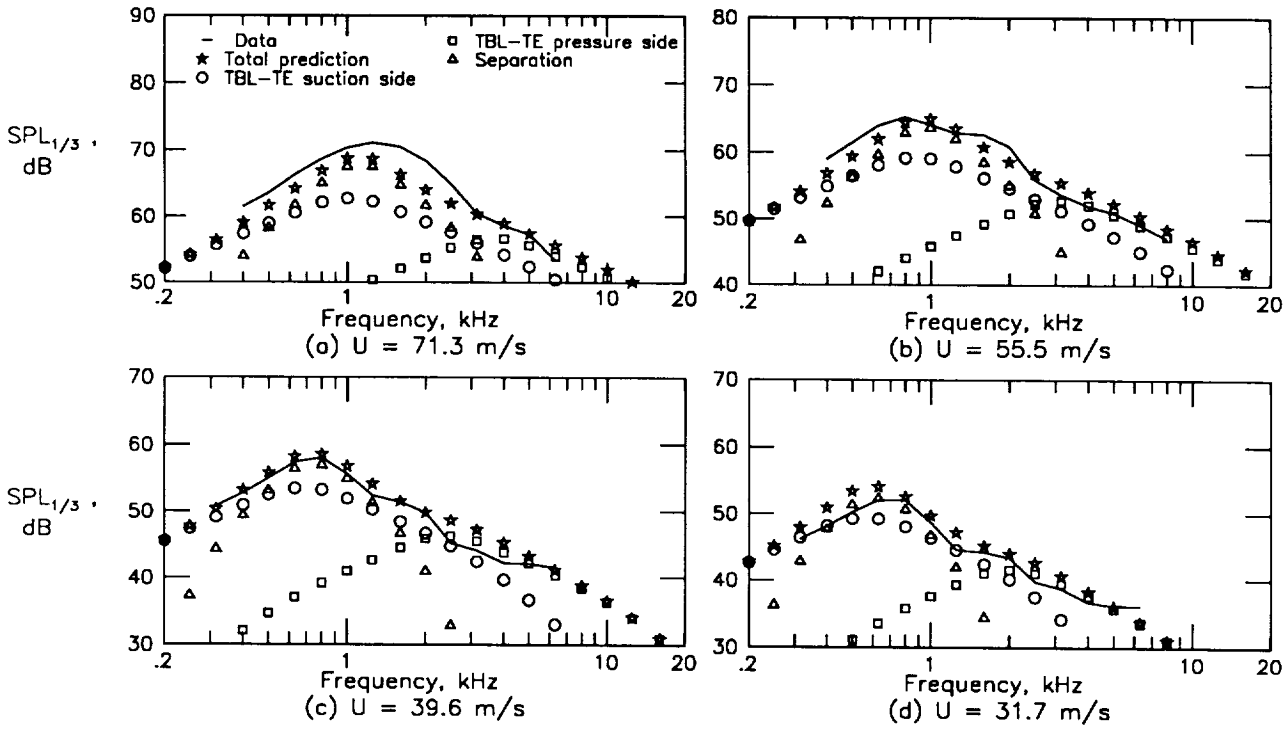

Figure 22. Self-noise spectra for 15.24-cm-chord airfoil with tripped BL at $\alpha_t = 10.8°$ ($\alpha_* = 5.4°$).

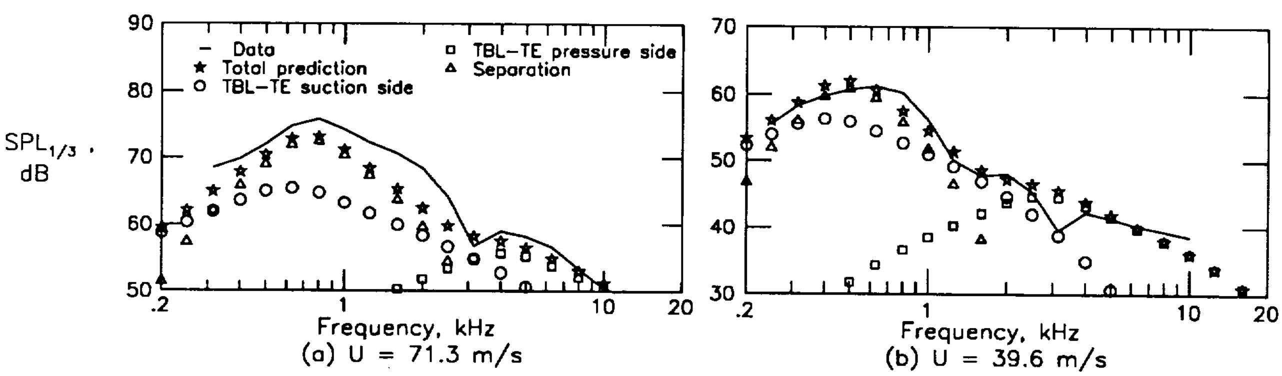

Figure 23. Self-noise spectra for 15.24-cm-chord airfoil with tripped BL at $\alpha_t = 14.4°$ ($\alpha_* = 7.2°$).

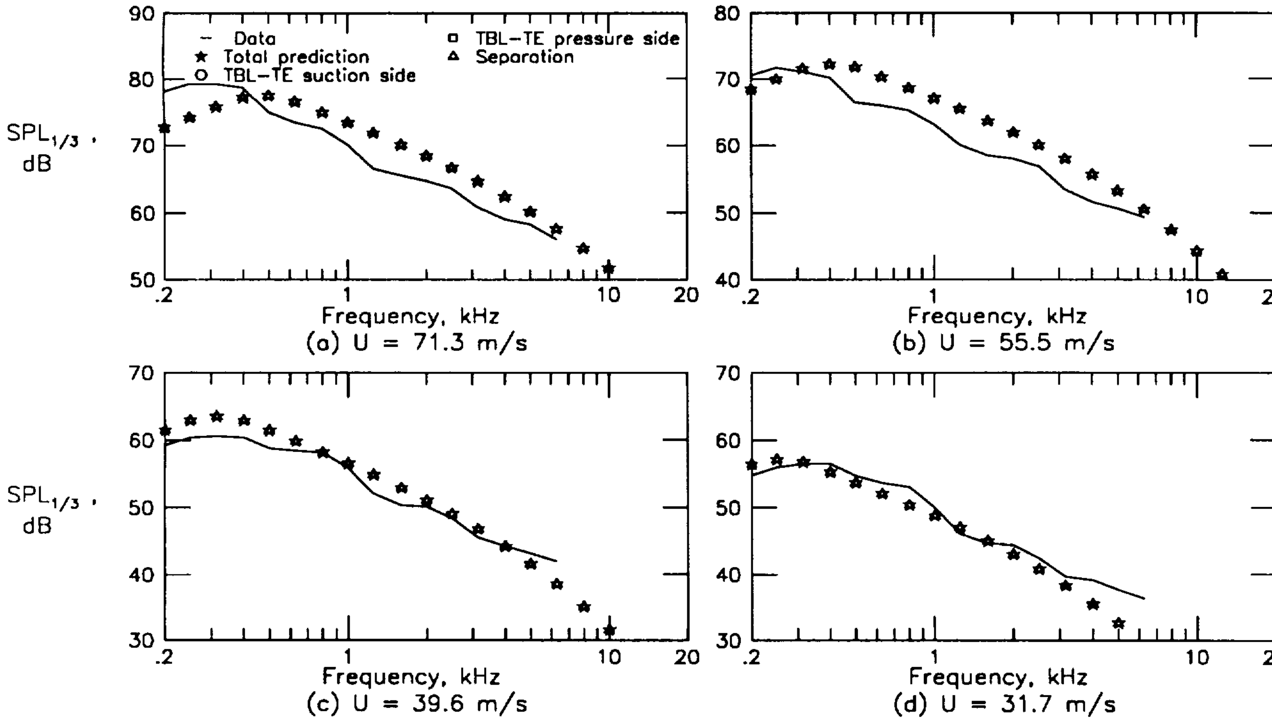

Figure 24. Self-noise spectra for 15.24-cm-chord airfoil with tripped BL at $\alpha_t = 19.8°$ ($\alpha_* = 9.9°$).

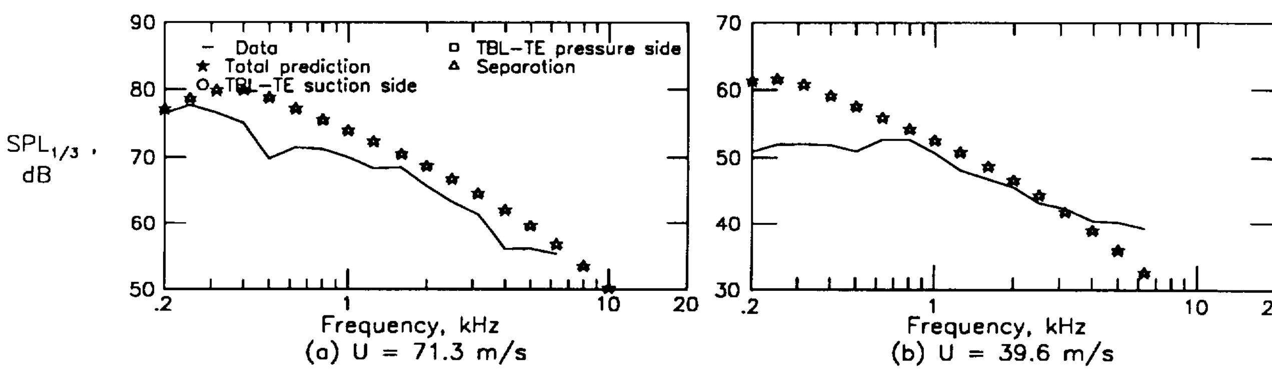

Figure 25. Self-noise spectra for 15.24-cm-chord airfoil with tripped BL at $\alpha_t = 25.2°$ ($\alpha_* = 12.6°$).

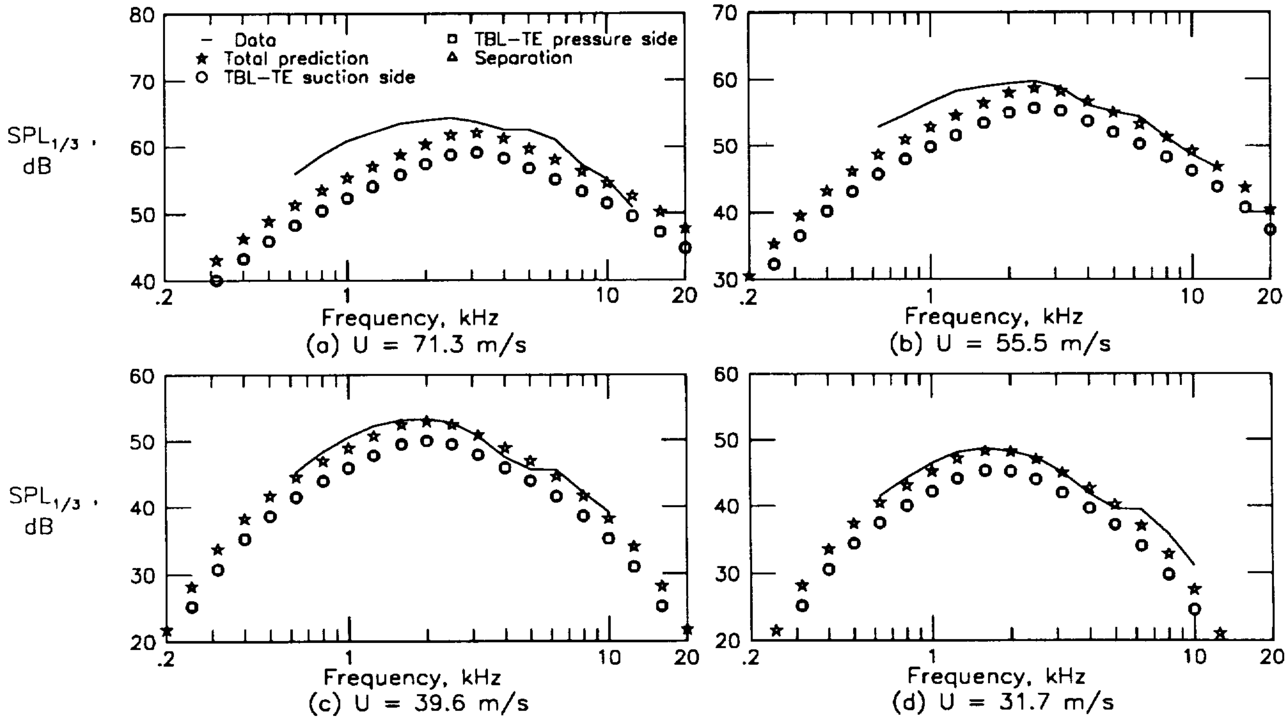

Figure 26. Self-noise spectra for 10.16-cm-chord airfoil with tripped BL at $\alpha_t = 0°$ ($\alpha_* = 0°$).

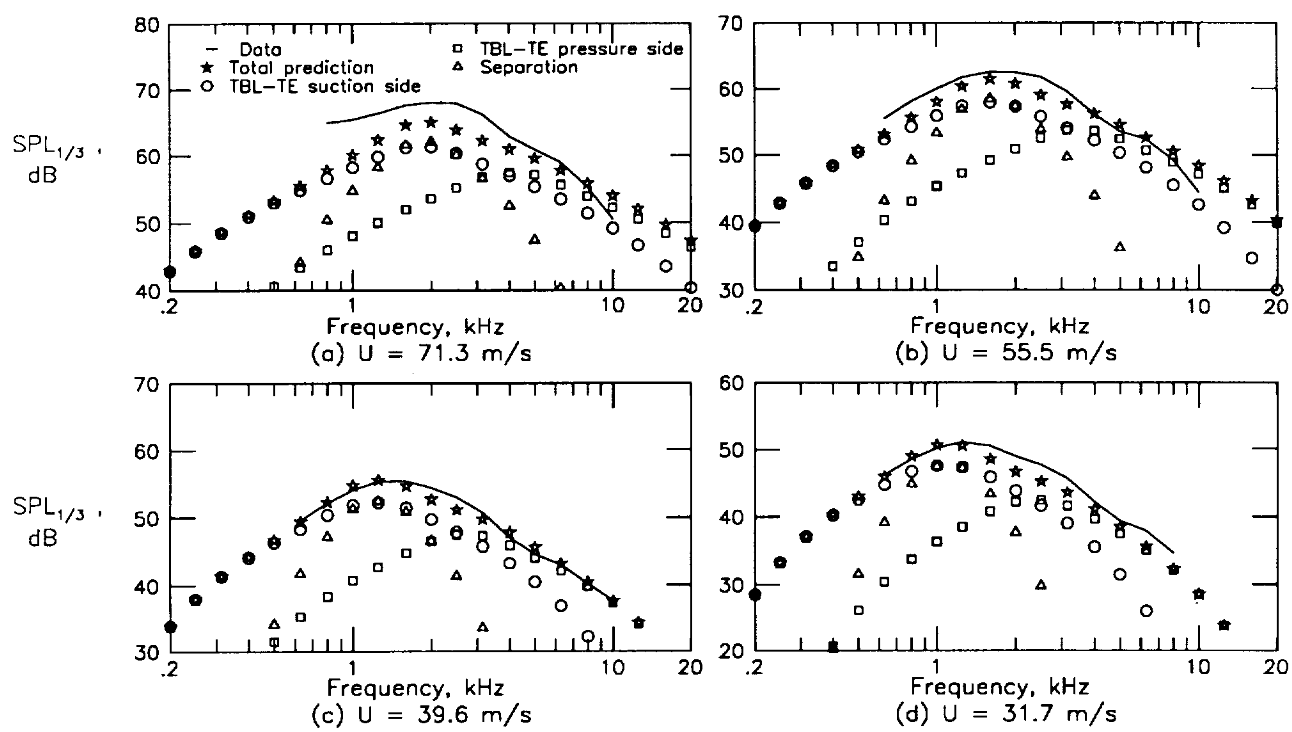

Figure 27. Self-noise spectra for 10.16-cm-chord airfoil with tripped BL at $\alpha_t = 5.4°$ ($\alpha_* = 3.3°$).

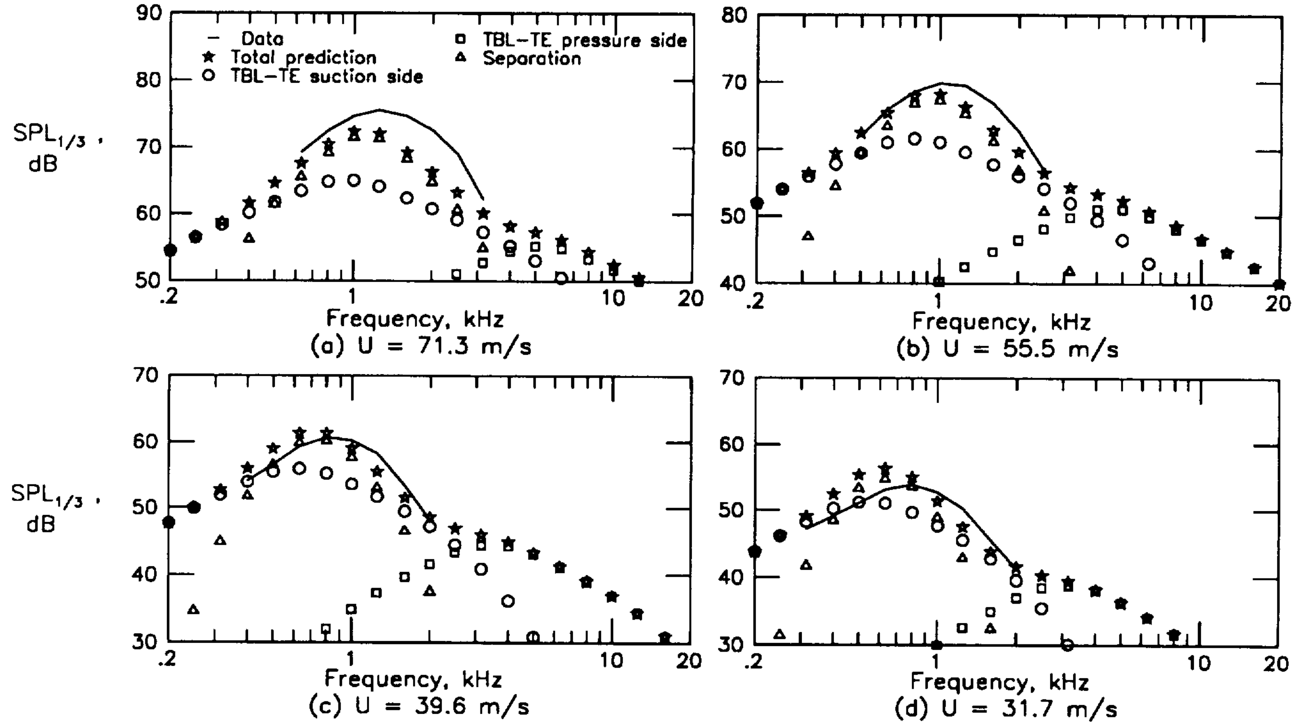

Figure 28. Self-noise spectra for 10.16-cm-chord airfoil with tripped BL at $\alpha_t = 10.8°$ ($\alpha_* = 6.7°$).

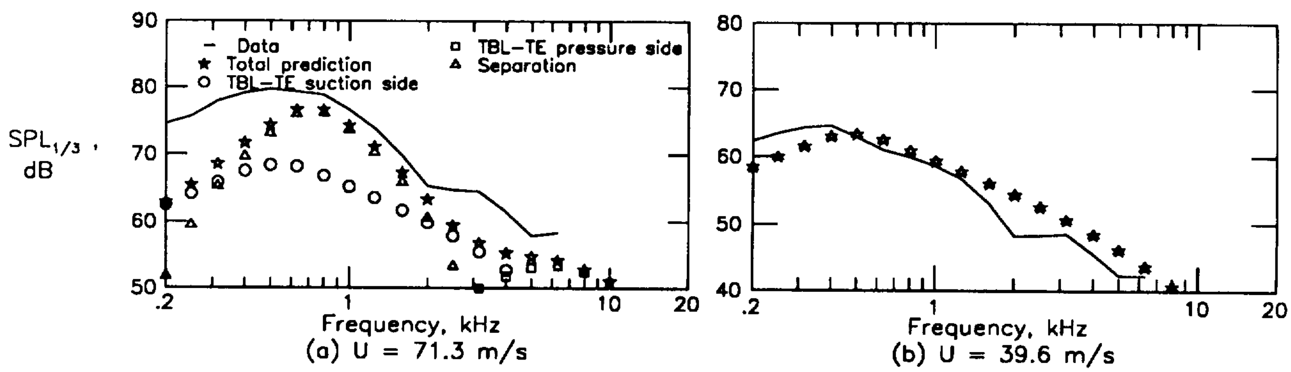

Figure 29. Self-noise spectra for 10.16-cm-chord airfoil with tripped BL at $\alpha_t = 14.4°$ ($\alpha_* = 8.9°$).

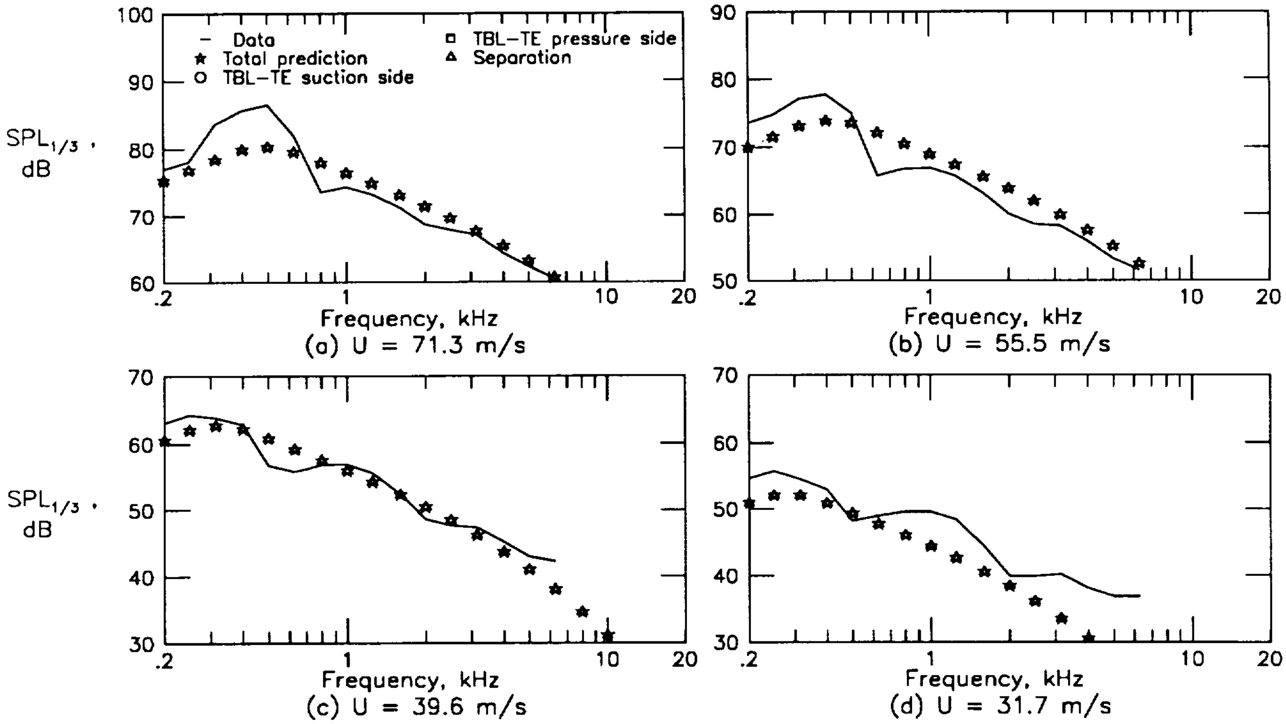

Figure 30. Self-noise spectra for 10.16-cm-chord airfoil with tripped BL at $\alpha_t = 19.8°$ ($\alpha_* = 12.3°$).

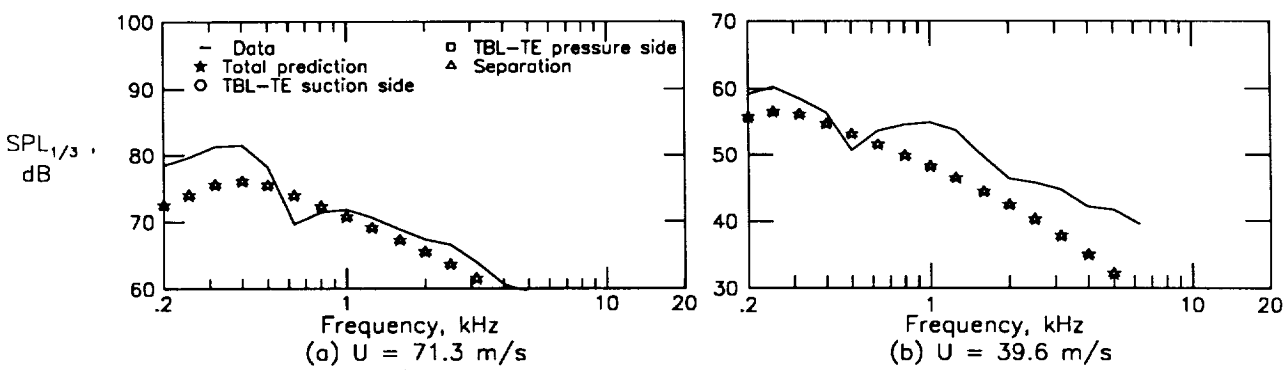

Figure 31. Self-noise spectra for 10.16-cm-chord airfoil with tripped BL at $\alpha_t = 25.2°$ ($\alpha_* = 15.6°$).

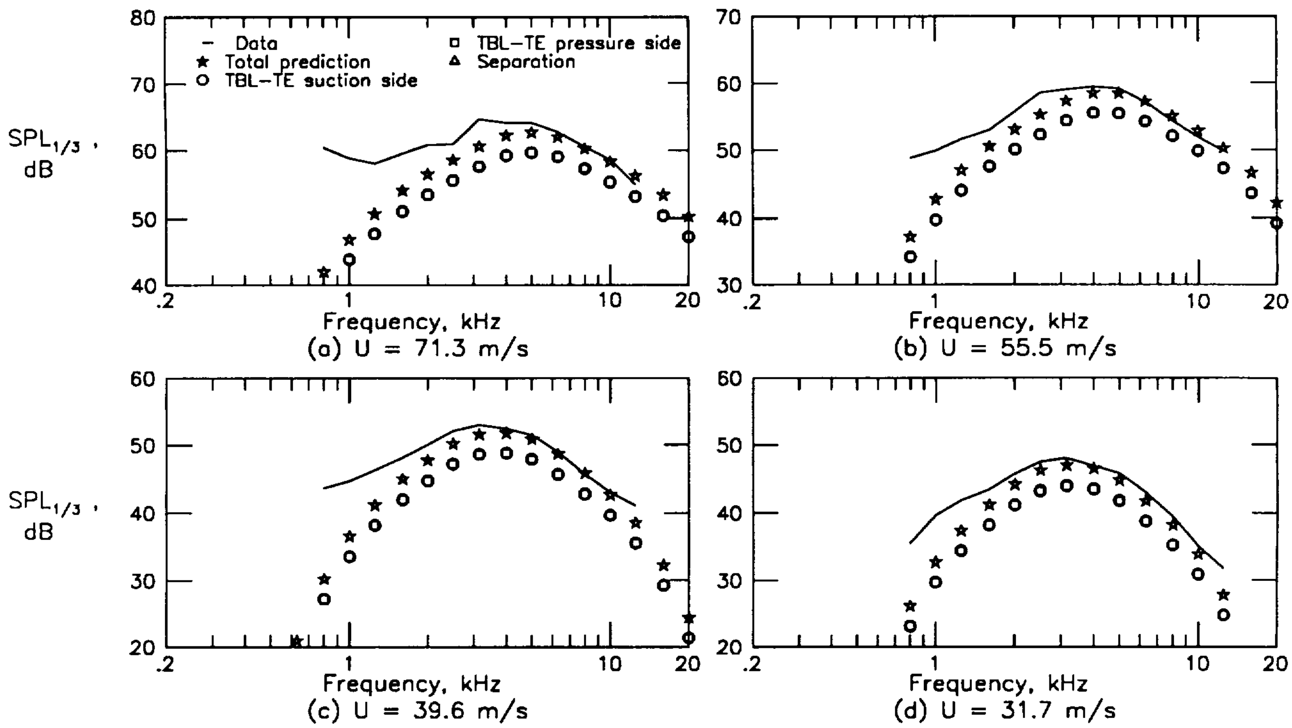

Figure 32. Self-noise spectra for 5.08-cm-chord airfoil with tripped BL at $\alpha_t = 0°$ ($\alpha_* = 0°$).

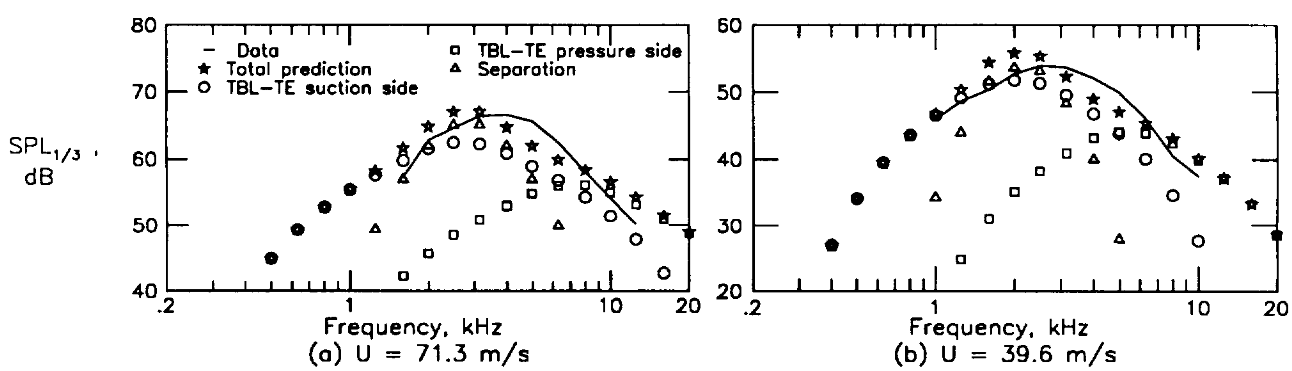

Figure 33. Self-noise spectra for 5.08-cm-chord airfoil with tripped BL at $\alpha_t = 5.4°$ ($\alpha_* = 4.2°$).

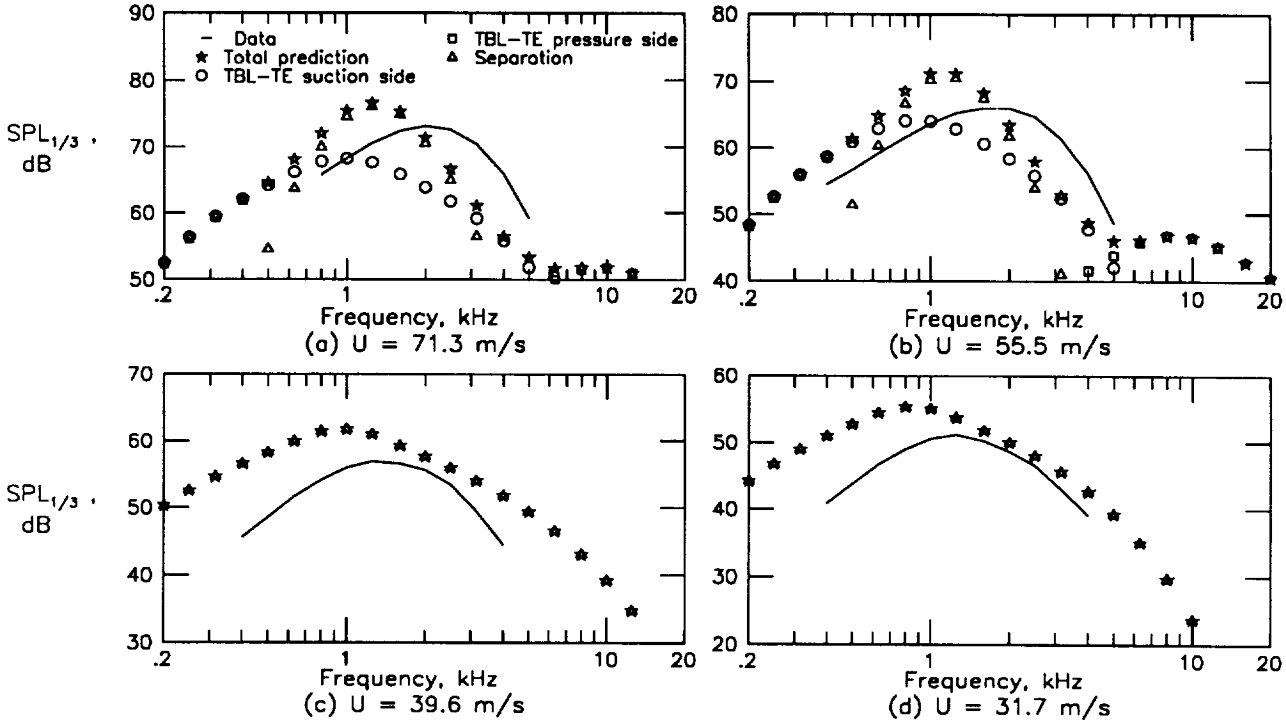

Figure 34. Self-noise spectra for 5.08-cm-chord airfoil with tripped BL at $\alpha_t = 10.8°$ ($\alpha_* = 8.4°$).

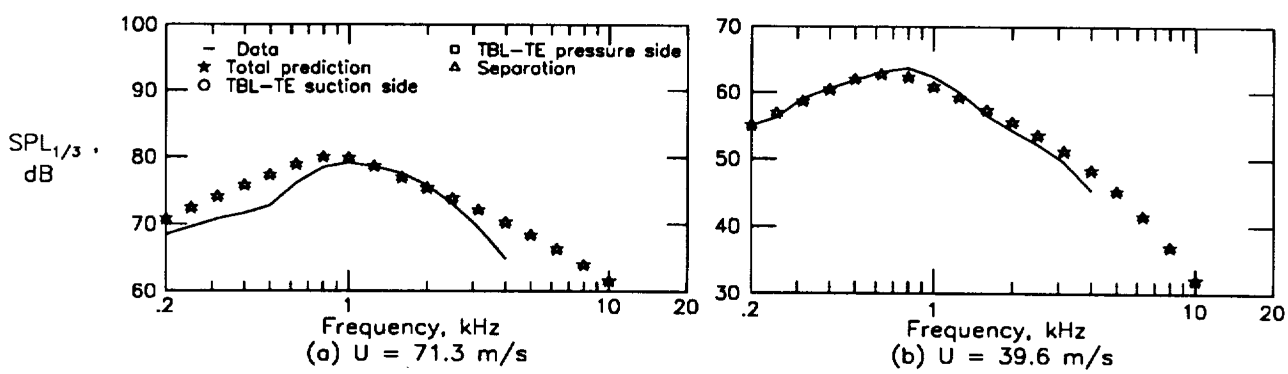

Figure 35. Self-noise spectra for 5.08-cm-chord airfoil with tripped BL at $\alpha_t = 14.4°$ ($\alpha_* = 11.2°$).

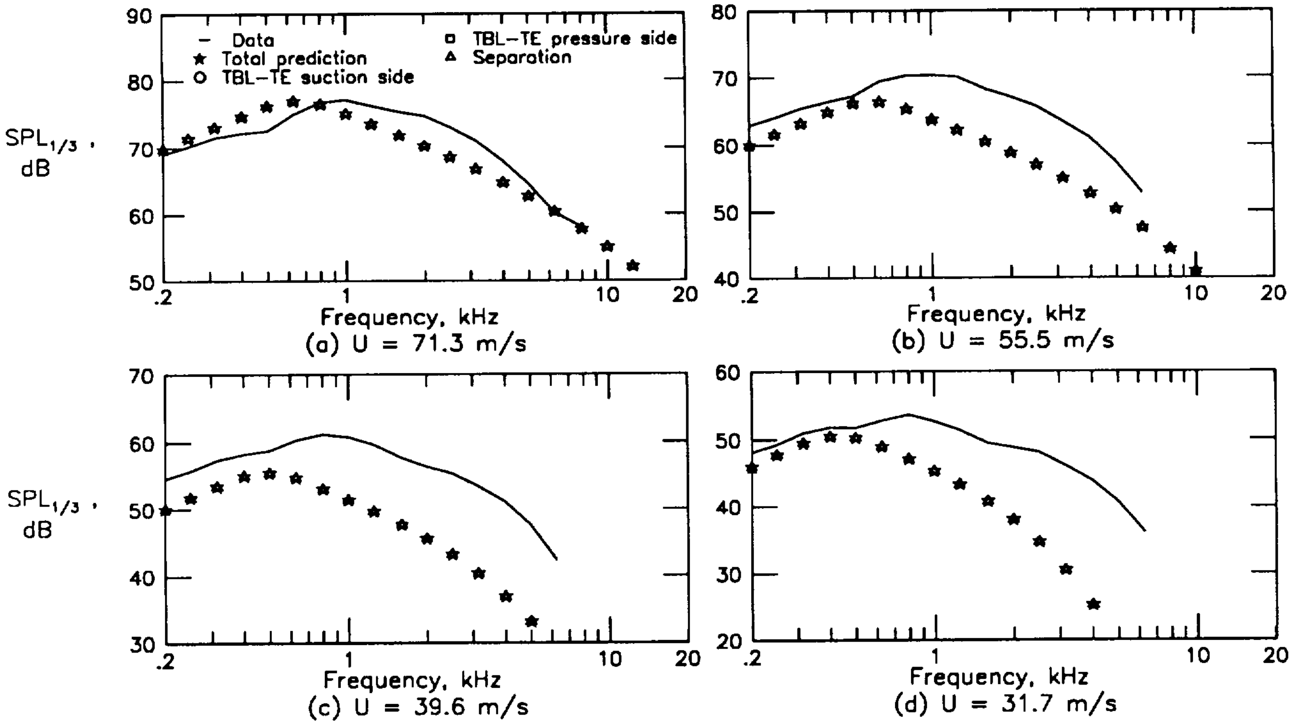

Figure 36. Self-noise spectra for 5.08-cm-chord airfoil with tripped BL at $\alpha_t = 19.8°$ ($\alpha_* = 15.4°$).

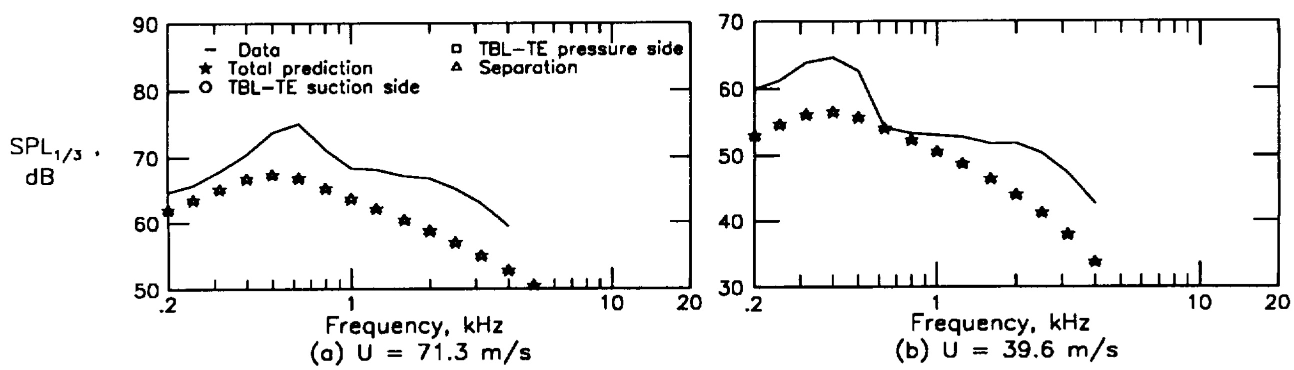

Figure 37. Self-noise spectra for 5.08-cm-chord airfoil with tripped BL at $\alpha_t = 25.2°$ ($\alpha_* = 19.7°$).

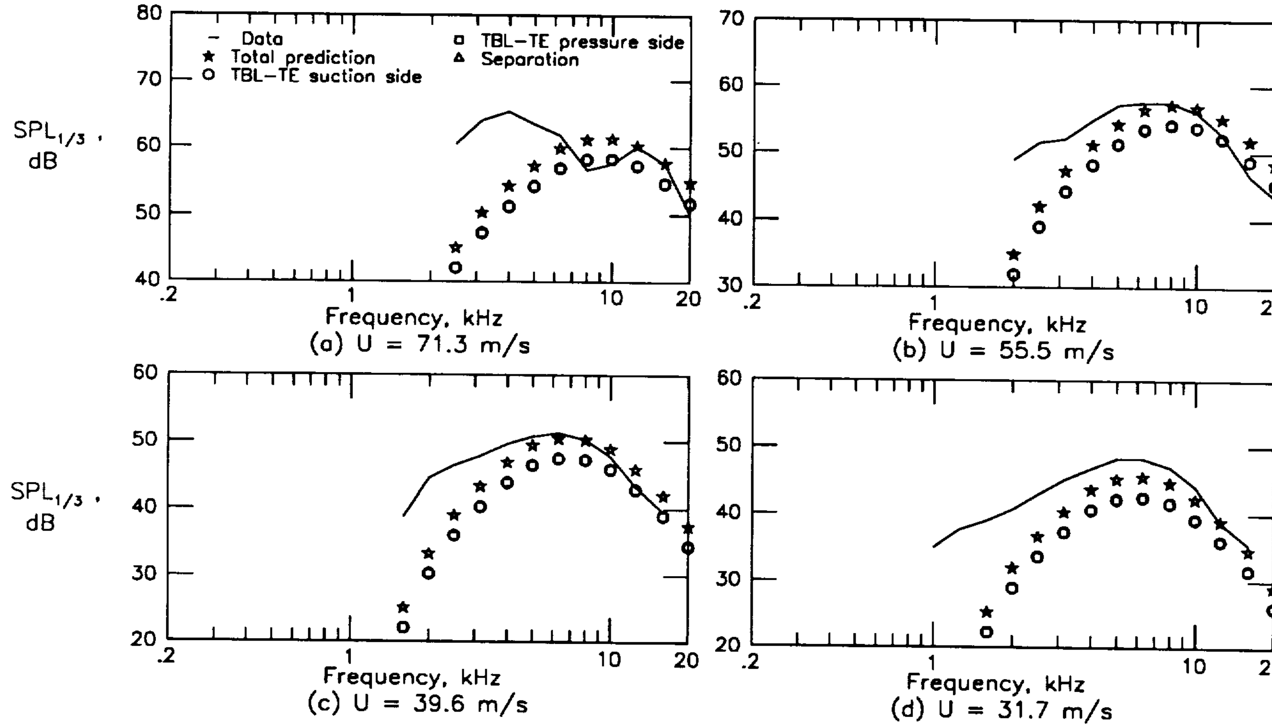

Figure 38. Self-noise spectra for 2.54-cm-chord airfoil with tripped BL at $\alpha_t = 0°$ ($\alpha_* = 0°$).

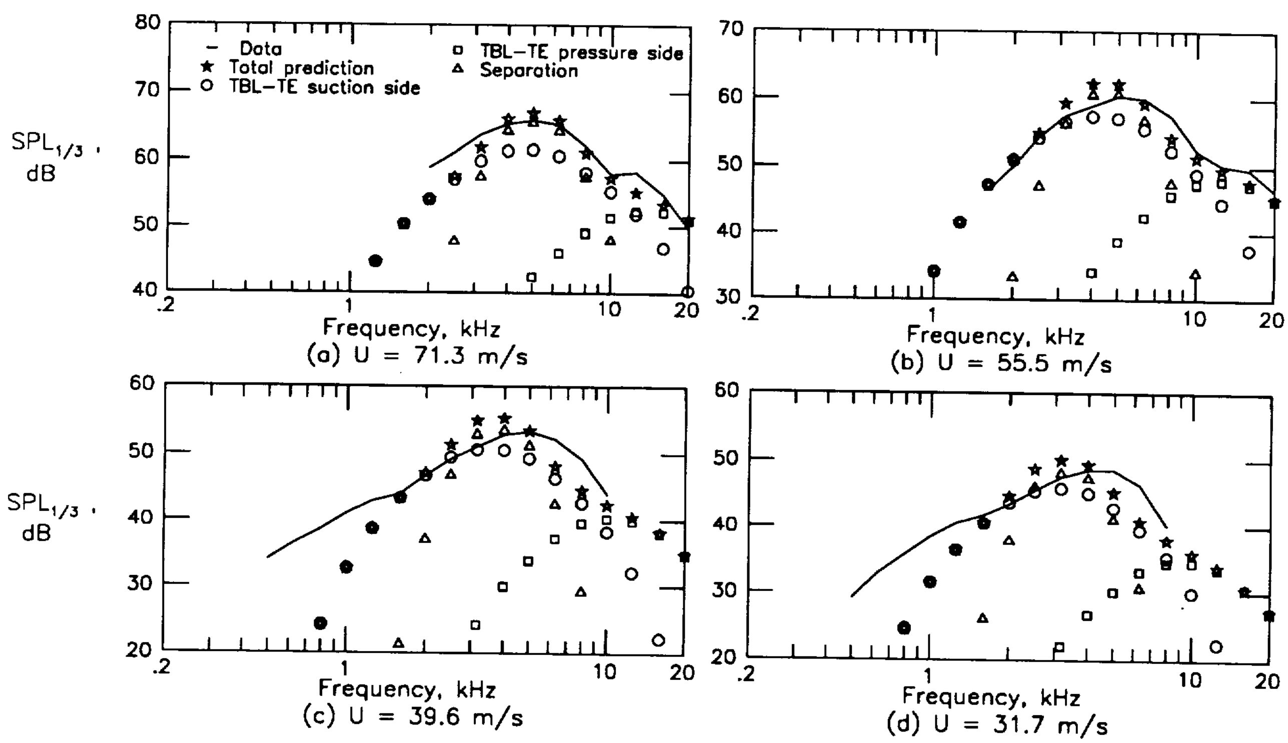

Figure 39. Self-noise spectra for 2.54-cm-chord airfoil with tripped BL at $\alpha_t = 5.4°$ ($\alpha_* = 4.8°$).

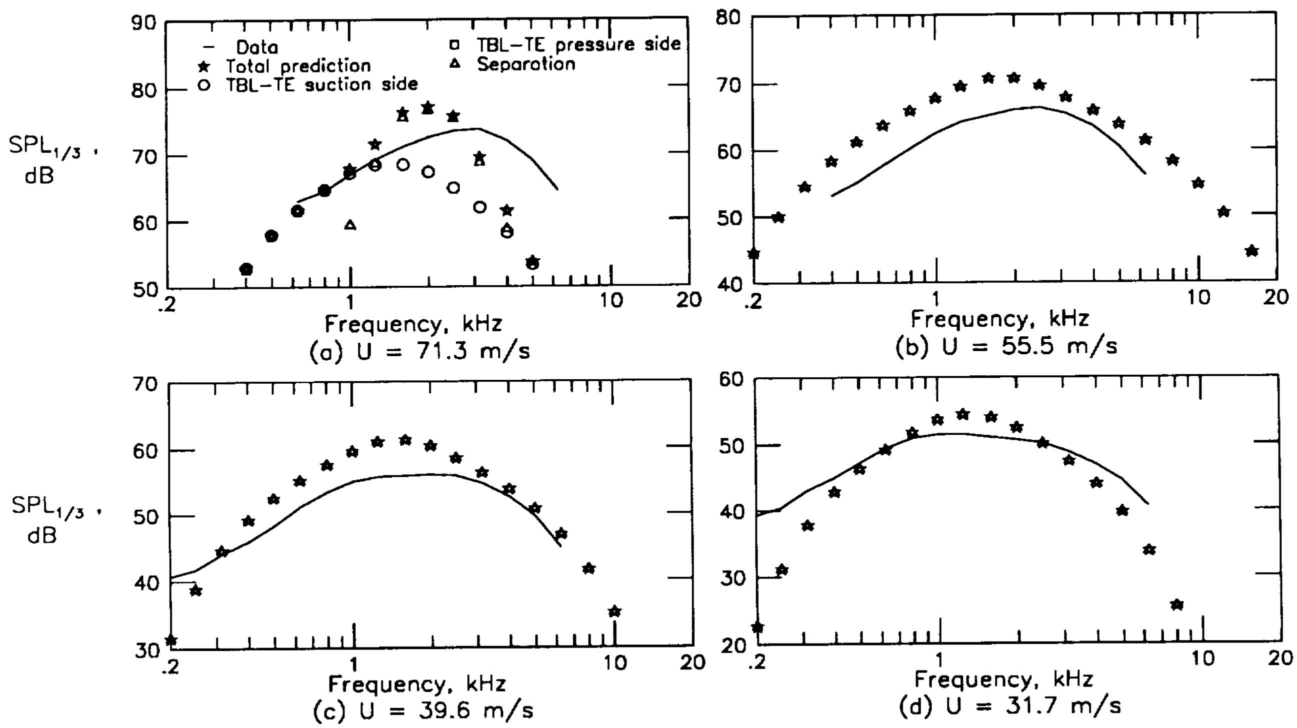

Figure 40. Self-noise spectra for 2.54-cm-chord airfoil with tripped BL at $\alpha_t = 10.8°$ ($\alpha_* = 9.5°$).

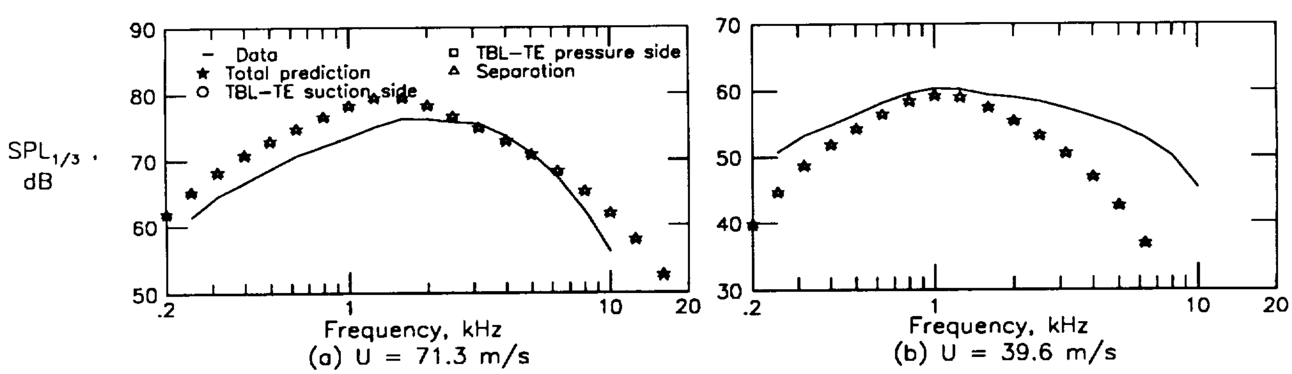

Figure 41. Self-noise spectra for 2.54-cm-chord airfoil with tripped BL at $\alpha_t = 14.4°$ ($\alpha_* = 12.7°$).

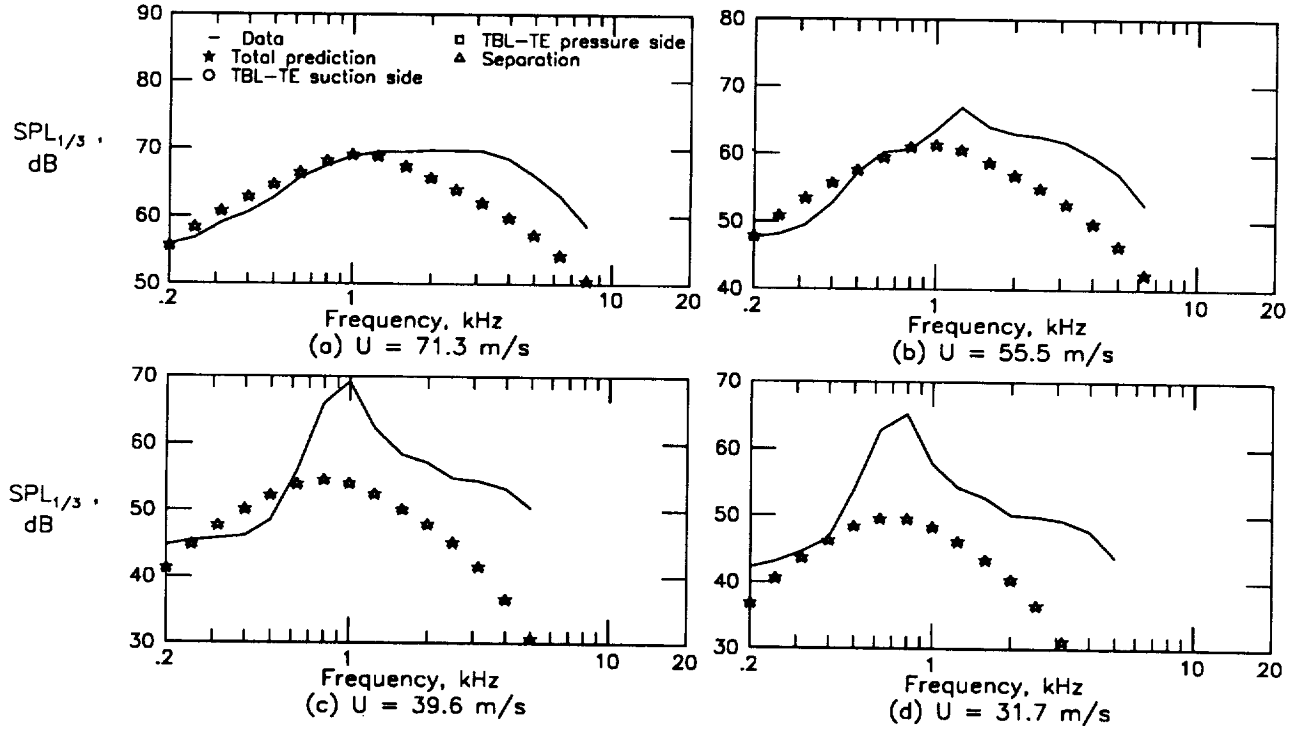

Figure 42. Self-noise spectra for 2.54-cm-chord airfoil with tripped BL at $\alpha_t = 19.8°$ ($\alpha_* = 17.4°$).

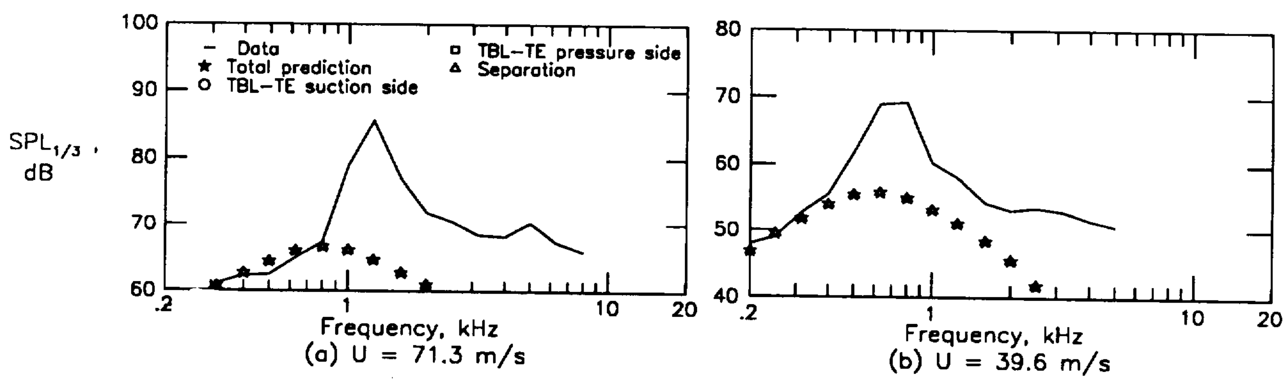

Figure 43. Self-noise spectra for 2.54-cm-chord airfoil with tripped BL at $\alpha_t = 25.2°$ ($\alpha_* = 22.2°$).

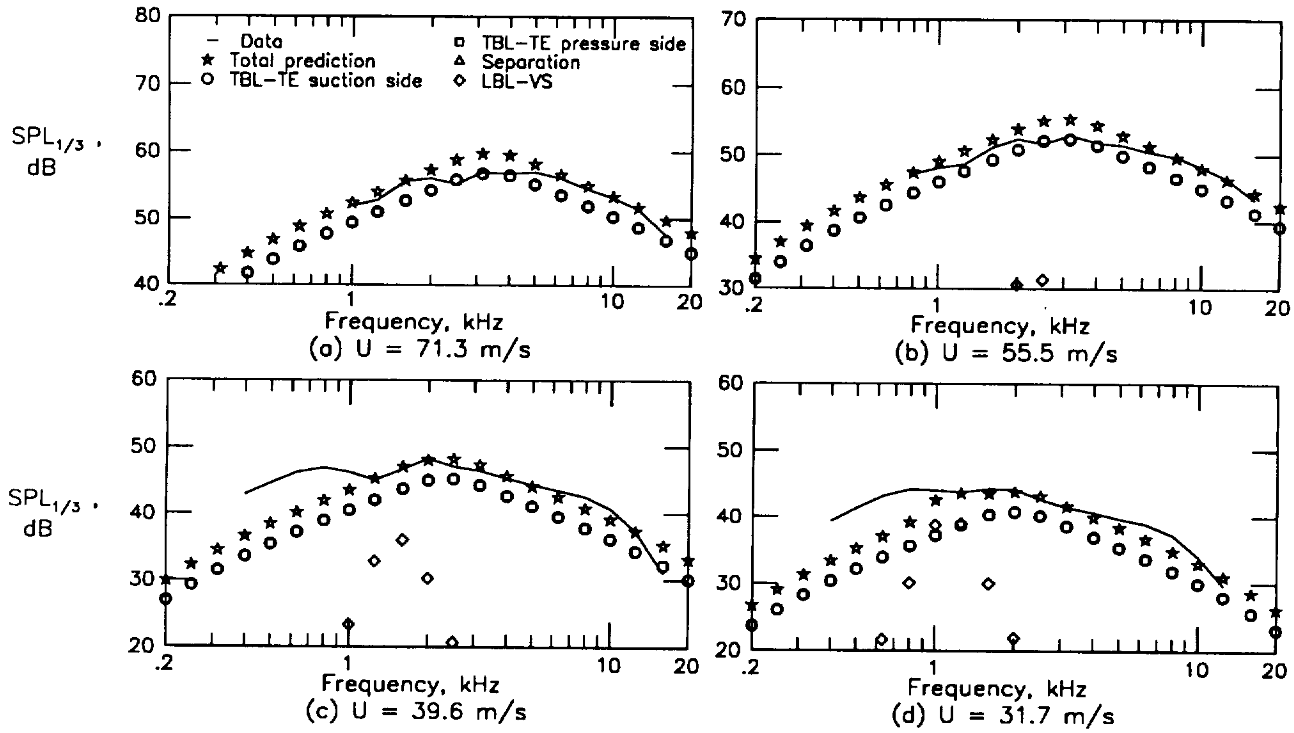

Figure 44. Self-noise spectra for 30.48-cm-chord airfoil with untripped BL (natural transition) at $\alpha_t = 0°$ ($\alpha_* = 0°$).

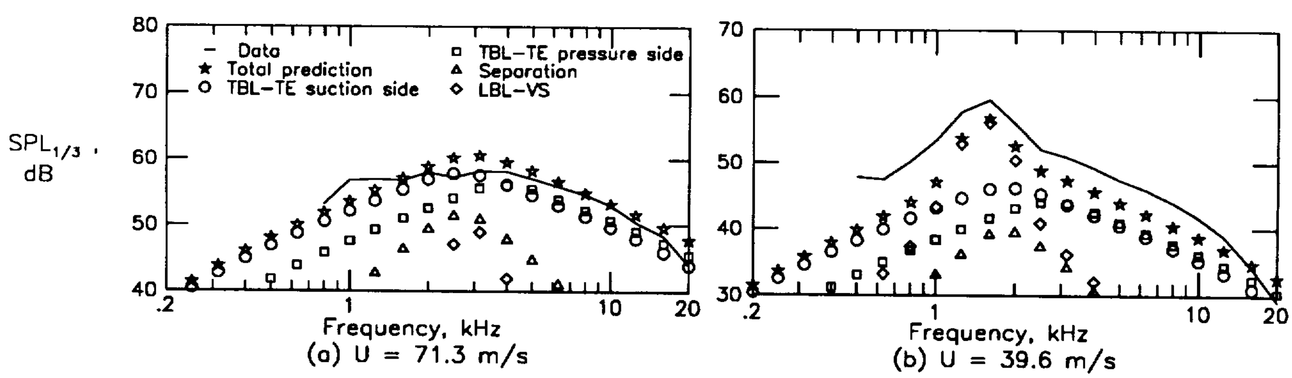

Figure 45. Self-noise spectra for 30.48-cm-chord airfoil with untripped BL at $\alpha_t = 5.4°$ ($\alpha_* = 1.5°$).

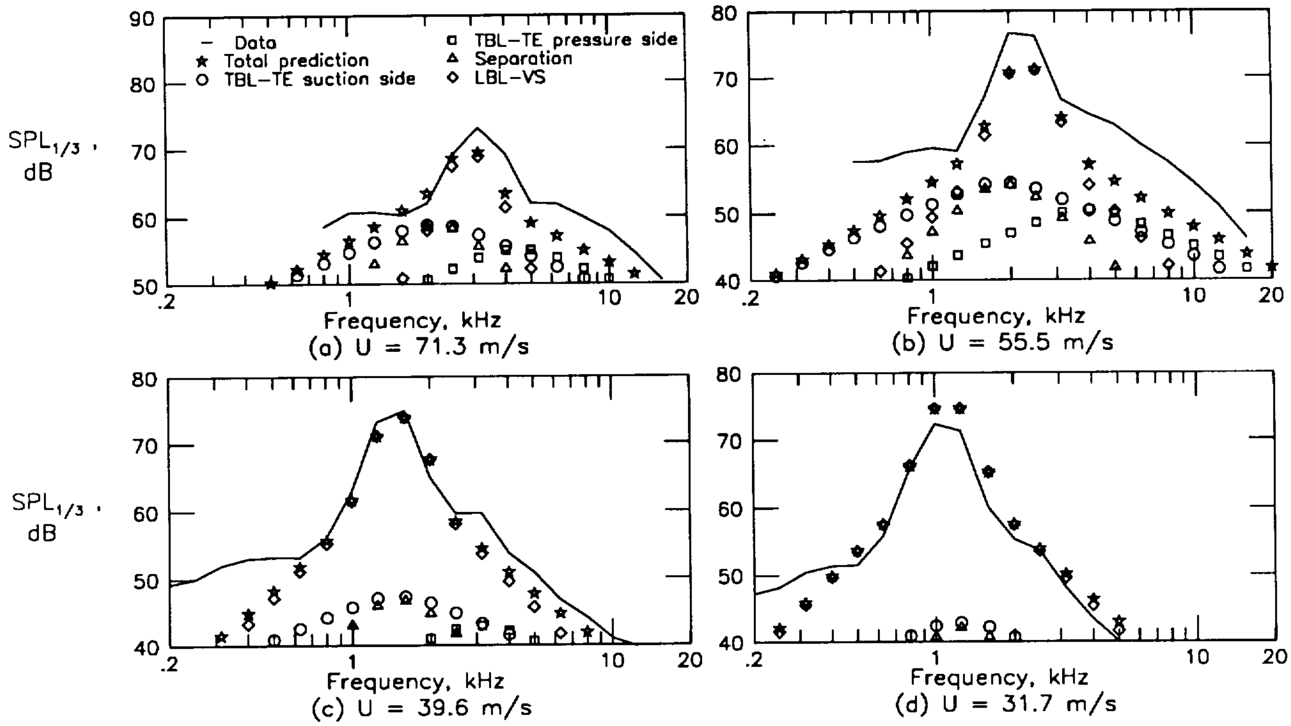

Figure 46. Self-noise spectra for 30.48-cm-chord airfoil with untripped BL at $\alpha_t = 10.8°$ ($\alpha_* = 3.0°$).

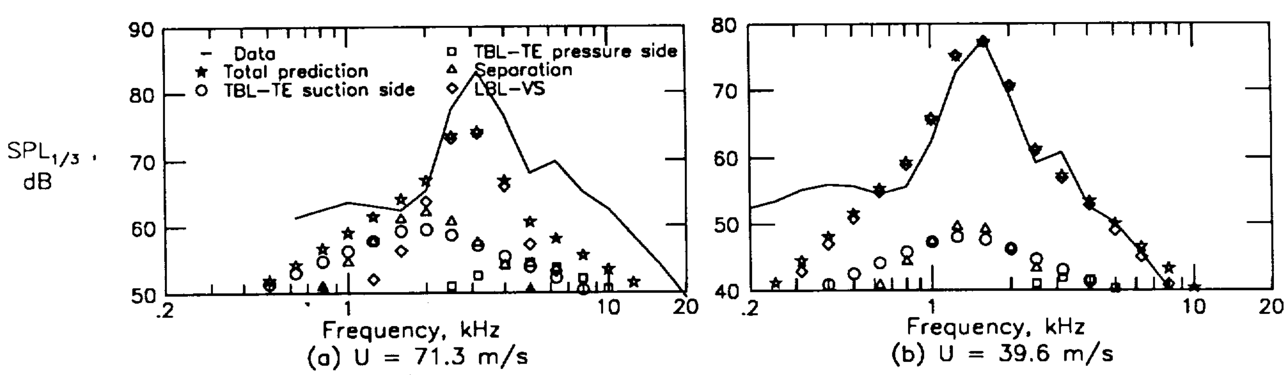

Figure 47. Self-noise spectra for 30.48-cm-chord airfoil with untripped BL at $\alpha_t = 14.4°$ ($\alpha_* = 4.0°$).

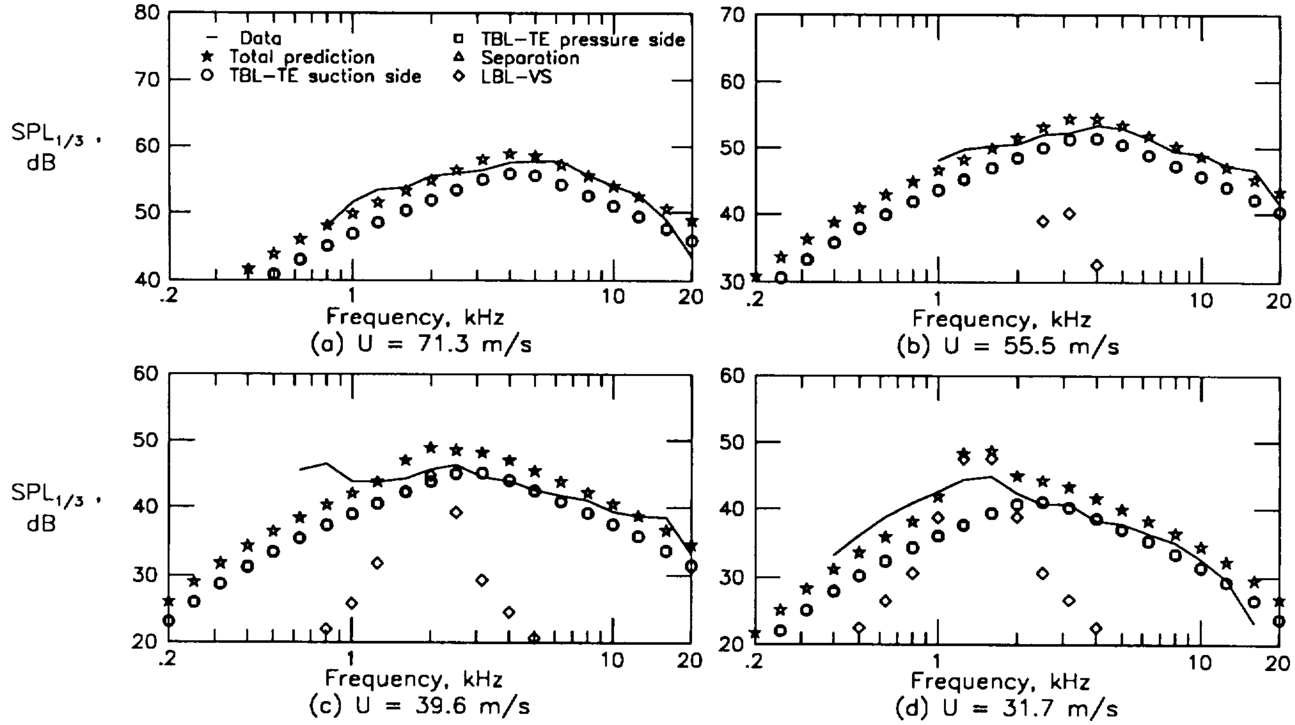

Figure 48. Self-noise spectra for 22.86-cm-chord airfoil with untripped BL at $\alpha_t = 0°$ ($\alpha_* = 0°$).

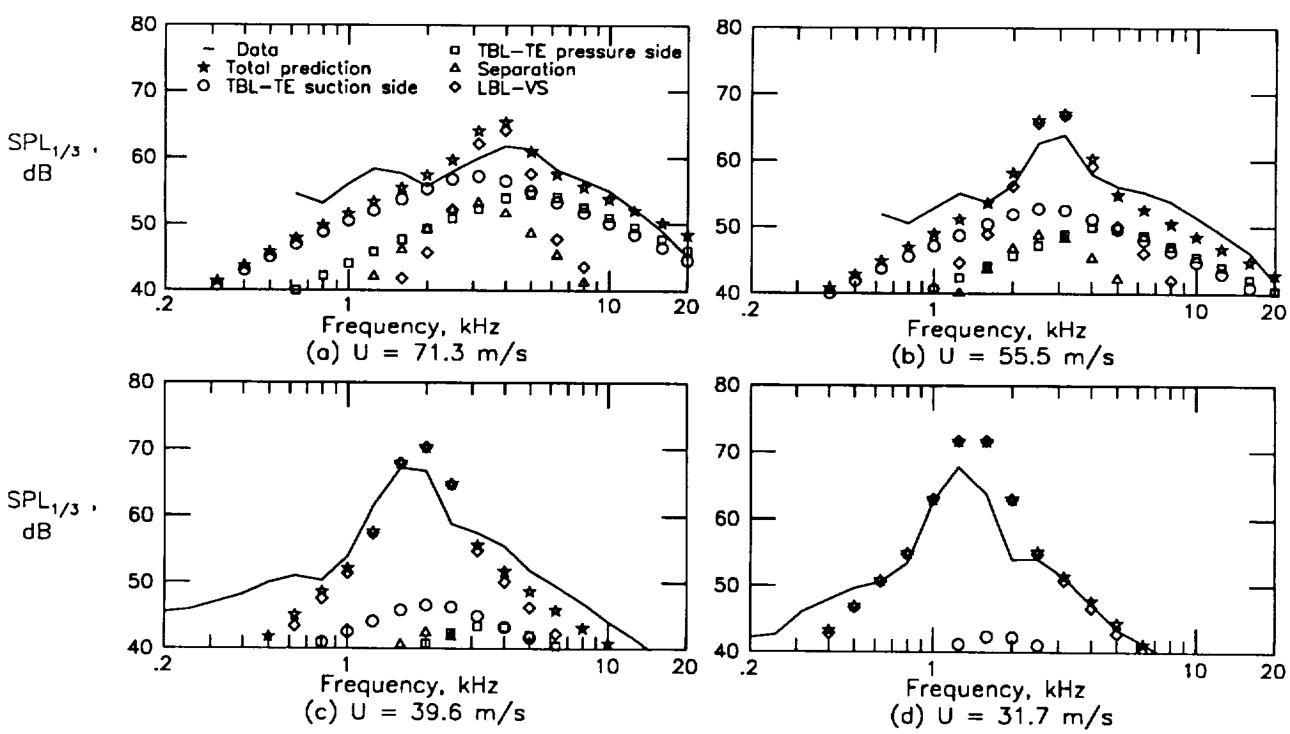

Figure 49. Self-noise spectra for 22.86-cm-chord airfoil with untripped BL at $\alpha_t = 5.4°$ ($\alpha_* = 2.0°$).

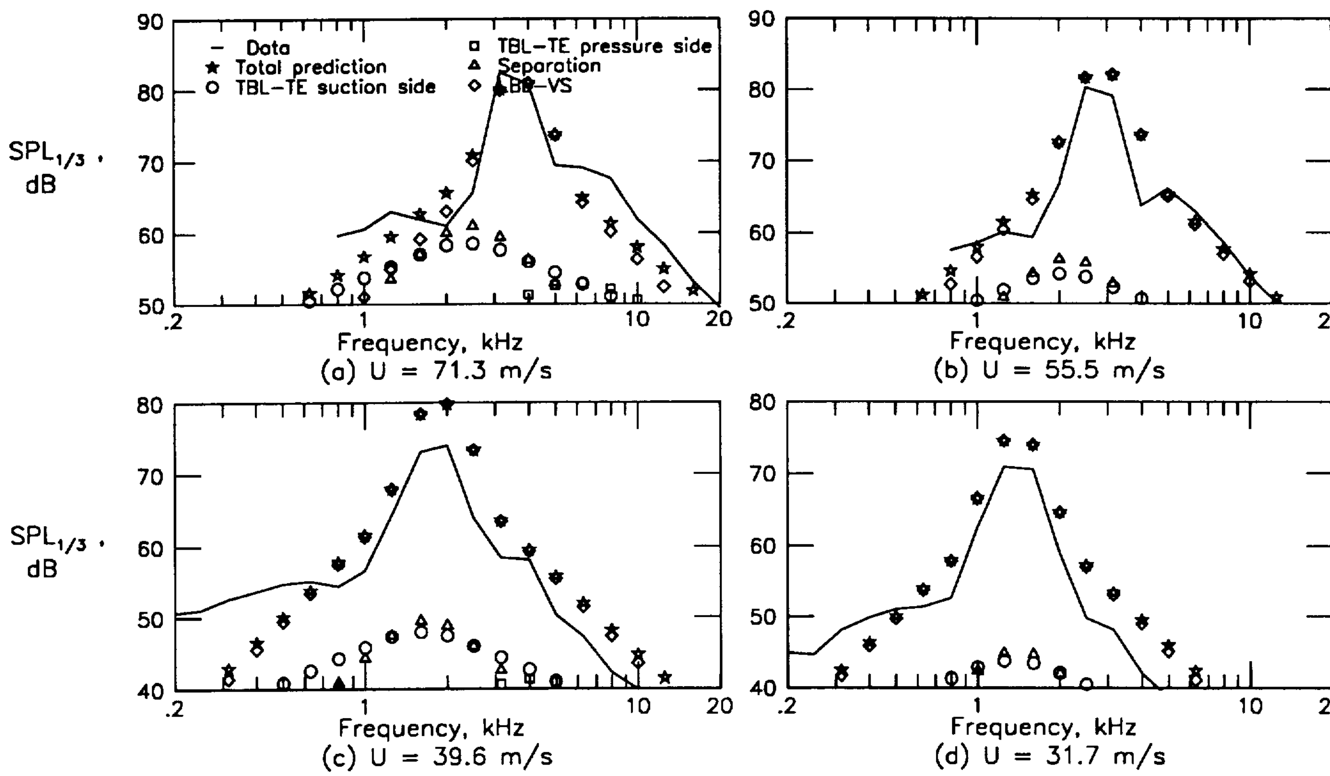

Figure 50. Self-noise spectra for 22.86-cm-chord airfoil with untripped BL at $\alpha_t = 10.8°$ ($\alpha_* = 4.0°$).

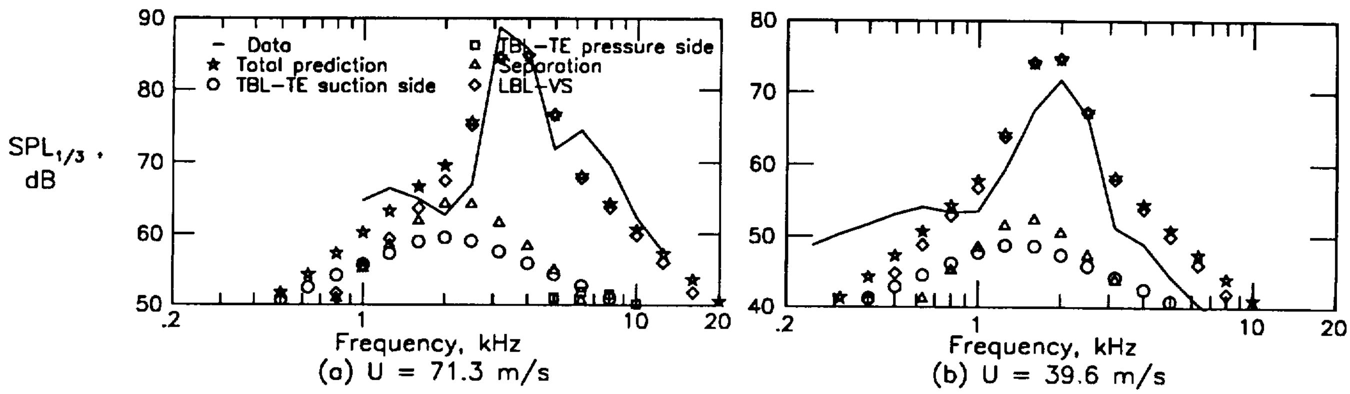

Figure 51. Self-noise spectra for 22.86-cm-chord airfoil with untripped BL at $\alpha_t = 14.4°$ ($\alpha_* = 5.3°$).

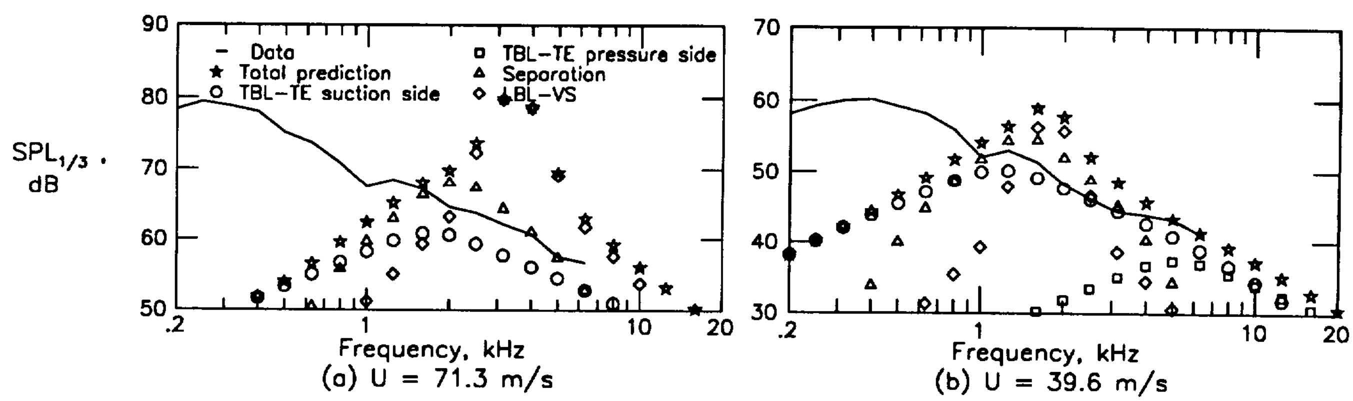

Figure 52. Self-noise spectra for 22.86-cm-chord airfoil with untripped BL at $\alpha_t = 19.8°$ ($\alpha_* = 7.3°$).

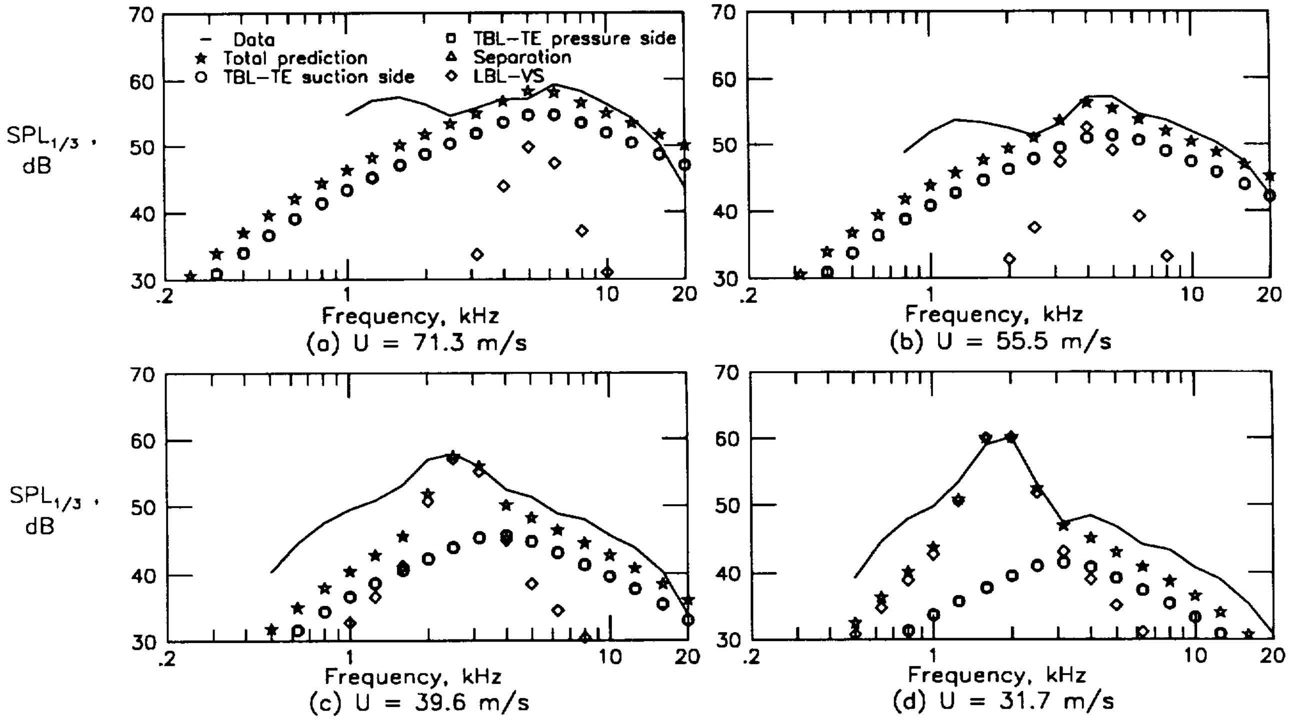

Figure 53. Self-noise spectra for 15.24-cm-chord airfoil with untripped BL at $\alpha_t = 0°$ ($\alpha_* = 0°$).

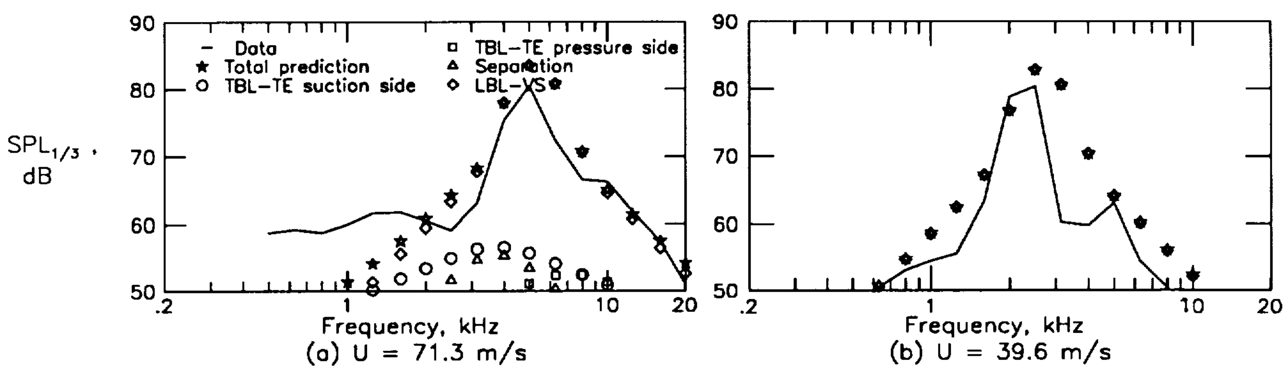

Figure 54. Self-noise spectra for 15.24-cm-chord airfoil with untripped BL at $\alpha_t = 5.4°$ ($\alpha_* = 2.7°$).

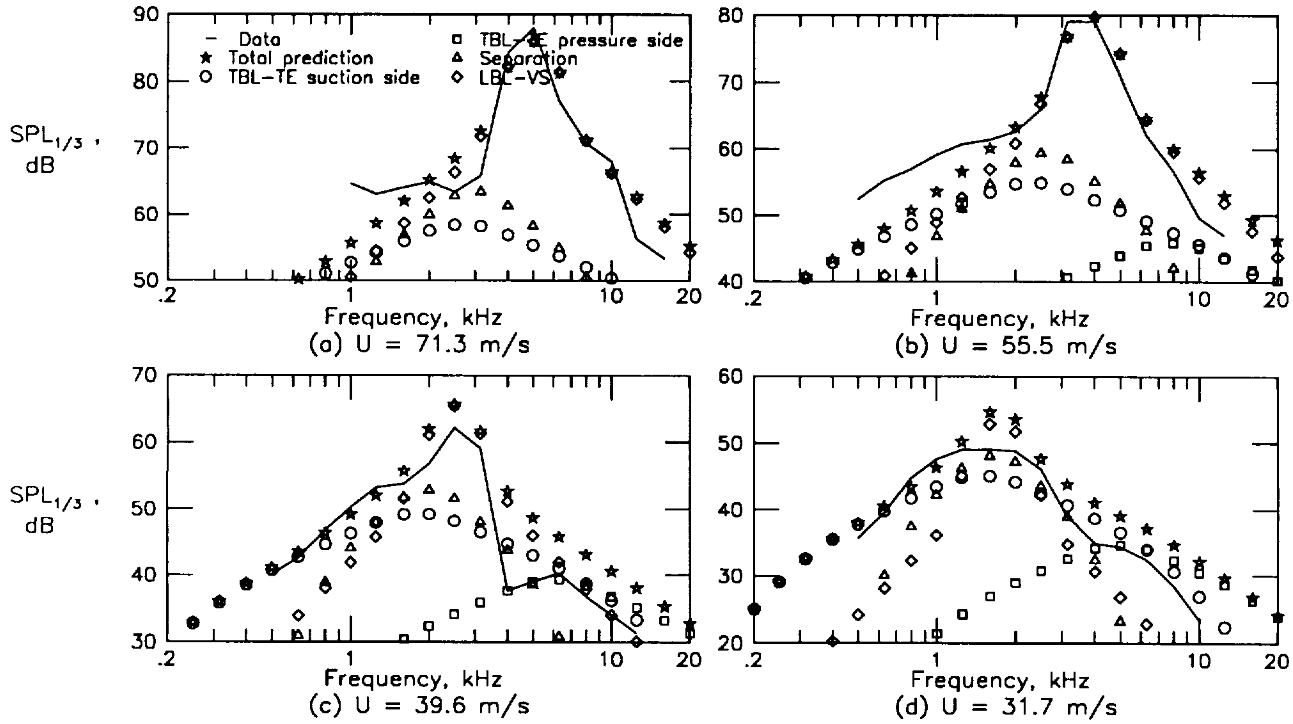

Figure 55. Self-noise spectra for 15.24-cm-chord airfoil with untripped BL at $\alpha_t = 10.8°$ ($\alpha_* = 5.4°$).

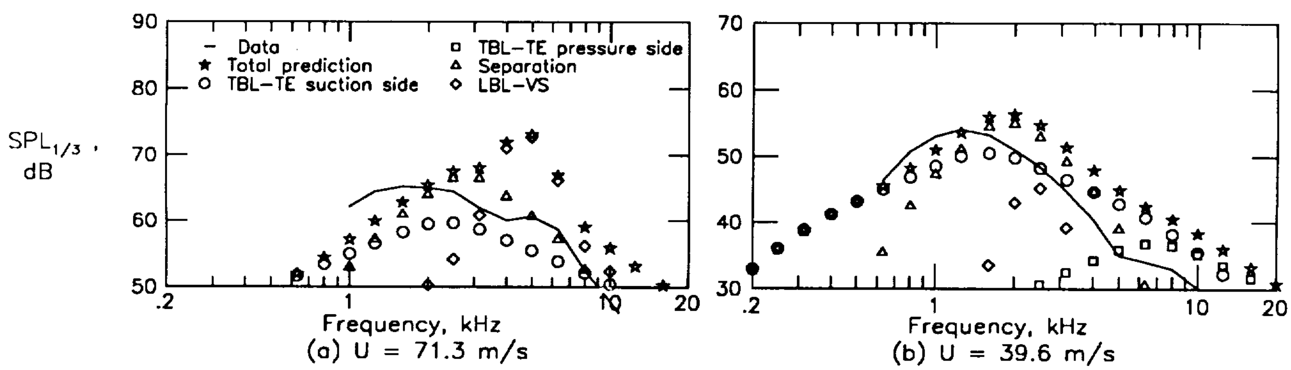

Figure 56. Self-noise spectra for 15.24-cm-chord airfoil with untripped BL at $\alpha_t = 14.4°$ ($\alpha_* = 7.2°$).

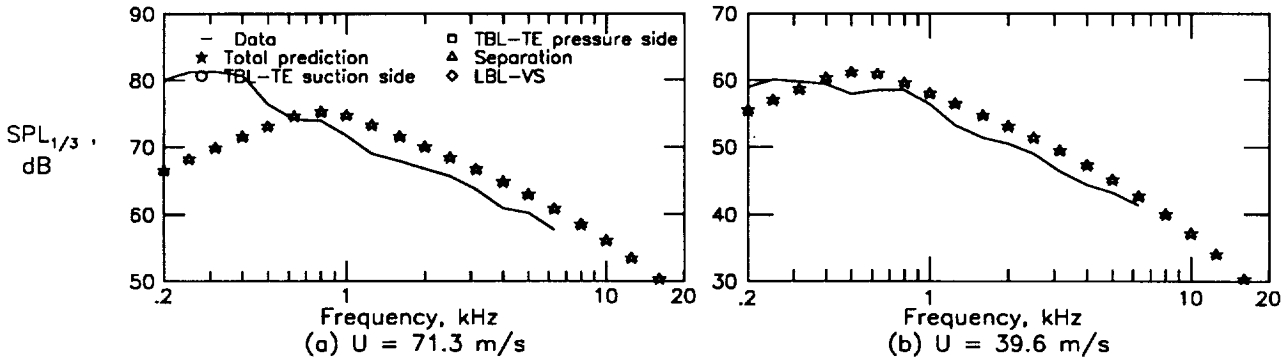

Figure 57. Self-noise spectra for 15.24-cm-chord airfoil with untripped BL at $\alpha_t = 19.8°$ ($\alpha_* = 9.9°$).

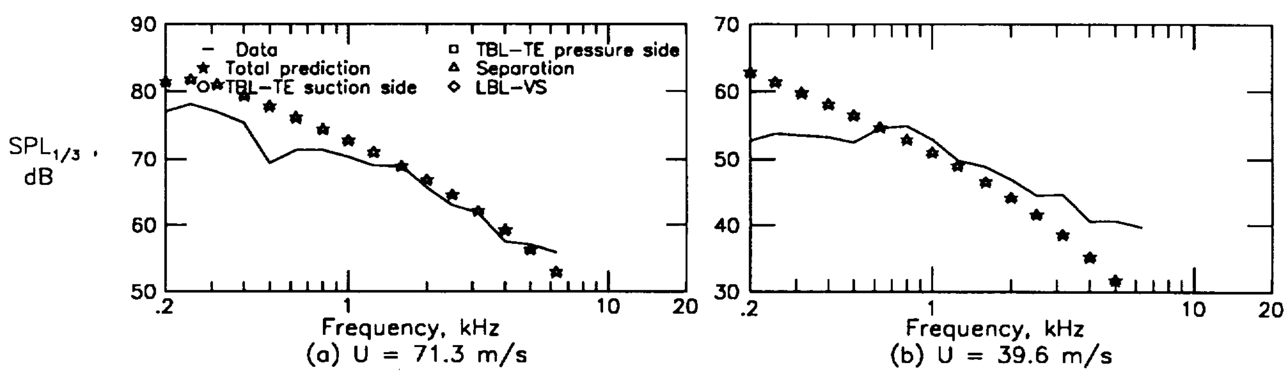

Figure 58. Self-noise spectra for 15.24-cm-chord airfoil with untripped BL at $\alpha_t = 25.2°$ ($\alpha_* = 12.6°$).

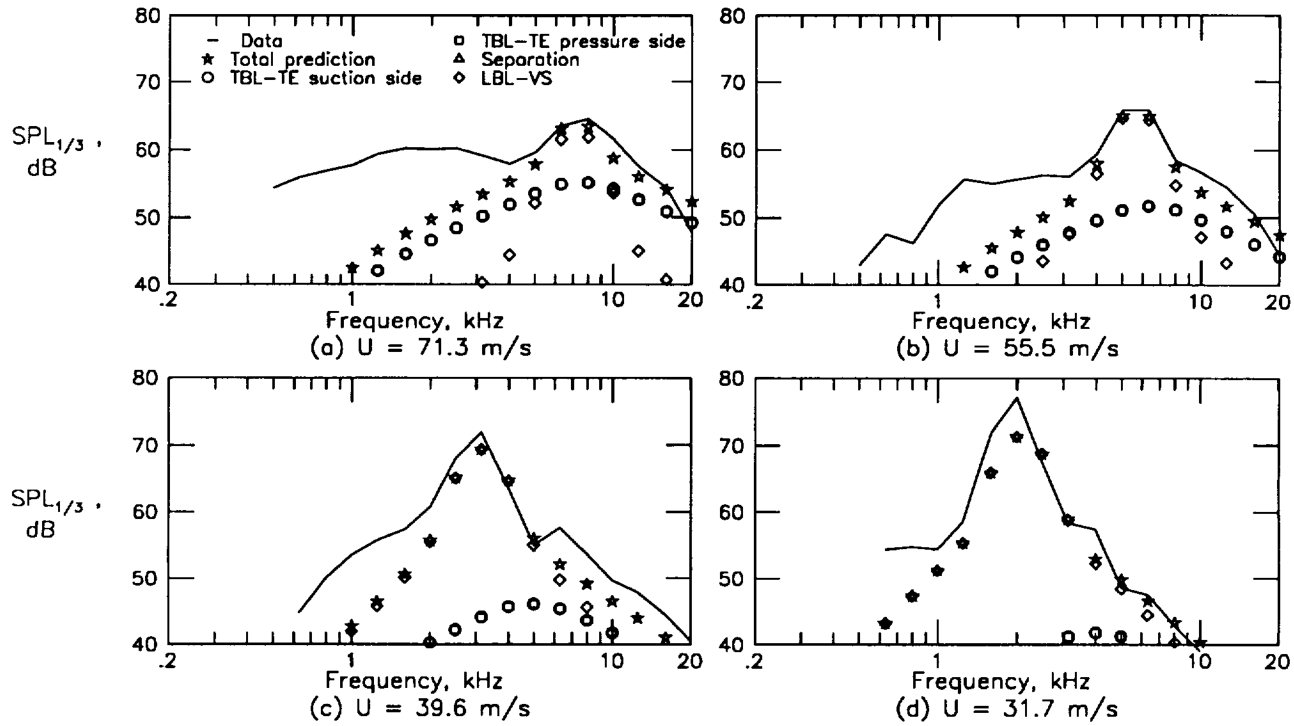

Figure 59. Self-noise spectra for 10.16-cm-chord airfoil with untripped BL at $\alpha_t = 0°$ ($\alpha_* = 0°$).

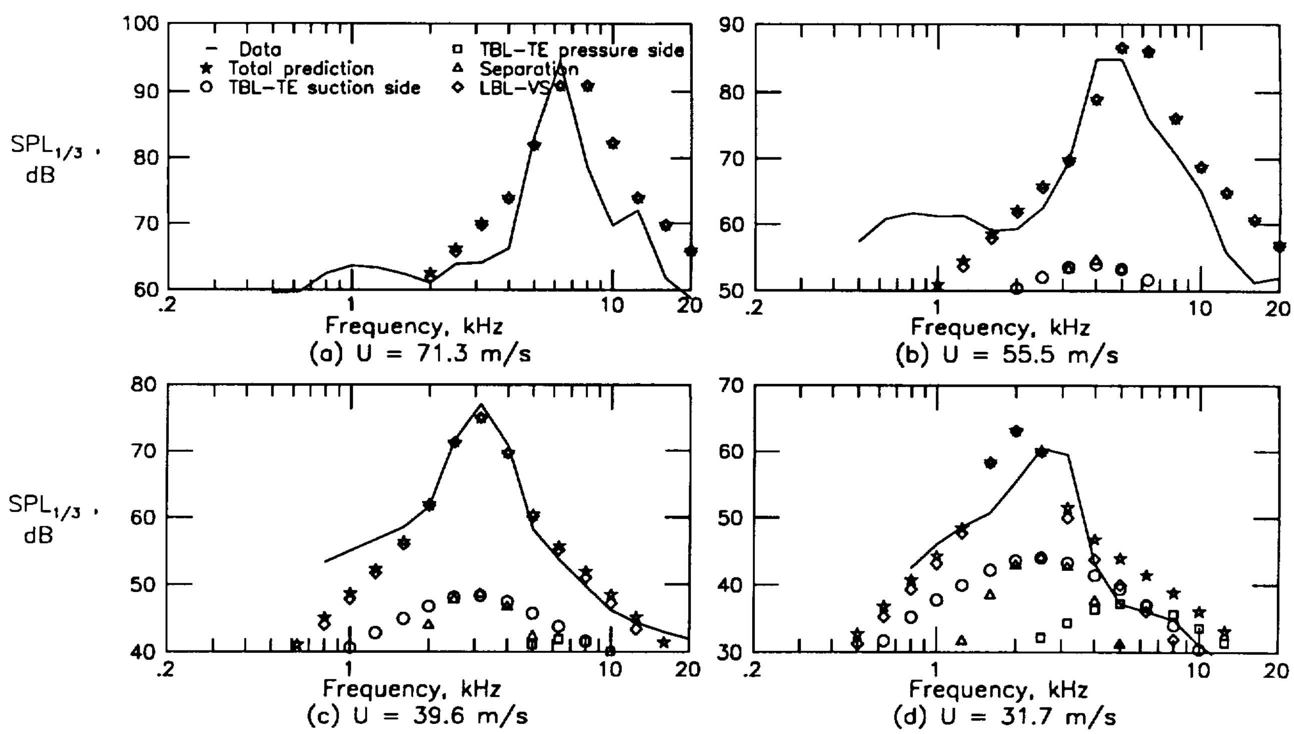

Figure 60. Self-noise spectra for 10.16-cm-chord airfoil with untripped BL at $\alpha_t = 5.4°$ ($\alpha_* = 3.3°$).

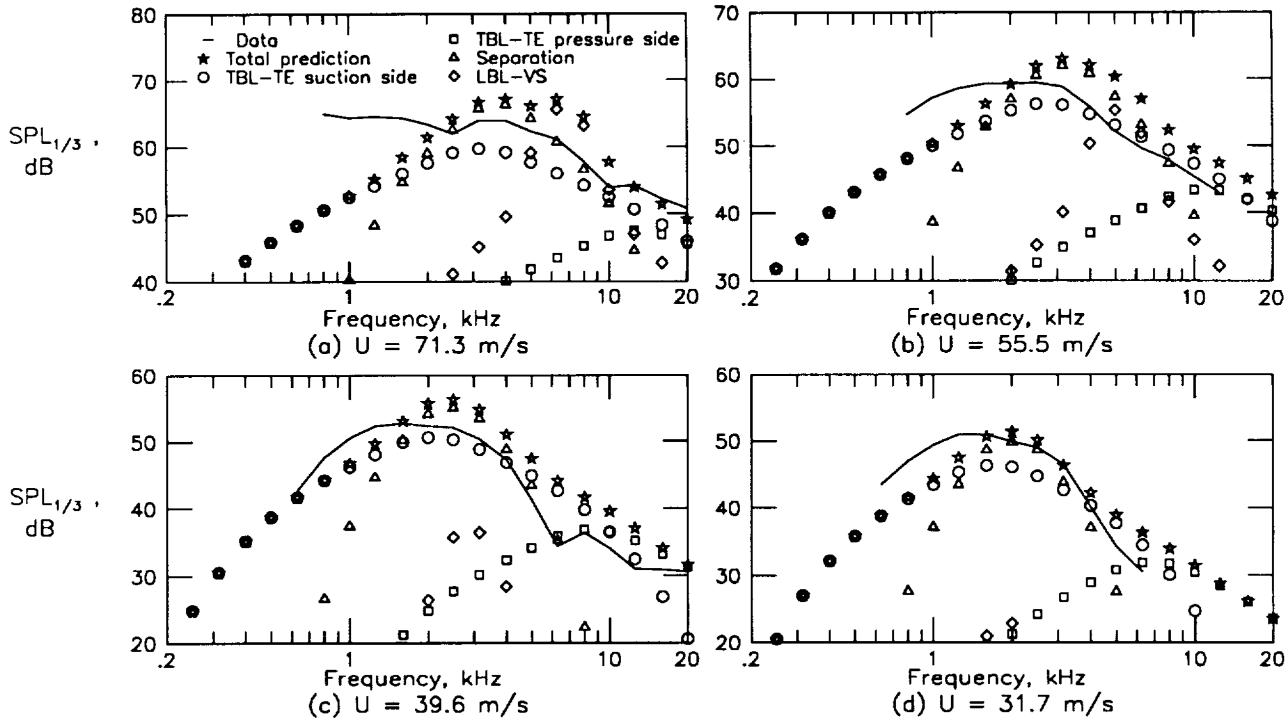

Figure 61. Self-noise spectra for 10.16-cm-chord airfoil with untripped BL at $\alpha_t = 10.8°$ ($\alpha_* = 6.7°$).

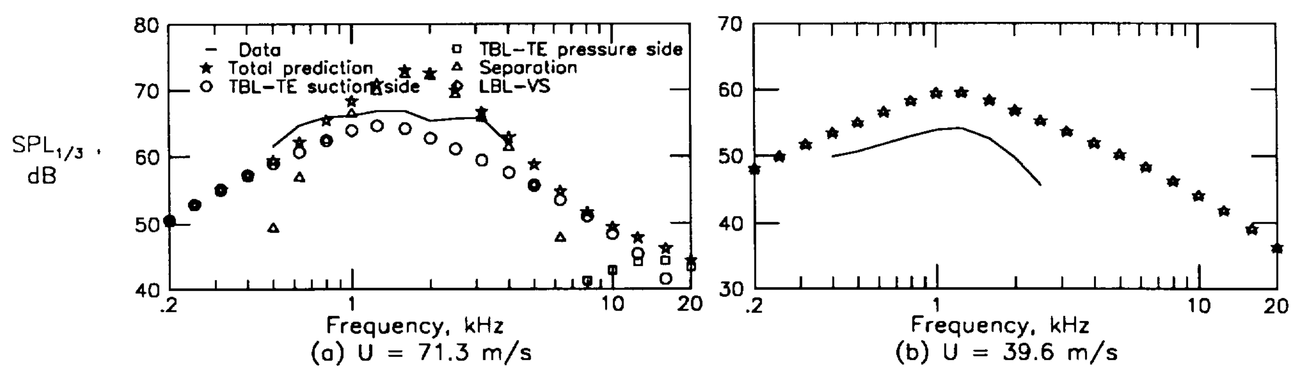

Figure 62. Self-noise spectra for 10.16-cm-chord airfoil with untripped BL at $\alpha_t = 14.4°$ ($\alpha_* = 8.9°$).

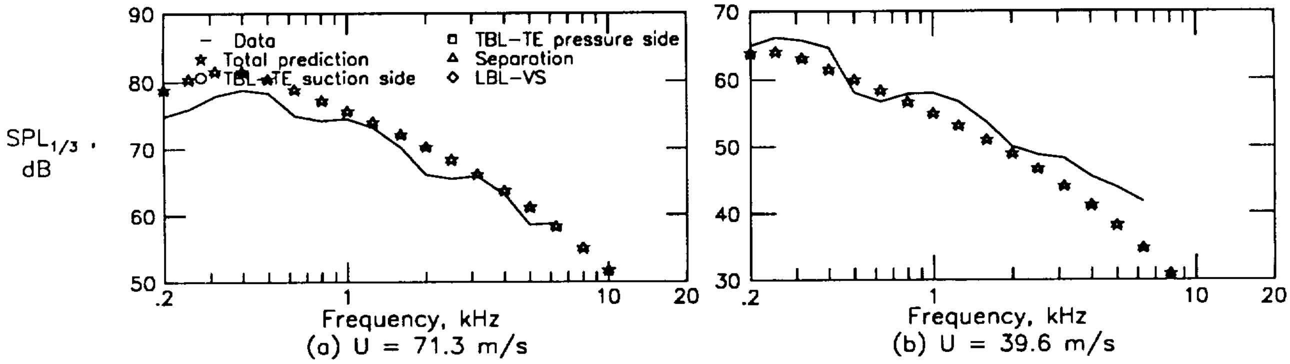

Figure 63. Self-noise spectra for 10.16-cm-chord airfoil with untripped BL at $\alpha_t = 19.8°$ ($\alpha_* = 12.3°$).

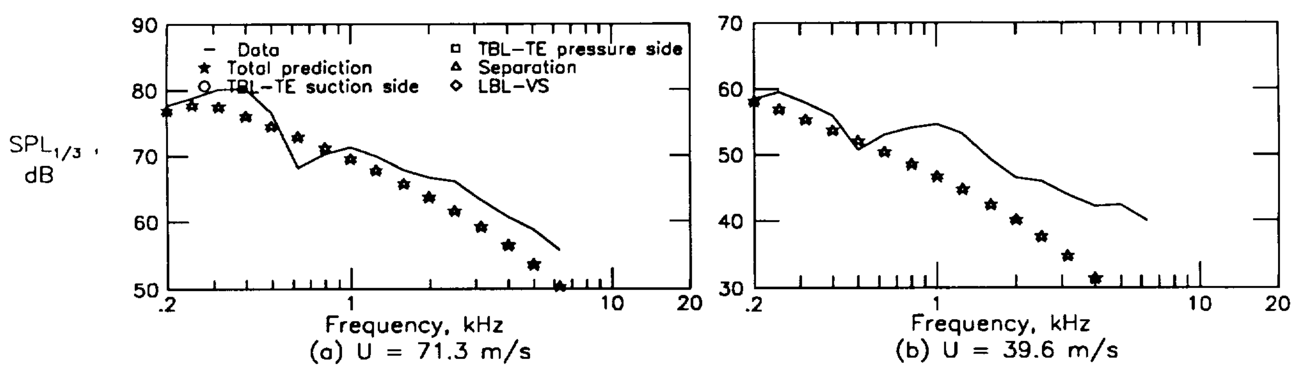

Figure 64. Self-noise spectra for 10.16-cm-chord airfoil with untripped BL at $\alpha_t = 25.2°$ ($\alpha_* = 15.6°$).

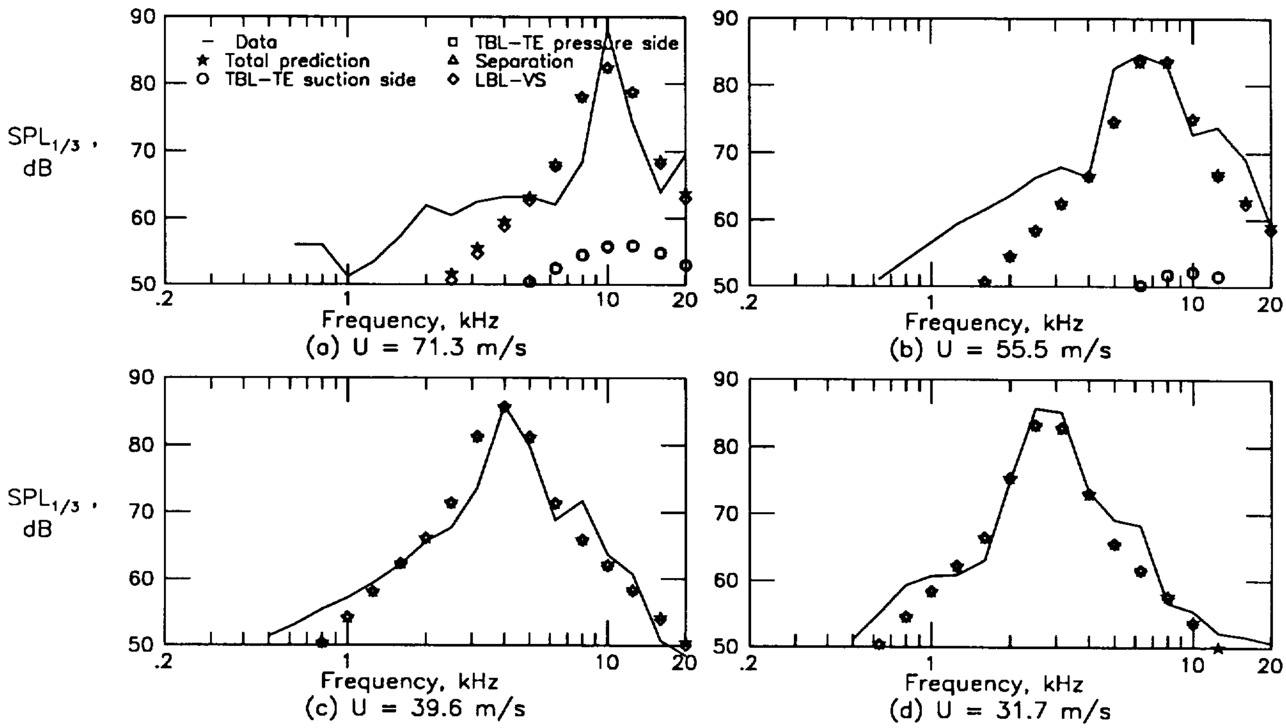

Figure 65. Self-noise spectra for 5.08-cm-chord airfoil with untripped BL at $\alpha_t = 0°$ ($\alpha_* = 0°$).

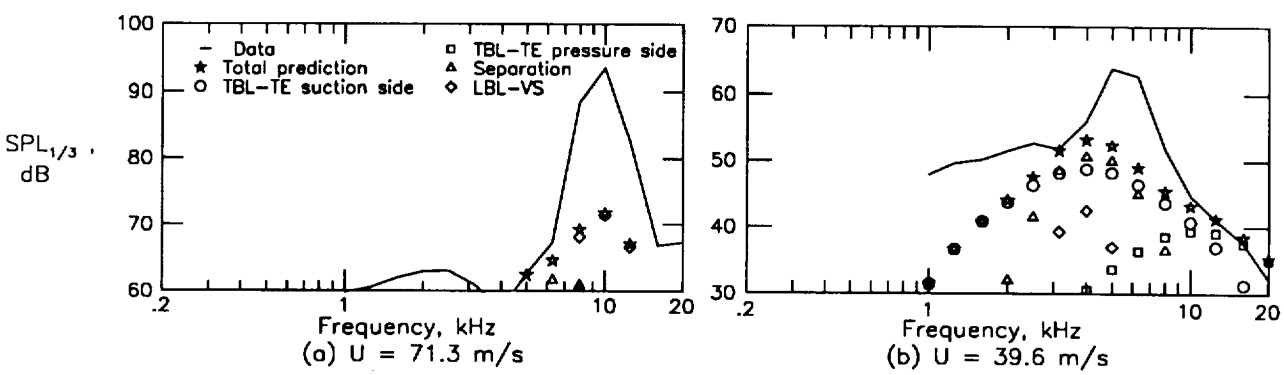

Figure 66. Self-noise spectra for 5.08-cm-chord airfoil with untripped BL at $\alpha_t = 5.4°$ ($\alpha_* = 4.2°$).

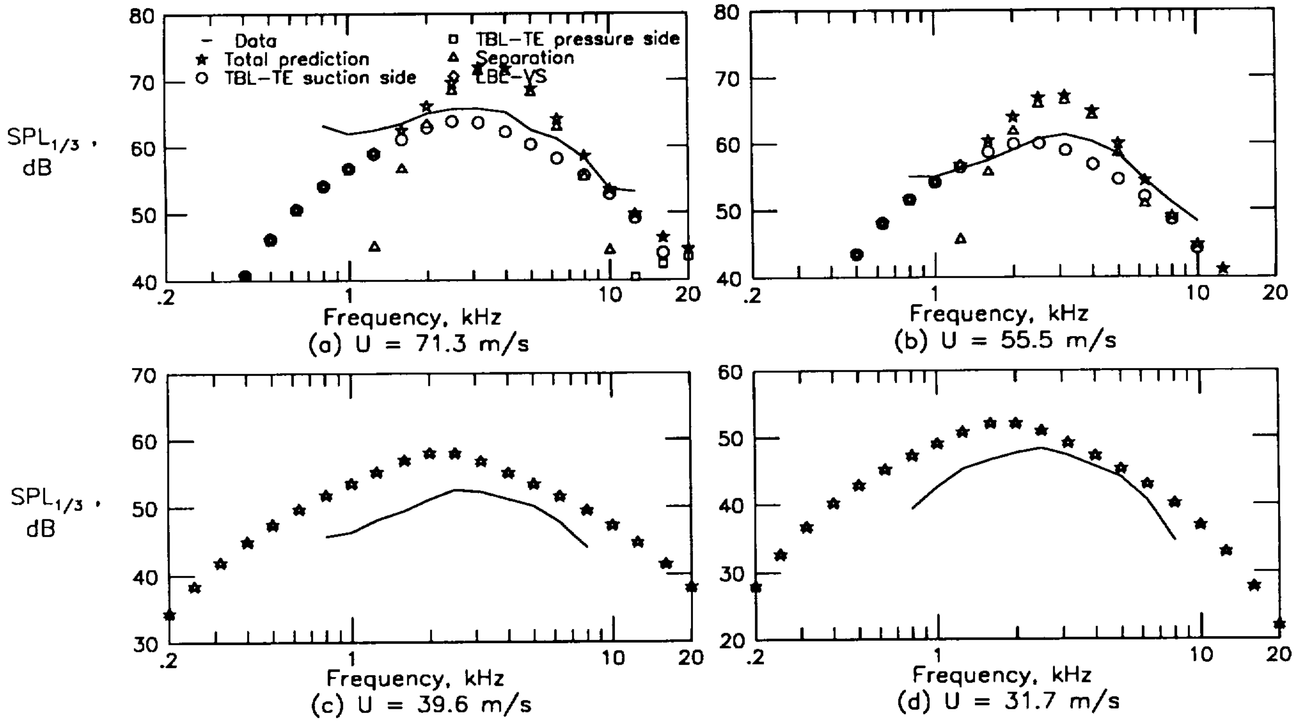

Figure 67. Self-noise spectra for 5.08-cm-chord airfoil with untripped BL at $\alpha_t = 10.8^\circ$ ($\alpha_* = 8.4^\circ$).

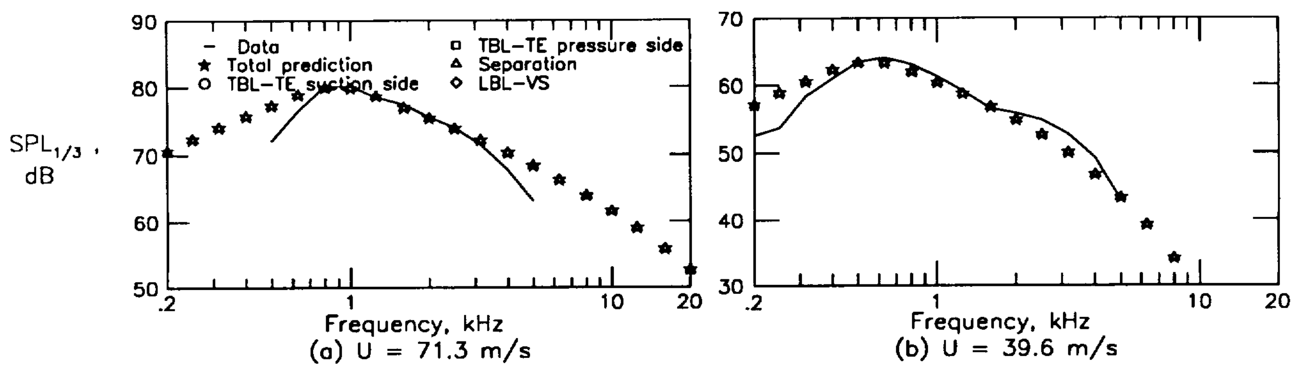

Figure 68. Self-noise spectra for 5.08-cm-chord airfoil with untripped BL at $\alpha_t = 14.4^\circ$ ($\alpha_* = 11.2^\circ$).

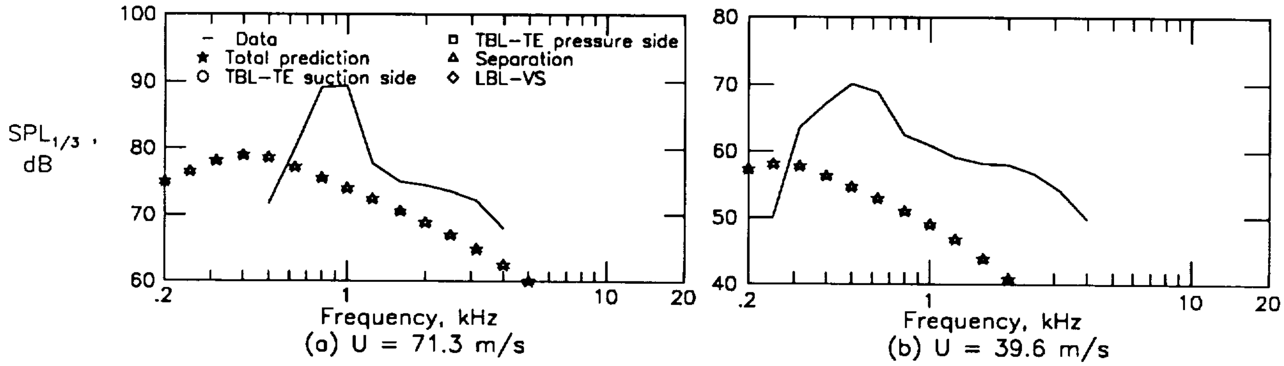

Figure 69. Self-noise spectra for 5.08-cm-chord airfoil with untripped BL at $\alpha_t = 19.8°$ ($\alpha_* = 15.4°$).

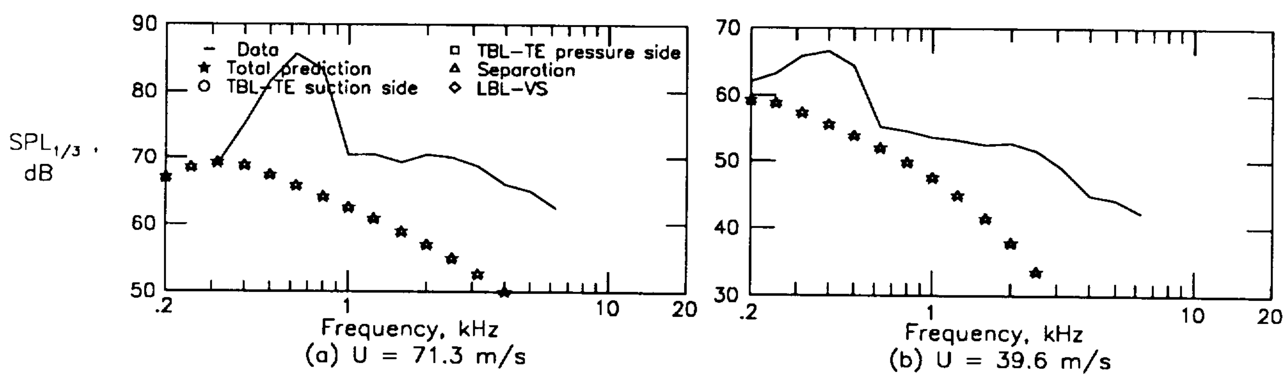

Figure 70. Self-noise spectra for 5.08-cm-chord airfoil with untripped BL at $\alpha_t = 25.2°$ ($\alpha_* = 19.6°$).

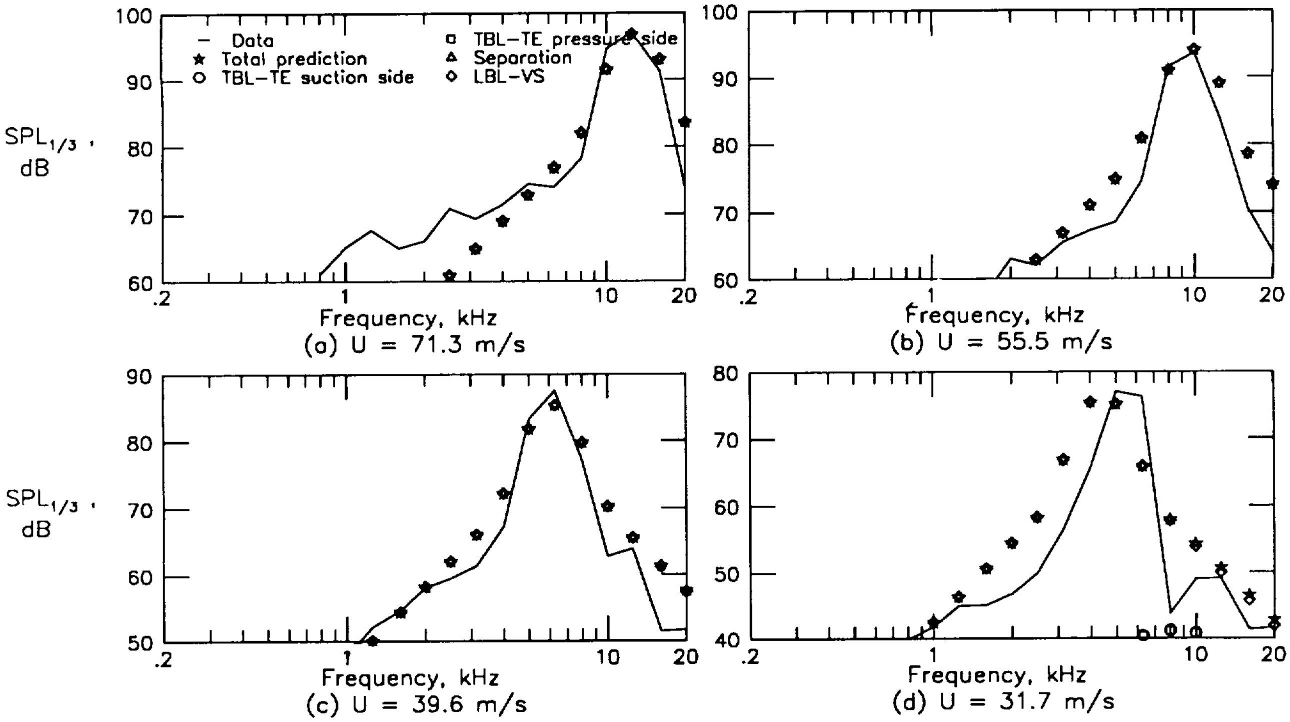

Figure 71. Self-noise spectra for 2.54-cm-chord airfoil with untripped BL at $\alpha_t = 0°$ ($\alpha_* = 0°$).

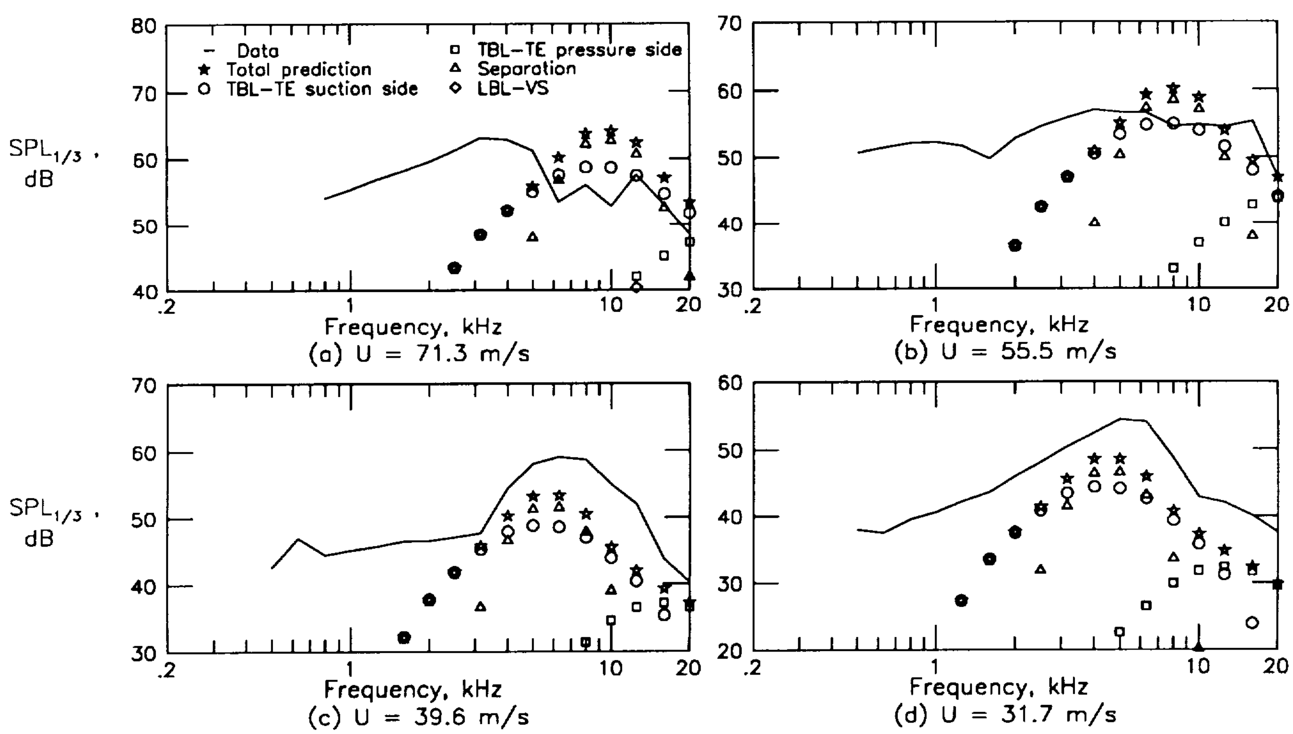

Figure 72. Self-noise spectra for 2.54-cm-chord airfoil with untripped BL at $\alpha_t = 5.4°$ ($\alpha_* = 4.8°$).

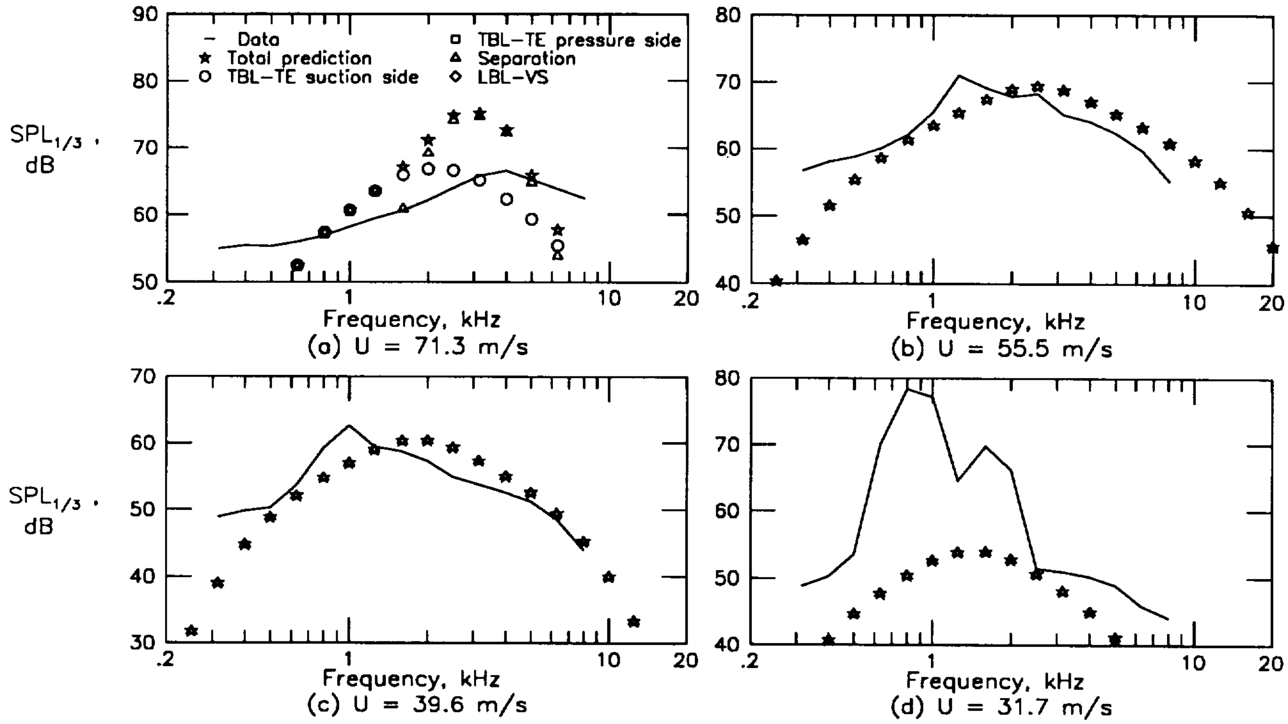

Figure 73. Self-noise spectra for 2.54-cm-chord airfoil with untripped BL at $\alpha_t = 10.8°$ ($\alpha_* = 9.5°$).

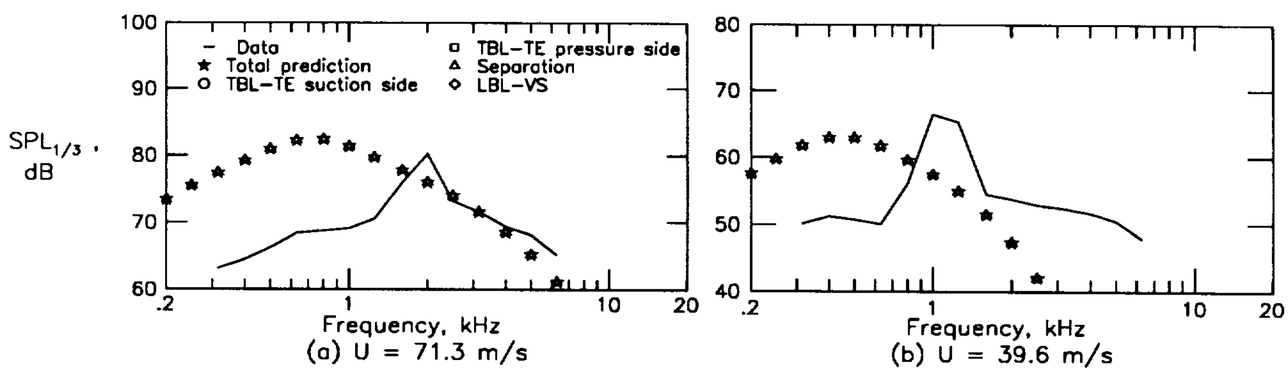

Figure 74. Self-noise spectra for 2.54-cm-chord airfoil with untripped BL at $\alpha_t = 14.4°$ ($\alpha_* = 12.7°$).

5. Spectral Scaling

In this section, the scaling laws are developed for the five self-noise mechanisms. The spectra of figures 11 to 74 form the basis of the scaling for three of the mechanisms: turbulent-boundary-layer-trailing-edge (TBL–TE) noise and separation noise were scaled from the tripped boundary-layer cases, and laminar-boundary-layer-vortex-shedding (LBL–VS) noise was scaled from the untripped cases. For the tip vortex formation noise mechanism, both the data and the scaling approach are obtained from reference 18. Finally, for TE-bluntness–vortex-shedding noise, spectral data from the study of reference 2, as well as previously unpublished data from that study, form the basis of scaling analysis.

5.1. Turbulent-Boundary-Layer–Trailing-Edge Noise and Separated Flow Noise

What has become traditional TE noise scaling is based on the analysis of Ffowcs Williams and Hall (ref. 5). For the problem of turbulence convecting at low subsonic velocity U_c above a large plate and past the trailing edge into the wake, the primary result is

$$\langle p^2 \rangle \propto \rho_0^2 v'^2 \frac{U_c^3}{c_0} \left(\frac{L\mathcal{L}}{r^2} \right) \overline{D} \qquad (17)$$

where $\langle p^2 \rangle$ is the mean-square sound pressure at the observer located a distance r from the edge. The medium density is ρ_0, v'^2 is the mean-square turbulence velocity, c_0 is the speed of sound, L is the spanwise extent wetted by the flow, and $\mathcal{L}$ is a characteristic turbulence correlation scale. The directivity factor $\overline{D}$ equals 1 for observers normal to the surface from the TE. The usual assumptions for boundary-layer flow are that $v' \propto U_c \propto U$ and $\mathcal{L} \propto \delta$ or δ^*, where δ and δ^* are, respectively, the boundary-layer thickness and displacement thickness. Fink (ref. 25), when normalizing airframe noise data where TBL–TE noise was believed to be dominant, assumed a universal spectrum shape $F(\mathrm{St})$ for the noise, where St is the Strouhal number $f\delta/U$. The shape $F(\mathrm{St})$ depended only on the ratio of St to its peak value $\mathrm{St}_{\mathrm{peak}}$. This gave the following normalization form for the 1/3-octave sound pressure level spectral presentation:

$$\mathrm{SPL}_{1/3} - 10 \log \left[\left(\frac{U}{100} \right)^5 \frac{\delta L}{r^2} \right] = F(\mathrm{St}) + K \qquad (18)$$

with $\mathrm{SPL}_{1/3} = \mathrm{OASPL} + F(\mathrm{St})$ and where K is an empirical constant which was determined when the velocity U is given in units of knots.

As mentioned in section 1, some of the airfoil self-noise spectral data of the present report were presented, in uncorrected form, in reference 6, and normalized in the manner of equation (18) using measured values of δ. It was found that, contrary to what was previously assumed (e.g., refs. 25 and 3), the normalized levels, spectral shape, and Strouhal number were not independent of airfoil size, airfoil angle of attack, and free-stream velocity. However, the limited scope of the paper, as well as the uncertainty caused by the aforementioned extraneous noise contamination of the uncorrected spectra, prevented a clear definition of the functional dependences. The corrected spectra of the present report are used to determine the parametric dependences and to account for these in the spectral scaling.

5.1.1. Scaled Data

Zero angle of attack. In figure 75, 1/3-octave spectra for four airfoil sizes, each at four tunnel speeds, are scaled. The spectra are obtained from figures 11, 20, 26, and 32. The angle of attack is zero and the boundary layers are tripped. The form of the normalization is

$$\text{Scaled } \mathrm{SPL}_{1/3} = \mathrm{SPL}_{1/3} - 10 \log \left(M^5 \frac{\delta_0^* L}{r_e^2} \right) \qquad (19)$$

where Mach number replaces the velocity in knots, δ_0^* replaces δ, and r_e replaces r. The retarded observer distance r_e equals here the measured value, 122 cm (see appendix B). For the right side of equation (19) to be accurately expressible by the form $F(\mathrm{St})+K$ of equation (18), the scaled spectra of figure 75 should be identical to one another for all cases. However, the peak Strouhal number, spectral shape, and scaled level vary significantly.

For each spectrum in figure 75, a symbol indicates the approximate spectral peak location. The peak locations were based on gross spectral shapes and trends rather than specific peak maximums. The peak Strouhal number, $\mathrm{St}_{\mathrm{peak}} = (f\delta^*/U)_{\mathrm{peak}}$, and scaled levels corresponding to these peak locations are shown in figures 76 and 77, respectively, as a function of Reynolds number R_c. These data are also presented in table 1 (at the back of this report). Included in the figures are the other cases for tripped BL airfoils of different chord lengths. Also included are data at nonzero angle of attack for subsequent discussion. The displacement thicknesses for the suction side, δ_s^*, are used for these normalizations. In figure 76, $\mathrm{St}_{\mathrm{peak}}$ for zero angle of attack (solid symbols) shows no clear R_c-dependence, but a Mach number dependence is apparent. The horizontal lines through the data correspond to the function

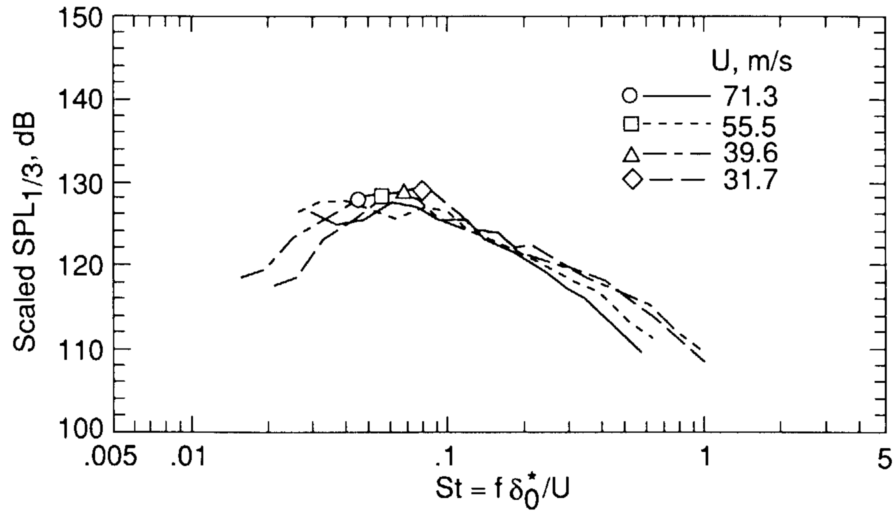

(a) 30.48-cm-chord airfoil.

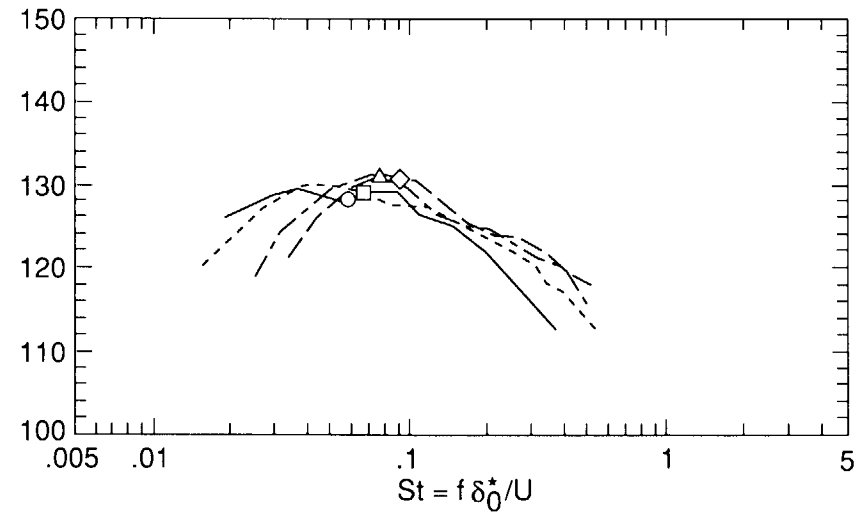

(b) 15.24-cm-chord airfoil.

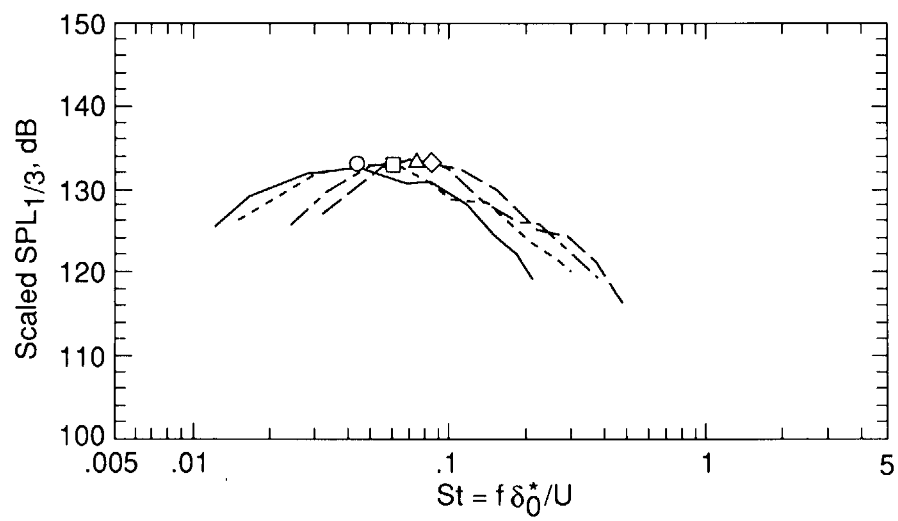

(c) 10.16-cm-chord airfoil.

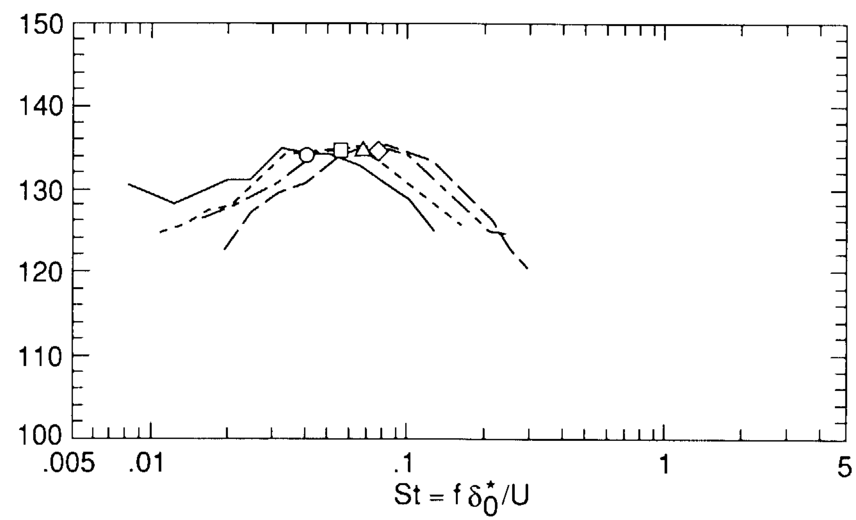

(d) 5.08-cm-chord airfoil.

Figure 75. Scaled 1/3-octave spectra of tripped BL airfoils at $\alpha_t = 0°$ ($\alpha_* = 0°$). Symbols indicate approximate spectral peak locations.

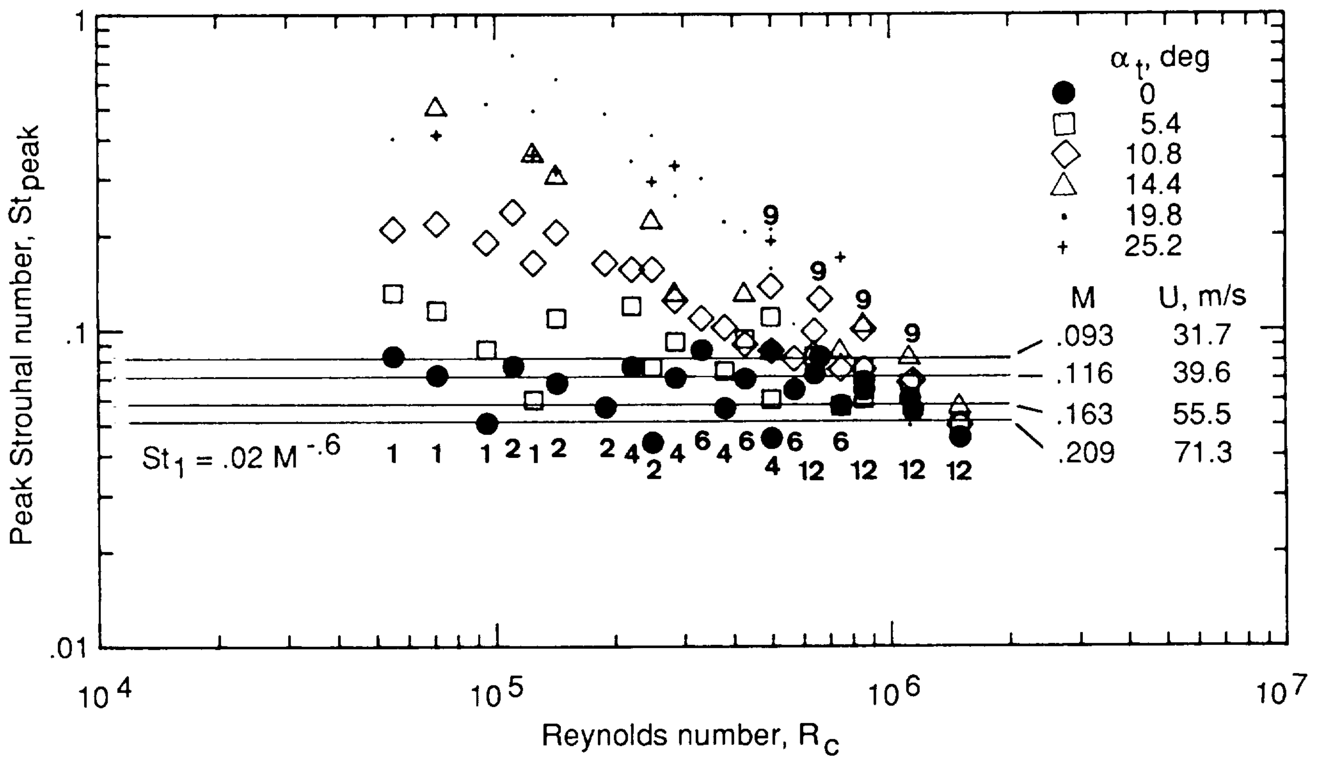

Figure 76. Peak Strouhal number for TBL–TE noise versus Reynolds number. Numbers aligned with data are chord sizes in inches (for brevity of notation).

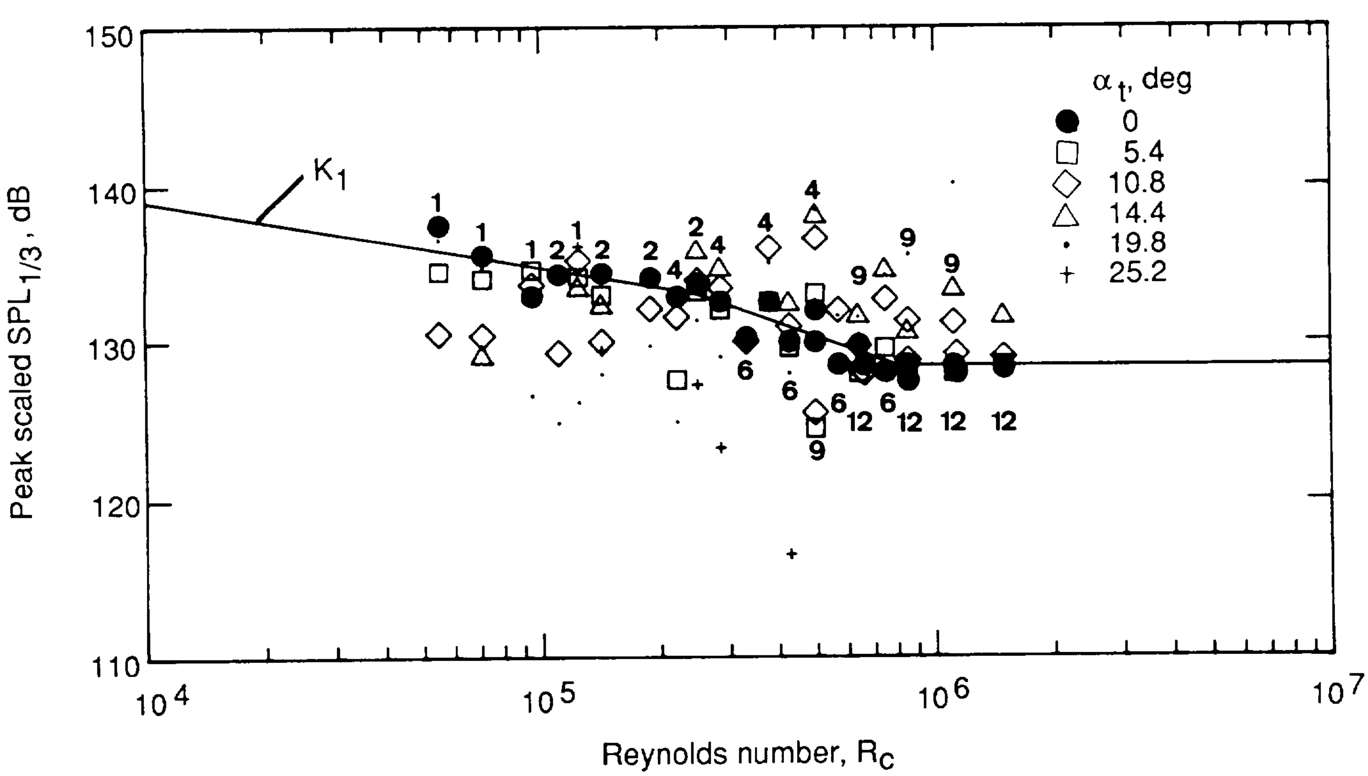

Figure 77. Peak scaled level for TBL–TE noise versus Reynolds number. Numbers aligned with data are chord sizes in inches.

$St_1 = 0.02M^{-0.6}$ for the presented values of Mach number and is taken to approximate the behavior of St_{peak}. For the scaled levels in figure 77, a continuous function, designated as K_1, that is comprised of R_c-dependent segmented lines is drawn to approximate the zero-angle-of-attack data. Other choices for a function to approximate these data are possible but the one shown, which is chosen to be constant for high R_c, was found to be compatible with higher Reynolds number data obtained from other studies, as is shown subsequently. Note that the behavior of K_1 at very low R_c is at most academic because of the lack of importance of this TBL–TE noise mechanism in this range.

In figure 78(a), a shape function denoted by A is proposed as representative of the 1/3-octave spectral shape of the TBL–TE noise mechanism. (Fig. 78(b) presents a corresponding shape function for separated flow noise.) The spectrum A is a function of the ratio St/St_{peak} that is symmetric about $St/St_{peak} = 1.0$. The spectral width or broadness depends on R_c. Two extremes in A are shown corresponding to so-called maximum and minimum Reynolds numbers. Intermediate values of R_c require interpolation. As seen in figure 75, the larger chords have the broadest TBL–TE spectra. The spectrum A was matched to these and the other chord lengths. The specific details of A and the other functions are given in the calculation procedures section (5.1.2.).

One of the key results of reference 2 is that each side of an airfoil with well-developed boundary layers produces TBL–TE noise independently of the other side. This is not in conflict with our scaling approach for the symmetric airfoil at zero angle of attack. Consistency of this with equation (19) merely requires a level adjustment (−3 dB) of the scaling equations to account for the equal contributions of the two sides to the total spectrum. For the pressure and suction sides, $i = p$ or s,

$$\text{Scaled SPL}_i = \text{SPL}_i - 10\log\left(M^5 \frac{\delta_i^* L}{r_e^2}\right) = A\left(\frac{St_i}{St_1}\right) + (K_1 - 3) \qquad (20)$$

where $St_i = (f\delta_i^*/U)$. The total TBL–TE noise for zero angle of attack then is

$$\text{SPL}_{\text{TBL-TE}} = 10\log\left(10^{\text{SPL}_s/10} + 10^{\text{SPL}_p/10}\right) \qquad (21)$$

where a 1/3-octave presentation for spectra is understood.

Nonzero angle of attack. In figure 79, scaled noise spectra are presented for the same tripped BL airfoil models as in figure 75, but here the angle of attack is varied while holding tunnel velocity constant at $U = 71.3$ m/s. The tunnel angles of attack α_t are given along with the effective angles α_*. The level normalization approach and Strouhal scaling are the same as in figure 75 except that here the displacement thickness of the suction side of the airfoil δ_s^* is used. For increasing α_* the peak Strouhal number and level increase and the spectra become sharper at the peaks. Beyond limiting values of α_*, roughly corresponding to stall, substantial changes occur to the scaled spectra.

If equations (20) and (21) were used to predict the spectra in figure 79 and the predictions scaled accordingly, one would find for increasing angle of attack that peak Strouhal number would remain constant, peak level would decrease, and the spectral shape would become broader at the peak. This is because the suction side contribution would remain dominant and that of the pressure side would shift to higher frequencies at reduced levels. These trends, of course, are virtually opposite to those observed. The approach that is now taken is to postulate at nonzero angles of attack an additional contribution to the spectrum that controls the spectral peak. To justify this, one could hypothesize that the spectrum is the total from attached TBL contributions, as formulated in equations (20) and (21), and a contribution from a separated portion of the TBL on the suction side. The modeling approach, however, is not without conflict at the low Reynolds numbers, as is discussed subsequently. Model details are developed below, after establishing the Strouhal and level scaling behavior for the angle cases.

In figure 79, for each spectrum, symbols indicate the approximate peak Strouhal locations. As in figure 75, the locations of the peaks were based on gross trends and shapes of the spectra rather than precise peaks. These values of St_{peak} are included in figure 76 for the various chords, speeds, and angles of attack, along with the zero angle values previously discussed. Again little direct R_c-dependence is noted for St_{peak}. The basic trends observed can be explained by velocity and angle dependence. The values of St_{peak} are plotted versus corrected angle of attack α_* in figure 80. For reference, the chord lengths (in units of inches for presentation convenience) are given. Through the data are drawn data-fit lines designated as St_2, corresponding to two velocity values. At $\alpha_* = 0°$, St_2 becomes the function St_1 of figure 76. In the hand-fitting procedure to determine St_2, some preference was given to the higher speed cases. This preference is discussed subsequently with regard to Strouhal peak level scaling. As for the substantial

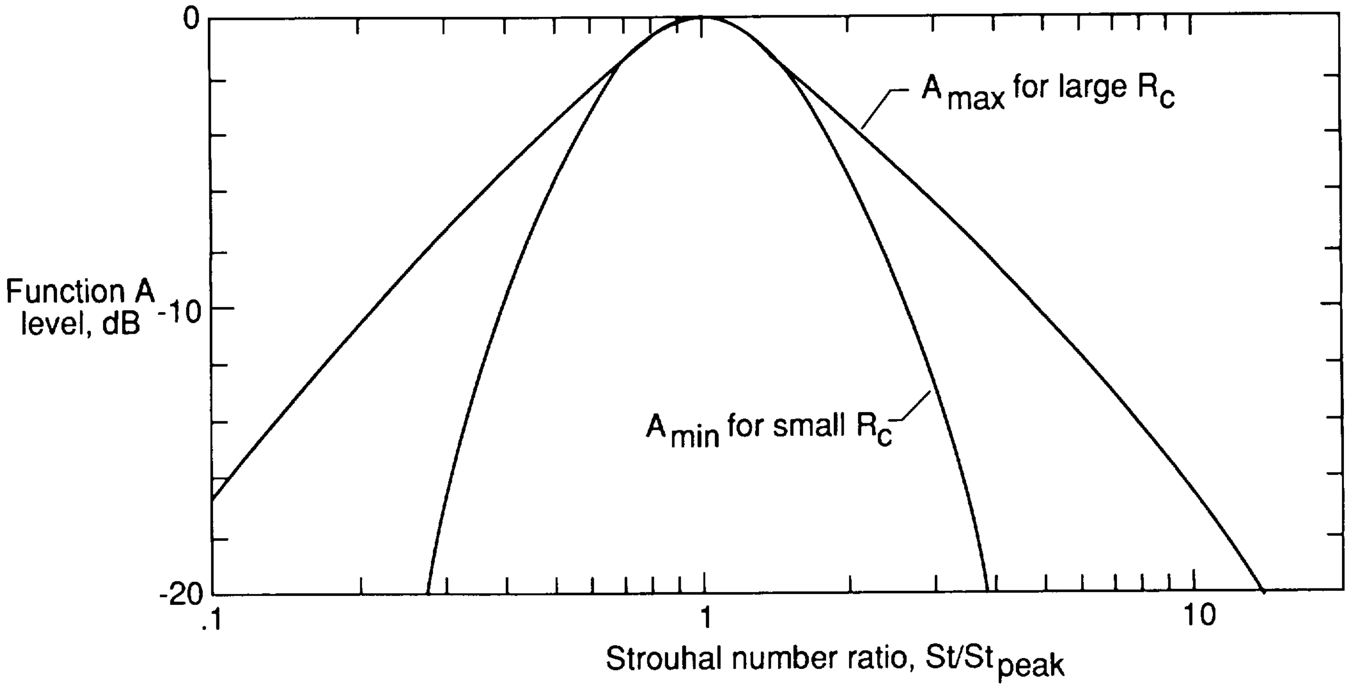

(a) Function A for TBL–TE noise, equations (35) to (40).

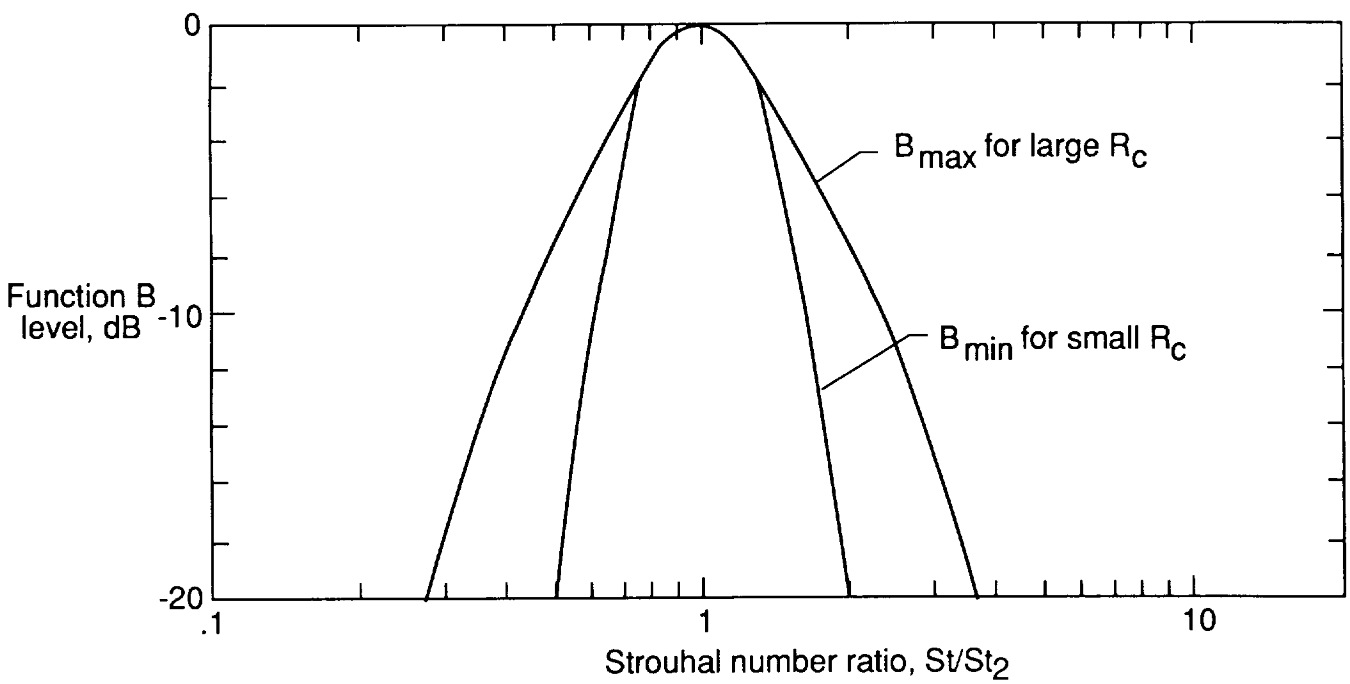

(b) Function B for separated flow noise, equations (41) to (46).

Figure 78. One-third-octave spectral shapes as functions of Strouhal and Reynolds numbers.

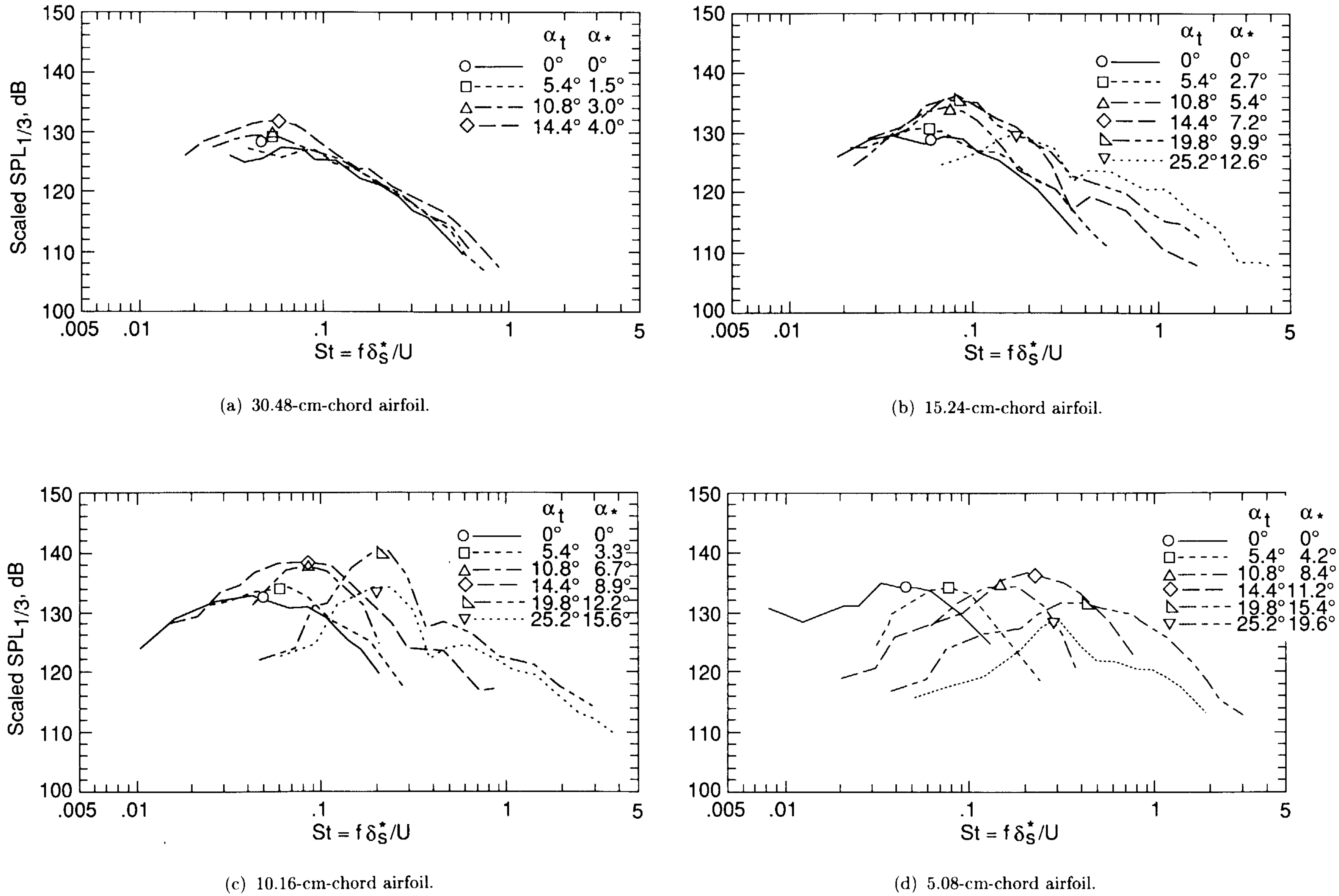

(a) 30.48-cm-chord airfoil.

(b) 15.24-cm-chord airfoil.

(c) 10.16-cm-chord airfoil.

(d) 5.08-cm-chord airfoil.

Figure 79. Scaled 1/3-octave spectra for tripped BL airfoils at various angles of attack. U = 71.3 m/s. Symbols indicate approximate spectral peak locations.

data scatter of figure 80, some comments are warranted. It was found that if one used the actual measured values of δ_s^* (where available) in the Strouhal scaling, one would have a similar degree of scatter to that shown in figure 80, where scaled values of δ_s^* (eq. (12)) were used. Also if untripped BL airfoil results were plotted, for those limited number of cases where the LBL–VS shedding source is not apparent in the spectra, the scatter and trend would be about the same as those shown in figure 80. Other deviations of the data from the St_2 lines occur at mid to high angles of attack, where the low-frequency parts of the spectra were limited by the experimental high-pass filtering and thus values of $\mathrm{St}_{\mathrm{peak}}$ were inaccurately large. The behavior of St_2 seen in figure 80 at the higher angles of attack (where the horizontal lines are placed lower than the data) was chosen to approximately correct this bias.

The scaled levels corresponding to spectral peaks chosen in figure 79 are shown in figure 77 with the other cases. The previously indicated conflict within the data base for the proposed modeling approach, which hypothesizes contributions from two attached TBL's and an angle-dependent separation-related portion, is seen in figure 77. Peak levels for the two smallest chord lengths, except at the highest speeds, significantly decrease as the angle of attack increases from zero. This is incompatible with the modeling approach. A choice is made to ignore the conflicting low Reynolds number data in the model development. While admitting that the inclusion of the low Reynolds number behavior would conceptually be desirable for completeness of the modeling, the exclusion is believed justifiable because of the greater interest in higher Reynolds number conditions. The TBL–TE noise mechanism is not considered important for low Reynolds numbers. Even if this were not the case, it is not certain that the present test flow conditions with heavy leading-edge tripping for airfoils at nonzero angles of attack properly represent the mechanism, especially for higher angles where relaminarization of the pressure-side boundary layer is possible. Regardless, the results of the scaling are compared subsequently with the spectra of all the data to allow a direct assessment of the effect of modeling choices.

The scaled levels of figure 77 for chord lengths of 10.16, 15.24, 22.86, and 30.48 cm are plotted in figure 81 versus α_*. If the portion of these levels that cannot be accounted for by the modeling of equations (20) and (21) can be extracted, this portion would be designated as the separated flow noise contribution. Calculations were performed by taking into account that the Strouhal dependence of A in equation (20) would follow St_1 of figure 76 rather than St_2 of figure 80, which applies to that portion extracted. The extracted levels are given in figure 82. These extracted levels are normalized by subtracting the zero-angle-of-attack function of figure 77 (K_1) for the particular chord lengths and speeds. Although substantial scatter is present, a basic trend of increasing importance for increasing angle and speed is seen. Drawn through the data is a function designated as $K_2 - K_1$ which represents a partially observed, partially postulated dependence on velocity and angle of attack. The assigned spectral shape for this additive source is function B, which is given in figure 78(b) and is defined in a manner similar to function A of figure 78(a) to have a width which is dependent on chord Reynolds number.

The resulting scaling model for the angle-dependent noise SPL_α is

$$\text{Scaled SPL}_\alpha = \mathrm{SPL}_\alpha - 10\log\left(M^5 \frac{\delta_s^* L}{r_e^2}\right) = B\left(\frac{\mathrm{St}_s}{\mathrm{St}_2}\right) + K_2 \qquad (22)$$

where this represents the separated-boundary-layer noise contribution to the total noise. The total TBL–TE and separation noise is then

$$\mathrm{SPL}_{\mathrm{TOT}} = 10\log\left(10^{\mathrm{SPL}_\alpha/10} + 10^{\mathrm{SPL}_s/10} + 10^{\mathrm{SPL}_p/10}\right) \qquad (23)$$

During development of the scaling procedures, equations (20), (22), and (23) were compared with spectra for all tripped BL airfoils and with spectra for the untripped BL airfoils for which TBL–TE noise appeared to significantly contribute. Analyses of comparisons resulted in optimization of curves A and B, as well as development of the specific calculation procedures. The analysis found that better results are obtained when the Strouhal dependency of the suction-side spectrum SPL_s is $(\mathrm{St}_1 + \mathrm{St}_2)/2$ rather than St_1. It was found that for better SPL agreement, one should make an adjustment in pressure-side level SPL_p (defined as ΔK_1 in the following section) as a function of angle of attack and Reynolds number based on the displacement thickness δ_p^*. This adjustment diminishes the pressure-side contribution for increasing angle and decreasing velocity. Also it was found that the drastic spectral shape changes that occur at sufficiently high angles of attack, near stall, are roughly simulated by a calculation procedure change. At the value of α_* corresponding to the peak of the appropriate K_2 curve, the spectral

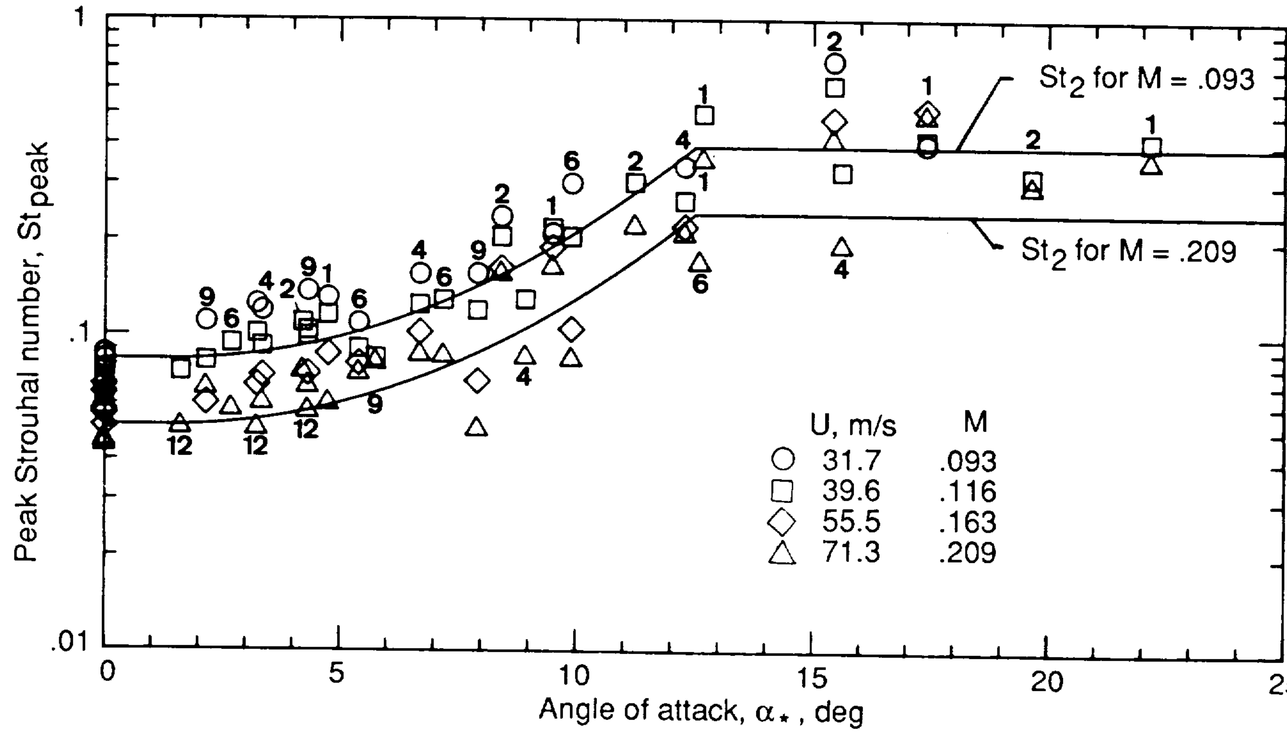

Figure 80. Peak Strouhal number for TBL–TE noise versus angle of attack. Data from figure 76. Numbers aligned with data are chord sizes in inches.

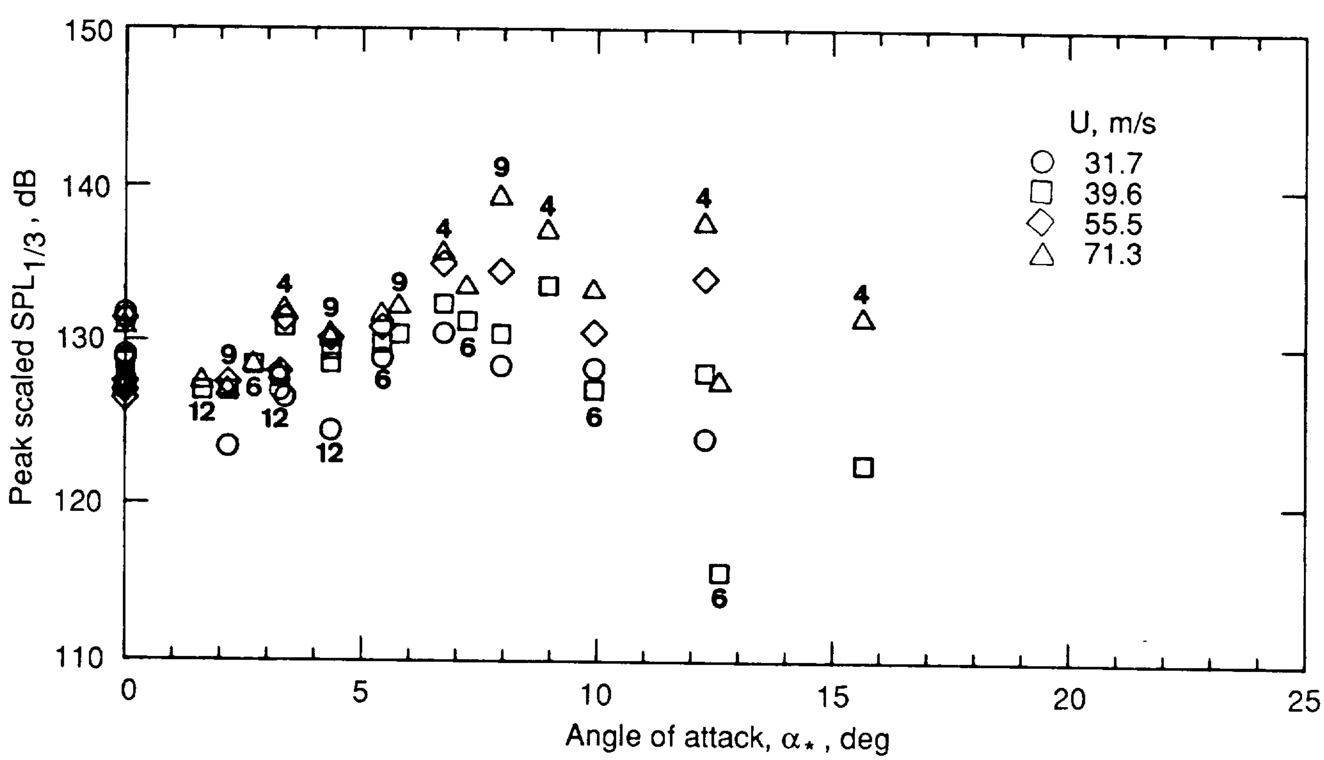

Figure 81. Peak scaled level for TBL–TE versus angle of attack. Data from figure 77. Numbers aligned with data are chord sizes in inches.

contributions SPL_s and SPL_p in equation (23) are eliminated and the B curve of equation (22) is replaced by an A curve corresponding to a value of R_c which is three times the actual value.

The calculation procedures are specified in the next section followed by comparison with the spectral data base.

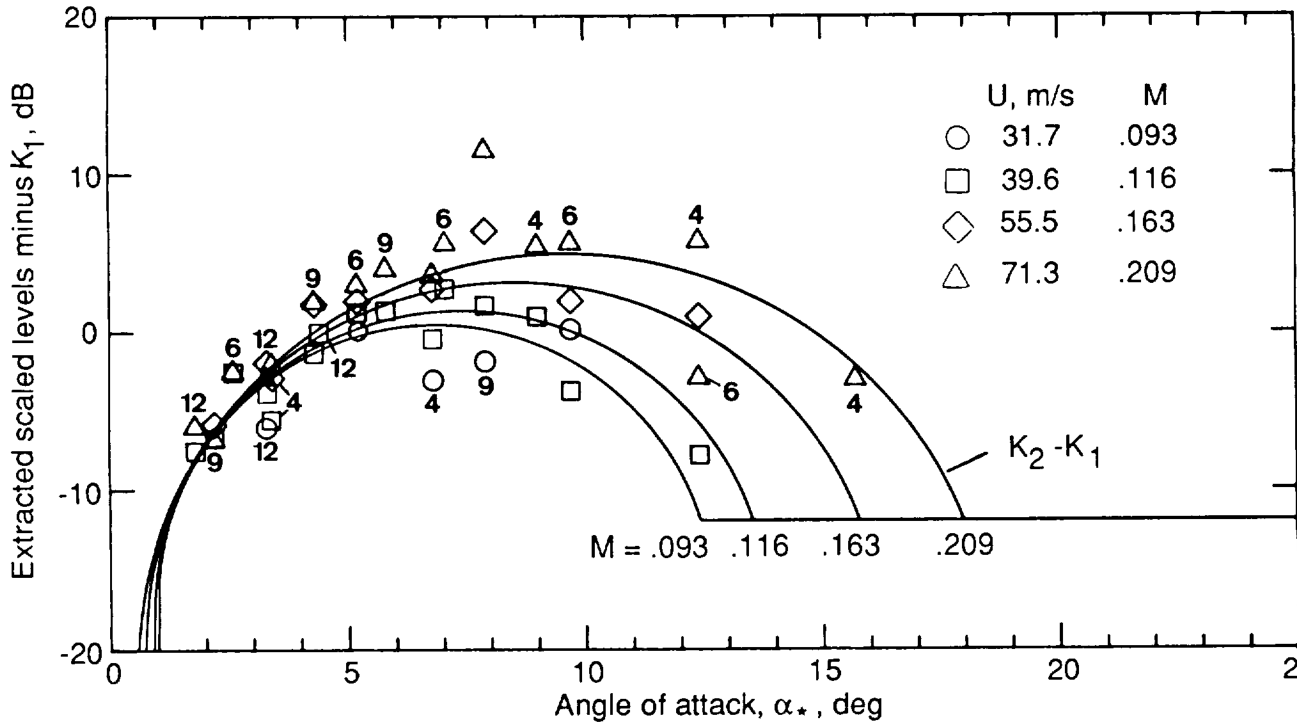

Figure 82. Angle-dependent scaled noise levels as referenced to zero angle of attack, TBL–TE noise model. Numbers aligned with data are chord sizes in inches.

5.1.2. Calculation Procedures

The total TBL–TE and separation noise spectrum in a 1/3-octave presentation is predicted by

$$\mathrm{SPL_{TOT}} = 10\log\left(10^{\mathrm{SPL}_\alpha/10} + 10^{\mathrm{SPL}_s/10} + 10^{\mathrm{SPL}_p/10}\right) \tag{24}$$

where

$$\mathrm{SPL}_p = 10\log\left(\frac{\delta_p^* M^5 L \overline{D}_h}{r_e^2}\right) + A\left(\frac{\mathrm{St}_p}{\mathrm{St}_1}\right) + (K_1 - 3) + \Delta K_1 \tag{25}$$

$$\mathrm{SPL}_s = 10\log\left(\frac{\delta_s^* M^5 L \overline{D}_h}{r_e^2}\right) + A\left(\frac{\mathrm{St}_s}{\mathrm{St}_1}\right) + (K_1 - 3) \tag{26}$$

and

$$\mathrm{SPL}_\alpha = 10\log\left(\frac{\delta_s^* M^5 L \overline{D}_h}{r_e^2}\right) + B\left(\frac{\mathrm{St}_s}{\mathrm{St}_2}\right) + K_2 \tag{27}$$

for angles of attack up to $(\alpha_*)_0$, an angle to be defined later in this section. At angles above $(\alpha_*)_0$,

$$\mathrm{SPL}_p = -\infty \tag{28}$$

$$\mathrm{SPL}_s = -\infty \tag{29}$$

and

$$\mathrm{SPL}_\alpha = 10\log\left(\frac{\delta_s^* M^5 L \overline{D}_\ell}{r_e^2}\right) + A'\left(\frac{\mathrm{St}_s}{\mathrm{St}_2}\right) + K_2 \tag{30}$$

where A' is the curve A but for a value of R_c which is three times the actual value. The directivity functions $\overline{D}_h$ and $\overline{D}_\ell$ are given in appendix B by equations (B1) and (B2), respectively.

The Strouhal definitions are (see figs. 76 and 80)

$$\mathrm{St}_p = \frac{f\delta_p^*}{U} \qquad \mathrm{St}_s = \frac{f\delta_s^*}{U} \tag{31}$$

$$\mathrm{St}_1 = 0.02M^{-0.6} \tag{32}$$

$$\overline{\mathrm{St}_1} = \frac{\mathrm{St}_1 + \mathrm{St}_2}{2} \tag{33}$$

and

$$\mathrm{St}_2 = \mathrm{St}_1 \times \begin{cases} 1 & (\alpha_* < 1.33^\circ) \\ 10^{0.0054(\alpha_* - 1.33)^2} & (1.33^\circ \le \alpha_* \le 12.5^\circ) \\ 4.72 & (12.5^\circ < \alpha_*) \end{cases} \tag{34}$$

For the spectral shape function definitions, we first consider the function A of figure 78(a). As discussed, the function A for a particular Reynolds number R_c is obtained from an interpolation of the curves A_{max} and A_{min}, corresponding to chosen values, $(R_c)_{\mathrm{max}}$ and $(R_c)_{\mathrm{min}}$. The two curves are defined as

$$A_{\mathrm{min}}(a) = \begin{cases} \sqrt{67.552 - 886.788a^2} - 8.219 & (a < 0.204) \\ -32.665a + 3.981 & (0.204 \le a \le 0.244) \\ -142.795a^3 + 103.656a^2 - 57.757a + 6.006 & (0.244 < a) \end{cases} \tag{35}$$

and

$$A_{\mathrm{max}}(a) = \begin{cases} \sqrt{67.552 - 886.788a^2} - 8.219 & (a < 0.13) \\ -15.901a + 1.098 & (0.13 \le a \le 0.321) \\ -4.669a^3 + 3.491a^2 - 16.699a + 1.149 & (0.321 < a) \end{cases} \tag{36}$$

where a is the absolute value of the logarithm of the ratio of Strouhal number, $\mathrm{St} = \mathrm{St}_p$ or St_s, to the peak Strouhal number, $\mathrm{St}_{\mathrm{peak}} = \mathrm{St}_1$, $\overline{\mathrm{St}_1}$, or St_2:

$$a = |\log(\mathrm{St}/\mathrm{St}_{\mathrm{peak}})| \tag{37}$$

The absolute value is used because the spectral shape is modeled to be symmetric about $a = 0$.

The interpolative procedure includes defining a value, $a_0(R_c)$, at which the spectrum has a value of −20 dB. This −20 dB corresponds to a horizontal axis intercept in figure 78(a) for an interpolated curve. The function

$a_0(R_c)$ is given by

$$a_0(R_c) = \begin{cases} 0.57 & (R_c < 9.52 \times 10^4) \\ (-9.57 \times 10^{-13})(R_c - 8.57 \times 10^5)^2 + 1.13 & (9.52 \times 10^4 \leq R_c \leq 8.57 \times 10^5) \\ 1.13 & (8.57 \times 10^5 < R_c) \end{cases} \tag{38}$$

An interpolation factor $A_R(a_0)$ is determined from

$$A_R(a_0) = \frac{-20 - A_{\min}(a_0)}{A_{\max}(a_0) - A_{\min}(a_0)} \tag{39}$$

where $A_{\min}(a_0)$ and $A_{\max}(a_0)$ are the $A_{\max}$ and $A_{\min}$ spectra evaluated at a_0. The spectrum shape A can now be evaluated for any frequency by computing the Strouhal number St and the corresponding a and using the interpolation factor. The result for use in equations (25), (26), and (30) is

$$A(a) = A_{\min}(a) + A_R(a_0)\left[A_{\max}(a) - A_{\min}(a)\right] \tag{40}$$

The function B in equation (27) and shown plotted in figure 78(b) is calculated in a manner similar to function A above. The two curves $B_{\max}$ and $B_{\min}$, through which B is obtained from interpolation, are

$$B_{\min}(b) = \begin{cases} \sqrt{16.888 - 886.788b^2} - 4.109 & (b < 0.13) \\ -83.607b + 8.138 & (0.13 \leq b \leq 0.145) \\ -817.810b^3 + 355.210b^2 - 135.024b + 10.619 & (0.145 < b) \end{cases} \tag{41}$$

and

$$B_{\max}(b) = \begin{cases} \sqrt{16.888 - 886.788b^2} - 4.109 & (b < 0.10) \\ -31.330b + 1.854 & (0.10 \leq b \leq 0.187) \\ -80.541b^3 + 44.174b^2 - 39.381b + 2.344 & (0.187 < b) \end{cases} \tag{42}$$

where

$$b = \left|\log(\mathrm{St}_s/\mathrm{St}_2)\right| \tag{43}$$

The spectral shape B for intermediate values of R_c have horizontal axis intercepts at -20 dB in figure 78(b) for values of b of

$$b_0(R_c) = \begin{cases} 0.30 & (R_c < 9.52 \times 10^4) \\ (-4.48 \times 10^{-13})(R_c - 8.57 \times 10^5)^2 + 0.56 & (9.52 \times 10^4 \leq R_c \leq 8.57 \times 10^5) \\ 0.56 & (8.57 \times 10^5 < R_c) \end{cases} \tag{44}$$

The interpolation factor $B_R(b_0)$ is defined as

$$B_R(b_0) = \frac{-20 - B_{\min}(b_0)}{B_{\max}(b_0) - B_{\min}(b_0)} \tag{45}$$

and thus the result for use in equation (27) is

$$B(b) = B_{\min}(b) + B_R(b_0)\left[B_{\max}(b) - B_{\min}(b)\right] \tag{46}$$

The amplitude function K_1 in equations (25) and (26) is plotted in figure 77 and is given by

$$K_1 = \begin{cases} -4.31\log(R_c) + 156.3 & (R_c < 2.47 \times 10^5) \\ -9.0\log(R_c) + 181.6 & (2.47 \times 10^5 \leq R_c \leq 8.0 \times 10^5) \\ 128.5 & (8.0 \times 10^5 < R_c) \end{cases} \tag{47}$$

The level adjustment previously mentioned for the pressure-side contribution for nonzero angles of attack appears as ΔK_1 in equation (25). This is given by

$$\Delta K_1 = \begin{cases} \alpha_* \left[1.43\log\left(R_{\delta_p^*}\right) - 5.29\right] & (R_{\delta_p^*} \leq 5000) \\ 0 & (5000 < R_{\delta_p^*}) \end{cases} \tag{48}$$

where $R_{\delta_p^*}$ is the Reynolds number based on pressure-side displacement thickness.

The amplitude function K_2 of equations (27) and (30) is plotted for some values of M in figure 82 and is given as

$$K_2 = K_1 + \begin{cases} -1000 & (\alpha_* < \gamma_0 - \gamma) \\ \sqrt{\beta^2 - (\beta/\gamma)^2(\alpha_* - \gamma_0)^2} + \beta_0 & (\gamma_0 - \gamma \leq \alpha_* \leq \gamma_0 + \gamma) \\ -12 & (\gamma_0 + \gamma < \alpha_*) \end{cases} \tag{49}$$

where

$$\left.\begin{aligned} \gamma &= 27.094M + 3.31 \qquad & \gamma_0 &= 23.43M + 4.651 \\ \beta &= 72.65M + 10.74 \qquad & \beta_0 &= -34.19M - 13.82 \end{aligned}\right\} \tag{50}$$

The angle definitions above are in units of degrees and are taken as positive in sign. The K_2 definition above is valid for all values of α_*, even when the calculation of the total noise in equation (24) switches from the use of equations (25), (26), and (27) for assumed attached TBL flow to equations (28), (29), and (30) for a supposedly stalled flow condition. The angle where the switch occurs, specified previously as $(\alpha_*)_0$, is taken to be equal to the peak of the K_2 function defined by γ_0 in equation (50) or whenever α_* exceeds 12.5°, whichever is first.

5.1.3. Comparison With Data

The scaling predictions of TBL–TE and separation noise are compared with the noise data in figures 11 to 43 for the tripped BL airfoils. The calculations used the appropriate values of δ^* from section 3 and the directivity functions from appendix B (where $r_e = 1.22$ m, $\Theta_e = 90°$, and $\Phi_e = 90°$). The total self-noise is given as well as the individual noise components of TBL–TE noise from the suction and pressure sides and separation noise. The predictions follow the shapes and levels of the data, especially for the larger airfoils and the lower angles of attack where the scaling accuracy was most emphasized. Predictions of TBL–TE and separation noise are also shown for the untripped BL airfoils in figures 44 to 74. For the many untripped cases where these sources are predicted to be dominant, the agreement is generally good. Even where the LBL–VS noise dominates, the TBL–TE and separation contributions help with the overall spectral agreement.

5.2. Laminar-Boundary-Layer–Vortex-Shedding Noise

As previously described in section 1, laminar-boundary-layer instabilities couple with acoustic feedback to produce quasi-tonal noise. In contrast to TBL–TE noise, there are no LBL–VS noise scaling methods established in the literature because of the erratic behavior of the multiple tones in the narrow-band spectra and the general complexity of the mechanism. Two key results from the literature which provide initial scaling guidance are (1) that the gross trend of the frequency dependence was found to scale on a Strouhal basis, with the relevant length scale being the laminar-boundary-layer thickness at the airfoil trailing edge (ref. 16), and (2) that on the basis of the limited data from the data base of the present paper as reported in reference (6), overall levels tended to coalesce to a unique function of R_c when normalized in the fashion of TBL–TE noise.

The scaling approach taken herein is similar to that taken for TBL–TE noise in the last section in that a universal spectral shape and Strouhal dependency is modeled in terms of boundary-layer parameters, Mach number, angle of attack, and Reynolds number. The use of 1/3-octave spectra, rather than narrow band, permits such an approach because the broad spectral bands overlap the tonal frequency spacing to give smoother and generally single-peaked spectra.

5.2.1. Scaled Data

Scaled 1/3-octave sound pressure level spectra for four airfoil sizes, each at four tunnel speeds, are presented in figure 83 from figures 44, 53, 59, and 65. The angle of attack for all is zero and the boundary layers are untripped. The normalization employs

$$\text{Scaled SPL}_{1/3} = \text{SPL}_{1/3} - 10\log\left(M^5 \frac{\delta_p L}{r_e^2}\right) \quad (51)$$

for level scaling and

$$\text{St}' = \frac{f\delta_p}{U} \quad (52)$$

for Strouhal frequency scaling. For the symmetric airfoils at zero angle of attack, $\delta_p = \delta_s = \delta_0$. The scaling approach differs from the TBL–TE noise scaling because of the use of δ_p, the boundary-layer thickness on the pressure side of the airfoil, rather than δ_s^*, the boundary-layer displacement thickness on the suction side. The use of δ_p as the pertinent length scale follows from reference 16 and was found to give seemingly better results in initial scaling of the present data base than δ_p^* and by far better than c, δ_s, or δ_s^* for angles of attack other than zero.

In figure 83(a) for the large 30.48-cm-chord airfoil, the spectra appear to be of smooth broad hump shapes. There is no apparent contribution to the spectra from LBL–VS noise which is peaked in character. The boundary layers are fully turbulent in the vicinity of the trailing edge at all four tunnel speeds (ref. 21), so no laminar vortex shedding is established. The noise produced is assumed to be all TBL–TE noise. In figure 83(b) for the 15.24-cm-chord airfoil, the broad spectral shapes are changed by the addition of a peak when the flow velocity is diminished. The peak levels increase with decreasing velocity. Although the boundary layer is turbulent at the trailing edge at all velocities shown, laminar flow exists over larger portions of the airfoil at the lower velocities. As mentioned for the LBL–VS noise mechanism, any spectral peaks containing a number of tonal contributions should scale with Strouhal numbers based on boundary-layer thickness. This is the case in figure 83(b) with $\text{St}' \approx 0.27$. For the shorter 10.16-cm-chord airfoil, in figure 83(c), the LBL–VS noise peaks become even more dominant for decreasing velocity. Note also the changing Strouhal dependence, not noted in previous studies. The shorter 5.08-cm-chord airfoil, in figure 83(d), has even more pronounced level and Strouhal dependence with velocity variations.

Whereas figure 83 shows the dependence of LBL–VS noise on velocity for the various airfoil sizes at zero angle of attack, figure 84 shows the effect of angle of attack α_* of the airfoils at a velocity of 71.3 m/s. The spectra for the 30.48-cm-chord airfoil, shown in figure 84(a), change from being dominated by TBL–TE noise, for $\alpha_* = 0°$, to being dominated by LBL–VS noise, for $\alpha_* = 4.0°$. So even with a large Reynolds number ($R_c = 1.52 \times 10^6$), LBL–VS noise occurs. With increasing α_*, the boundary layer on the pressure side becomes more laminar over a sufficiently large portion of the chord to result in increased shedding and corresponding noise. For the 15.24-cm-chord airfoil ($R_c = 7.58 \times 10^5$), shown in figure 84(b), the LBL–VS noise increases with α_* until a certain value is reached where it diminishes. At $\alpha_* = 7.2°$, no apparent shedding noise is shown. At $\alpha_* = 9.9°$, the noise changes appreciably to that for stalled flow as discussed in the last section. The use of δ_p as the characteristic length scale apparently results in a proper Strouhal scaling for the shedding noise peaks; but, as expected, the spectra for $\alpha_* =$ 0°, 7.2°, and 9.9°, which are dominated by TBL–TE and separated flow noise, diverge in this normalized format. A similar angle-dependent behavior where spectra do not coalesce is seen for the 10.16-cm-chord airfoil, in figure 84(c), where LBL–VS noise is apparent at $\alpha_* = 0°$ and 3.3° but not at the higher angles. For the 5.08-cm-chord model, figure 84(d) shows large-amplitude LBL–VS noise at $\alpha_* = 0°$ and 4.2°.

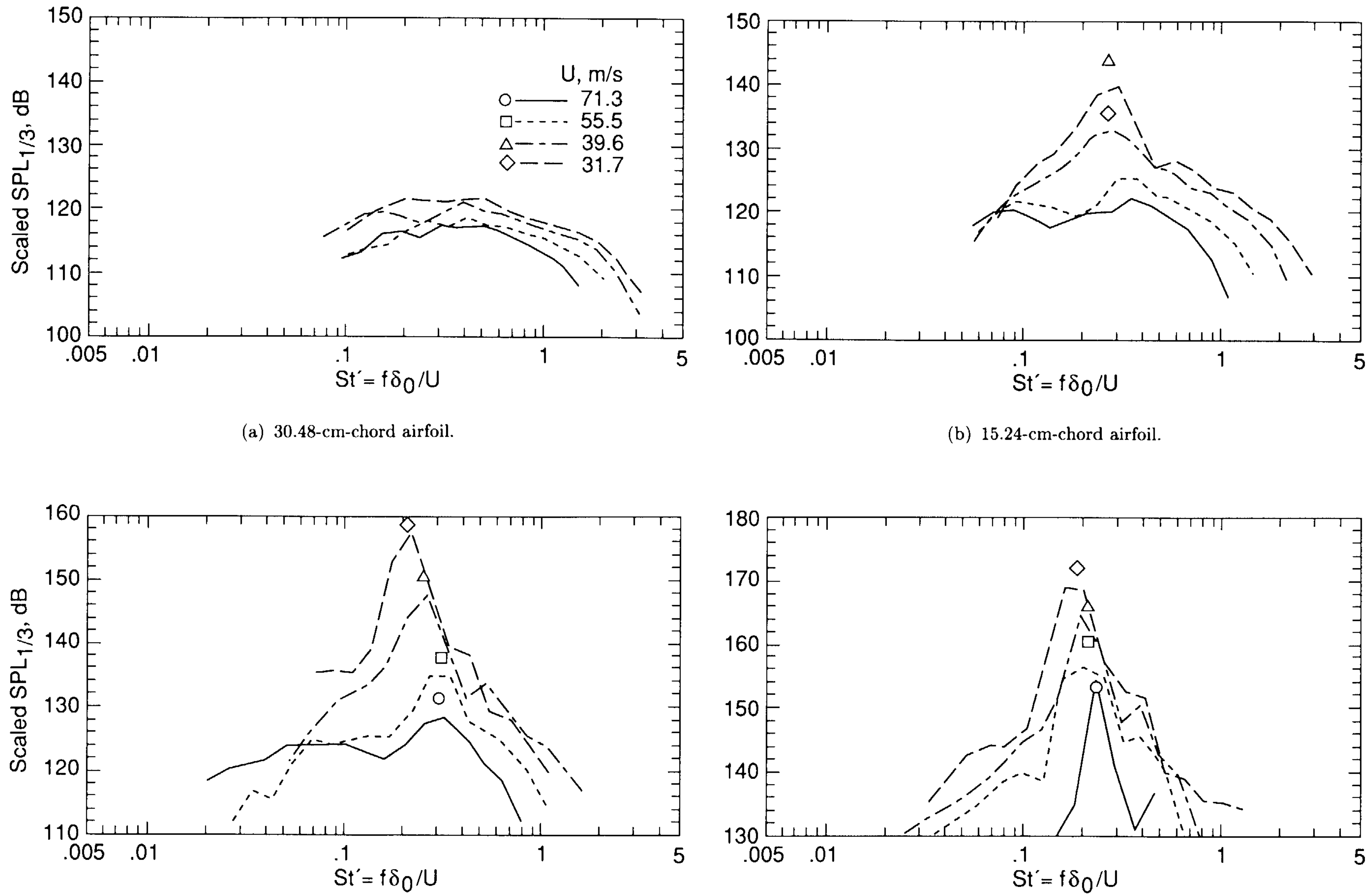

(a) 30.48-cm-chord airfoil.

(b) 15.24-cm-chord airfoil.

(c) 10.16-cm-chord airfoil.

(d) 5.08-cm-chord airfoil.

Figure 83. Scaled 1/3-octave spectra for untripped BL airfoils at $\alpha_t = 0°$ ($\alpha_* = 0°$). Symbols indicate approximate LBL VS reference peak location.

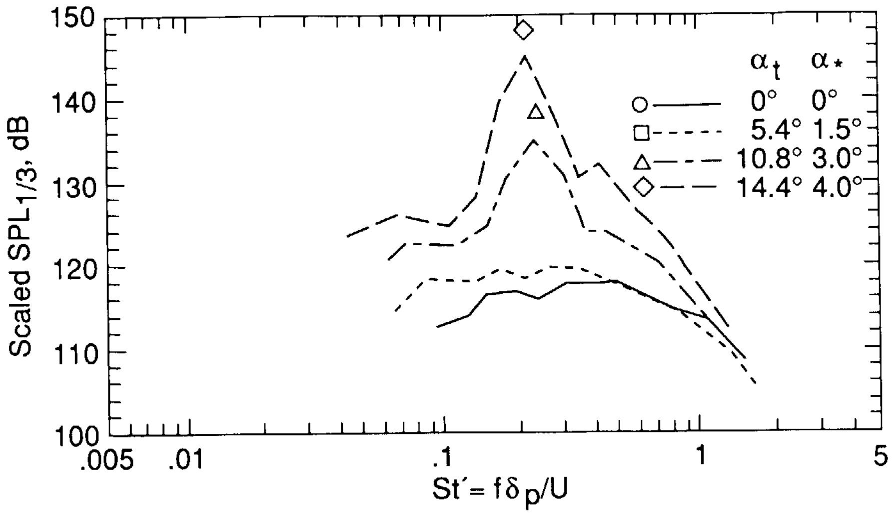

(a) 30.48-cm-chord airfoil.

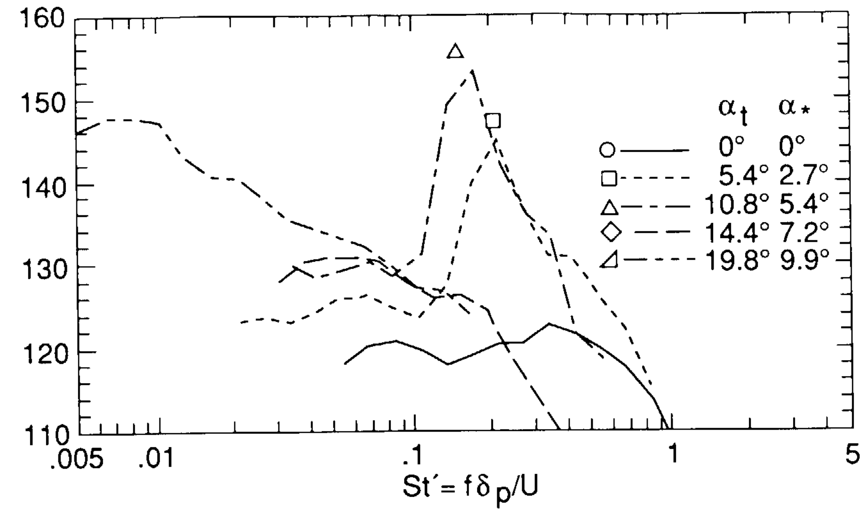

(b) 15.24-cm-chord airfoil.

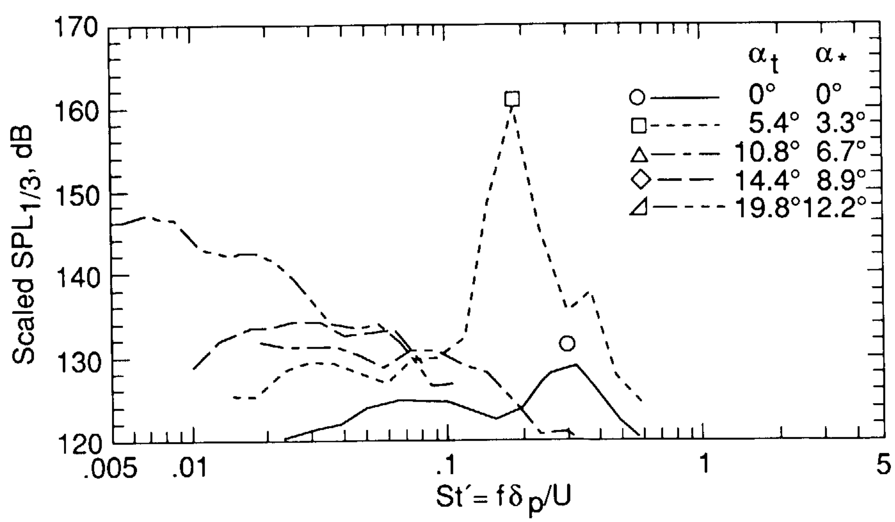

(c) 10.16-cm-chord airfoil.

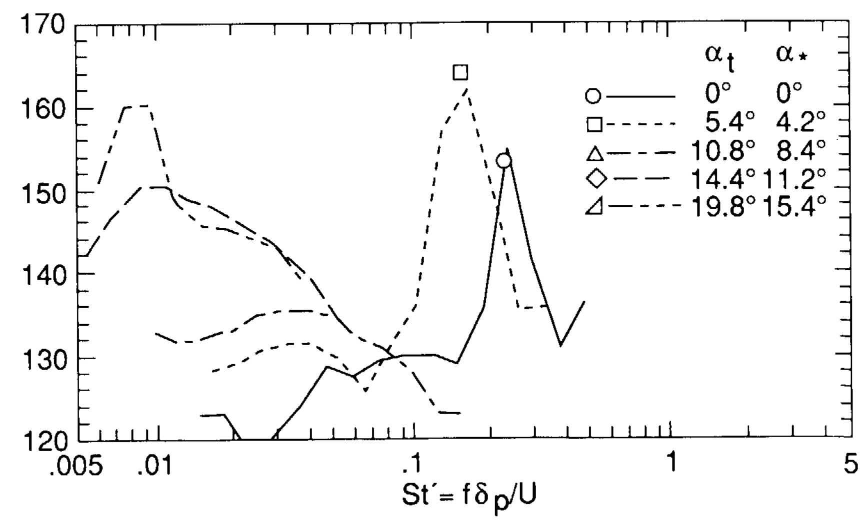

(d) 5.08-cm-chord airfoil.

Figure 84. Scaled 1/3-octave spectra for untripped BL airfoils at various angles of attack. $U = 71.3$ m/s. Symbols indicate approximate LBL–VS reference peak locations.

The LBL–VS noise portions of the spectra (figs. 83 and 84) are rather invariant with respect to spectral shape. Based on this observation, a function G_1 (shown in fig. 85) was chosen as a shape to represent the LBL–VS contribution to the self-noise 1/3-octave spectra for all cases. The level of G_1 at $\mathrm{St}' = \mathrm{St}'_{\mathrm{peak}}$ has a value of −3.5 dB. The reference level of 0 dB is the integrated total of G_1. To permit an orderly study of the Reynolds number and angle dependences of the spectral data, the shape G_1 was matched to the individual spectra to obtain reference overall peak levels and Strouhal numbers. Emphasis was placed on matching the global spectral shape of G_1 to the data rather than matching 1/3-octave band peak or overall levels. Reference peak locations are indicated by the symbols in figures 83 and 84.

In figure 86, the chosen values of $\mathrm{St}'_{\mathrm{peak}}$ are plotted versus the Reynolds number R_c for the 42 cases where LBL–VS noise is prominent. The values are also given in table 2 (at the back of this report) along with the effective angles of attack α_* corresponding to α_t. For $\alpha_* = 0$, $\mathrm{St}'_{\mathrm{peak}}$ is approximately constant at low R_c and increases with R_c in the mid-range of R_c shown. The values of $\mathrm{St}'_{\mathrm{peak}}$ are lower for nonzero angles of attack. A function St'_1 is drawn to approximate the data of zero angle of attack. A constant value for St'_1 is chosen for high R_c, where no zero-angle-of-attack data are present, because the value permits a simple angle dependence definition for $\mathrm{St}'_{\mathrm{peak}}$. In figure 87, $\mathrm{St}'_{\mathrm{peak}}$ is normalized by St'_1 and plotted versus α_*. For each of the six airfoils, the line described by $10^{-0.04\alpha_*}$ approximates the angle dependence.

The reference peak scaled levels which correspond to $\mathrm{St}'_{\mathrm{peak}}$ in figure 86 are plotted versus R_c in figure 88. To show general trends more clearly, the symbols are replaced by the value of α_*, rounded off to the nearest whole degree (see table 2 for more exact values). In this format it is seen that for each α_* the scaled levels tend to increase, peak, and decrease as R_c increases. For the larger angles of attack, the peak levels are lower and the corresponding values of R_c are larger. Superimposed on the data are curves of identical shape, called here "level shape curves," which are positioned in a monotonically decreasing fashion to approximately correspond to the data trends with angle variation. The angles indicated for each curve position should not necessarily match the angle values listed for the data because the data values are rounded off in the figure, as mentioned. The intent is to use the curves, with their functional relationship to α_* and R_c shown in figure 88, to represent the amplitude definition of LBL–VS noise. In the following calculation procedures section, a function G_2 specifies the curve shape, G_3 is the angle dependence for the level of the G_2 curve, and a reference $(R_c)_0$ value is defined as a function of angle to specify the Reynolds number dependence. The success of the functions in normalizing the data is shown in figure 89 where peak scaled 1/3-octave level minus G_3 is compared with the function G_2. In this format the individual angle numbers should ideally match the G_2 curve. Although the agreement shown is certainly not complete, it is regarded here as acceptable. Note that much better curve fits to the data would be possible if a requirement for monotonic functional behavior had not been imposed on G_3 and $(R_c)_0$.

5.2.2. Calculation Procedures

The LBL–VS noise spectrum in a 1/3-octave presentation is predicted by

$$\mathrm{SPL}_{\mathrm{LBL\text{-}VS}} = 10 \log \left(\frac{\delta_p M^5 L \overline{D}_h}{r_e^2} \right) + G_1 \left(\frac{\mathrm{St}'}{\mathrm{St}'_{\mathrm{peak}}} \right) + G_2 \left[\frac{R_c}{(R_c)_0} \right] + G_3(\alpha_*) \tag{53}$$

The Strouhal definitions are (see figs. 86 and 87)

$$\mathrm{St}' = \frac{f \delta_p}{U} \tag{54}$$

$$\mathrm{St}'_1 = \begin{cases} 0.18 & (R_c \leq 1.3 \times 10^5) \\ 0.001756 R_c^{0.3931} & (1.3 \times 10^5 < R_c \leq 4.0 \times 10^5) \\ 0.28 & (4.0 \times 10^5 < R_c) \end{cases} \tag{55}$$

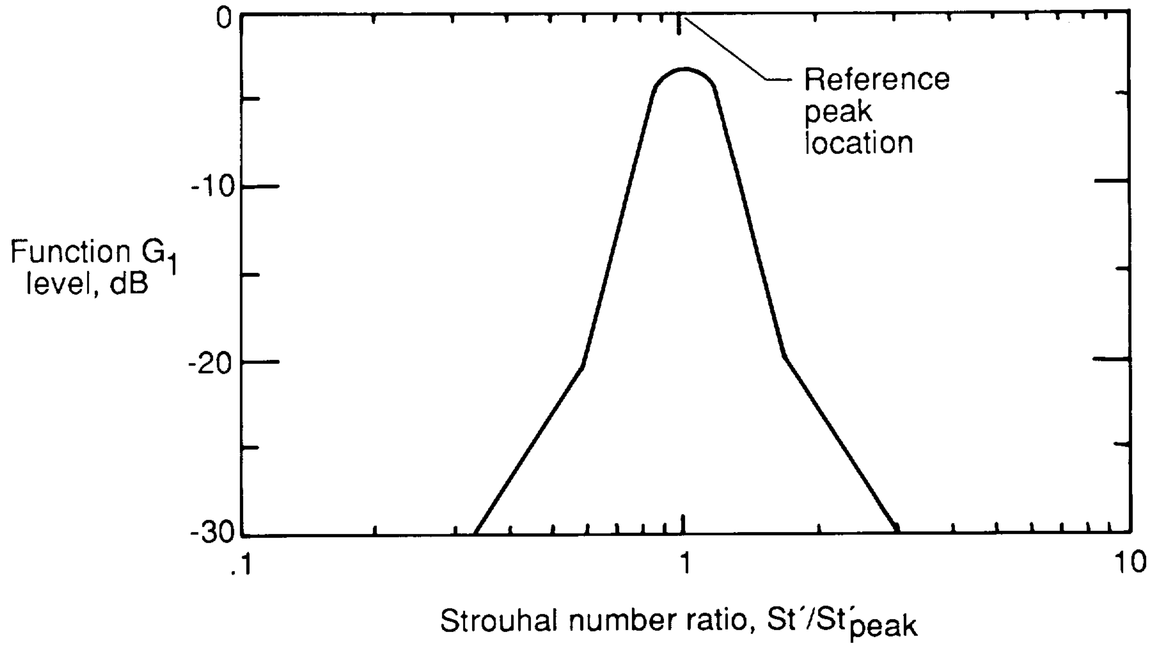

Figure 85. One-third-octave spectral shape function G_1 for LBL–VS noise, equation (57).

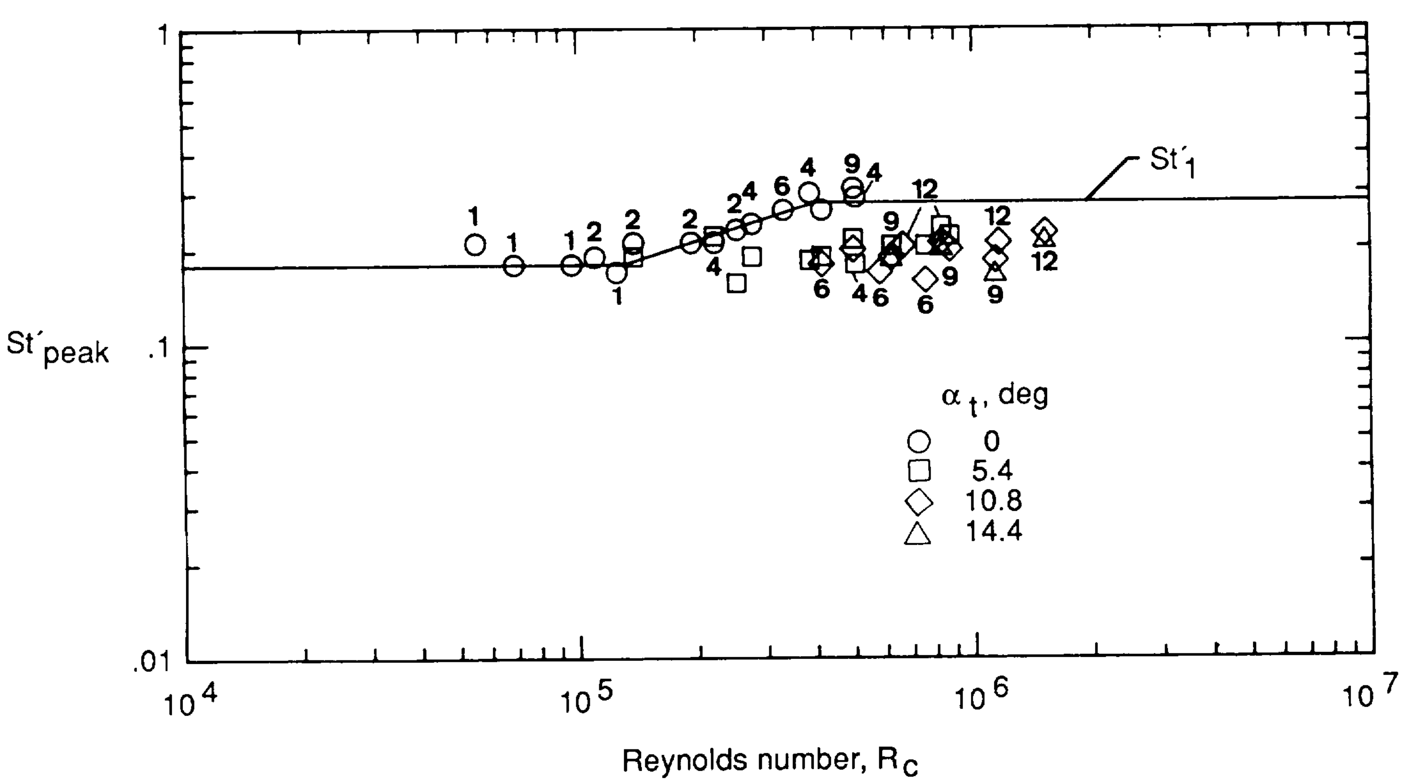

Figure 86. Peak Strouhal number for LBL–VS noise versus Reynolds number. Numbers aligned with data are chord sizes in inches.

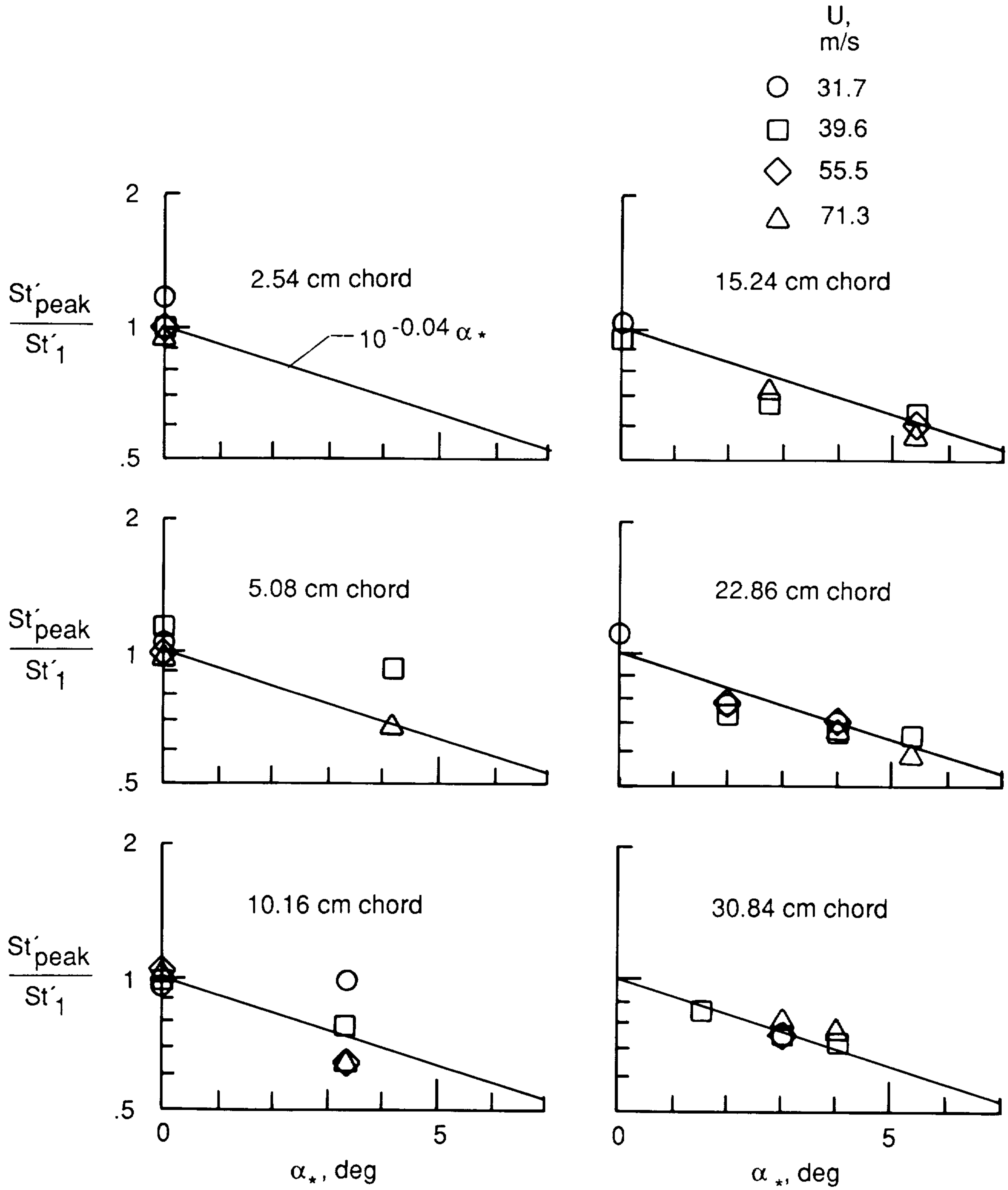

Figure 87. Peak Strouhal number for LBL–VS noise versus angle of attack. Data from figure 86.

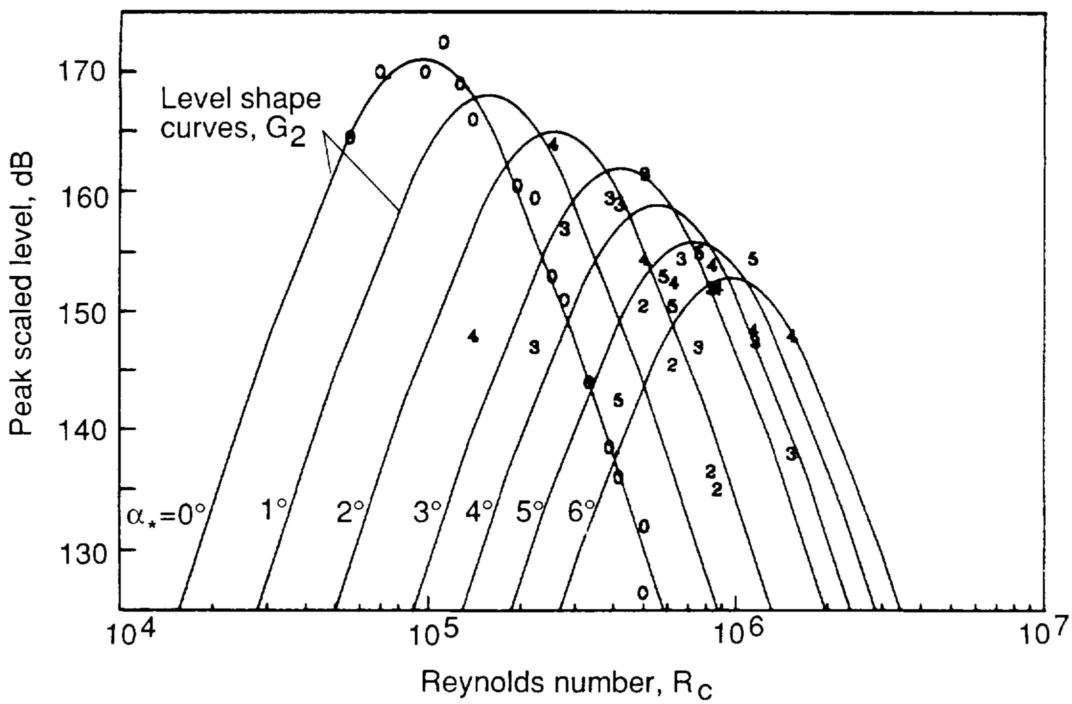

Figure 88. Peak scaled levels for LBL-VS noise versus Reynolds number. Data symbols are values of α_* rounded off to nearest degree.

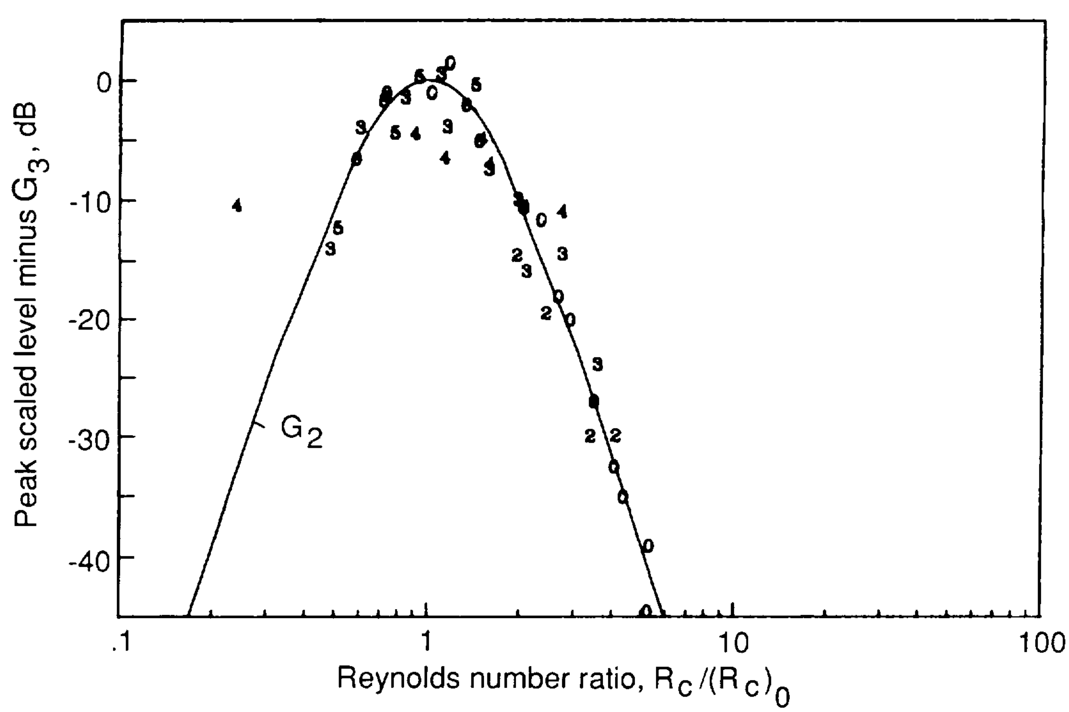

Figure 89. Normalization of LBL-VS noise peak scaled levels by functions G_2, equations (58) and (59), and G_3, equation (60). Data from figure 88. Data symbols are values of α_* rounded off to nearest degree.

and

$$\mathrm{St}'_{\mathrm{peak}} = \mathrm{St}'_1 \times 10^{-0.04\alpha_*} \tag{56}$$

The directivity function $\overline{D}_h$ is given by equation (B1) in appendix B. The function G_1 defines the spectral shape, in terms of the ratio of Strouhal number to its peak, as (see fig. 85)

$$G_1(e) = \begin{cases} 39.8\log(e) - 11.12 & (e \leq 0.5974) \\ 98.409\log(e) + 2.0 & (0.5974 < e \leq 0.8545) \\ -5.076 + \sqrt{2.484 - 506.25[\log(e)]^2} & (0.8545 < e \leq 1.17) \\ -98.409\log(e) + 2.0 & (1.17 < e \leq 1.674) \\ -39.8\log(e) - 11.12 & (1.674 < e) \end{cases} \tag{57}$$

where $e = \mathrm{St}'/\mathrm{St}'_{\mathrm{peak}}$. The peak scaled level shape curve G_2 depends on Reynolds number and angle and is (see figs. 88 and 89)

$$G_2(d) = \begin{cases} 77.852\log(d) + 15.328 & (d \leq 0.3237) \\ 65.188\log(d) + 9.125 & (0.3237 < d \leq 0.5689) \\ -114.052[\log(d)]^2 & (0.5689 < d \leq 1.7579) \\ -65.188\log(d) + 9.125 & (1.7579 < d \leq 3.0889) \\ -77.852\log(d) + 15.328 & (3.0889 < d) \end{cases} \tag{58}$$

where $d = R_c/(R_c)_0$ and the reference Reynolds number is

$$(R_c)_0 = \begin{cases} 10^{0.215\alpha_*+4.978} & (\alpha_* \leq 3.0) \\ 10^{0.120\alpha_*+5.263} & (3.0 < \alpha_*) \end{cases} \tag{59}$$

The angle-dependent level for the shape curve is

$$G_3(\alpha_*) = 171.04 - 3.03\alpha_* \tag{60}$$

5.2.3. Comparison With Data

The spectral predictions from the above equations are compared with the untripped BL airfoil noise data in figures 44 to 74. The great sensitivity of this mechanism to angle and velocity change can be clearly seen. In many respects the prediction agreement in shape, level, and actual occurrence of LBL–VS noise is good. Also as indicated in the last section, the combined contributions of LBL–VS, TBL–TE, and separation noise are important to the total predictions for this untripped BL airfoil data.

5.3. Tip Vortex Formation Noise

The prediction method proposed in this section for tip vortex formation noise is that developed by Brooks and Marcolini (ref. 18). The study isolated this high-frequency broadband self-noise by comparing aerodynamic and acoustic test results of both two-dimensional (2D) and three-dimensional (3D) airfoil models shown in figures 2 and 3, respectively. The premise of the tip noise determination method was that 3D models produce both tip noise and TBL–TE noise, while the 2D models produce only the latter. The study produced a prediction method in general agreement with the physical model of the mechanism first proposed by George, Najjar, and Kim (ref. 17). The noise is associated with the turbulence in the locally separated flow region at the tip of a lifting blade, where the tip vortex is formed. The flow field is illustrated in figure 90 for an airfoil blade tip at an angle of attack α_{TIP} to the flow of velocity U. The flow over the blade tip consists of a vortex of strength Γ with a thick viscous core whose spanwise extent at the TE is ℓ. The recirculating flow within the core is highly turbulent . The mechanism of noise production is taken to be TE noise due to the passage of this turbulence over the edge and into the wake.

5.3.1. Calculation Procedures

The tip vortex formation noise spectrum in a 1/3-octave presentation is predicted by

$$\mathrm{SPL}_{\mathrm{TIP}} = 10\log\left(\frac{M^2 M_{\mathrm{max}}^3 \ell^2 \overline{D}_h}{r_e^2}\right) - 30.5(\log \mathrm{St}'' + 0.3)^2 + 126 \qquad (61)$$

The Strouhal number is

$$\mathrm{St}'' = \frac{f\ell}{U_{\mathrm{max}}} \qquad (62)$$

The directivity function $\overline{D}_h$ is given by equation (B1) in appendix B. The second term on the right side of equation (61), which gives the frequency dependence, is a parabolic fit about a peak Strouhal number of 0.5. The spanwise extent at the TE of the separation due to the tip vortex is, for the tested rounded tip,

$$\ell/c \approx 0.008\alpha_{\mathrm{TIP}} \qquad (63)$$

where c is the chord length and α_{TIP} (see discussion below) is the angle of attack of the tip region to the oncoming flow. The maximum Mach number M_{max} of the flow within or about the separated flow region at the trailing edge is

$$M_{\mathrm{max}}/M \approx (1 + 0.036\alpha_{\mathrm{TIP}}) \qquad (64)$$

where M is the Mach number of the oncoming flow to the airfoil tip region. The velocity corresponding to M_{max} is

$$U_{\mathrm{max}} = c_o M_{\mathrm{max}} \qquad (65)$$

Note that in the use of equations (63) and (64) to determine ℓ and $M_{\mathrm{max}}, \alpha_{\mathrm{TIP}}$ is correctly regarded as the actual angle of attack of the tip to the oncoming flow when the blade under consideration has a large aspect ratio (large span), is untwisted, and encounters uniform flow over its span. This is the reference case in reference 18. When the tip loading characteristics differ from those for the reference case, such as for some rotor and propeller blades, α_{TIP} must be redefined according to computed sectional loading. The redefined α'_{TIP} is

$$\alpha'_{\mathrm{TIP}} = \left[\left(\frac{\partial L'/\partial y}{(\partial L'/\partial y)_{\mathrm{ref}}}\right)_{y\to\mathrm{TIP}}\right]\alpha_{\mathrm{TIP}} \qquad (66)$$

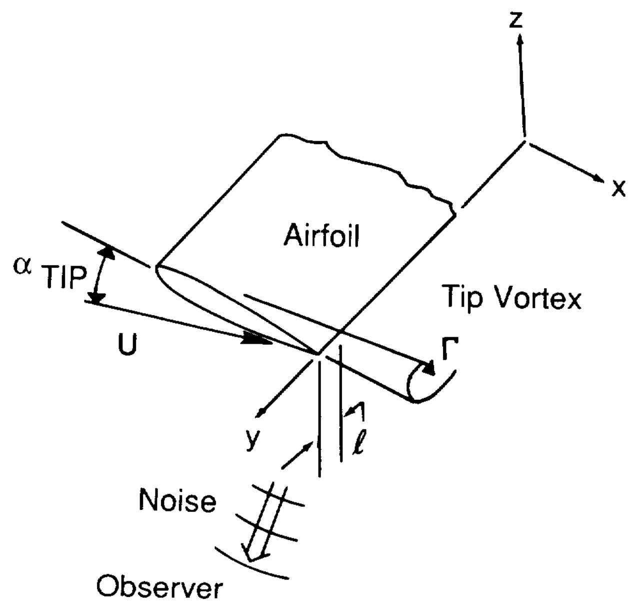

Figure 90. Formation of tip vortex.

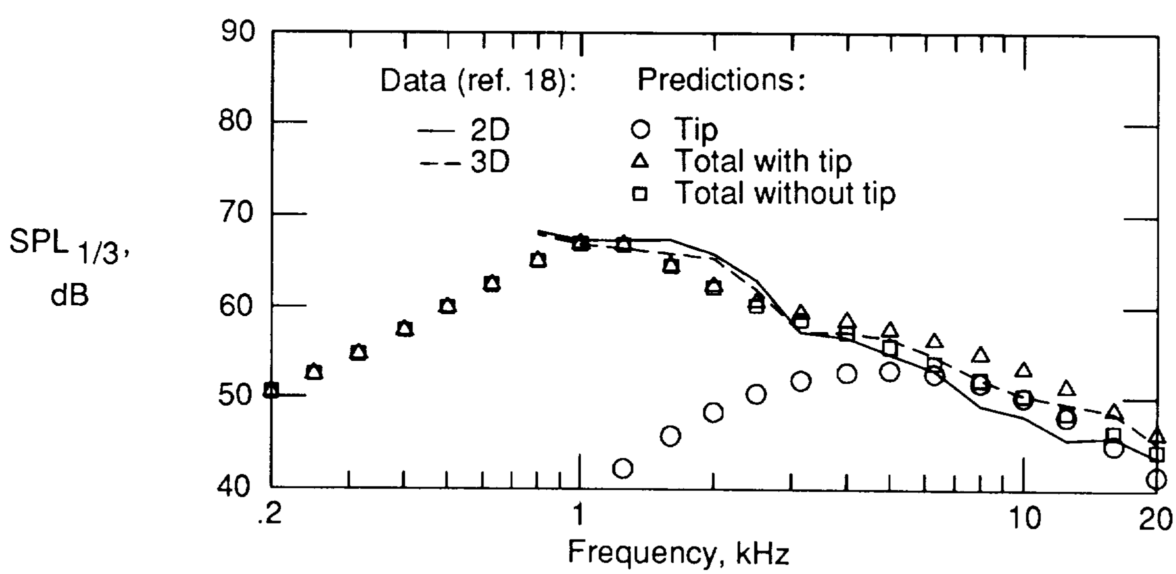

Figure 91. Noise spectra of a 3D 15.24-cm-chord airfoil with a span of 30.48 cm, and that of a 2D airfoil section where levels have been adjusted to match the same span. U = 71.3 m/s, α_t = 10.8°.

where α_{TIP} is the geometric angle and L' is the lift per unit span at the spanwise position y. The sectional lift slope $\partial L'/\partial y$ near the tip is taken to be proportional to the tip vortex strength Γ (of fig. 90). When tip loading is found to be high, the predicted tip noise levels increase. The use of α'_{TIP} rather than α_{TIP} in equations (63) and (64) generalizes the solution for arbitrary aspect ratios, blade twist, and spanwise flow variations. Reference 18 contains examples which provide guidance in the evaluation of equation (66) for aspect ratio, as well as tunnel testing effects.

The tip noise prediction equations are based on data from airfoils with rounded blade tips. Of interest is a flat (square-off or cut-off) tip geometry which reference 8 considered, along with rounded tips, in calculations employing limited tip flow measurements reported in the literature. The different tip geometries required a different definition of the separated flow region size ℓ. In applying the prediction equations of the present paper for flat tips, it does not appear appropriate to use the definition of reference 8. The constants in equation (61) reflect the definition of ℓ in equation (63). The measurements did not confirm the definition of ℓ for rounded tips proposed by reference 8. For consistency, the following definition for ℓ is proposed for flat tips for the present prediction equations:

$$\ell/c = \begin{cases} 0.0230 + 0.0169\alpha'_{\mathrm{TIP}} & (0^\circ \leq \alpha'_{\mathrm{TIP}} \leq 2^\circ) \\ 0.0378 + 0.0095\alpha'_{\mathrm{TIP}} & (2^\circ < \alpha'_{\mathrm{TIP}}) \end{cases} \tag{67}$$

This definition of ℓ approximately accounts for differences between the definition of reference 8 and that of equation (63) for rounded tips. There is at present no experimental confirmation of equation (67).

5.3.2. Comparison With Data

Noise data from reference 18 (fig. 7) are presented in figure 91 along with predictions of tip noise and the combined contributions of TBL–TE and separation noise. The rounded tip 3D model has a chord of 15.24 cm and a span of 30.5 cm. The corresponding 2D model has a span of 45.7 cm so its noise spectrum levels in the figure were adjusted downward by 1.8 dB (based on a $10\log(L)$ dependency) to obtain that expected for a 30.5-cm span. The difference between the 2D and 3D spectra should be that due to tip noise. The predictions in figure 91 for TBL–TE and separation noise, which employed the angle $\alpha_* = 0.5(10.8^\circ)$ to account for the wind tunnel correction, should ideally match the 2D model spectrum. The tip noise prediction adds to the prediction to obtain a total which should match the 3D model spectrum. The tip noise prediction involved the use of equation (66) because of the finite extent of the span as well as open wind tunnel influences. Based on the lift distributions presented in reference 18, the tip angle becomes $\alpha'_{\mathrm{TIP}} = 0.71(10.8^\circ)$. While a slight overprediction at higher frequencies is seen in figure 91 for this particular example, the differences between levels with and without tip noise are the same for both data and prediction. The comparison shows consistency and compatibility not only with the data but also between the self-noise prediction methods.

5.4. Trailing-Edge-Bluntness–Vortex-Shedding Noise

In this section, the experiment of reference 2 is briefly described, published and previously unpublished TE bluntness noise data from the study are presented, and a prediction method is developed.

5.4.1. Experiment

The Brooks-Hodgson experiment (ref. 2) employed an experimental arrangement similar to that reported in section 2 of the present paper with respect to hardware and acoustic measurement. However, in reference 2, the model airfoil tested was large with a 60.96-cm chord length. When BL tripping was used, 2.0-cm-wide strips of No. 40 grit were applied at 15 percent of the chord. Rather than the TE being sharp, the model TE thickness, or bluntness, was $h = 2.5$ mm. Figure 92 shows the TE region of the airfoil. The TE geometry was rounded at the two edges and flat between the rounded edge portions, which each comprised about one-third of the 2.5-mm thickness. The thickness h was varied, with edges of similar geometry, by alternately attaching extensions on the edge, as illustrated in figure 92(a). Also tested were sharp-edge ($h = 0$) plate extensions 15.24 and 30.48 cm long, as shown in figure 92(b). Another sharp-edge extension (not shown) was a 2.54-cm-long "flap" extension placed at 17.5° off the chord mean axis at the trailing edge. In addition, blunt plate extensions were tested which were 15.24 cm long with

h = 2.5 and 4.8 mm and 30.48 cm long with h = 4.8 mm. These extensions with rounded TE corners are shown in figure 92(c). Tape, 0.08 mm thick, was used to provide a smooth surface transition from the airfoil to the extensions.

Presented in figure 93, from reference 2, are power spectral noise data of the airfoil at four flow velocities. The airfoil is at zero angle of attack and the boundary layers are tripped. The microphone observer position is $r_e = 1.22$ m and $\Theta_e = 90°$ with respect to the model trailing edge. For two speeds, the spectra are given for the four TE thicknesses of figure 92(a). The spectral results for the sharp, $h = 0$, TE cases should be all due to TBL–TE noise. The bluntness contributes additively at high frequencies to the spectrum levels. The values given for h/δ^* in figure 93 differ slightly from those specified in reference 2 because δ^* here is calculated from the BL thickness scaling equations of the present paper. Data are presented in reference 2 for the sharp geometries of figure 92(b), as well as the mentioned 17.5° sharp flap extension. These geometries give essentially the same spectra as the sharp extension of figure 92(a). This demonstrates that TBL–TE noise is rather invariant with regard to geometry changes in the edge region, as long as the TE is sharp and the boundary layers are substantially the same.

Trailing-edge bluntness noise spectra in a smoothed 1/3-octave format are presented in figure 94 for the edge geometries of figures 92(a) and 92(c). These spectra are the result of a spectral subtraction process between the total spectra and the corresponding sharp TE spectra and should thus represent the bluntness contribution only. With the exception of the eight spectra also represented in figure 93, the data have not been previously published. The indicated values of h/δ^* for the extensions are based on calculations of δ^* for the TE of the airfoil without the extensions. This is justified by indications that the boundary layers did not substantially change over the zero pressure gradient extension plates due to the influence of the upstream adverse pressure gradient (ref. 2). The spectrum for the airfoil with h = 2.5 mm and $h/\delta^* = 1.15$ in figure 94 is for naturally transitional boundary layers; all others are for tripped boundary layers.

5.4.2. Scaled Data

The spectra of figure 94, as well as limited frequency data of Blake (ref. 19), form the foundation of the scaling approach. As with the scaling approach for TBL–TE and LBL–VS noise, the level, frequency, and spectral shape are modeled as functions of flow and geometric parameters. For the level and frequency definition, we chose the peak of the spectral humps as the reference. The peak value of Strouhal number, defined as

$$\mathrm{St}'''_{\mathrm{peak}} = \frac{f_{\mathrm{peak}} h}{U} \tag{68}$$

is plotted versus the thickness ratio h/δ^* in figure 95. The Strouhal numbers increase with increases in thickness ratio. The Strouhal numbers for the plate extensions of figure 92(c) are uniformly higher, for the same thickness ratios, than for the edge extensions of figure 92(a). Also shown are two results obtained from Blake (ref. 19). Blake presents surface pressure data for a large array of plate edge geometries—all for very large values of h/δ^* (with the exception of the ref. 2 data reported and the one case shown in fig. 95 at $h/\delta^* = 5.19$). Blake, for most data, employed Strouhal relationships which depend on special wake stream thicknesses, and convection velocities not available without measurements. From Blake, however, it is obvious that different TE geometries have different frequency dependences, consistent with the result of figure 95 that Strouhal numbers for the flat plate extension and the airfoil TE geometries differ. The primary difference between the geometries is that the NACA 0012 airfoil has a beveled or sloping surface upstream of the trailing edge with a solid angle Ψ of 14° and the flat plate has $\Psi = 0°$. The result shown from Blake in figure 95 at $h/\delta^* = 5.19$ is for a plate with $\Psi = 12.5°$ and nonrounded TE corners. In figure 95, parallel curves are fitted to the data. The curves, designated with values of Ψ, are defined on the basis of a match point at $h/\delta^* = 20$ for $\Psi = 0°$. From Blake's scaling for a thick flat plate (h/δ^* large) with nonrounded TE corners, one can determine that $fh/U = 0.21$ at $h/\delta^* = 20$. The curve for $\Psi = 14°$ intercepts Blake's $\Psi = 12.5°$ result, but this is deemed an acceptable deviation from the curve fit. For scaling purposes, values of $\mathrm{St}'''_{\mathrm{peak}}$ for Ψ values other than 0° and 14° could be determined by linear interpolation as described in the calculation procedure section to follow.

For amplitude scaling, the peak values of the 1/3-octave spectra of figure 94 were normalized as

$$\text{Scaled peak SPL}_{1/3} = \text{Peak SPL}_{1/3} - 10\log\left(\frac{M^{5.5}hL}{r_e^2}\right) \tag{69}$$

The 5.5 power for Mach number dependence was determined to give better overall scaling success than either a 5 or 6 power. Figure 96 shows the scaled levels plotted versus the thickness ratio h/δ^*. As in figure 95 for the Strouhal dependency, the scaled levels are uniformly higher for the plates than for the

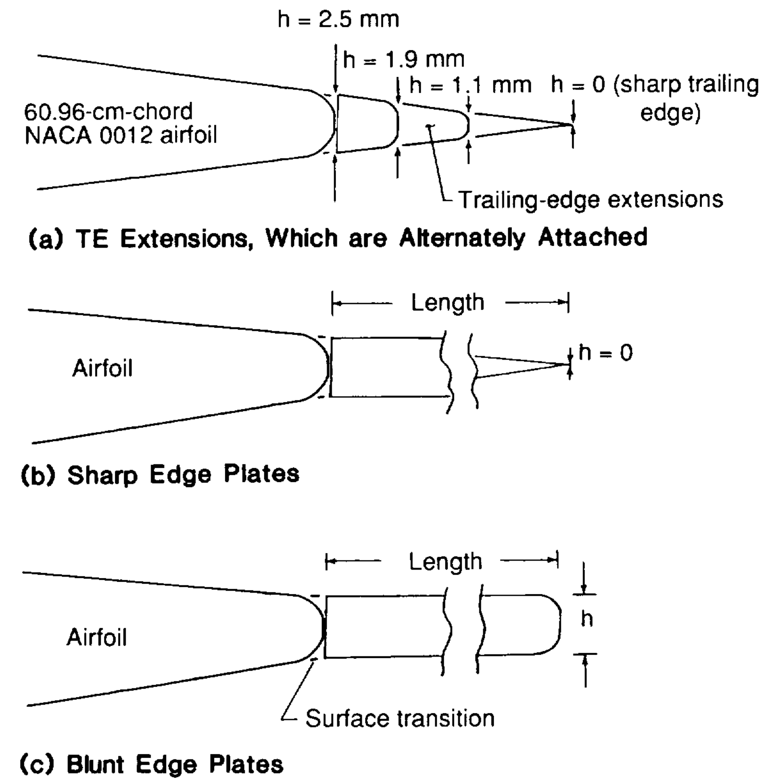

Figure 92. Illustration of trailing-edge extensions and plates. Smooth surface transition is provided for all geometries.

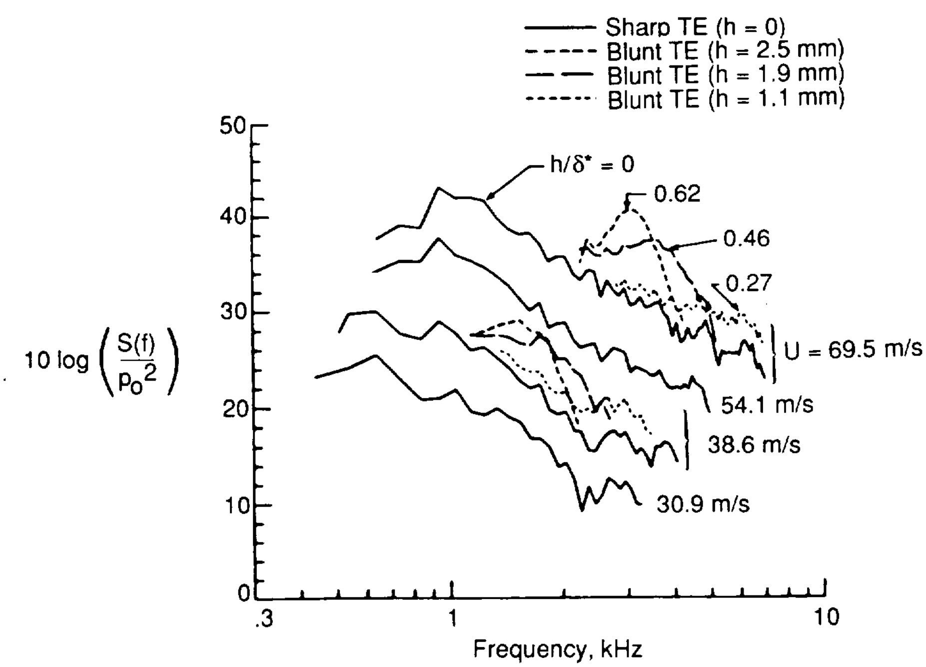

Figure 93. Spectral density for TE noise for 60.96-cm-chord airfoil with various degrees of TE bluntness. Tripped BL; $\alpha_t = 0°$; $\Theta_e = 90°$. Level referenced to 1-Hz bandwidth. Data from reference 2.

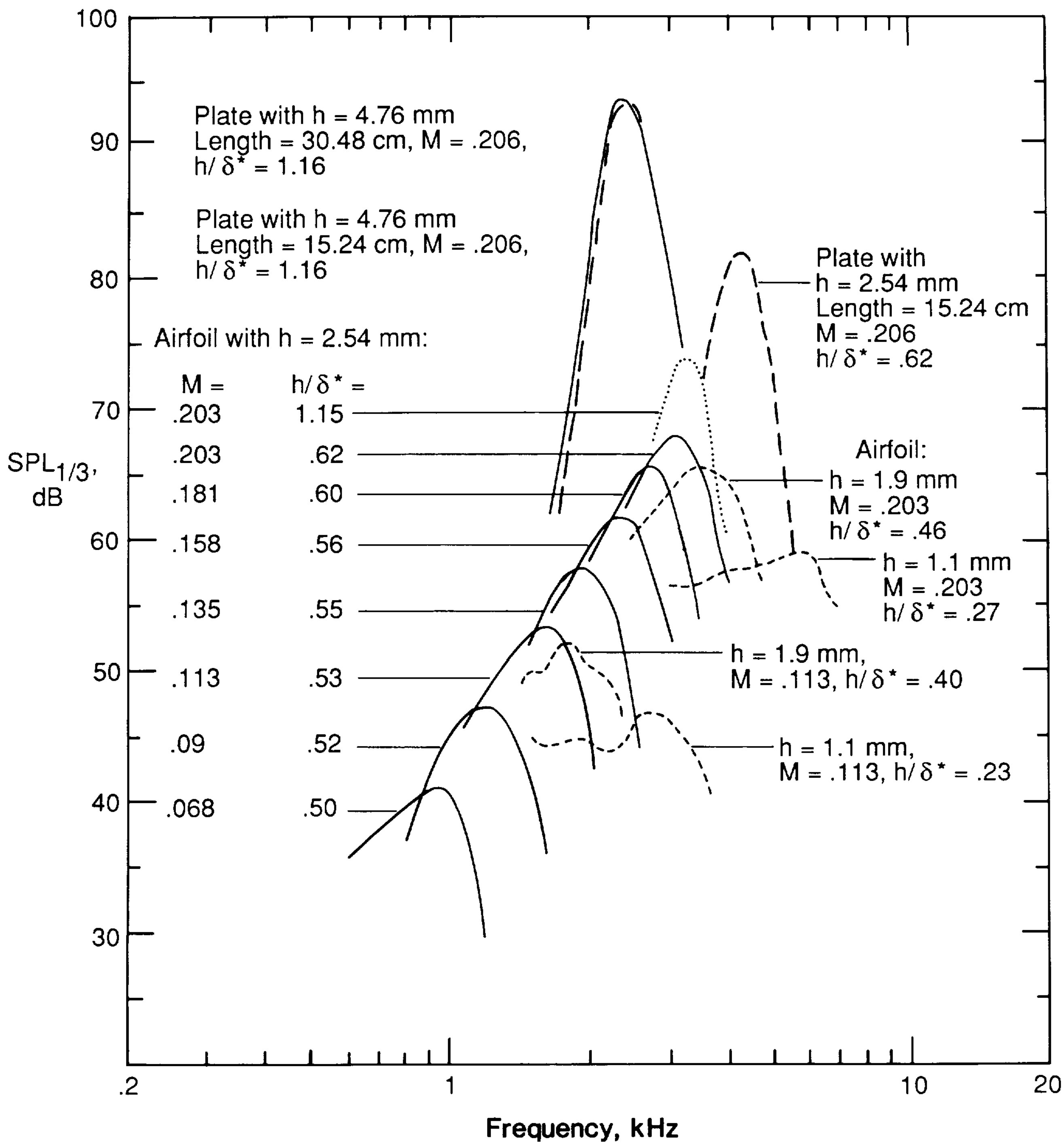

Figure 94. TE-bluntness–vortex-shedding noise, extracted from data of figure 93, data for untripped BL, and data with plate extensions (fig. 92(c)) attached.

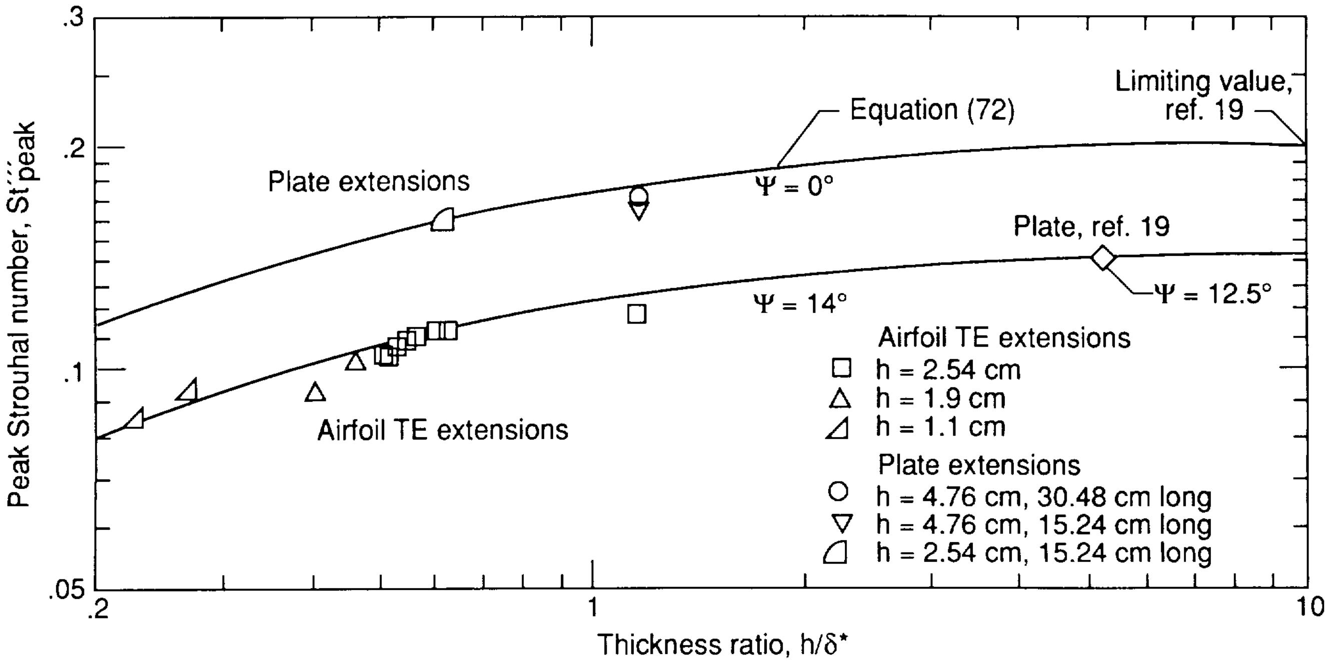

Figure 95. Peak Strouhal number for bluntness noise versus thickness ratio h/δ^* determined from figure 94 and Blake (ref. 19).

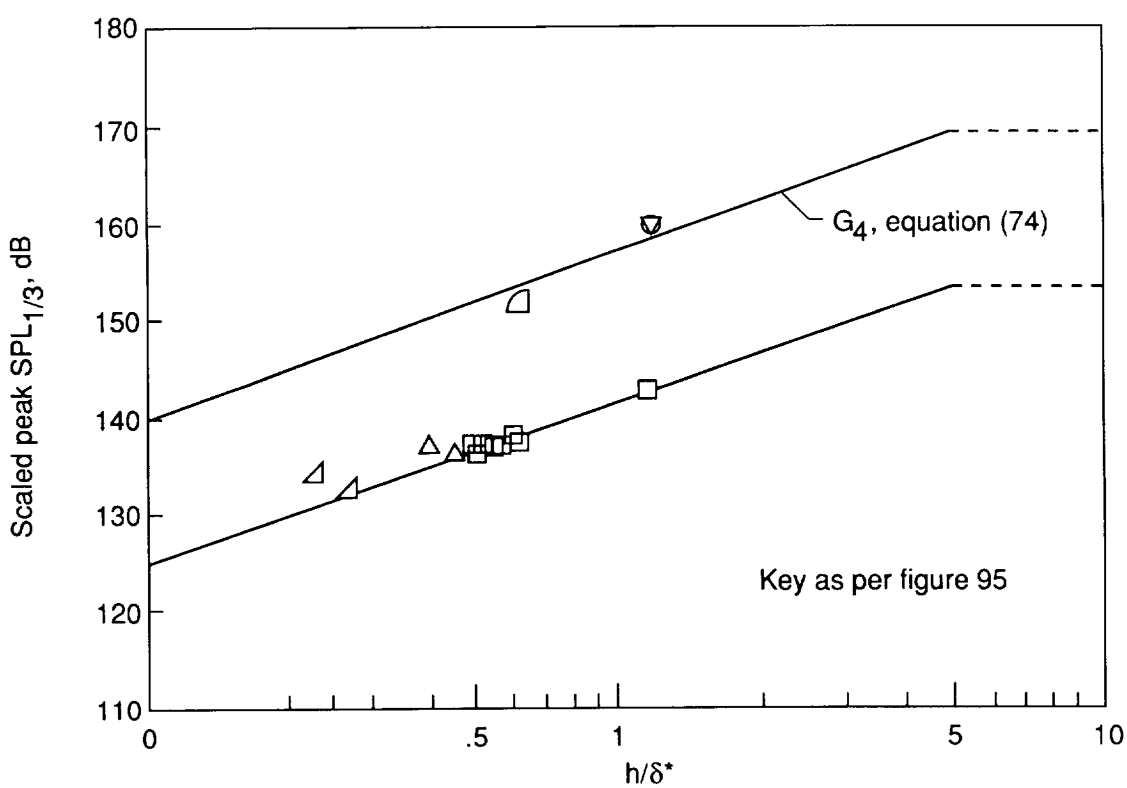

Figure 96. Peak scaled levels for bluntness noise versus thickness ratio h/δ^* determined from figure 94.

edge extensions for the same thickness ratios. The levels increase with increasing thickness ratios. The edge extension data for the two smaller thicknesses of h = 1.1 and 1.9 mm at M = 0.113 deviate most from a straight line trend. Because of signal-to-noise concerns in the specification of these points, these data have the least confidence in the figure and are thus ignored in the specification of a curve fit. However, the accuracy of the resultant scaling equations in predicting these data is subsequently examined. The curve fits, designated as $G_4(h/\delta^*, \Psi)$, shown for the data are straight lines which are chosen to level off at $h/\delta^* = 5$. The curve fit behavior at high h/δ^* is admittedly rather arbitrary, but there are no noise data available for guidance, unlike in the above Strouhal scaling where some frequency data from Blake are used. Fortunately, in practice, the likely values of h/δ^* to be found for rotor blades and wings should be in the range where data are present and scaling confidence is greatest.

Given the specification of the functions $\mathrm{St}'''_{\mathrm{peak}}$ and G_4, a definition of the spectral shape completes the scaling. Spectral curve fits for the data of figure 94 are shown for the airfoil TE extensions, $\Psi = 14°$, and for the plate extensions, $\Psi = 0°$, in figures 97(a) and 97(b), respectively. The shapes reflect the observations that the spectra are sharper for the plates for the same h/δ^*, and the spectra widen in the lower frequencies for decreased h/δ^* values for both the plates and the edge extensions. The spectral curve fit is specified as the function $G_5(h/\delta^*, \Psi)$ whose peak level is 0 dB and whose shape is defined in terms of $\mathrm{St}'''/\mathrm{St}'''_{\mathrm{peak}}$. The specification of G_5 for in-between values of Ψ would be an interpolation between the limiting cases shown in figures 97(a) and 97(b).

5.4.3. Calculation Procedures

The TE bluntness noise spectrum in a 1/3-octave presentation is predicted by

$$\mathrm{SPL}_{\mathrm{BLUNT}} = 10\log\left(\frac{hM^{5.5}L\overline{D}_h}{r_e^2}\right) + G_4\left(\frac{h}{\delta^*_{\mathrm{avg}}}, \Psi\right) + G_5\left(\frac{h}{\delta^*_{\mathrm{avg}}}, \Psi, \frac{\mathrm{St}'''}{\mathrm{St}'''_{\mathrm{peak}}}\right) \qquad (70)$$

The directivity function $\overline{D}_h$ is given by equation (B1) in appendix B. The Strouhal definitions are (see fig. 95)

$$\mathrm{St}''' = \frac{fh}{U} \qquad (71)$$

and

$$\mathrm{St}'''_{\mathrm{peak}} = \begin{cases} \dfrac{0.212 - 0.0045\Psi}{1 + 0.235\left(h/\delta^*_{\mathrm{avg}}\right)^{-1} - 0.0132\left(h/\delta^*_{\mathrm{avg}}\right)^{-2}} & (0.2 \le h/\delta^*_{\mathrm{avg}}) \\ 0.1(h/\delta^*_{\mathrm{avg}}) + 0.095 - 0.00243\Psi & (h/\delta^*_{\mathrm{avg}} < 0.2) \end{cases} \qquad (72)$$

The $h/\delta^*_{\mathrm{avg}}$ term is the ratio of TE thickness (degree of bluntness) h to the average boundary-layer displacement thickness δ^*_{avg}, where

$$\delta^*_{\mathrm{avg}} = \frac{\delta^*_p + \delta^*_s}{2} \qquad (73)$$

The angle Ψ is the solid angle, in degrees, between the sloping surfaces upstream of the trailing edge. For an edge on a flat plate $\Psi = 0°$, whereas $\Psi = 14°$ for an NACA 0012 airfoil. The determination for this parameter for other TE geometries is discussed in section 6 and appendix C.

The peak level of the spectrum is determined from the function G_4 (see fig. 96) where

$$G_4\left(h/\delta^*_{\mathrm{avg}}, \Psi\right) = \begin{cases} 17.5\log\left(h/\delta^*_{\mathrm{avg}}\right) + 157.5 - 1.114\Psi & (h/\delta^*_{\mathrm{avg}} \le 5) \\ 169.7 - 1.114\Psi & (5 < h/\delta^*_{\mathrm{avg}}) \end{cases} \qquad (74)$$

The shape of the spectrum is defined by the function G_5 (see figs. 97(a) and 97(b)) where the calculation procedure involves an interpolation between the spectra for $\Psi = 0°$ and 14° as follows:

$$G_5\left(\frac{h}{\delta^*_{\mathrm{avg}}}, \Psi, \frac{\mathrm{St}'''}{\mathrm{St}'''_{\mathrm{peak}}}\right) = (G_5)_{\Psi=0°} + 0.0714\Psi\left[(G_5)_{\Psi=14°} - (G_5)_{\Psi=0°}\right] \qquad (75)$$

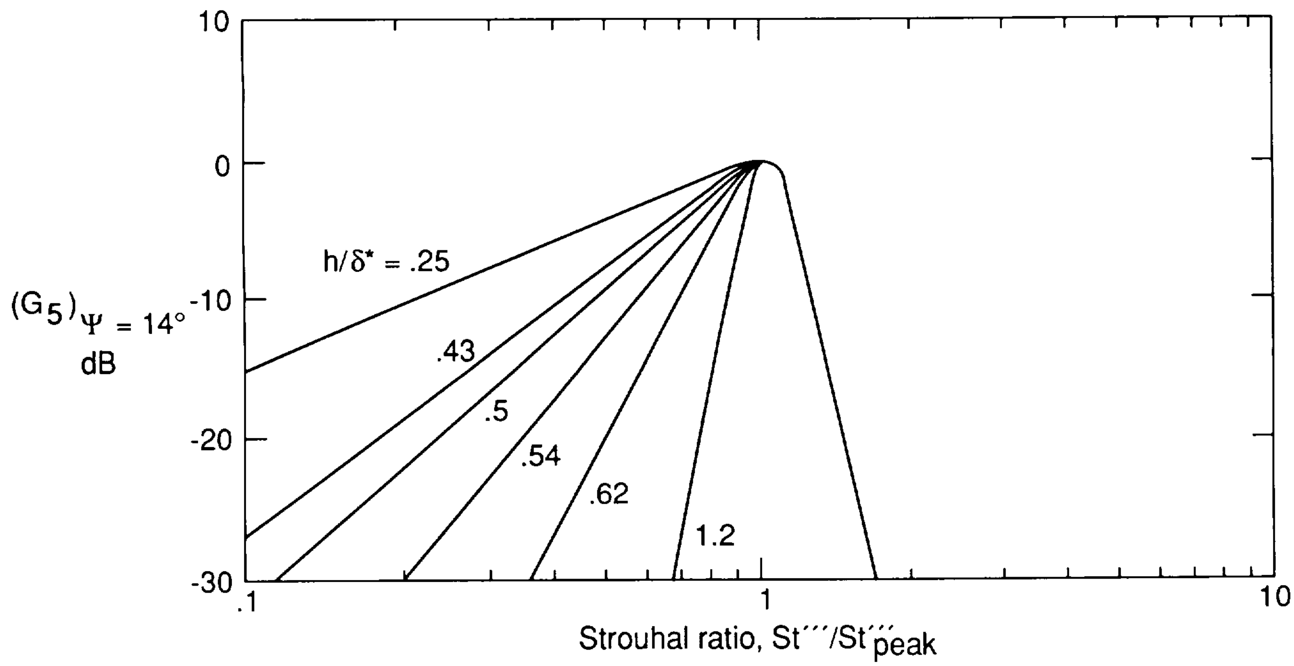

(a) $\Psi = 14°$.

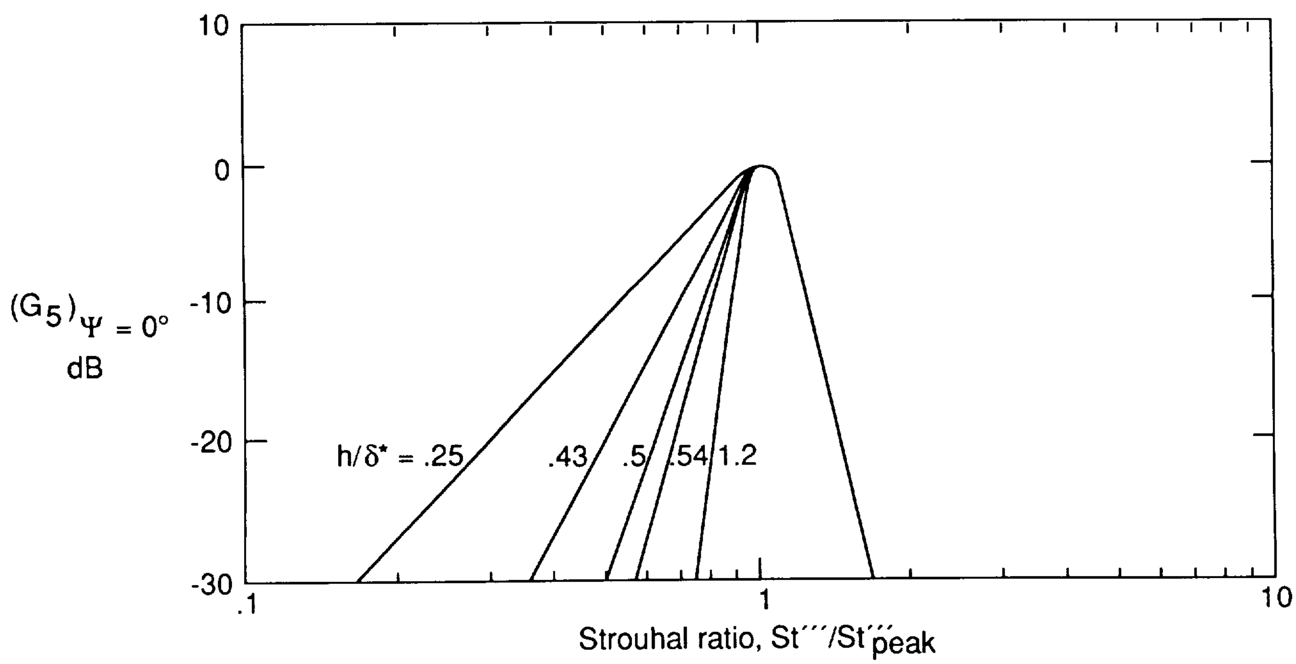

(b) $\Psi = 0°$.

Figure 97. Spectral shape functions for TE bluntness noise.

where

$$(G_5)_{\Psi=14^\circ} = \begin{cases} m\eta + k & (\eta < \eta_0) \\ 2.5\sqrt{1-(\eta/\mu)^2} - 2.5 & (\eta_0 \le \eta < 0) \\ \sqrt{1.5625 - 1194.99\eta^2} - 1.25 & (0 \le \eta < 0.03616) \\ -155.543\eta + 4.375 & (0.03616 \le \eta) \end{cases} \tag{76}$$

$$\eta = \log(\mathrm{St}'''/\mathrm{St}'''_{\mathrm{peak}}) \tag{77}$$

$$\mu = \begin{cases} 0.1221 & (h/\delta^*_{\mathrm{avg}} < 0.25) \\ -0.2175(h/\delta^*_{\mathrm{avg}}) + 0.1755 & (0.25 \le h/\delta^*_{\mathrm{avg}} < 0.62) \\ -0.0308(h/\delta^*_{\mathrm{avg}}) + 0.0596 & (0.62 \le h/\delta^*_{\mathrm{avg}} < 1.15) \\ 0.0242 & (1.15 \le h/\delta^*_{\mathrm{avg}}) \end{cases} \tag{78}$$

$$m = \begin{cases} 0 & (h/\delta^*_{\mathrm{avg}} \le 0.02) \\ 68.724(h/\delta^*_{\mathrm{avg}}) - 1.35 & (0.02 < h/\delta^*_{\mathrm{avg}} \le 0.5) \\ 308.475(h/\delta^*_{\mathrm{avg}}) - 121.23 & (0.5 < h/\delta^*_{\mathrm{avg}} \le 0.62) \\ 224.811(h/\delta^*_{\mathrm{avg}}) - 69.35 & (0.62 < h/\delta^*_{\mathrm{avg}} \le 1.15) \\ 1583.28(h/\delta^*_{\mathrm{avg}}) - 1631.59 & (1.15 < h/\delta^*_{\mathrm{avg}} < 1.2) \\ 268.344 & (1.2 < h/\delta^*_{\mathrm{avg}}) \end{cases} \tag{79}$$

$$\eta_0 = -\sqrt{\frac{m^2\mu^4}{6.25 + m^2\mu^2}} \tag{80}$$

and

$$k = 2.5\sqrt{1 - \left(\frac{\eta_0}{\mu}\right)^2} - 2.5 - m\eta_0 \tag{81}$$

The spectrum $(G_5)_{\Psi=0^\circ}$ is obtained by computing equations (76) through (81), as one would for $(G_5)_{\Psi=14^\circ}$, but replacing $(h/\delta^*_{\mathrm{avg}})$ by $(h/\delta^*_{\mathrm{avg}})'$ where

$$\left(\frac{h}{\delta^*_{\mathrm{avg}}}\right)' = 6.724\left(\frac{h}{\delta^*_{\mathrm{avg}}}\right)^2 - 4.019\left(\frac{h}{\delta^*_{\mathrm{avg}}}\right) + 1.107 \tag{82}$$

5.4.4. Comparison With Data

Noise spectra for the airfoil with different TE thicknesses (geometry of fig. 92(a)) are presented for the flow Mach numbers of $M = 0.21$ and 0.12 in figures 98 and 99, respectively. The data were obtained by digitizing the spectra of figure 93 and converting these to 1/3-octave levels. The prediction curves shown are those of TBL–TE and bluntness noise sources. For the sharp TE of figures 98(a) and 99(a), there is no bluntness contribution. Overprediction is seen for the TBL–TE noise at the lowest frequencies and some underprediction is apparent in the higher frequencies for the highest flow speed. For the nonzero TE thicknesses the bluntness noise contributes to the total spectra at high frequencies and renders good comparisons with the data. Good agreement is found even for the aforementioned smaller thickness cases at low Mach number (figs. 99(c) and 99(d)).

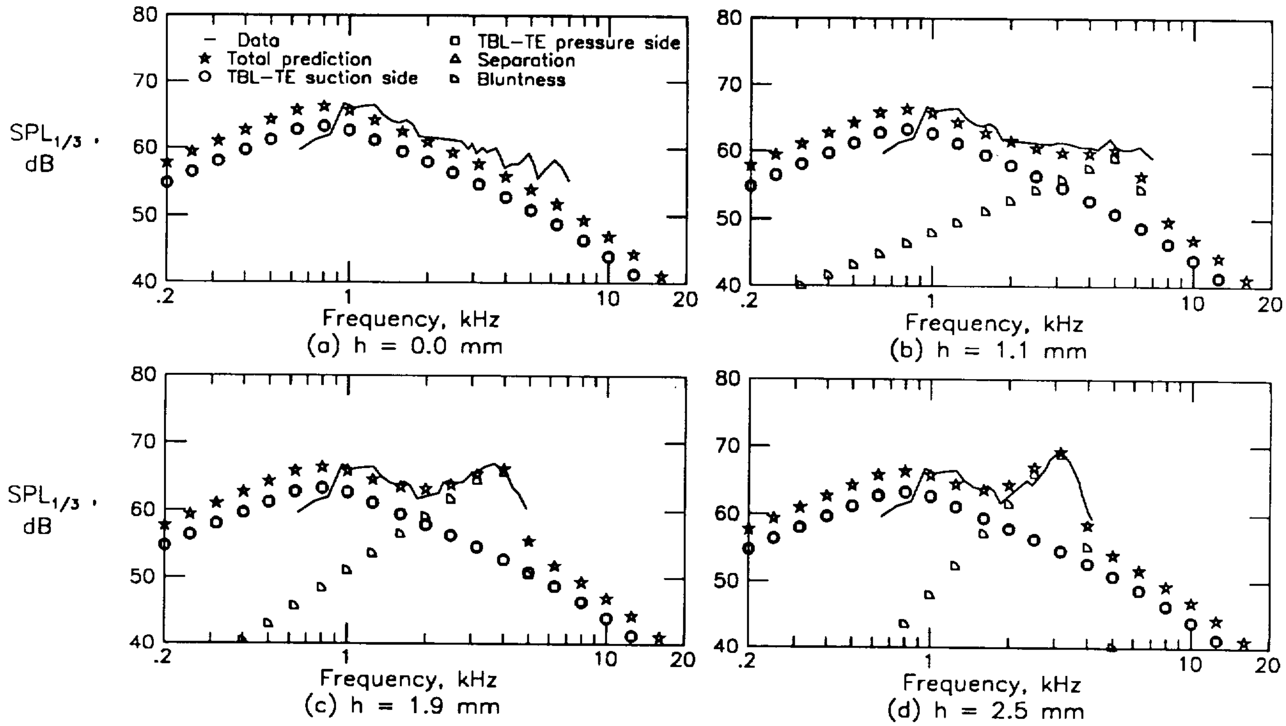

Figure 98. One-third-octave presentation of spectra of figure 93 at $U = 69.5$ m/s with predictions for various degrees of bluntness.

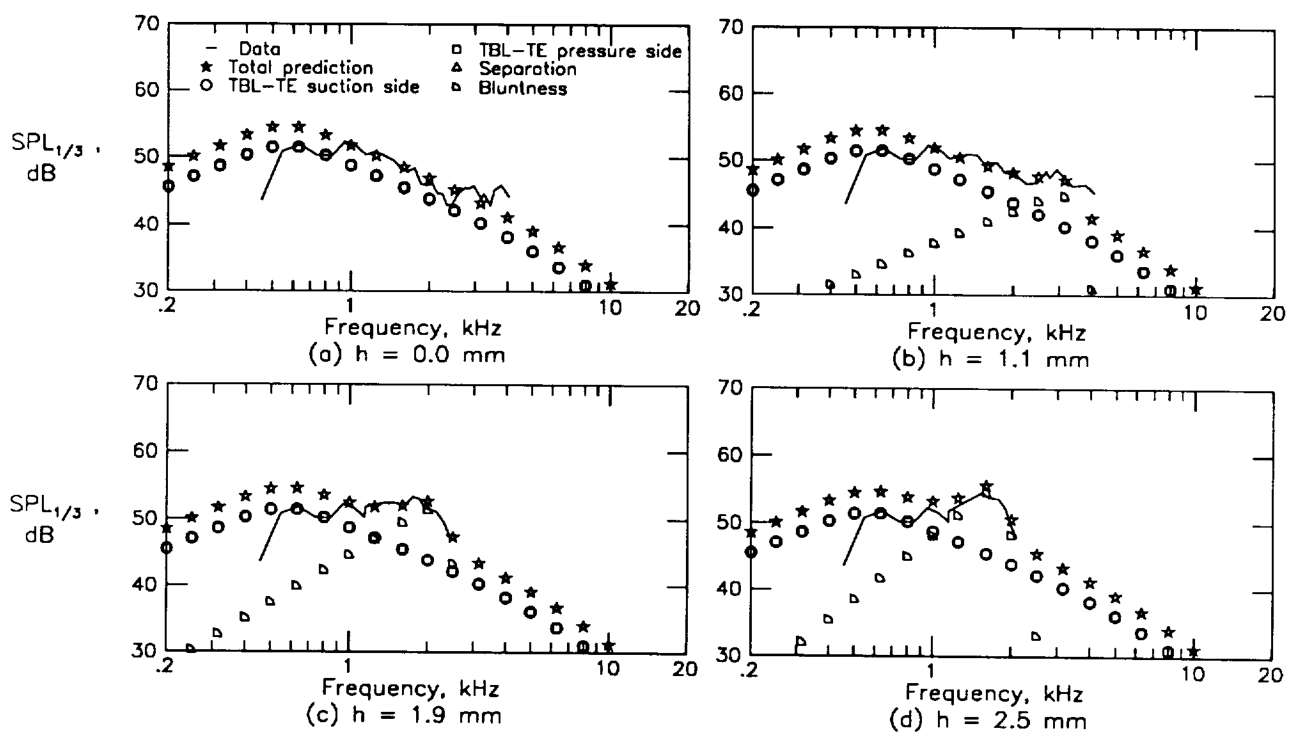

Figure 99. One-third-octave presentation of spectra of figure 93 at $U = 38.6$ m/s with predictions for various degrees of bluntness.

6. Comparison of Predictions With Published Results

The scaling law predictions are compared in this section with data from self-noise studies of airfoil sections performed at the United Technologies Research Center (UTRC).

6.1. Study of Schlinker and Amiet

Schlinker and Amiet (ref. 3) conducted tests in the UTRC Acoustic Research Tunnel to study TBL–TE noise from a cambered helicopter blade section. The cross section of the 40.6-cm-chord and 53.3-cm-span model is shown in figure 100. As in the present NASA Langley studies, the model was mounted on sidewalls and spanned the width of the open tunnel jet, so that the flow across the model was two-dimensional. The nozzle providing the flow had a rectangular exit of dimensions of 29 cm × 53.3 cm. To isolate the TBL–TE noise from facility background noise, a directional microphone system was used. The experimental configuration, illustrating the shear layer refraction effect on the TE noise received by the directional microphone, is shown in figure 101. The Mach numbers tested ranged from 0.1 to 0.5 and the tunnel angle of attack α_t varied from $-0.4°$ (zero lift for this cambered airfoil) to 12°.

6.1.1. Boundary-Layer Definition

Because only TBL–TE noise measurements were desired, the boundary layers were tripped by applying thin serrated aluminum tape at the blade locations indicated in figure 100. The tape thickness was on the order of the BL displacement thickness at the points of application, providing minimum surface protrusion to avoid unnaturally large TBL thicknesses downstream. This "light" trip is in contrast to the present study where the trips were "heavy" for reasons discussed.

Hot-wire measurements were made in the boundary-layer/near-wake region at the TE of the model. In figure 102, measured BL thicknesses are plotted versus Mach number for various tunnel angles of attack α_t. These data are from figure 17 of reference. 3. At zero lift, $\alpha_t = -0.4°$, in figure 102(a), the BL thicknesses δ_0 on the pressure and suction sides are approximately the same. This should be expected since they developed under approximately the same adverse pressure gradient. Included in figure 102(a) are corresponding values of BL displacement thicknesses, which were calculated by the present authors from velocity profiles presented in reference 3 (δ^* was not a quantity of interest in ref. 3). In figures 102(b) and 102(c), δ/c values are shown for $\alpha_t = 7.6°$ and 12°, respectively. Comparing figures 102(a), 102(b), and 102(c), one can see that as angle of attack increases, δ_s increases and δ_p decreases.

These measurements are compared with the thickness scaling equations of the present paper. First, equations (2) and (3) are used to calculate the BL thickness ratio δ_0/c and displacement thickness ratio δ_0^*/c. To make the calculations agree with the data of figure 102(a), all calculated values of δ_0/c and δ_0^*/c were multiplied by a factor 0.6. This factor is taken to be the adjustment in equations (2) and (3) needed to make them appropriate for the "light" trip of reference 3. Next, the corrected angles of attack are determined by (1) adding 0.4° to α_t so that the tunnel angle is referenced to the zero-lift case and (2) using equation (1), with c = 40.6 cm and H = 79 cm, to obtain $\alpha_* = 0°$, 3.9°, and 6.1° for $\alpha_t = -0.4°$, 7.6°, and 12°, respectively. These values of α_* are now used in equations (8) and (11) to obtain δ_p/δ_0 and δ_s/δ_0, respectively. The resultant values of δ_s/c and δ_p/c are compared with the data in figures 102(b) and 102(c).

6.1.2. Trailing-Edge Noise Measurements and Predictions

Trailing-edge noise spectra in a 1/3-octave presentation are given in figure 103 for the airfoil at $\alpha_t = -0.4°$ with Mach number ranging from M = 0.1 to 0.5. The data were obtained by the directional microphone system at differing orientations to the airfoil. Shear layer corrections and directional microphone gain adjustments were made so that the data shown represent the noise radiated from a unit length of L = 0.3048 m of the TE span, at an observer distance of r_e = 3 m, and an observer angle Θ_e which is specified in the figure. Figures 104 and 105 contain spectra for the airfoil at $\alpha_t = 7.6°$ and 12°, respectively.

The TBL–TE and separation noise spectra were predicted using the calculation procedures of the present paper. The values of α_*, δ_s^*, and δ_p^* used were calculated as described in the previous section. Because of the BL trips and the 2D flow, no LBL–VS or tip noise calculations were made. In performing the calculations for TE bluntness noise, one has to assign values of the TE thickness h and the TE flow angle parameter Ψ. The thickness was indicated in reference 3 to be h = 0.38 mm but the shape of this small TE region was not given. A value of $\Psi = 17°$ has been used in the prediction because it gives reasonable prediction-data comparisons.

In figures 103 to 105, the predictions are compared with the measurements. As in the presentation of figures 11 to 74, the individual noise contributions are shown, along with the total summed spectra. The prediction-data comparisons are good, especially

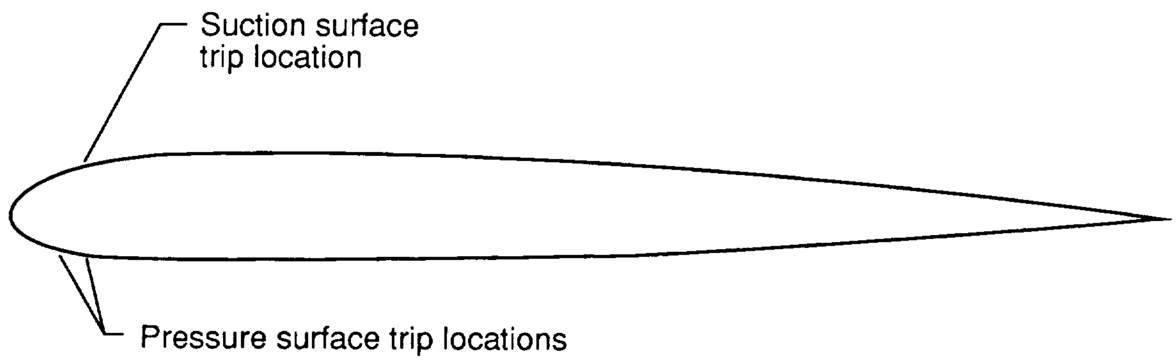

Figure 100. Cross section of Sikorsky rotor blade (ref. 3). Span is 53.3 cm and chord length is 40.6 cm.

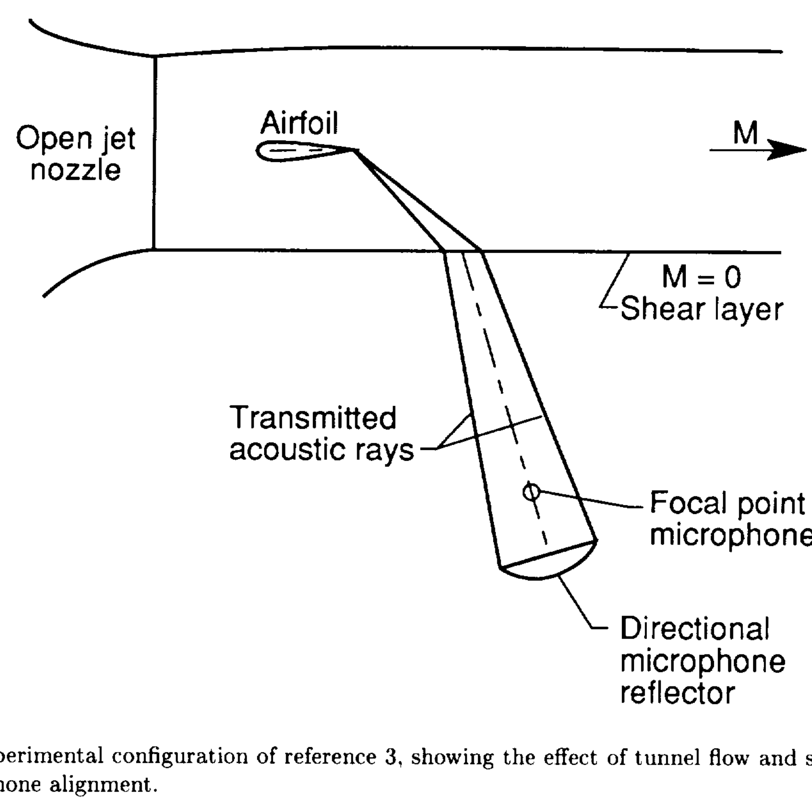

Figure 101. UTRC experimental configuration of reference 3, showing the effect of tunnel flow and shear layer refraction on the directional microphone alignment.

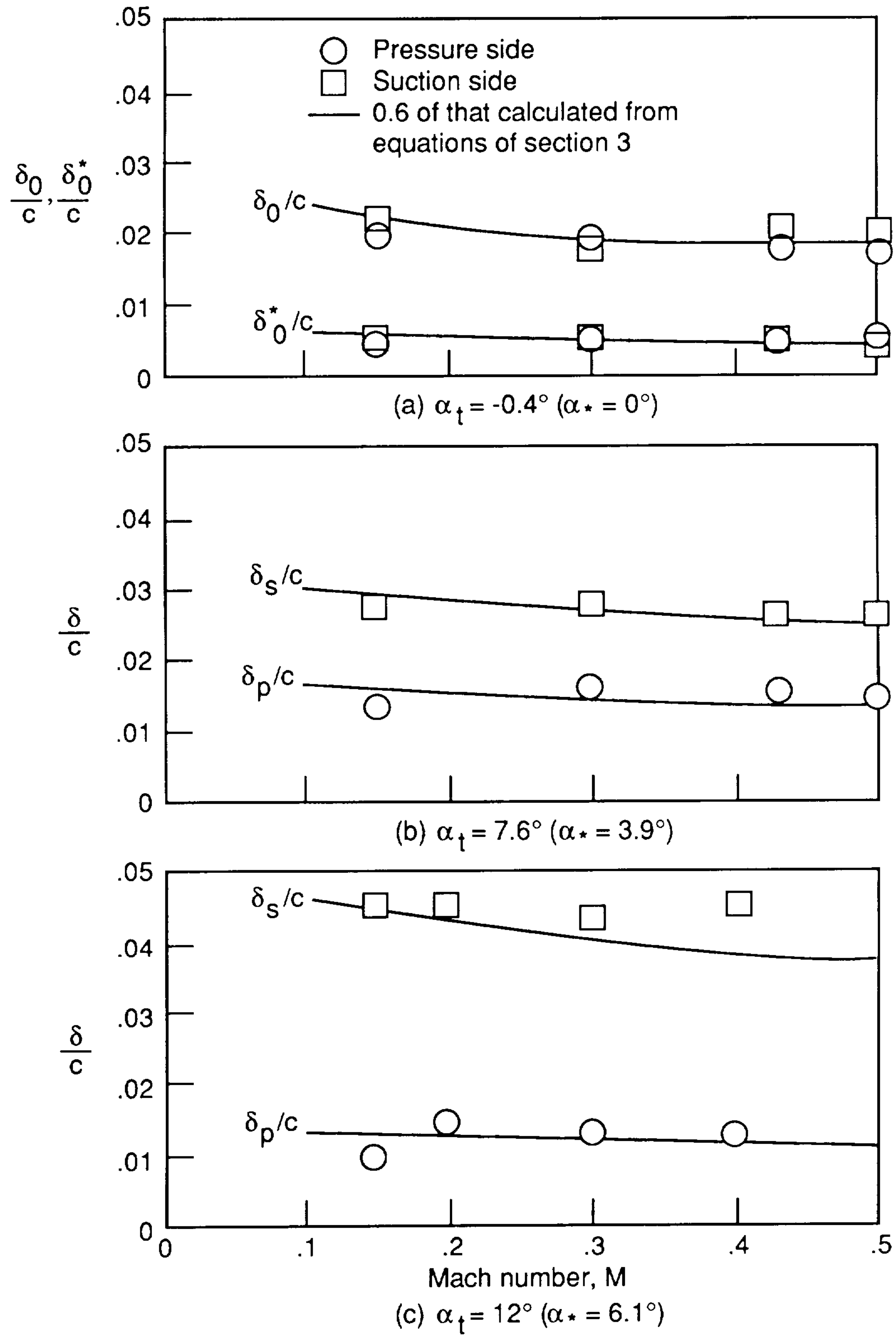

Figure 102. Measured boundary-layer thickness at the TE of the Sikorsky airfoil (ref. 3). Comparison is made with scaling equation results of present paper, multiplied by 0.6 to account for light trip condition.

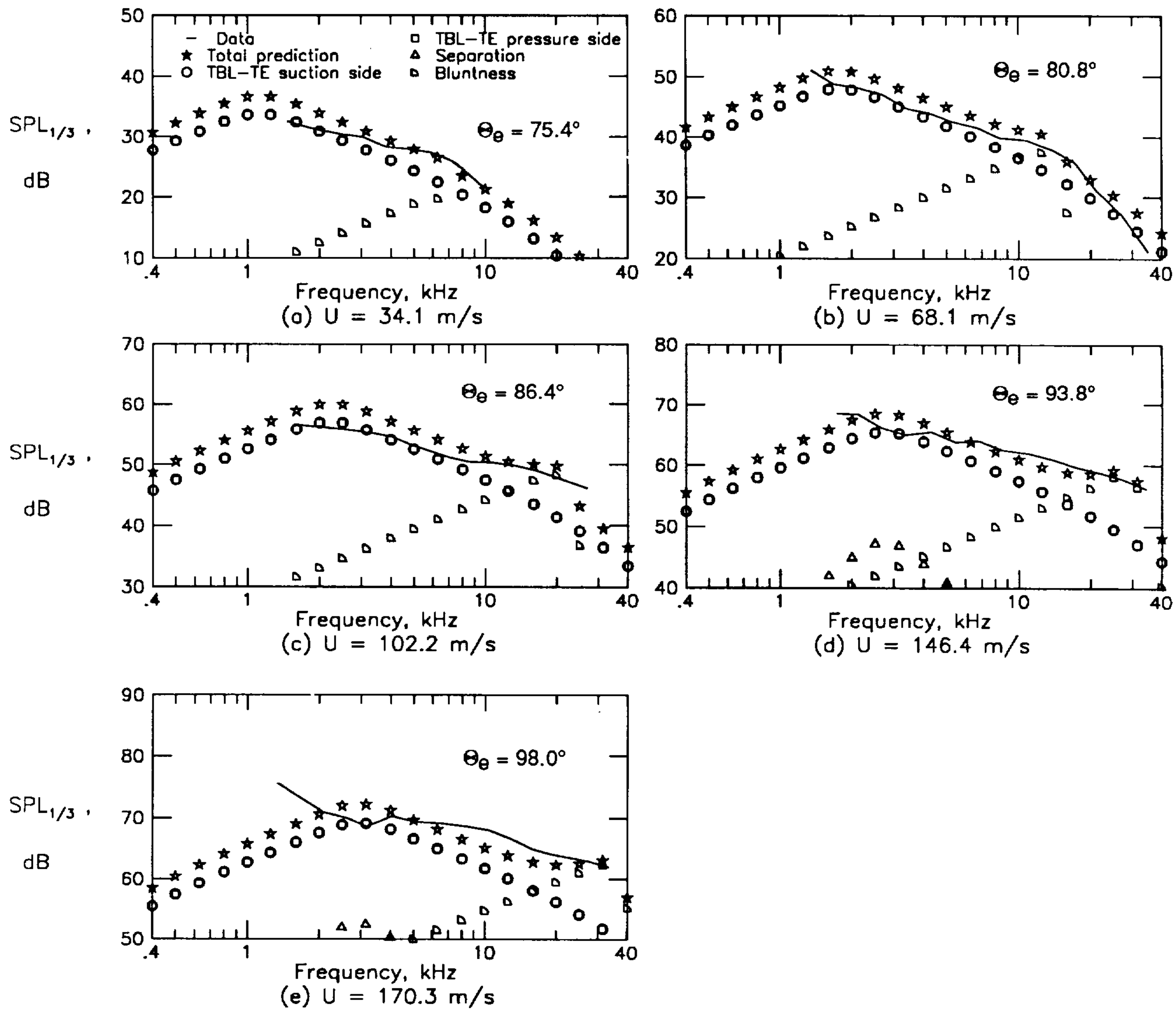

Figure 103. Noise spectra for Sikorsky airfoil at $\alpha_t = -0.4°$ ($\alpha_* = 0°$) from reference 3 compared with prediction of present paper.

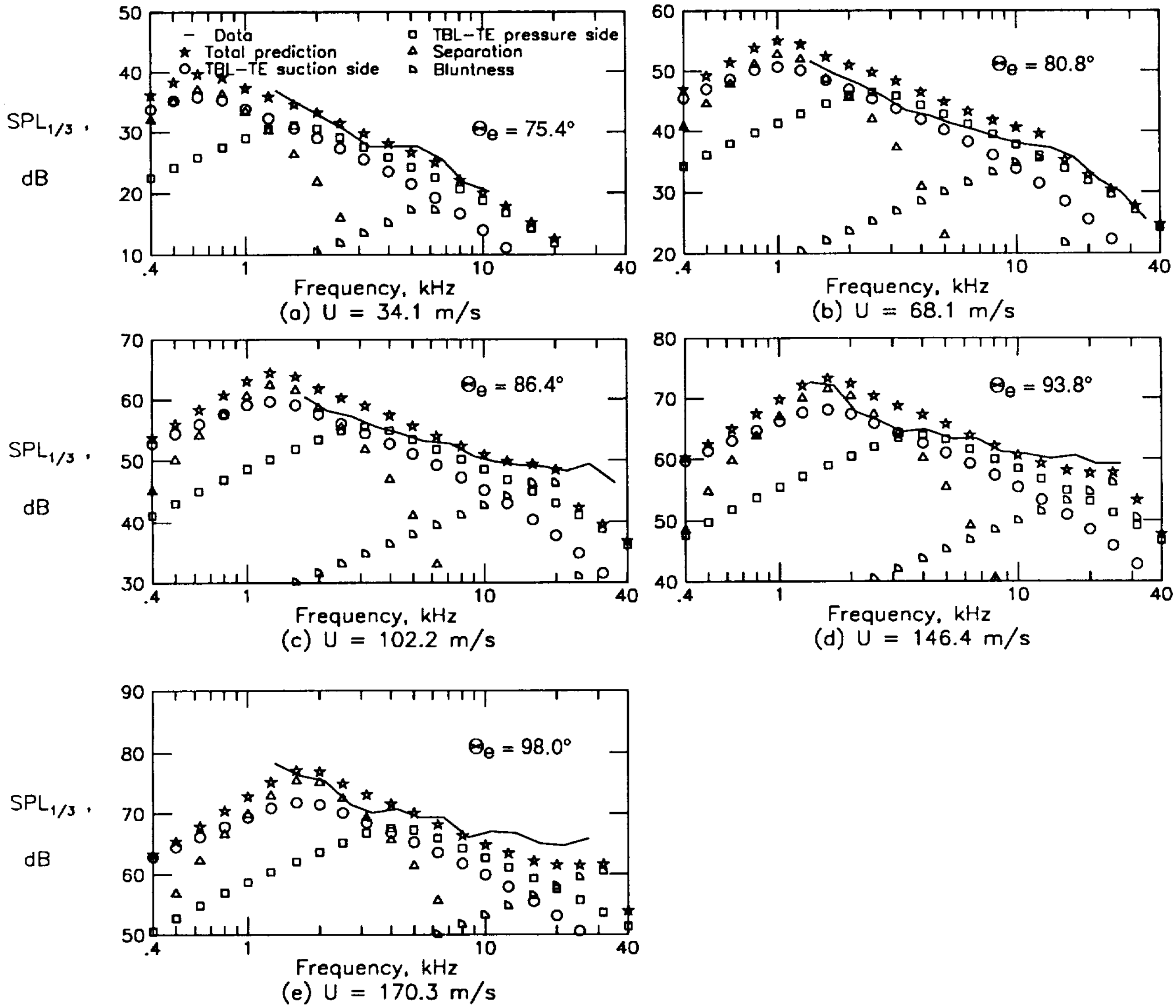

Figure 104. Noise spectra for Sikorsky airfoil at $\alpha_t = 7.6°$ ($\alpha_* = 3.9°$) from reference 3 compared with prediction of present paper.

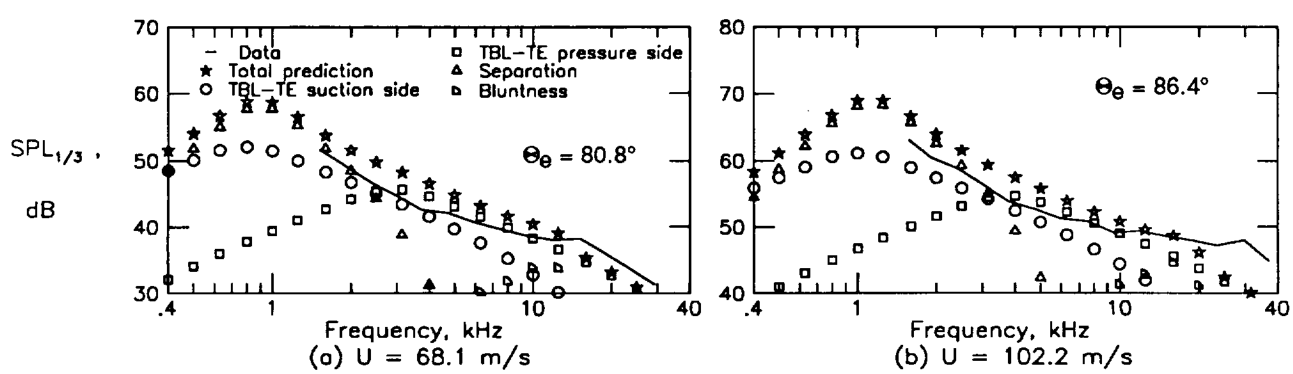

Figure 105. Noise spectra for Sikorsky airfoil at $\alpha_t = 12°$ ($\alpha_* = 6.1°$) from reference 3 compared with prediction of present paper.

considering that the predictions are based empirically on a different airfoil section and that the noise measurement methods were quite different. There does appear to be a mild overprediction of the TBL–TE noise, although not consistently so. The extent of agreement in the spectra where the TE bluntness noise contributes is substantially due to the aforementioned choice of $\Psi = 17°$ (the previously used $\Psi = 14°$ would result in a contribution about 3 dB higher than that shown).

6.2. Study of Schlinker

The tests of Schlinker (ref. 26) were similar in design to that of reference 3, whose measurement configuration is shown in figure 101. The 2D airfoil model, however, was an NACA 0012 section (as in the present study) with a chord length of $c = 22.9$ cm. Again, the aim of the tests was to measure TBL–TE and not LBL–VS noise. However, no BL trip was used at zero angle of attack because no LBL–VS noise was identified (except for the lowest speed tested and those data were not presented). At $\alpha_t = 6°$, the LBL-VS noise was pervasive so a trip was placed on the pressure side at 30 percent of the chord to eliminate the LBL–VS noise.

The TE noise spectra at various tunnel velocities are shown in figures 106 and 107 for the airfoil at $\alpha_t = 0°$ and $6°$, respectively. The data were processed so that the levels shown are for the full airfoil span of $L = 53.3$ cm and an omnidirectional observer positioned at $r_e = 2.81$ m and $\Theta_e = 90°$. For this airfoil, the corrected angles of attack, using equation (1) with $c = 22.9$ cm and $H = 79$ cm, are $\alpha_* = 0°$ and $3.9°$ for $\alpha_t = 0°$ and $6°$, respectively. The predictions shown in figure 106 for zero angle of attack are for TBL–TE, LBL–VS, and TE bluntness noise. The values of δ_0 and δ_0^* used in the predictions were obtained from equations (5) and (6), for an untripped BL airfoil. The predictions shown in figure 107 for $\alpha_t = 6°$ are for only TBL–TE, separation, and TE bluntness noise, since the LBL–VS noise was eliminated by the pressure side tripping. The required values of δ_s^* were calculated from equation (14), for an untripped BL. However, the values of δ_p^* were determined from equations (3) and (9), for a tripped BL and then multiplying the result by 0.6 (to reflect the "light" trip condition as discussed for the Schlinker and Amiet study). For the calculations for TE bluntness noise, there was no guidance from the paper for the specification of h and Ψ. A reasonable TE thickness of $h = 0.63$ mm was assumed and the TE flow angle parameter was set at $\Psi = 23°$, because it gave good agreement for the high frequencies in figures 106 and 107. The overall agreement between the total predictions and the data appears good.

6.3. Study of Fink, Schlinker, and Amiet

Fink, Schlinker, and Amiet (ref. 27) conducted tests in the UTRC tunnel to study LBL–VS noise from three airfoil geometries. The untripped BL airfoil models had an NACA 0012 planform and their geometries are shown in figure 108. The first had a constant-chord length of 11.4 cm across the span while the other two were spanwise tapered, having linearly varying chord lengths along the span. Of the tapered airfoils, the first had a taper ratio of 2 to 1 with chord length varying from 15.2 cm down to 7.6 cm. The other airfoil had a taper ratio of 4 to 1 with chord length varying from 18.3 cm to 4.6 cm. The span was $L = 79$ cm for all cases. Because the levels of the LBL–VS noise were sufficiently intense compared with the tunnel background noise, a directional microphone system was not used to measure the noise. Instead, far-field spectra were obtained with individual microphones placed on an arc of 2.25-m radius about the midspan of the models. The noise data from reference 27 which are presented in the present report are all from a microphone for which $\Theta_e \approx 90°$.

Reference 27 presented most noise data in narrow-band form at various bandwidths to allow examination of the tonal character of the LBL–VS noise. To compare these data with the predictions of the present paper, the narrow-band data were digitized and converted to 1/3-octave presentations. As a check on this procedure, as well as a check on the consistency of the data presented in reference 27, overall sound pressure levels (OASPL) were computed from the digitized data and compared with overall levels reported from direct measurement. The values generally agreed to within 1.0 dB.

For the constant-chord airfoil at $\alpha_t = 4°$, 1/3-octave spectra are shown in figure 109 for various tunnel velocities between $U = 37$ m/s and 116 m/s. The number of spectral bands, as well as the frequency range, presented for the spectra varies for the different speeds. This variation is due to the different narrow-band analysis ranges used in reference 27, as all available data were used to generate the 1/3-octave band spectra. For $U = 37$ m/s, figure 109(a), the spectrum is flat at the lower frequencies but is peaked between 1 and 3 kHz. From the narrow-band presentation of reference 27 (fig. 22), one finds that the flat portion is dominated by broadband noise, which is characteristic of tunnel background contamination. It is noted again that these spectra are single microphone results from which the background noise has not been subtracted. The spectral peak region is due to the presence of three quasi-tones, representing the LBL–VS noise portion. At $U = 52$, 64,

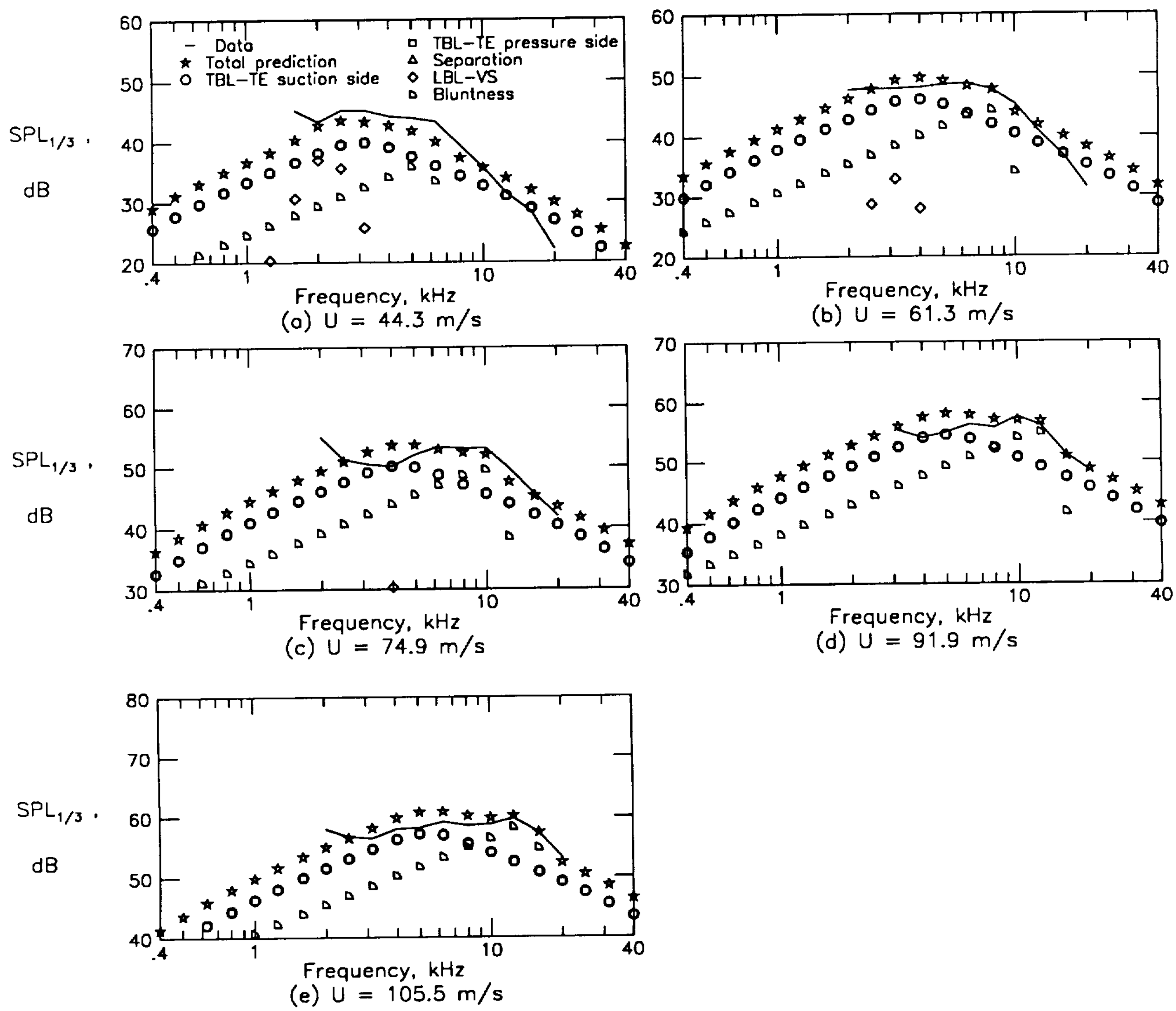

Figure 106. Noise spectra for NACA 0012 airfoil at $\alpha_t = 0°$ ($\alpha_* = 0°$) from reference 26 compared with prediction of present paper.

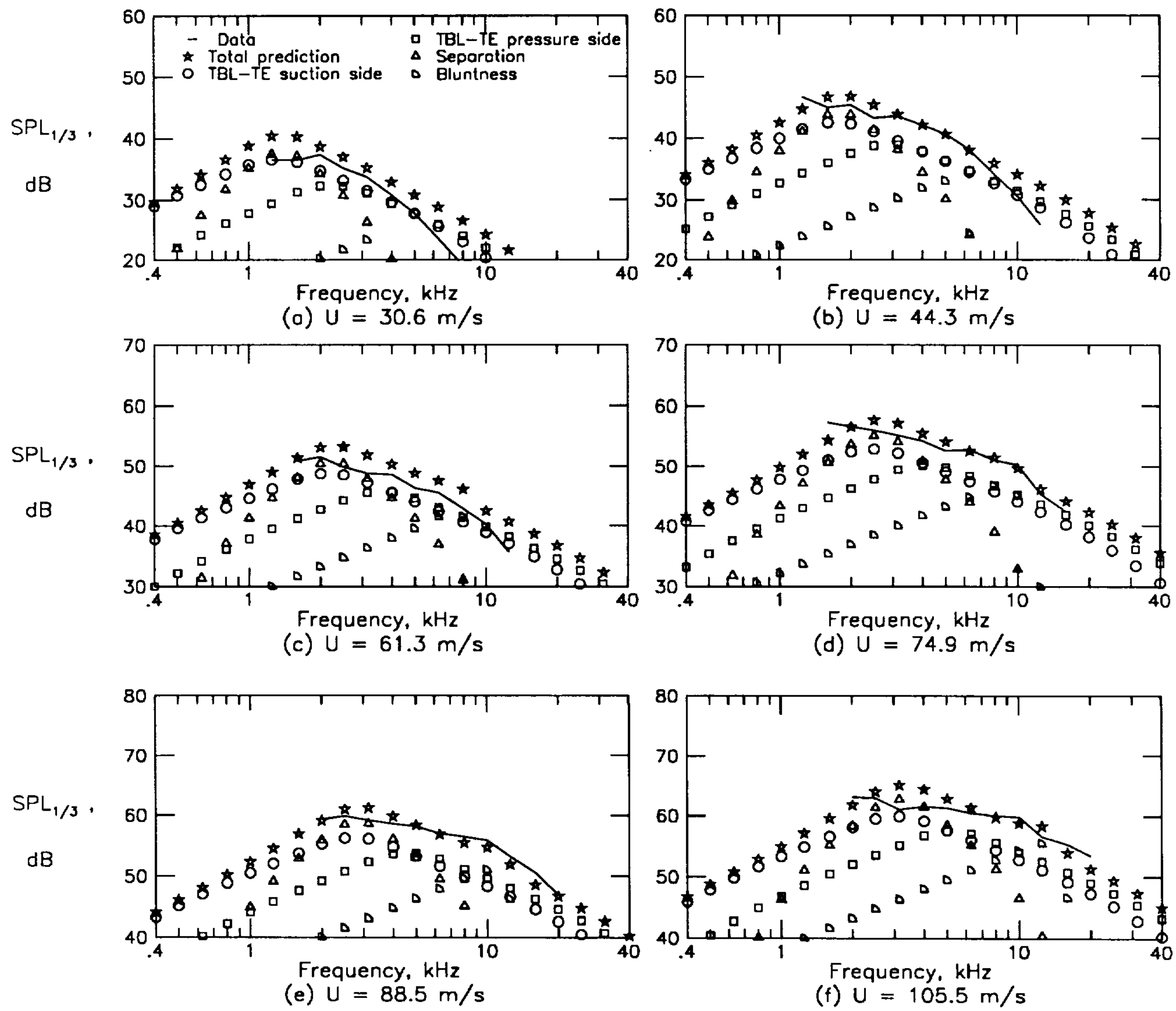

Figure 107. Noise spectra for NACA 0012 airfoil at $\alpha_t = 6°$ ($\alpha_* = 3.9°$) from reference 26 compared with prediction of present paper.

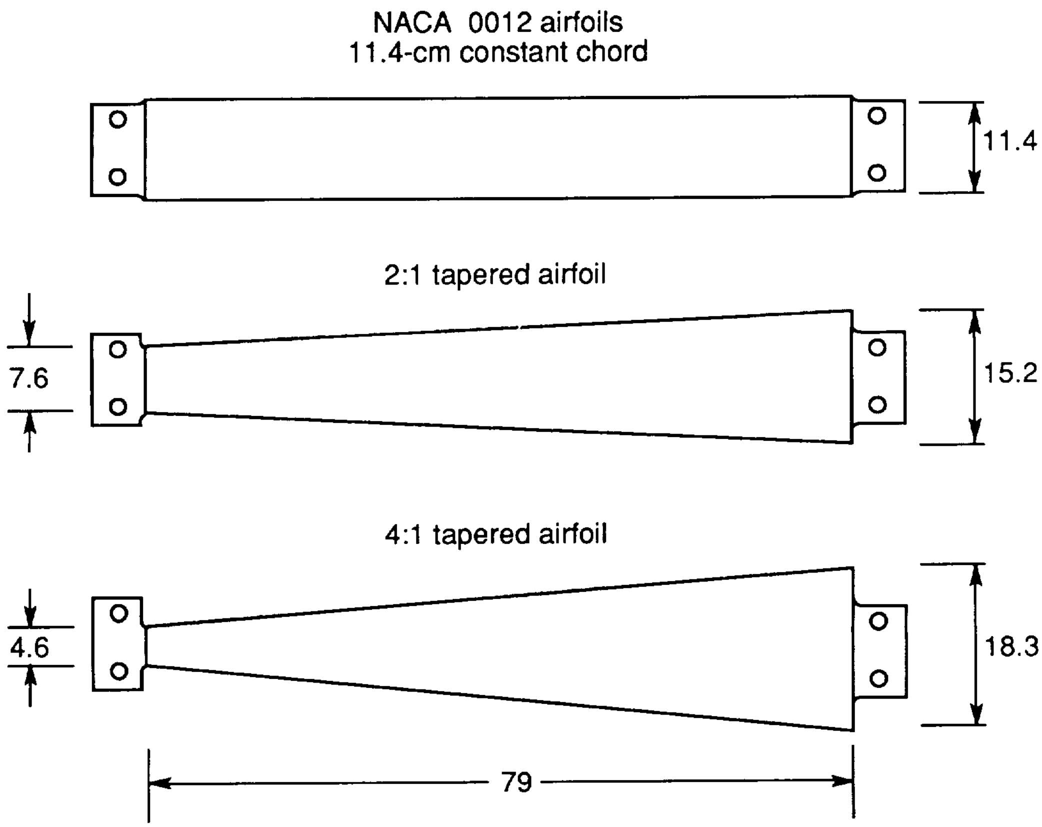

Figure 108. Airfoil models of reference 27. All dimensions are in centimeters.

and 79 m/s, in figures 109(b), 109(c), and 109(d), the spectra are very peaked because of the dominating contributions from large numbers (10 to 15) of LBL–VS quasi-tones. At U = 98 and 116 m/s, in figures 109(e) and 109(f), the spectra are less peaked because of a somewhat decreased number of quasi-tones which become submerged within broadband background noise (which itself increases with speed).

The strong velocity dependence of the noise is seen clearly in figure 110 (from fig. 25 of ref. 27) where the OASPL is plotted as a function of velocity. The overall levels were directly measured, for the noise between 200 Hz and 20 kHz, rather than determined by integrating measured spectra. The levels rise and then stabilize with increases in velocity. The resumed increase in levels at the highest speeds (approximately 100 m/s) is where the background noise appears to become dominant.

Compared with the data in figures 109 and 110 are noise predictions of LBL–VS, TBL–TE, and separation noise. No consideration was given to bluntness noise because of the lack of information about the TE geometry as well as the fact that LBL–VS noise dominates the predictions where comparative data are available. For the BL thickness determinations, the equations of section 3 for untripped boundary layers were used. The corrected angles of attack were calculated from equation (1), with $c = 11.4$ cm and $H = 53$ cm, which rendered $\alpha_* = 0°$ and 1.9° for $\alpha_t = 0°$ and 4°, respectively. These were employed with the prediction equations for an observer at $r_e = 2.25$ m, $\Theta_e = 90°$, and $\Phi_e = 90°$. The predictions in figure 109 give good comparisons, except that the peak frequencies are lower than predicted. The previously described background noise contributions explain the differences for the lowest and highest speeds. For the predictions of OASPL in figure 110, the spectra for LBL–VS, TBL–TE, and separation noise were summed. Predictions are presented for not only $\alpha_t = 4°$ but also $\alpha_t = 0°$, 2°, and 6°. This is done to show the great sensitivity of the predictions to airfoil angle of attack. It is seen that the data would most agree with predictions for about $\alpha_t \approx 5°$ rather than $\alpha_t = 4°$. This could be interpreted to mean that the agreement is on the order of possible experimental bias error in angle definition.

The tapered-chord airfoils were used in reference 27 to provide a continuous variation in expected vortex tone frequency to compare with an analogous rotating constant-chord blade. The tone variation

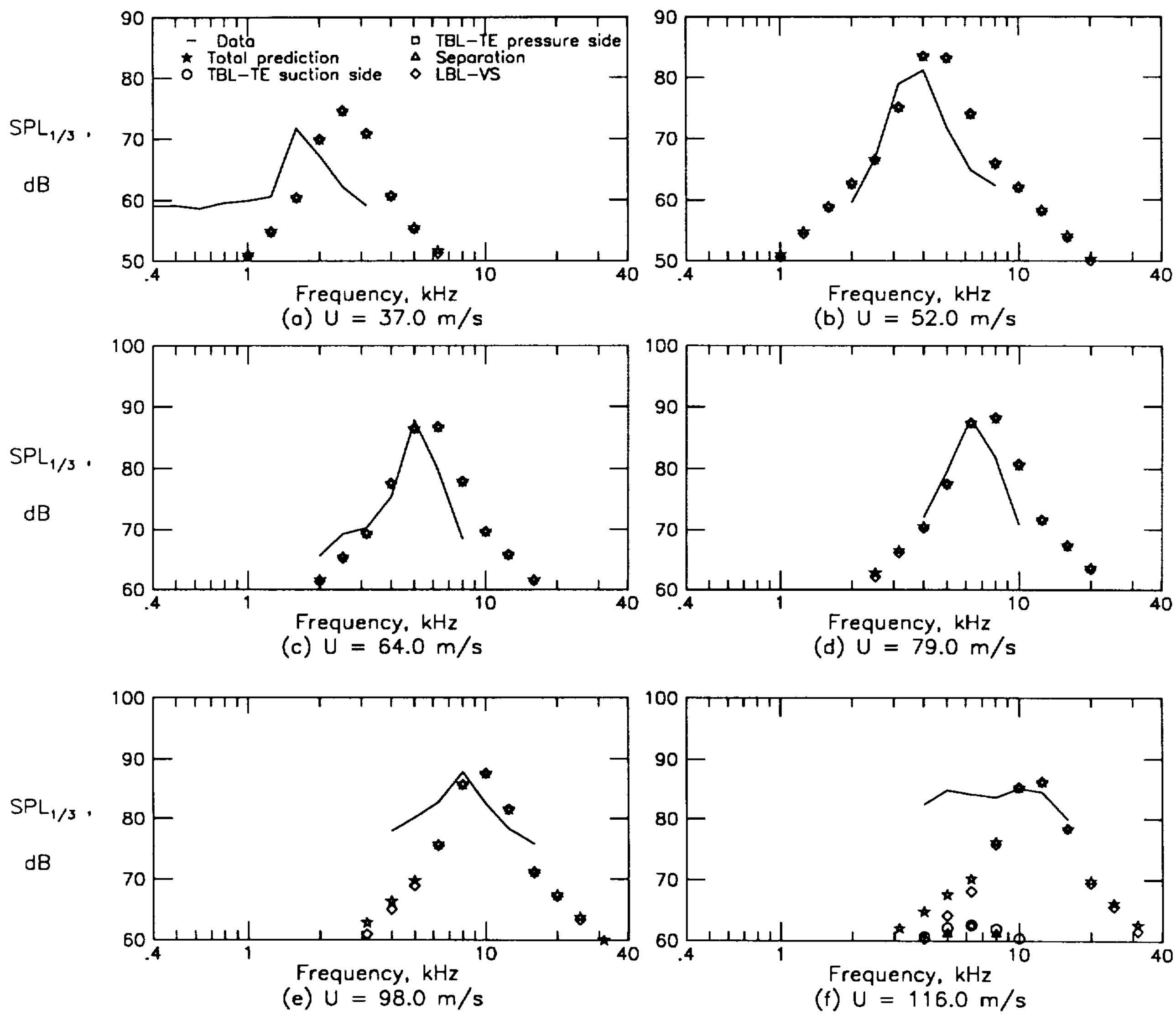

Figure 109. Noise spectra for constant-chord airfoil at $\alpha_t = 4°$ ($\alpha_* = 1.9°$) from reference 27 compared with prediction of present paper.

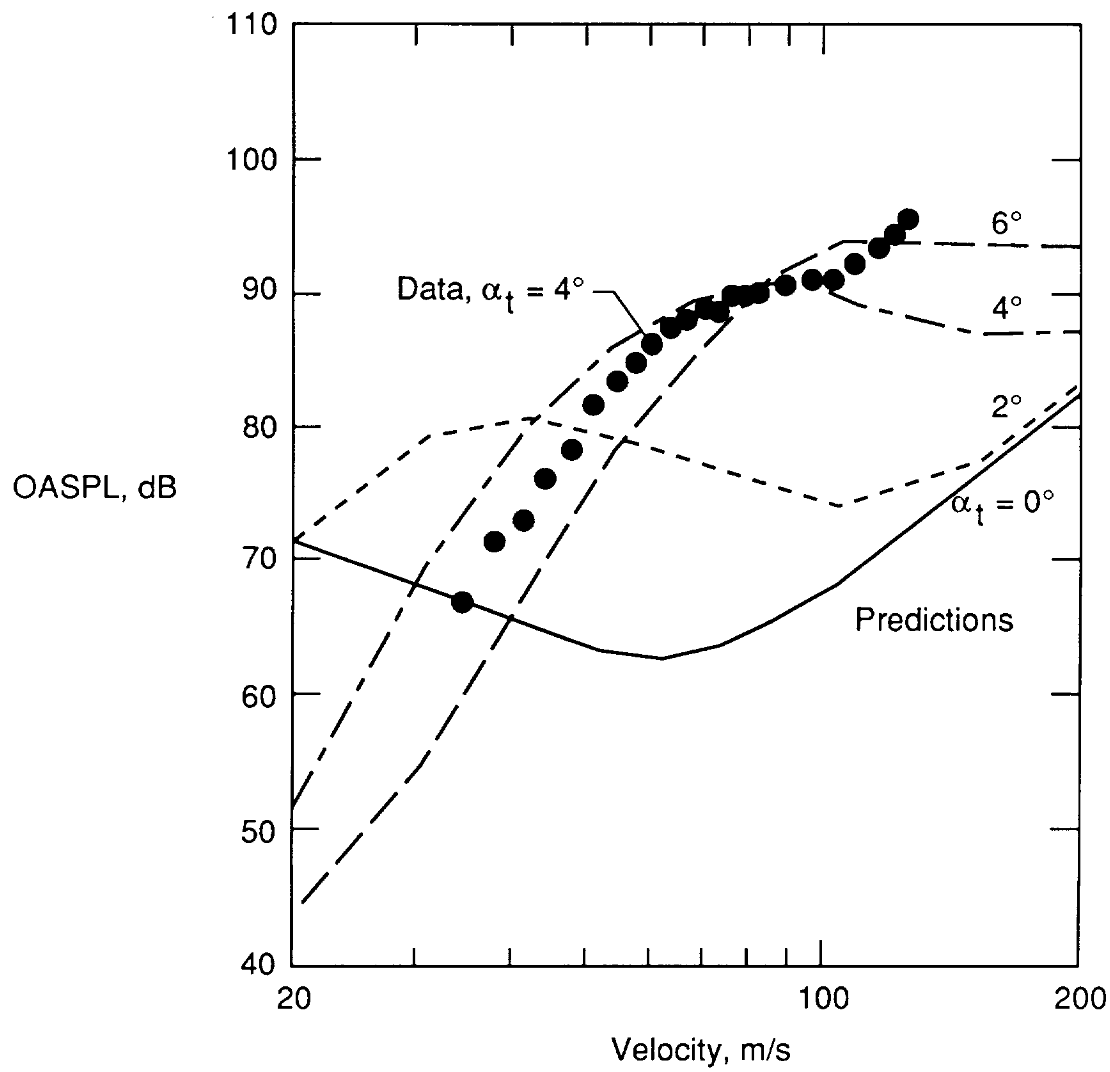

Figure 110. Overall sound pressure level versus velocity for constant-chord airfoil from reference 27 compared with predictions of present paper.

was found not to be continuous; however the tapered models did produce spectra containing a large number of peaks spread over a somewhat wider frequency range than those for the constant-chord airfoil at about the same velocities. In figure 111, 1/3-octave spectra are shown for the 2-to-1 taper airfoil at $\alpha_t = 4°$ for tunnel velocities between $U = 27$ and 107 m/s. The data are similar to those for the constant-chord model, except that the peaks are generally less well defined. In figure 112, corresponding OASPL variations with tunnel velocity are shown for $\alpha_t = 4°$. Also in this figure, OASPL is shown for a range of velocities where $\alpha_t = 0°$.

The predictions shown in figures 111 and 112 were obtained by dividing the models into 10 segments of constant chord (where actual chord length for each segment varied according to the blade taper), then making predictions for each segment, and summing on a pressure-squared basis the contributions of each. Angle-of-attack corrections for each segment were made by calculating the correction based on the mean chord (11.4 cm) across the span. This correction was then applied to the angle of attack for each of the blade segments. The corrected angles, therefore, were the same as for the constant-chord model, that is, $\alpha_* = 0°$ and 1.9° for $\alpha_t = 0°$ and 4°, respectively. The comparisons between predictions and data for the 2-to-1 taper airfoil appear about as good as those for constant-chord comparisons. It appears that the predictions for OASPL at $\alpha_t = 4°$ (fig. 112) would best agree if $\alpha_t \approx 3.5°$ had been used rather than 4°. This again indicates that agreement is on the order of possible experimental angle definition error. The OASPL comparisons for zero angle of attack show the predicted trends to be quite good but the levels to be overpredicted by 5 to 7 dB.

In figures 113 and 114 are the data and prediction comparisons for the 4-to-1 taper model at $\alpha_t = 0°$. The predictions are not as good as for the constant-chord and the less tapered model, although the data still fall within a predictive range of $\alpha_t = 2°$ to 3°. One should bear in mind that the flow behavior in the vicinity of the tapered models would be expected to deviate from the idealized 2D behavior assumed to be occurring over the small spanwise segments employed for the predictions. This makes it difficult to assess the meaning of the comparison deviations for the tapered models.

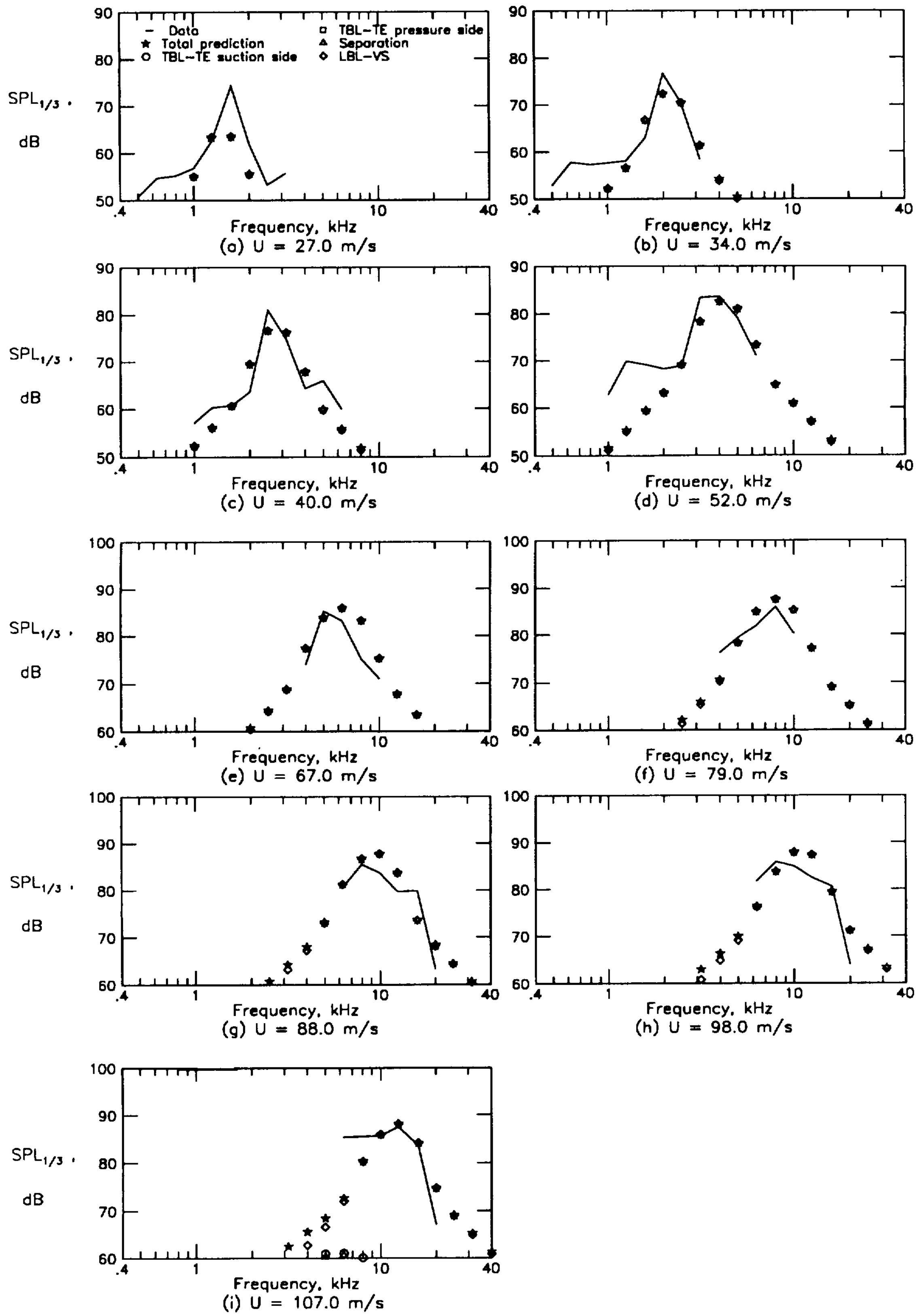

Figure 111. Noise spectra for 2-to-1 tapered-chord airfoil at $\alpha_t = 4^\circ$ ($\alpha_* = 1.9^\circ$) from reference 27 compared with prediction of present paper.

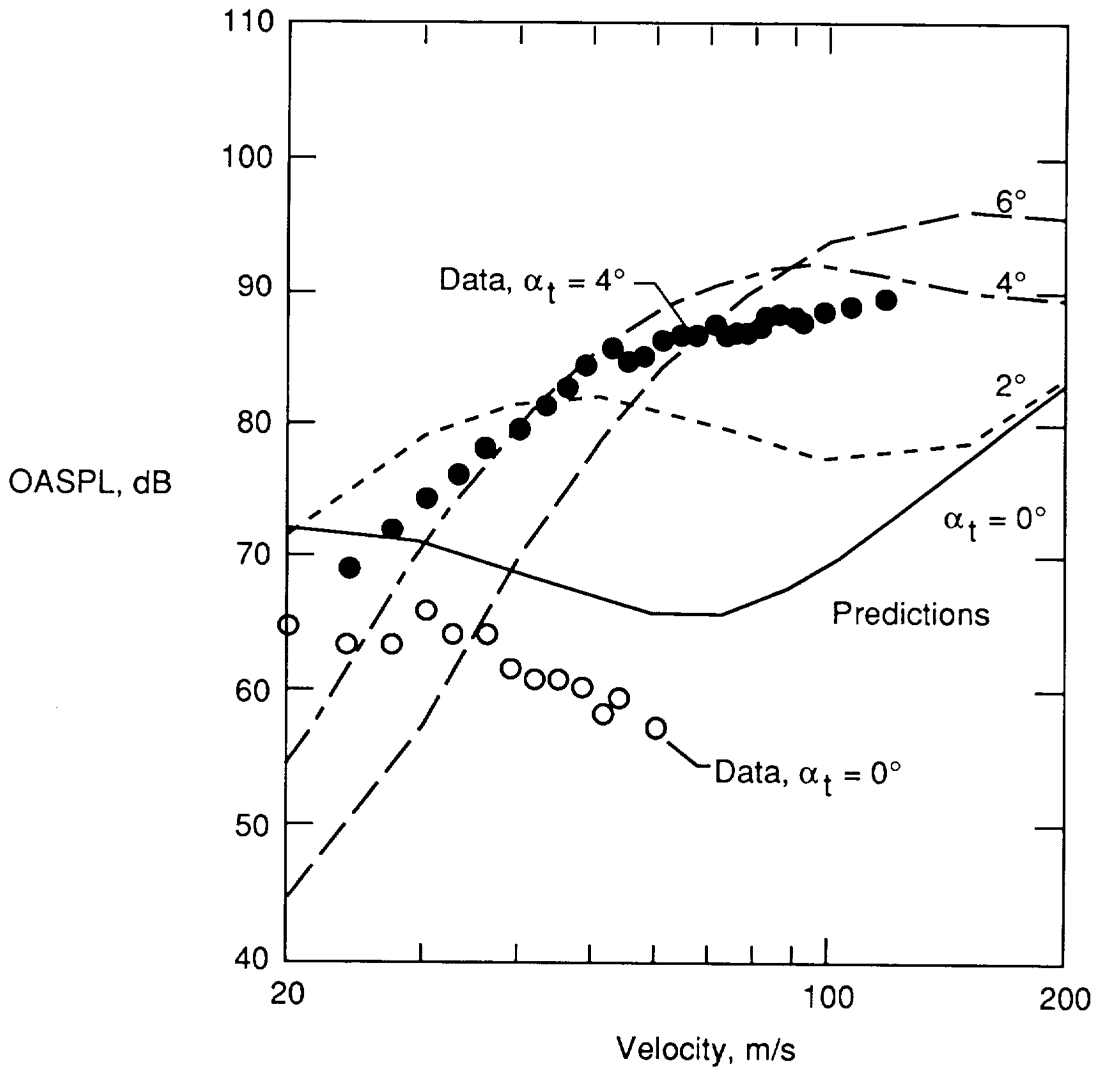

Figure 112. Overall sound pressure level versus velocity for 2-to-1 tapered-chord airfoil from reference 27 compared with predictions of present paper.

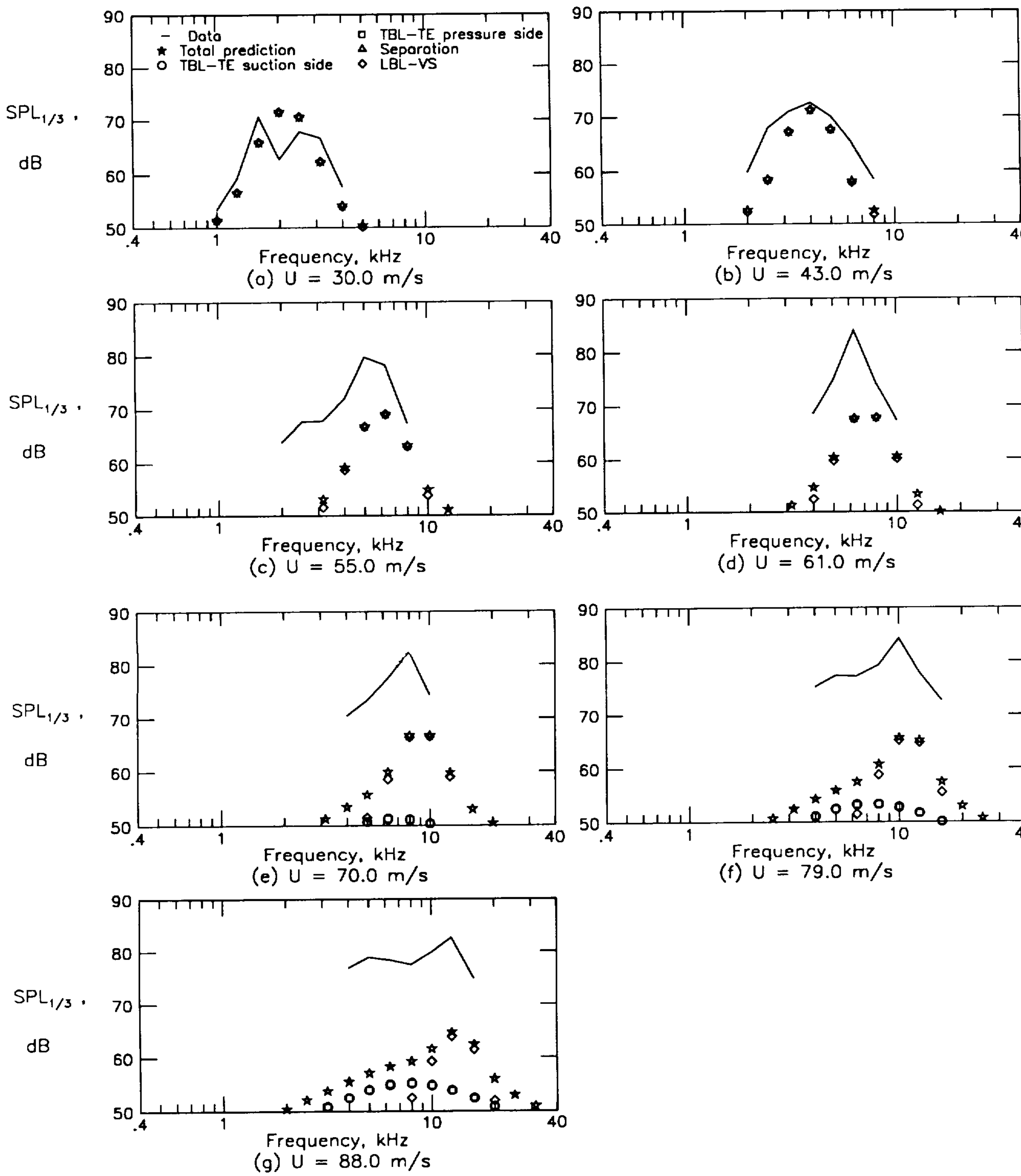

Figure 113. Noise spectra for 4-to-1 tapered-chord airfoil at $\alpha_t = 0°$ ($\alpha_* = 0°$) from reference 27 compared with prediction of present paper.

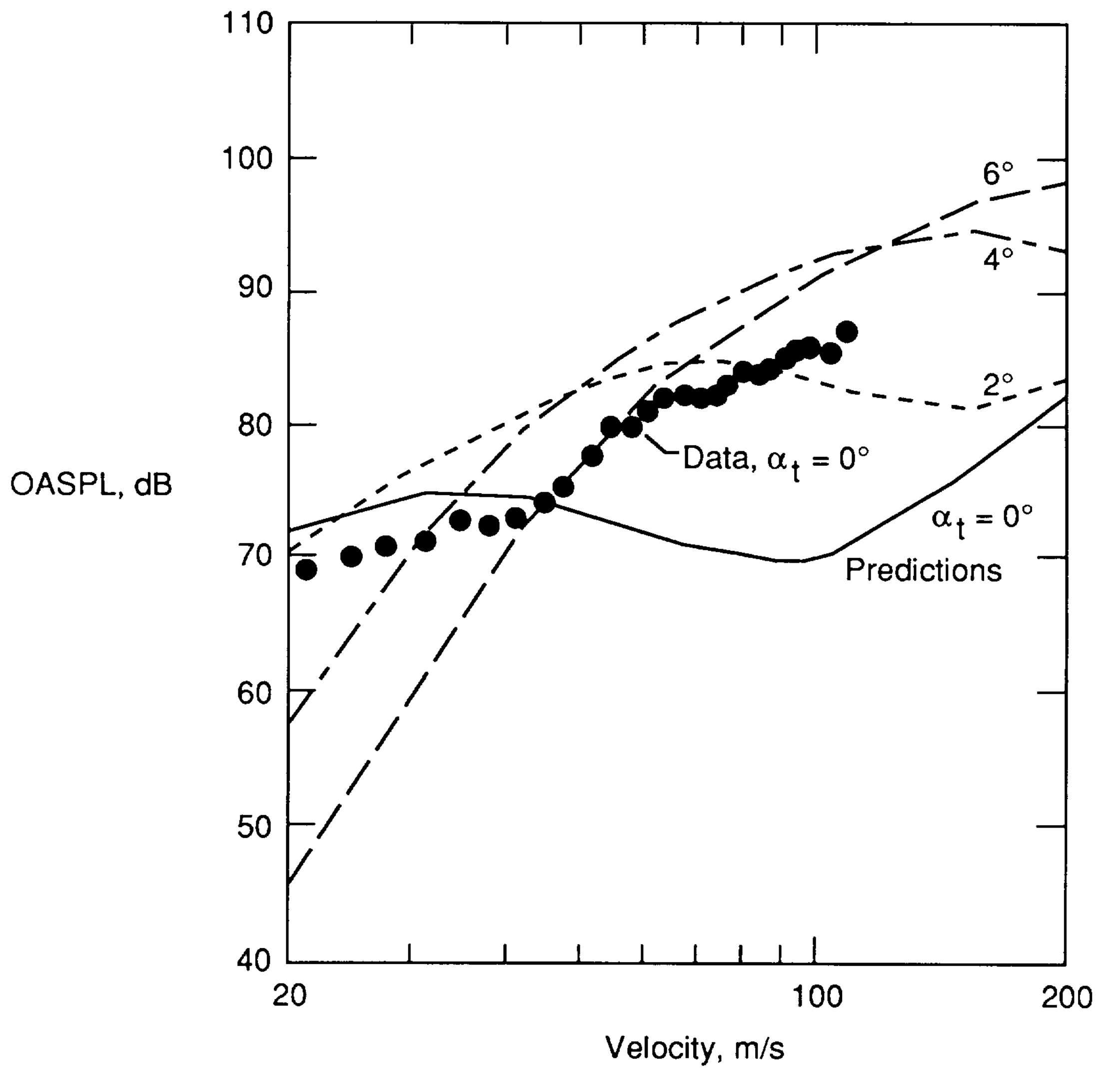

Figure 114. Overall sound pressure level versus velocity for 4-to-1 tapered-chord airfoil from reference 27 compared with predictions of present paper.

7. Conclusions

This paper documents the development of an overall prediction method for airfoil self-noise. The approach is semiempirical and is based on previous theoretical studies and data from a series of aerodynamic and acoustic tests of isolated airfoil sections. The acoustic data processing employed a correlation editing procedure to obtain self-noise spectra uncontaminated by extraneous noise. Five self-noise mechanisms, each related to specific boundary-layer phenomena, are identified in the data and modeled. For each mechanism, the data are first normalized by fundamental techniques using scaled aerodynamic parameters. The spectral shape, level, and frequencies are then examined and modeled for dependences on parameters such as Reynolds number, Mach number, and geometry.

The modeling accuracy of the resulting self-noise prediction methods is established by comparing predictions with the complete data base. The methods are shown to have general applicability by comparing predictions with airfoil self-noise data reported in the literature from three studies. A successful application of the methods is reported for a large-scale-model helicopter rotor broadband noise test.

Conclusions can be drawn regarding the specific self-noise mechanisms. For the turbulent-boundary-layer–trailing-edge noise and separation noise sources, an accurate and generally applicable predictive capability is demonstrated, especially for the important conditions of high Reynolds number and low to moderate angle of attack. The mechanism which can dominate the spectra for low Reynolds number, laminar-boundary-layer–vortex-shedding noise, is also demonstrated to have good predictive capability. For this quasi-tonal noise mechanism, there are some issues, not fully addressed herein, about how to apply the formulations in the most appropriate way to different airfoil geometries. The tip vortex formation noise source appears to be well predicted, although its relative lack of importance compared with the other self-noise sources prevents a full assessment of accuracy. The trailing-edge-bluntness–vortex-shedding noise source is shown to be very important and predictable by the method developed. For this source, there is an associated "flow angle" parameter which is found to be constant for any given trailing-edge geometry, but is difficult to determine a priori. However, for application of the bluntness noise prediction method, reasonable estimates for this parameter can be made based on the examples in this report.

The unique prediction capability presented should prove useful for the determination of broadband noise for helicopter rotors, wind turbines, airframe noise, and other cases where airfoil shapes encounter low- to moderate-speed flow. For modern propeller designs, the present equations should be applied with some caution because the high-speed, high-loading, and skewed-flow conditions existing about propeller blades do not match the low- to moderate-speed and generally 2D flow conditions of the present data base. The computer codes given herein can be readily incorporated into existing or future noise prediction codes. The documentation provided in this report should provide the means to evaluate where and how any needed future refinements can be made in the prediction codes for particular applications.

NASA Langley Research Center
Hampton, VA 23665-5225
April 19, 1989

Appendix A

Data Processing and Spectral Determination

In section 4, the special processing approach used to determine the self-noise spectra for the 2D airfoil models was summarized. Details are given here.

A.1. Data Acquisition and Initial Processing

Signals from the microphones shown in figure 4 were recorded during the test on a 14-channel FM analog tape recorder, operated to provide a flat frequency response up to 40 kHz. Individual amplifiers were used to optimize signal-to-noise ratio for each microphone channel, and pure-tone and white-noise insertions were used to calibrate amplitude and phase response, respectively. These calibrations and signal-conditioning techniques were the same as in reference 2, where additional details are given. The data were reduced from tape on a spectrum analyzer interfaced with a minicomputer. Pairs of microphones were used to obtain 1024-point cross-correlations at an analysis range of ±4.167 milliseconds.

A.2. Correlation Editing

The correlation records are modified to eliminate contributions from extraneous noise sources prior to taking the Fourier transforms to obtain the spectra. The first step is to remove, to the extent possible, the noise from the test hardware by subtracting the correlation $R_{45}(\tau)$ without the airfoil in place (the background noise) from $R_{45}(\tau)$ with the airfoil in place. (See fig. 9.) The resulting record should then be comprised of correlation peaks from the desired TE noise, LE noise, and other extraneous noise related to interaction between the model and test rig not accounted for in the subtraction. The TE and LE noise peaks in the cross-correlation are assumed to represent the autocorrelation of the TE and LE noise, respectively.

To eliminate the LE contribution, the correlation record on the right-hand-side (RHS) of τ_{TE} is discarded and replaced by the mirror image of the left-hand-side (LHS). However, for this folding process, it was found that it is important to preserve the basic shape of the TE peak to more accurately represent the spectra at higher frequencies. Because this is a digital correlation, made up of discrete points which are $\Delta\tau$ apart, it is likely that the true TE noise peak falls somewhere between two discrete values of τ. Folding about a discrete point instead of the actual effective peak center would introduce error by distorting the peak shape. In figure A1, the discrete points of the TE correlation peak are illustrated to show how the folding was accomplished. The discrete center is at τ_{TE}, whereas the effective center is to the left. The correlation values at $\tau_{TE} + \Delta\tau$ and $\tau_{TE} + 2\,\Delta\tau$ must not be changed to avoid modifying the shape near the very peak. The correlation value at $\tau_{TE} + 2\,\Delta\tau$ is projected to the LHS to intercept a line connecting $\tau_{TE} - 3\,\Delta\tau$ and $\tau_{TE} - 2\,\Delta\tau$. This defines the constants $\bar{a}$ and $\bar{b}$ which are shown. These constants then are used to interpolate between the points on the LHS to determine values at the points on the RHS, that is

$$R(\tau_{TE} + N\,\Delta\tau) = \frac{\bar{b}}{\Delta\tau} R(\tau_{TE} - N\,\Delta\tau) + \frac{\bar{a}}{\Delta\tau} R(\tau_{TE} - (N+1)\Delta\tau) \quad \text{(A1)}$$

for $N > 2$. The entire LHS of the correlation is folded about the effective peak center using this interpolation scheme.

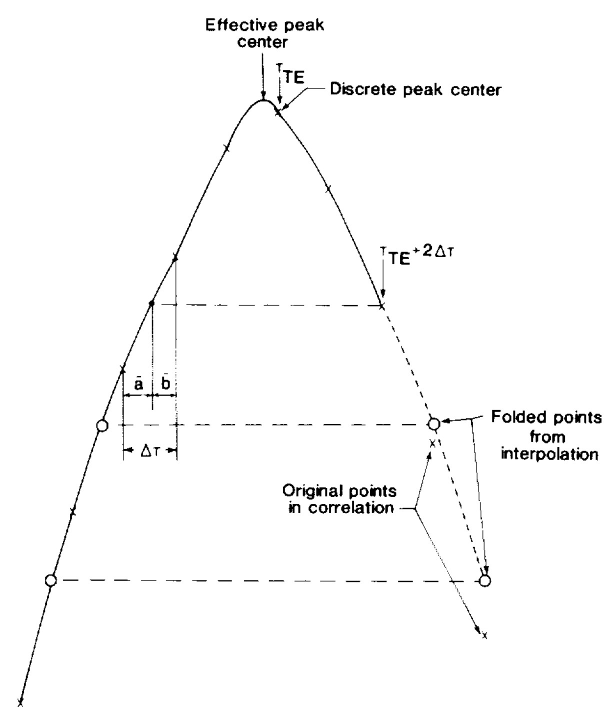

Figure A1. Sample correlation peak.

A.3. Separation of TE and LE Peaks

As indicated in section 4, for some of the correlation data for the three smaller chord lengths, the LE and TE peaks are so close that the LE contribution overlaps and distorts the TE peak shape. For many such cases a procedure was found to successfully remove the distortion prior to implementing the TE peak folding process described above. This procedure is explained by way of example for the 5.08-cm-chord airfoil shown in the bottom trace of figure A2. The predicted locations of the TE and LE noise peaks in the correlations are indicated and agree well with the peaks in the actual trace. Note the proximity of the two peaks.

The procedure to separate these two peaks involves combining the original $R_{45}(\tau)$ at the bottom of figure A2 with time-shifted versions of itself, so that the peaks are separated by larger time delays. The procedure depends on the implied symmetry of the LE and TE peaks, inherent in the assumption that they represent the autocorrelations for the LE and TE noise, respectively. The first step is to invert $R_{45}(\tau)$ in sign, and reverse it in time, by "flipping" the correlation about τ_{LE}. The result of combining these two curves is seen in the second trace from the bottom of figure A2, denoted $R'_{45}(\tau)$. The two peaks seen here are the original TE noise peak, and an inverted TE noise peak at $2\tau_{\mathrm{LE}} - \tau_{\mathrm{TE}}$. There is some increase in level and some distortion in the correlation record away from the peaks, as should be expected. The LE noise peak has been removed, but the inverted TE noise peak still affects the original peak at τ_{TE}. To remove the inverted peak, the initial $R_{45}(\tau)$ must be shifted by $2(\tau_{\mathrm{LE}} - \tau_{\mathrm{TE}})$ and summed with the previous result. This produces the third curve from the bottom in figure A2, denoted $R''_{45}(\tau)$. The TE noise peak has remained at τ_{TE}, while the LE noise peak is now at $3\tau_{\mathrm{LE}} - 2\tau_{\mathrm{TE}}$. The peaks are now separated in time so that details of each peak can be seen. Note that as the peaks no longer affect one another's shape, their basic symmetry is evident. This helps to validate the initial assumption that the peaks represent the autocorrelations of TE and LE noise. If the peaks must be further separated, this procedure can be successively repeated, with the results of the next two iterations seen in the top two traces of figure A2, $R'''_{45}(\tau)$ and $R''''_{45}(\tau)$. It should be noted that only the inner portion of the correlation is shown (the correlation was performed for ± 4.067 ms). Because of the data record manipulations, much of the outer portions of the correlations did not overlap and were thus zeroed out.

A.4. Determination of Spectra

Once the correlation records, or their modified forms after the separation processing, are folded about the effective peak center, the resulting TE noise correlations are transformed into spectra of the noise. Because the correlation record lengths are reduced by varying amounts (typically 20 percent) because of the editing described above, the use of fast Fourier transform techniques is not convenient. Instead, regular Fourier transform techniques are used in an approach based on chapter 9 of reference 28. In summary, a data window is applied to the correlation (eq. 9.116, ref. 28) and is used to provide the real and imaginary portions of the spectrum (eqs. 9.167–9.168, ref. 28). The resulting cross-spectra (eqs. 9.172–9.174, ref. 28) are presented in terms of magnitude and phase.

With the cross-spectra produced, amplitude corrections are applied to account for shear layer effects, using the technique of Amiet (ref. 22), as well as self-noise directivity effects, which are described in appendix B. The spectrum for each microphone pair was corrected to an effective position of 90° with respect to the airfoil chord line. The combined effect of both of these corrections tended to be small, with the corrections for many test conditions being less than 1 dB. Since cross-spectra were obtained, the corrections for each of the two microphones involved were averaged to correct the cross-spectral magnitude.

The results obtained from this method are given in figure A3 for the example correlation records of figure A2. Figure A3(a) shows the cross-spectrum obtained from the correlation of the original $R_{45}(\tau)$ record, which is the bottom curve of figure A2, while figure A3(b) shows the cross-spectrum obtained after folding the $R_{45}(\tau)$ record about the TE noise peak. Note that the cross-spectral phase ϕ is a partial indicator of how well the cross-spectrum represents the total TE self-noise. Ideally the phase should vary linearly with frequency, $\phi = 360° f \tau_{\mathrm{TE}}$. The breaks seen in this phase line and the corresponding spectral peculiarities indicate regions adversely affected by contamination, which was not removed by the background subtraction and, in the case of figure A3(b), the folding process. The contamination from the LE is seen to primarily affect the cross-spectrum of figure A3(a) below around 4 kHz. Folding the correlation removes most of this, leaving a dip in the spectrum of figure A3(b) at about 1.5 kHz. Figure A3(c) shows the spectrum for the third curve from the bottom in figure A2, $R''_{45}(\tau)$, which is the modified correlation after two manipulations have separated the TE and LE noise peaks. The phase difficulty and spectral dip at about 1.5 kHz in figure A3(b) are eliminated in figure A3(c). Figure A3(d) shows the spectrum for the top curve of figure A2, $R''''_{45}(\tau)$, which is for four manipulations. This spectrum is similar to that of figure A3(c) except for some apparent increase in contamination at the low- and high-frequency ends. For the airfoil presented here, a choice was made to use the spectrum of figure A3(c), based on two

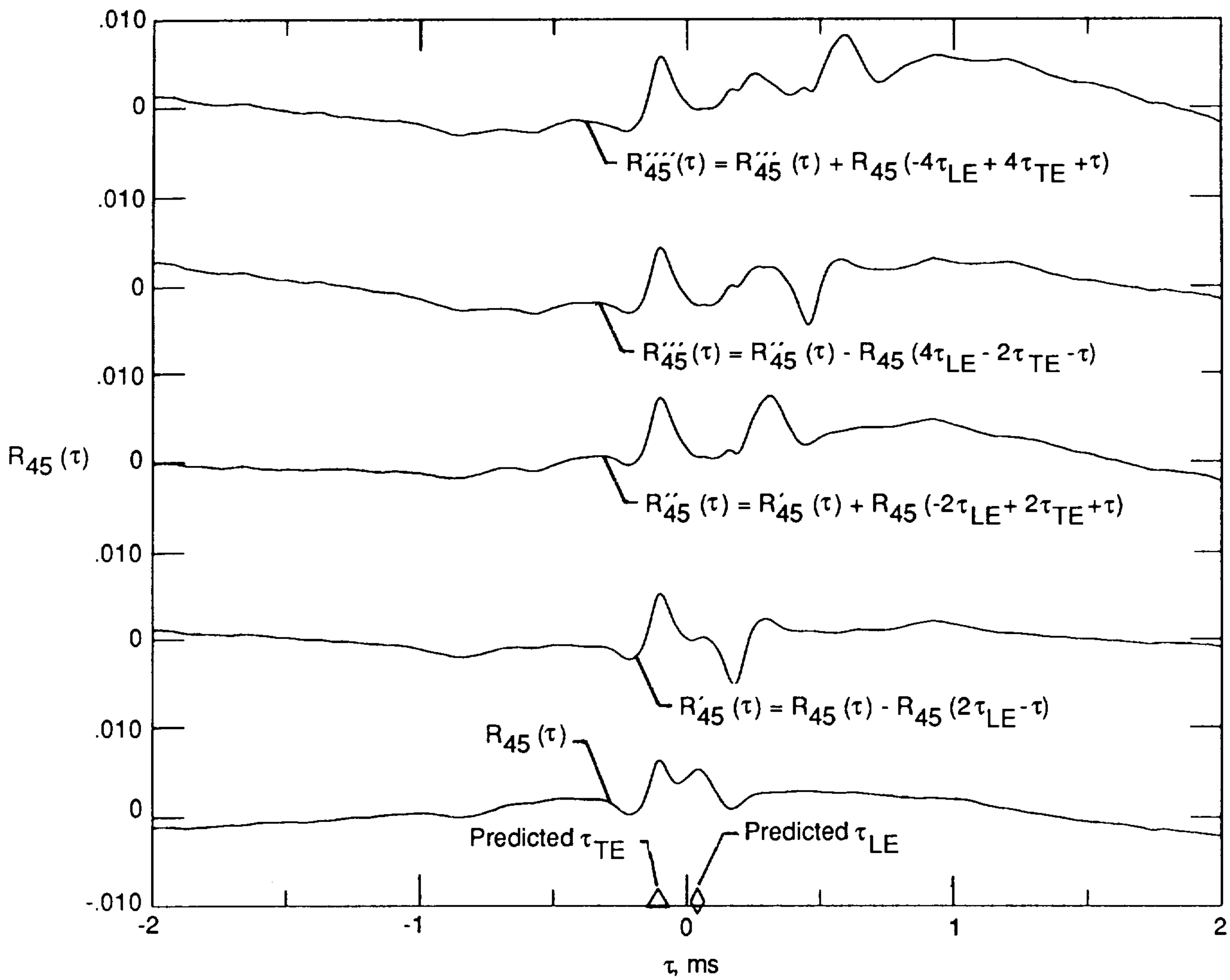

Figure A2. Separation of TE and LE peaks in a cross-correlation. Example is cross-correlation between microphones M4 and M5 for the 5.08-cm-chord airfoil with tripped BL. $\alpha_* = 0°$, $U = 71.3$ m/s.

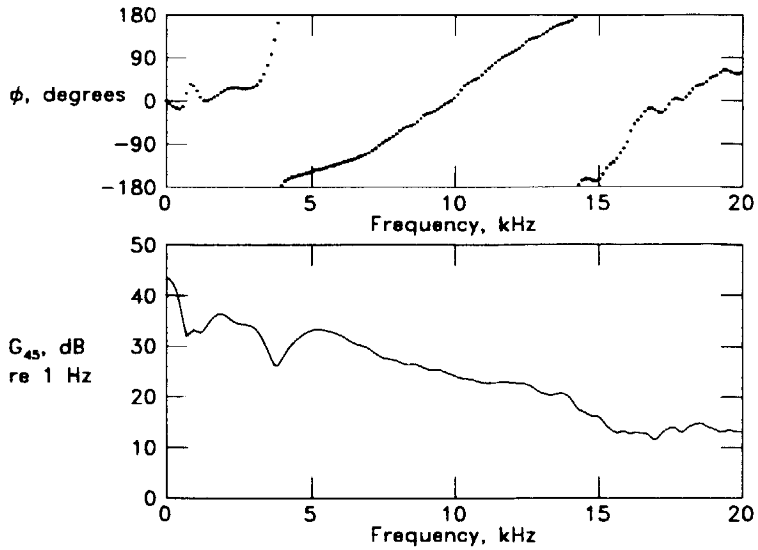

(a) Transform of $R_{45}(\tau)$ with no folding.

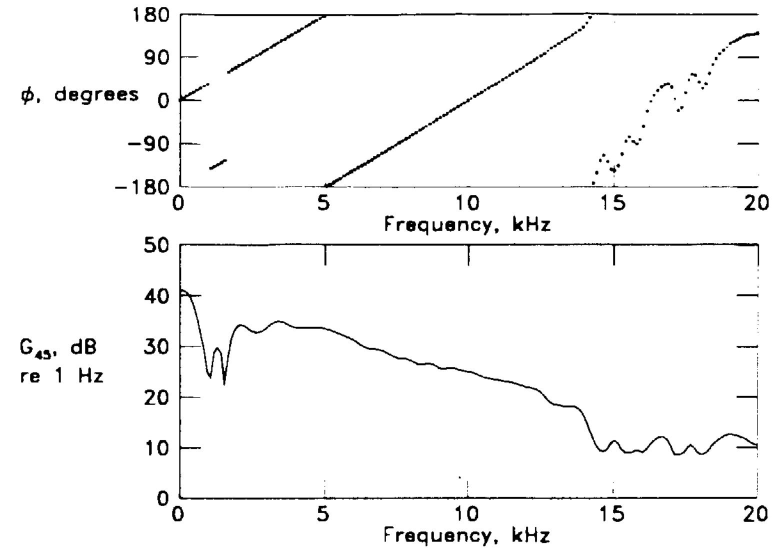

(b) Transform of $R_{45}(\tau)$ with folding about TE peak.

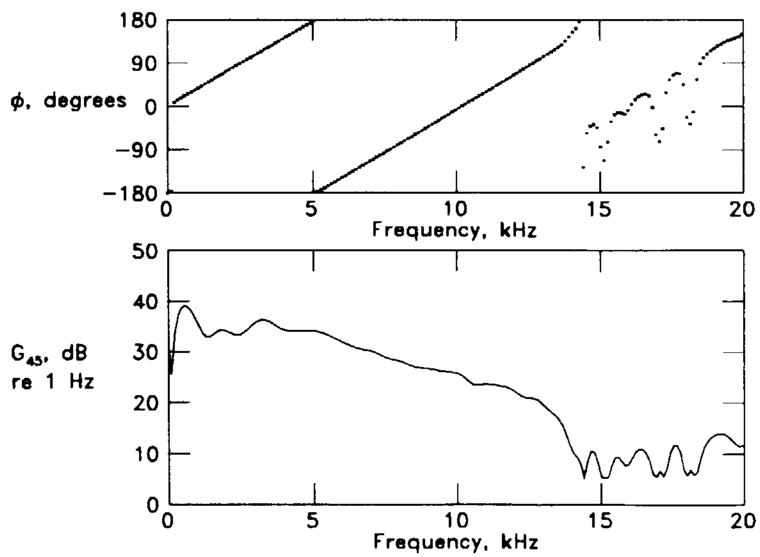

(c) Transform of $R''_{45}(\tau)$ with folding about TE peak.

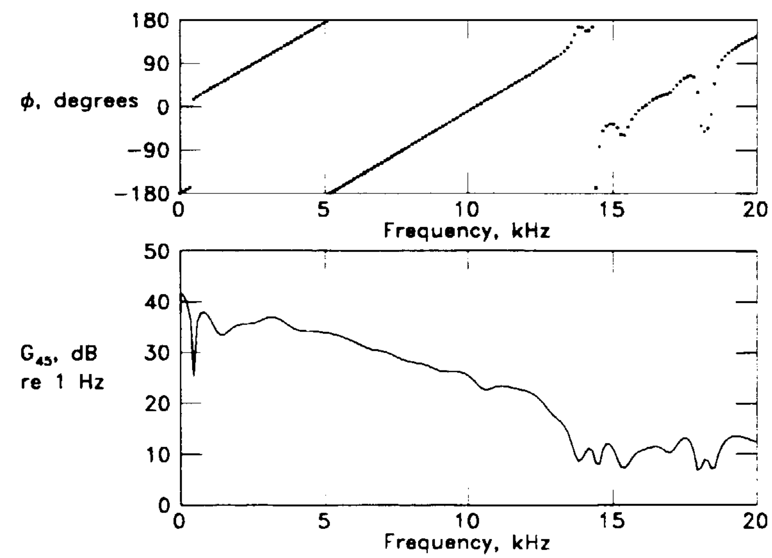

(d) Transform of $R''''_{45}(\tau)$ with folding about TE peak.

Figure A3. Cross-spectra obtained by transforming correlations of figure A2.

separation manipulations, to represent the self-noise. The lower and upper limits to which the spectrum is believed to be accurate are from about 0.8 to 13 kHz. For the other airfoils of this paper, similar evaluations of the limits were made and the spectra are cut off beyond these limits in their presentation, as indicated in section 4.

To increase confidence, all the 2D airfoil spectra presented in figures 11 to 74 were found by averaging independently determined spectra from two microphone pairs. After the shear layer and directivity corrections were applied, the spectra from the two microphone pairs generally agreed to within 1 dB. In tables 1 and 2, the data processing and manipulations, and whether the correlations were folded or not prior to taking the spectra, are specified for each test case. It is seen that for the three larger airfoils, no correlation manipulations were needed to separate the LE and TE correlation peaks. For the three smaller airfoils, performing two separation manipulations was advantageous for about a quarter of the cases. The table shows that a substantial number of correlations were not folded. For airfoils at sufficiently high angles of attack, low frequencies can dominate the noise. This results in large correlation humps, rather than the relatively sharp peaks which are needed in the folding process. For these cases, the raw cross-correlations are transformed, with only the background subtraction being performed. Also the correlations were not folded in the presence of strong LBL–VS noise. This noise can dominate all other self-noise sources, as well as the LE noise contamination, negating the need for the correlation editing. This correlation editing would have proved difficult, in any case, since vortex shedding produces noise at small bands of frequencies, appearing as damped sinusoidals in the correlation, which tended to mask other peaks. The effect of folding the correlation in such cases was examined, however, and found to have little effect on the spectra.

Appendix B

Noise Directivity

The purpose of this appendix is to define the directivity functions $\overline{D}_h$ and $\overline{D}_\ell$, which are employed in the tunnel noise data processing and proposed for use in the prediction equations for the self-noise sources.

B.1. Retarded Coordinates

The retarded coordinate system is explained by first referring to figure B1 where the airfoil is at zero angle of attack to the tunnel flow. If the velocity were zero everywhere, sound from the model which reaches the microphones (M2 is shown) would follow the ray path defined by the measured distance r_m and angle Θ_m. But with the velocity in the free jet equal to U, the ray which reaches the microphones follows first the radiation angle Θ_c until it encounters the shear layer where it is refracted. It emerges at angle Θ_t with an amplitude change and travels to the microphone. The theoretical treatment employed in this study for the angle and amplitude corrections is that due to Amiet (refs. 22 and 23). A convenient reference for the corrected microphone measurements is a retarded coordinate system where the source and the observer are at corrected positions. The angle Θ_e is referenced to a retarded source position and a corrected observer position where the distance between the positions is $r_e = r_m$. As defined, if there were no shear layer present with flow extending to infinity, the center of the wave front emitted from the source would be at the retarded source position when the wave front reaches the corrected observer position. The retarded coordinates are equivalent to the emission time coordinates employed in the literature, for example, see reference 29, for moving sources and stationary observers. Figure B2 shows a source flyover geometry corresponding to the open jet wind tunnel geometry of figure B1. Physical equivalence between the cases is attained by accounting for the Doppler-related frequency shifts due to the relative motion between the source and observer in one instance and no relative motion in the other. There are no Doppler-related amplitude corrections required between the flyover and wind tunnel cases as the effect of the flow on the source definition is already included in the wind tunnel environment.

B.2. Directivity Functions

In figure B3, a 3D retarded coordinate system is defined where the origin is located at the trailing edge of a thin flat plate, representing an airfoil. The flat plate is in rectilinear motion of velocity U in direction of the negative x_e axis. The observer is stationary. Trailing-edge noise is produced when boundary-layer turbulence and its associated surface pressure pattern convect downstream (with respect to the plate) at a velocity U_c (Mach number M_c) past the trailing edge. If the noise-producing turbulence eddies are sufficiently small and the convection velocities are sufficiently large to produce acoustic wavelengths much shorter than the chord length, the directivity can be shown to be (based on analysis of Schlinker and Amiet, ref. 3)

$$\overline{D}_h(\Theta_e, \Phi_e) \approx \frac{2\sin^2(\Theta_e/2)\sin^2\,\Phi_e}{(1+M\cos\Theta_e)[1+(M-M_c)\cos\Theta_e]^2} \qquad \text{(B1)}$$

where the h subscript indicates the high-frequency (or large-chord) limit for $\overline{D}$. The overbar on $\overline{D}_h$ indicates that it is normalized by the TE noise radiated in the $\Theta_e = 90°$ and $\Phi_e = 90°$ direction, so $\overline{D}_h(90°, 90°) = 1$. For the flyover plane ($\Phi_e = 90°$), equation (B1) is the same as equation (32a) of reference 3. In reference 3, the equation was compared favorably with measured airfoil TE noise results, for limited M and Θ_e ranges, as well as with previous theoretical results. The directivity expression used in reference 2 was found to give virtually identical results for low Mach numbers.

Although developed for when the velocity U is parallel to the plate along the x_e axis, equation (B1) can be applied when the plate or airfoil is at an angle of attack α to the flow. In application (refer to fig. B3), one should define the angles with respect to a coordinate system that is fixed with respect to the airfoil with the x_e axis fixed along the chord line, rather than one where the x_e axis is fixed along the direction of motion. Note, however, that any analysis of Doppler frequency shifts (not treated in this paper) should reference angles with respect to the direction of motion. Applications of equation (B1) at angles of attack should result in little additional error to that already built into the relation. Because it was derived with the plate assumed to be semi-infinite, $\overline{D}_h$ becomes inaccurate at shallow upstream angles ($\Theta_e \to 180°$), when applied to finite airfoils even for high frequencies. As frequency is lowered, the wavelengths become larger with respect to the chord and the directivity becomes increasingly in error. However, $\overline{D}_h$ should be of sufficient accuracy to define the directivity of all the self-noise sources discussed because of their high-frequency character. The one exception to this is the stalled-airfoil noise.

When the angle of attack of the airfoil is increased sufficiently, the attached or mildly separated TBL flow on the suction side gives way to large-scale

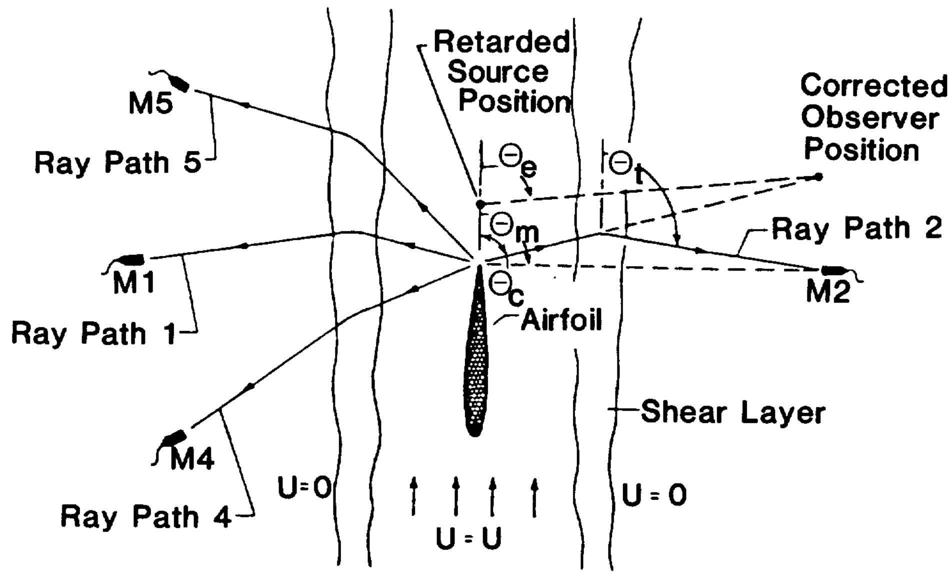

Figure B1. Sketch of shear layer refraction of acoustic transmission paths.

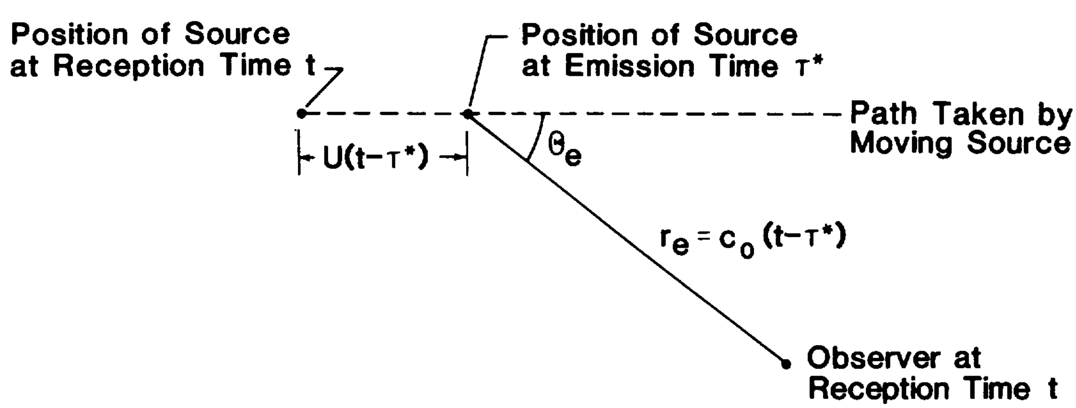

Figure B2. Emission from a source moving with a constant velocity.

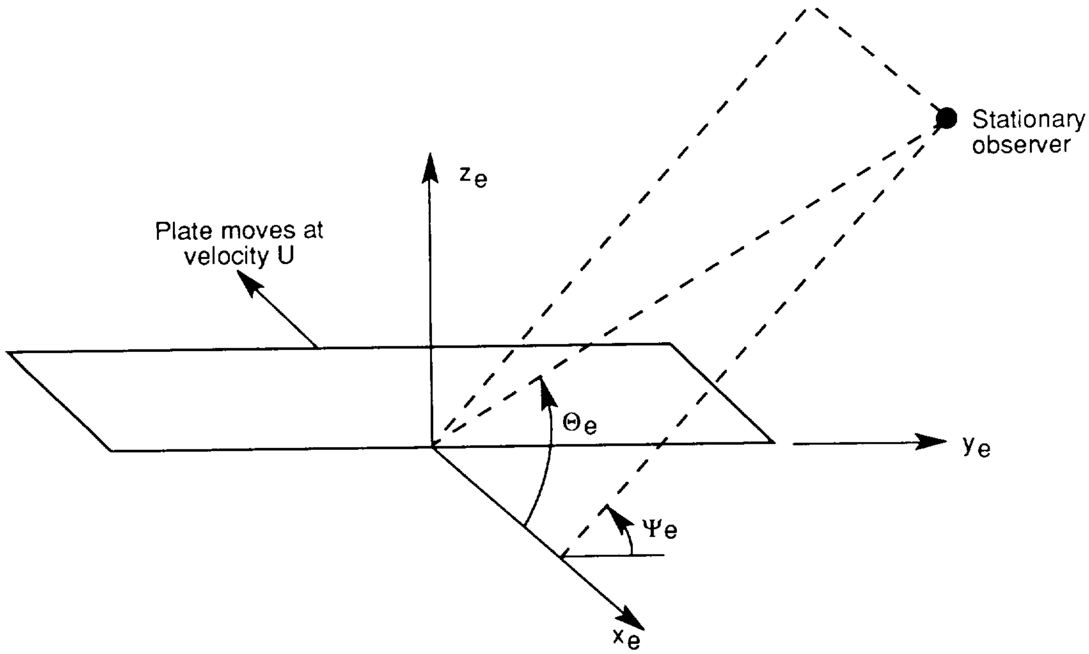

Figure B3. Flat plate in rectilinear motion.

separation. The turbulence eddies are then comparable in size to the airfoil chord length and the eddie convection speeds are low. The directivity for this low-frequency noise is more properly defined as that of a translating dipole, which is

$$\overline{D}_\ell(\Theta_e, \Phi_e) \approx \frac{\sin^2 \Theta_e \sin^2 \Phi_e}{(1 + M \cos \Theta_e)^4} \tag{B2}$$

where the ℓ subscript indicates a low-frequency limit. The coordinate system and comments about angle definitions in equation (B1) apply also in equation (B2). Equation (B2) is employed for the directivity in the expression for stalled flow noise (eq. (30)).

For the noise data reduction in the present study, equation (B1) was used in the determination of the self-noise spectral levels for the reference observer position, at r_e = 122 cm and Θ_e = 90°. First, shear layer refraction corrections were calculated to determine the spectral level adjustments, to add to measured values, and a resultant source-observer location at r_e and Θ_e. This was done while keeping track of the actual physical coordinates of the trailing edge which varied with airfoil angle of attack. Finally, equation (B1), with Φ = 90° and an assumed convection Mach number of $M_c \approx 0.8M$, was used to determine final level adjustments required to match results to the Θ_e = 90° location.

Appendix C

Application of Predictions to a Rotor Broadband Noise Test

An acoustics test of a 40-percent scale model BO-105 helicopter main rotor was conducted in the German-Dutch Wind Tunnel (DNW). Figure C1 shows an overview of the test setup in the large open anechoic test section. The 4-meter-diameter rotor is shown positioned in the flow between the nozzle on the right and the flow collector on the left. A key aim of the test was to produce a large benchmark aero-acoustic data base to aid and verify rotor broadband noise prediction. In reference 30, the present authors compared data with predictions of rotor broadband self-noise for a number of rotor operating conditions. The predictions employed the self-noise prediction methods, which are documented in section 5 of the present paper, and the NASA ROTONET program (ref. 31) to define rotor performance and to sum contributions of noise from individual blade segments.

In this appendix, the experiment is not reviewed in detail nor are data-prediction comparisons presented, as reference 30 is complete in this regard. Rather, reference 30 is complemented by specifying how the self-noise prediction methods of the present paper were applied. Given below is a summary of the rotor prediction method, a definition of the rotor blade geometry and test modifications and a specification of input parameters for the individual source predictions. The degrees of success of data-prediction comparisons in reference 30 are discussed along with recommended refinements to the prediction methods.

To produce a rotor prediction, the rotor geometry definition and flight conditions, specified as thrust, rotor angle, rotor speed, flight velocity, and trim condition, are provided as inputs to the ROTONET rotor performance module. The particular module used assumes a fully articulated rotor with rigid blades and a simple uniform inflow model. The module determines local blade segment velocities and angles of attack for a number of radial and azimuthal positions. Ten radial segments were considered at 16 azimuthal positions. The BL thicknesses and other parameters needed are calculated. The noise due to each source is predicted for each blade segment, and the ROTONET noise radiation module is used to sum contributions from all blade segments to obtain, after accounting for Doppler shifts and the actual number of blades, the noise spectrum at the observer.

As indicated in reference 30, the accuracy of predictions depends on a number of factors including the accuracy of the performance module used. One may question the quasi-steady assumptions used in defining the local BL characteristics, which ignore unsteadiness and resultant hysteresis effects. Likely more important is how well the aeroacoustic scaling determined from low-speed data extends to higher speed. The Mach number at the tip of the blades is 0.64 for rotor hover, whereas the 2D airfoil model tests were limited to Mach 0.21. Also there are questions on how to apply scaling obtained from symmetrical NACA 0012 sections with particular TE geometries to the cambered NACA 23012 rotor blade with different TE geometries.

The model rotor is a 40-percent-scale, four-bladed, hingeless BO-105 rotor, with a diameter of 4.0 m and a chord of 0.121 m. A blade and its details are shown in figure C2. The blades have −8° linear twist and a 20-percent cutout from the hub center. The effects of several blade modifications were examined, including (1) application of Carborundum grit from the blade leading edge to 20 percent chord to match the BL trip condition for the 2D blade sections described in section 2 of the present paper, (2) taping of the TE with 0.064-mm-thick plastic tape to modify the "step tab" geometry, and (3) attachment of a rounded tip to each blade (the standard blades have a squared-off tip).

C.1. Boundary-Layer Definition

With the local blade segment mean velocities and angles of attack determined by the rotor performance module, the equations of section 3 were directly applied to determine the BL thicknesses required in the noise predictions. Most noise comparisons in reference 30 are for the blades with untripped BL. For the tripped BL, the fact that the BL trip conditions for the rotor blades matched the 2D test models assured the appropriateness of using the equations for a heavy trip rather than modifying the equations as required for the UTRC comparisons reported in section 6. For all BL thickness calculations, the aerodynamic angles of attack were used in the equations. The aerodynamic angle is referenced to the zero lift angle, which is −1.4° from the geometric angle for the NACA 23012 airfoil.

C.2. TBL–TE and Separation Noise Prediction

Given the definitions of segment chord length, span width, velocity, aerodynamic angle of attack, and BL thicknesses, the calculation of TBL–TE and separation noise is straightforward as specified in section 5. From the data-prediction comparisons of reference 30, it is concluded that the TBL–TE and separation noise calculations demonstrated a good predictive capability for these mechanisms. The rotor was tested from hover to moderately high flight

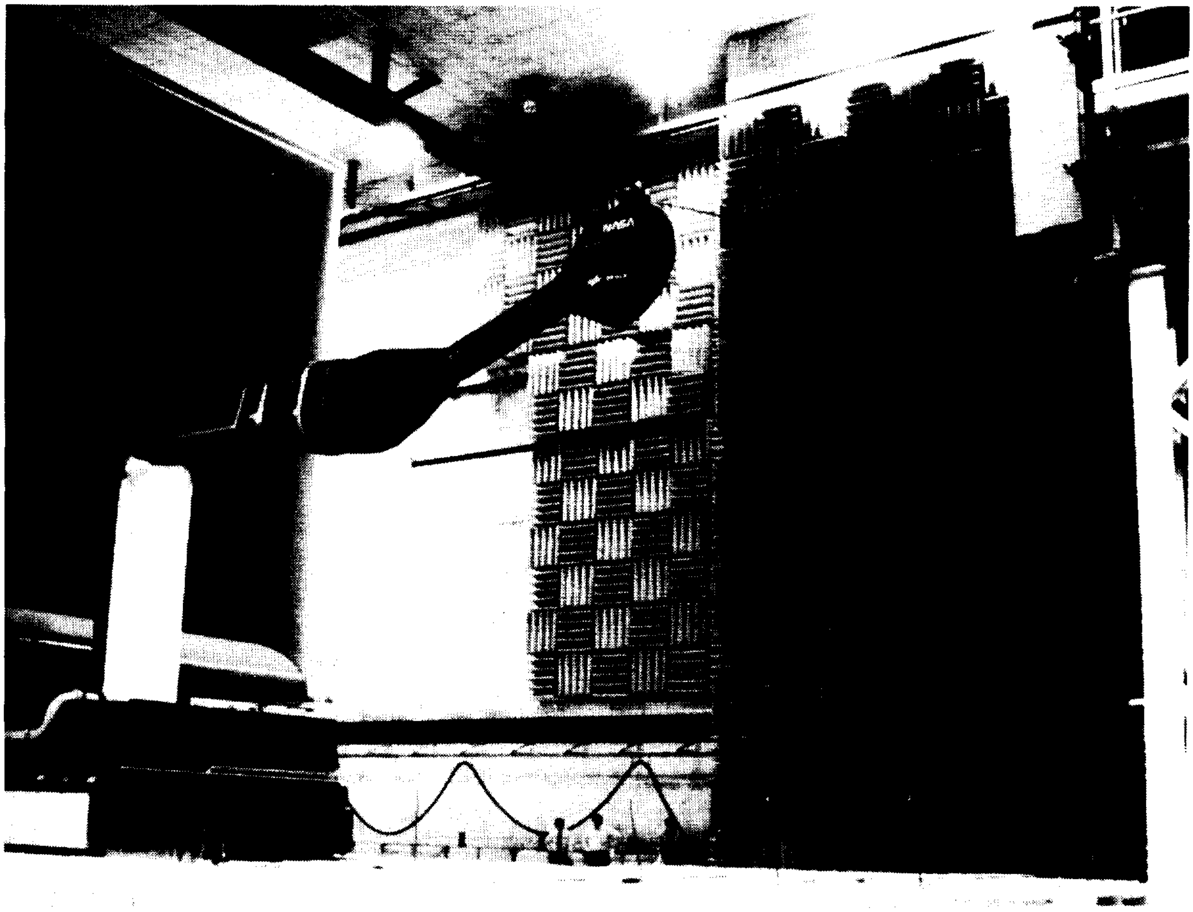

L-89-44

Figure C1. Test setup in DNW for helicopter main rotor broadband noise study reported in reference 30.

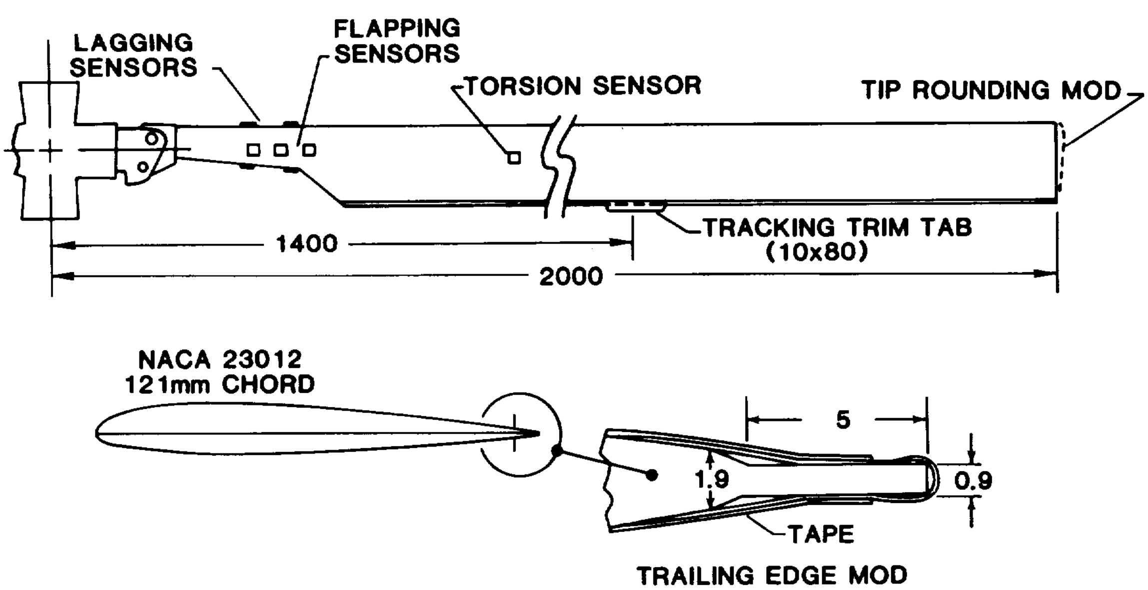

Figure C2. Model BO-105 blade details. All dimensions in mm.

speeds for various climb and descent rates at different thrust settings. Diagnostics included 1/2 rotor speed tests and the BL tripping tests. It is noted that the TBL–TE and separation noise predictions for a number of rotor conditions fell below contributions of LBL–VS, especially at the 1/2 rotor speed, and of TE bluntness noise. This represents a limitation of the comparisons which prevents sweeping statements regarding predictive accuracy of TBL–TE and separation noise sources. Still the agreements were quite good except when the rotor operated at full speed (tip speed of $M = 0.64$) and the boundary layers were tripped. Then the noise was underpredicted by about 6 dB. It is believed that for this high speed the heavy trip disturbed the flow substantially, made it dissimilar to the 2D model cases, where the speed was limited to $M = 0.21$, and perhaps changed the controlling noise mechanisms. Comparisons for the tripped BL rotor at 1/2 speed and the untripped BL blades at full and 1/2 speed produced good results.

C.3. LBL–VS Noise Prediction

The comparisons for LBL–VS noise in reference 30 showed, for a broad range of rotor conditions, very good predictions. As with the TBL–TE and separation noise predictions, the calculation of LBL–VS noise is straightforward given the specification of local flow conditions at the blade segments. A special note should be made for one key parameter involved in the calculations. The angle of attack α_* employed in the LBL–VS noise prediction (eqs. (53) to (60)) was the geometric angle rather than the aerodynamic angle for the NACA 23012 airfoil section. The BL thickness calculations, however, used the aerodynamic angle, as previously stated. The use of the geometric angle for the noise calculation is justified by (1) the better rotor data-prediction comparisons found using the geometric rather than the aerodynamic angle and (2) the lack of guidance one has in applying the acoustic scaling laws which were based on symmetrical airfoil results, to airfoils that are cambered. Remember that the controlling mechanism of LBL–VS noise is the presence of aeroacoustic feedback loops between the trailing edge and an upstream location on the airfoil surface where laminar instabilities occur. This geometric connection indicates that a purely aerodynamic angle definition for the LBL–VS mechanism would not likely be correct. An alternate viewpoint of the angle definition problem would be that the aerodynamic angle should be used, which would increase the noise predicted over that measured, but that allowance should be made for the fact that the inflow to the rotor blade segments is not the assumed smooth quasi-steady flow. The presence of sufficiently unsteady flow conditions over portions of the rotor would prevent the establishment of the LBL–VS mechanism and related noise. Limiting LBL–VS noise production to some measure of inflow turbulence offers promise as a refinement to the self-noise prediction method.

C.4. Tip Vortex Formation Noise

The tip noise predictions were made for both the rounded and the squared-off blade tips tested. The performance module was used to determine the local flow velocities and angles for the tips at different azimuth locations. The α_{TIP} used was the NACA 23012 aerodynamic angle. Because the tip loading characteristics for the rotor blades differed from the reference case of the tip noise model, which was an untwisted large-aspect-ratio blade with uniform flow over the span, the sectional lift term of equation (66) was evaluated. The sectional lift slopes for the rotor blades were analyzed by employing a lifting-surface model adapted from reference 18. The velocity and angle of attack were linearly varied over the span near the tip of the lifting surface blade. It was found that the tip loading is increased over the reference case by a small amount. For equation (66), the redefined α'_{TIP} angle was then given by $\alpha'_{\mathrm{TIP}} = 1.1\alpha_{\mathrm{TIP}}$.

The predictions for tip noise in reference 30 were in all cases significantly below predictions for TBL–TE noise. This makes it impossible to truly assess the accuracy of the tip noise modeling for the rotor. However, since the data comparisons with the total levels predicted were good for both low and normal rotor speeds, the tip noise is apparently well predicted. It is noted that a review of data for a number of rotor cases, not all given in reference 30, indicated no significant effect due to the blade tip modification. This is in line with prediction for this rotor.

C.5. TE-Bluntness–Vortex-Shedding Noise

Given the flow definition for the blade segments from the performance module, the bluntness predictions require the specification of thickness h and flow angle parameter Ψ. As with the UTRC test comparisons of section 6, it is not clear how to apply scaling laws obtained from an airfoil with a particular TE geometry to a rotor blade with a different TE. For the step tab TE geometry, shown in figure C2, h was specified as the actual 0.9 mm and Ψ was taken as 14°, which is actual solid angle of the surface at the TE of the NACA 23012 airfoil (same as the NACA 0012 airfoil). However, because of the 0.5-mm step 5 mm upstream of the TE, 0.5 mm was added to the calculated value of δ^*_{avg} to approximately account for the anticipated step-caused BL flow deficit. For the TE tape modification case, δ^*_{avg} was taken as that calculated, because the step was removed, but h was increased by four tape thicknesses. Had the tape remained fully attached to the TE surface (see fig. C2) during the test, two thicknesses would have been added. The flow angle Ψ was taken as 18°. The choice of this specific number was rather arbitrary, but is in line with that used for the UTRC comparisons (section 6) for rounded trailing edges. The tape rounded the TE bluntness which should reduce the persistence of and noise due to the separated flow in the near wake. The larger Ψ angle value (18° compared with 14°) results in less noise predicted.

The comparisons of reference 30 obtained using the above "reasonable" choices for the TE parameters give good results for all 1/2 rotor speed cases. For the full rotor speed cases the levels were consistently overpredicted. This is believed to be due to a speed dependence for the bluntness mechanism that could not have been anticipated from the low speed airfoil data, from which the scaling laws were developed. Subsequent analysis indicates that much better agreement with data could have been obtained if the bluntness noise contribution was eliminated for blade segments exceeding Mach numbers of 0.45 or 0.5. This is in some conflict with comparisons in section 6 for the blade section noise of Schlinker and Amiet (ref. 3), which shows apparently strong bluntness noise at $M = 0.43$ and 0.5. However, based on the rotor results, an upper limit of 0.45 for the bluntness noise contribution is recommended as a refinement to the prediction method.

Appendix D

Prediction Code

The airfoil self-noise prediction method is available as a computer code written in standard FORTRAN 5 specifically for the Digital Equipment Corp. VAX-11/780 series machine running under the VMS operating system. To the extent possible, the code has been made machine independent. There is one input file to the code and one output file. Input consists of user supplied NAMELIST parameters while output is a table of 1/3-octave centered frequencies with corresponding sound pressure levels for each noise mechanism followed by their total. The user selects which of the mechanisms to calculate.

The airfoil section for which a prediction is desired is assumed to be composed of a number of segments, each having its own chord, span, angle of attack, free-stream velocity, trailing-edge bluntness, and angle parameter, as well as observer directivity angles and distance. This permits a variety of configurations such as taper, twist, spanwise-varying free-stream velocity (for rotor blades), etc. The user may specify as many or few segments as desired depending on the complexity of the geometry. Characteristics for each segment are specified in the input file, which contains the FORTRAN variables given in table D1.

Table D1. Segment Characteristics Specified in Input File

FORTRAN name	Symbol	Description
NSEG		Number of segments
C	c	Chord length, m
L	L	Span, m
R	r_e	Observer distance, m
THETA	Θ_e	Observer angle from x-axis, deg
PHI	Φ_e	Observer angle from y-axis, deg
ALPSTAR	α_*	Aerodynamic angle of attack, deg
ALPHTIP	α'_{TIP}	Tip flow angle, deg
H	h	Trailing-edge bluntness, m
PSI	Ψ	Trailing-edge angle, deg
U	U	Free-stream velocity, m/sec
ITRIP		0—Use untripped BL condition 1—Use tripped BL condition 2—Use lightly tripped BL condition
ILAM		1—Compute LBL-VS noise 0—Do not compute LBL-VS noise
ITURB		1—Compute turbulent TBL-TE noise 0—Do not compute TBL-TE noise
IBLUNT		1—Compute TE bluntness noise 0—Do not compute TE bluntness noise
ITIP		1—Compute tip noise 0—Do not compute tip noise
IROUND		.TRUE.—Use rounded tip in tip calculation .FALSE.—Use square tip in tip calculation
VISC	ν	Kinematic viscosity, m^2/sec
CO	c_o	Speed of sound, m/sec

The prediction shown in figure 45(a) was obtained using the following input:

```
$INDATA
  NSEG    = 1,
  C       = .3048,
  L       = .4572,
  R       = 1.22,
  THETA   = 90.,
  PHI     = 90.,
  ALPSTAR = 1.516,
  U       = 71.3,
  ITRIP   = 0,
  ILAM    = 1,
  ITURB   = 1,
$END
```

Note that all parameters need not be included in the input if their default values are desired (see program listing for default values). In this example, only the laminar and turbulent mechanisms are computed and the untripped boundary layer condition is used in both mechanisms. The airfoil consists of one segment of constant chord and the observer is 122 cm directly beneath the trailing edge at the midspan. The free-stream velocity has a constant value of 71.3 m/sec across the span. For this example, the output file is given in table D2.

Similarly, the prediction shown in figure 91, was obtained using the following input:

```
$INDATA
  NSEG    = 10.,
  C       = 10*.1524
  L       = 10*.0305
  R       = 10* 1.22,
  THETA   = 10* 90.,
  PHI     = 10* 90.,
  ALPSTAR = 10* 5.4,
  ALPHTIP = 7.7,
  U       = 10* 71.3,
  ITRIP   = 1,
  ILAM    = 0,
  ITURB   = 1,
  ITIP    = 1,
  ROUND   = .TRUE.,
$END
```

This is an example of a multisegmented case where each segment has the same geometry and inflow conditions. Turbulent-boundary-layer noise and tip noise are calculated where the tip is rounded and at an effective angle of attack of 7.7°. All segments are summed to yield a total prediction for each mechanism as shown in table D3.

For the VAX-11/780 machine running under VMS, the following commands will compile, link, and execute the code (assumed to reside on PREDICT.FOR), read input from a file EXAMPLE.IN, and write results to a file EXAMPLE.OUT:

```
$ FOR PREDICT
$ LINK PREDICT
$ ASSIGN EXAMPLE.IN FOR004
$ ASSIGN EXAMPLE.OUT FOR005
$ RUN PREDICT
```

The details of execution for other machines or operating systems may vary. A listing of the code follows.

Table D2. Output File From Prediction Code for Test Case of Figure 45(a)

ONE-THIRD OCTAVE
SOUND PRESSURE LEVELS

FREQUENCY(HZ)	PRESSURE SIDE TBL	SUCTION SIDE TBL	SEPARATION SIDE TBL	LAMINAR	BLUNTNESS	TIP	TOTAL
100.000	20.654	28.704	-100.000	-17.142	0.000	0.000	29.336
125.000	24.461	31.965	-100.000	-13.285	0.000	0.000	32.676
160.000	28.291	35.244	-75.254	-9.018	0.000	0.000	36.042
200.000	31.437	37.937	-49.243	-5.161	0.000	0.000	38.815
250.000	34.309	40.400	-27.506	-1.304	0.000	0.000	41.356
315.000	37.023	42.736	-9.030	2.690	0.000	0.000	43.768
400.000	39.577	44.949	6.266	6.820	0.000	0.000	46.057
500.000	41.761	46.859	17.532	10.677	0.000	0.000	48.034
630.000	43.845	48.706	26.603	14.671	0.000	0.000	49.954
800.000	45.839	50.503	33.718	18.801	0.000	0.000	51.849
1000.000	47.581	52.106	38.756	22.658	0.000	0.000	53.568
1250.000	49.233	53.664	42.692	26.515	0.000	0.000	55.255
1600.000	50.987	55.368	46.294	30.782	0.000	0.000	57.106
2000.000	52.533	56.907	49.334	37.725	0.000	0.000	58.817
2500.000	54.074	57.750	51.298	47.262	0.000	0.000	60.167
3150.000	55.570	57.500	50.766	48.959	0.000	0.000	60.496
4000.000	56.044	56.082	47.711	41.796	0.000	0.000	59.455
5000.000	55.399	54.541	44.617	32.428	0.000	0.000	58.208
6300.000	53.840	52.942	40.974	28.433	0.000	0.000	56.553
8000.000	52.190	51.253	36.227	24.304	0.000	0.000	54.821
10000.000	50.638	49.614	30.419	20.447	0.000	0.000	53.192
12500.000	49.044	47.890	22.834	16.590	0.000	0.000	51.523
16000.000	47.202	45.851	11.842	12.323	0.000	0.000	49.591
20000.000	45.436	43.863	-0.924	8.466	0.000	0.000	47.731
25000.000	43.549	41.710	-16.833	4.609	0.000	0.000	45.737
31500.000	41.440	39.279	-37.092	0.614	0.000	0.000	43.503
40000.000	39.065	36.522	-62.593	-3.515	0.000	0.000	40.987

Table D3. Output File From Prediction Code for Test Case of Figure 91

ONE-THIRD OCTAVE
SOUND PRESSURE LEVELS

FREQUENCY(HZ)	PRESSURE SIDE TBL	SUCTION SIDE TBL	SEPARATION SIDE TBL	LAMINAR	BLUNTNESS	TIP	TOTAL
100.000	19.913	43.883	-19.803	0.000	0.000	-34.005	43.900
125.000	23.788	46.159	-0.396	0.000	0.000	-24.312	46.184
160.000	27.673	48.459	16.851	0.000	0.000	-14.255	48.498
200.000	30.853	50.372	29.124	0.000	0.000	-5.769	50.452
250.000	33.746	52.155	38.723	0.000	0.000	2.145	52.407
315.000	36.470	53.894	46.334	0.000	0.000	9.738	54.662
400.000	39.024	55.609	52.245	0.000	0.000	16.940	57.320
500.000	41.202	57.165	56.460	0.000	0.000	23.074	59.897
630.000	43.274	58.766	59.996	0.000	0.000	28.824	62.489
800.000	45.252	60.360	63.297	0.000	0.000	34.121	65.130
1000.000	46.980	60.940	65.719	0.000	0.000	38.475	67.016
1250.000	48.620	60.473	65.697	0.000	0.000	42.257	66.917
1600.000	50.364	58.874	62.909	0.000	0.000	45.774	64.582
2000.000	51.911	57.328	59.818	0.000	0.000	48.349	62.363
2500.000	53.456	55.775	56.383	0.000	0.000	50.351	60.580
3150.000	54.709	54.122	51.975	0.000	0.000	51.821	59.364
4000.000	54.799	52.336	45.974	0.000	0.000	52.694	58.443
5000.000	53.761	50.565	38.550	0.000	0.000	52.917	57.439
6300.000	52.162	48.597	28.510	0.000	0.000	52.544	56.204
8000.000	50.507	46.387	15.081	0.000	0.000	51.512	54.736
10000.000	48.936	44.132	-0.755	0.000	0.000	49.955	53.078
12500.000	47.311	41.665	-20.241	0.000	0.000	47.826	51.110
16000.000	45.415	38.655	-46.603	0.000	0.000	44.802	48.594
20000.000	43.583	35.650	-75.275	0.000	0.000	41.466	46.075
25000.000	41.611	32.347	-90.000	0.000	0.000	37.557	43.405
31500.000	39.390	28.582	-90.000	0.000	0.000	32.904	40.555
40000.000	36.873	24.291	-90.000	0.000	0.000	27.449	37.552

```
      PROGRAM PREDICT


C                 ------------------------------
C                 ***** VARIABLE DEFINITIONS *****
C                 ------------------------------

C        VARIABLE NAME              DEFINITION                    UNITS
C        -------------              ----------                    -----

C        ALPHTIP          TIP ANGLE OF ATTACK                DEGREES
C        ALPSTAR          SEGMENT ANGLE OF ATTACK            DEGREES
C        ALPRAT           TIP LIFT CURVE SLOPE               ---
C        C                SEGMENT CHORDLENGTH                METERS
C        C0               SPEED OF SOUND                     METERS/SEC
C        FRCEN            1/3 OCTAVE CENTERED FREQUENCIES    HERTZ
C        H                SEGMENT TRAILING EDGE THICKNESS    METERS
C        IBLUNT           FLAG TO COMPUTE BLUNTNESS NOISE    ---
C        ILAM             FLAG TO COMPUTE LBL NOISE          ---
C        ITIP             FLAG TO COMPUTE TIP NOISE          ---
C        ITRIP            FLAG TO TRIP BOUNDARY LAYER        ---
C        ITURB            FLAG TO COMPUTE TBLTE NOISE        ---
C        L                SEGMENT SPAN LENGTH                METERS
C        MAXFREQ          MAXIMUM NUMBER OF FREQUENCIES      ---
C        MAXSEG           MAXIMUM NUMBER OF SEGMENTS         ---
C        NFREQ            NUMBER OF 1/3 OCTAVE FREQUENCIES   ---
C        NSEG             NUMBER OF SEGMENTS                 ---
C        P1               PRESSURE ASSOCIATED WITH
C                           TBLTE PREDICTION                 NT/M2
C        P2               PRESSURE ASSOCIATED WITH
C                           TBLTE PREDICTION                 NT/M2
C        P3               PRESSURE ASSOCIATED WITH
C                           TBLTE PREDICTION                 NT/M2
C        P4               PRESSURE ASSOCIATED WITH
C                           TOTAL PREDICTION                 NT/M2
C        P5               PRESSURE ASSOCIATED WITH
C                           LBLVS PREDICTION                 NT/M2
C        P6               PRESSURE ASSOCIATED WITH
C                           BLUNTNESS PREDICTION             NT/M2
C        P7               PRESSURE ASSOCIATED WITH
C                           TIP NOISE PREDICTION             NT/M2
C        PHI              DIRECTIVITY ANGLE                  DEGREES
C        PSI              BLUNTNESS ANGLE                    DEGREES
C        R                SEGMENT TO OBSERVER DISTANCE       METERS
C        ROUND            LOGICAL INDICATING ROUNDED TIP     ---
C        SPL              TOTAL SOUND PRESSURE LEVEL         DB
C        SPLALPH          SOUND PRESSURE LEVEL ASSOCIATED
C                           WITH TBLTE PREDICTION            DB
C        SPLBLNT          SOUND PRESSURE LEVEL ASSOCIATED
C                           WITH BLUNTNESS PREDICTION        DB
C        SPLLBL           SOUND PRESSURE LEVEL ASSOCIATED
C                           WITH LBL PREDICTION              DB
C        SPLP             SOUND PRESSURE LEVEL ASSOCIATED
C                           WITH TBLTE PREDICTION            DB
C        SPLS             SOUND PRESSURE LEVEL ASSOCIATED
C                           WITH TBLTE PREDICTION            DB
C        SPLTBL           TOTAL PRESSURE LEVEL ASSOCIATED
C                           WITH TBLTE PREDICTION            DB
C        SPLTIP           SOUND PRESSURE LEVEL ASSOCIATED
C                           WITH TIP NOISE PREDICTION        DB
C        ST               STROUHAL NUMBER                    --
C        THETA            DIRECTIVITY ANGLE                  DEGREES
C        U                SEGMENT FREESTREAM VELOCITY        METERS/SEC
C        VISC             KINEMATIC VISCOSITY                M2/SEC


      PARAMETER (MAXSEG = 20, MAXFREQ = 27)


      DIMENSION     FRCEN(MAXFREQ)    ,C(MAXSEG)         ,L(MAXSEG)         ,
     1              ST(MAXFREQ)       ,SPLLBL(MAXFREQ)   ,SPLTBL(MAXFREQ)   ,
     2              U(MAXSEG)         ,SPLP(MAXFREQ)     ,SPLS(MAXFREQ)     ,
     3              SPLALPH(MAXFREQ)  ,SPL(7,MAXFREQ)    ,R(MAXSEG)         ,
     5              SPLBLNT(MAXFREQ)  ,PHI(MAXSEG)       ,SPLTIP(MAXFREQ)   ,
     7              THETA(MAXSEG)     ,ALPSTAR(MAXSEG)   ,PSI(MAXSEG)       ,
```

```
     8              H(MAXSEG)        ,P1(MAXFREQ)      ,P2(MAXFREQ)     ,
     9              P3(MAXFREQ)      ,P4(MAXFREQ)      ,P5(MAXFREQ)     ,
     1              P6(MAXFREQ)      ,P7(MAXFREQ)


      REAL          L
      LOGICAL       ROUND

C    DEFINE DEFAULT VALUES FOR NAMELIST DATA
C    ---------------------------------------


      DATA C        /  MAXSEG*1.0     /
      DATA L        /  MAXSEG*.10     /
      DATA R        /  MAXSEG * 1.    /
      DATA THETA    /  MAXSEG * 90.   /
      DATA PHI      /  MAXSEG * 90.   /
      DATA ALPSTAR  /  MAXSEG * 0.0   /
      DATA H        /  MAXSEG * .0005/
      DATA PSI      /  MAXSEG * 14.0 /
      DATA U        /  MAXSEG * 100. /
      DATA ITRIP    /   0        /
      DATA ILAM     /   0        /
      DATA ITURB    /   0        /
      DATA IBLUNT   /   0        /
      DATA ITIP     /   0        /
      DATA ALPHTIP  /   0.0      /
      DATA NSEG     /  10        /
      DATA VISC     / 1.4529E-5  /
      DATA C0       /  340.46    /
      DATA ALPRAT   /   1.0      /
      DATA ROUND    /  .FALSE.  /

      DATA NFREQ    /   27       /

C     SET UP VALUES OF 1/3 OCTAVE CENTERED FREQUENCIES
C     ------------------------------------------------

      DATA FRCEN / 100.    ,  125.    ,  160.    ,  200.    ,  250.    ,
     1             315.    ,  400.    ,  500.    ,  630.    ,  800.    ,
     1            1000.    , 1250.    , 1600.    , 2000.    , 2500.    ,
     3            3150.    , 4000.    , 5000.    , 6300.    , 8000.    ,
     2           10000.    ,12500.    ,16000.    ,20000.    ,25000.    ,
     3           31500.    ,40000.    /


      NAMELIST /INDATA / C        ,L        ,R        ,
     1                   THETA    ,PHI      ,ALPSTAR  ,
     2                   H        ,PSI      ,U        ,
     1                   ITRIP    ,ILAM     ,ITURB    ,
     2                   IBLUNT   ,ITIP     ,ROUND    ,
     3                   ALPHTIP  ,NSEG     ,C0       ,
     4                   VISC



C      READ IN NAMELIST DATA AND ECHO INPUT TO OUTPUT FILE
C      ---------------------------------------------------

      OPEN(UNIT=4, STATUS = 'OLD')
      READ(4,INDATA)

      OPEN(UNIT=5, STATUS = 'NEW')
      WRITE(5,INDATA)


C      INITIALIZE ALL PREDICTED PRESSURES AND SOUND
C      PRESSURE LEVELS TO ZERO
C      --------------------------------------------

      DO 6001 I=1,NFREQ
        P1(I) = 0.0
        P2(I) = 0.0
        P3(I) = 0.0
        P4(I) = 0.0
```

```
          P5(I) = 0.0
          P6(I) = 0.0
          P7(I) = 0.0

          DO 6002 J=1,7
            SPL(J,I) = 0.0
 6002     CONTINUE
 6001   CONTINUE


C       FOR EACH BLADE SEGMENT, MAKE A NOISE PREDICTION ACCORDING
C       TO THE MECHANISMS SELECTED. TIP NOISE IS PREDICTED FOR
C       THE LAST SEGMENT ONLY.
C       ---------------------------------------------------------

        DO 6000 III=1,NSEG

          IF (ILAM .EQ. 1)
     1      CALL LBLVS(ALPSTAR(III),C(III),U(III),FRCEN,SPLLBL,
     2                THETA(III),PHI(III),L(III),R(III),NFREQ,
     3                VISC,C0)

          IF (ITURB .EQ. 1)
     1     CALL TBLTE(ALPSTAR(III),C(III),U(III),FRCEN,ITRIP,SPLP,
     1               SPLS,SPLALPH,SPLTBL,THETA(III),PHI(III),L(III),R(III),
     2               NFREQ,VISC,C0)

          IF (IBLUNT .EQ. 1)
     1      CALL BLUNT(ALPSTAR(III),C(III),U(III),FRCEN,ITRIP,SPLBLNT,
     1                THETA(III),PHI(III),L(III),R(III),H(III),PSI(III),
     2                NFREQ,VISC,C0)

          IF ((ITIP .EQ. 1) .AND. (III .EQ. NSEG))
     1      CALL TIPNOIS(ALPHTIP,ALPRAT,C(III),U(III),FRCEN,SPLTIP,
     2                    THETA,PHI,R(III),NFREQ,VISC,C0,ROUND)


C        ADD IN THIS SEGMENT'S CONTRIBUTION ON A MEAN-SQUARE
C        PRESSURE BASIS
C        ---------------------------------------------------

          DO 989 I=1,NFREQ

            IF (ILAM .EQ. 1) THEN
              P5(I) = P5(I) + 10.**(SPLLBL(I)/10.)
            ENDIF

            IF (ITURB .EQ. 1) THEN
              P1(I) = P1(I) + 10.**(SPLP(I)/10.)
              P2(I) = P2(I) + 10.**(SPLS(I)/10.)
              P3(I) = P3(I) + 10.**(SPLALPH(I)/10.)
            ENDIF

            IF (IBLUNT .EQ. 1) THEN
              P6(I) = P6(I) + 10.**(SPLBLNT(I)/10.)
            ENDIF

            IF ((ITIP .EQ. 1) .AND. (III .EQ. NSEG)) THEN
              P7(I) = P7(I) + 10.**(SPLTIP(I)/10.)
            ENDIF


C        COMPUTE TOTAL PRESSURE FOR THE SEGMENT FOR ALL MECHANISMS
C        ---------------------------------------------------------

            P4(I) = P1(I) + P2(I) + P3(I) + P5(I) + P6(I) + P7(I)

  989     CONTINUE
 6000   CONTINUE

C        CONTRIBUTIONS FROM ALL SEGMENTS ARE NOW ACCOUNTED FOR.
C        COMPUTE SOUND PRESSURE LEVELS FOR EACH MECHANISM AND
C        FOR THE TOTAL
C        ---------------------------------------------------

```

```
      DO 6003 I=1,NFREQ
        IF (P1(I) .NE. 0.) SPL(1,I) = 10.*ALOG10(P1(I))
        IF (P2(I) .NE. 0.) SPL(2,I) = 10.*ALOG10(P2(I))
        IF (P3(I) .NE. 0.) SPL(3,I) = 10.*ALOG10(P3(I))
        IF (P4(I) .NE. 0.) SPL(4,I) = 10.*ALOG10(P4(I))
        IF (P5(I) .NE. 0.) SPL(5,I) = 10.*ALOG10(P5(I))
        IF (P6(I) .NE. 0.) SPL(6,I) = 10.*ALOG10(P6(I))
        IF (P7(I) .NE. 0.) SPL(7,I) = 10.*ALOG10(P7(I))
 6003 CONTINUE


C       WRITE OUTPUT FILE
C       -----------------

      WRITE(5,7000)

      DO 6005 I=1,NFREQ

        WRITE(5,7100) FRCEN(I),(SPL(J,I),J=1,3),(SPL(J,I),J=5,7),
     1                         SPL(4,I)
        IF (MOD(I,5) .EQ. 0) WRITE(5,7200)
 6005 CONTINUE

 7000 FORMAT(1H1,52X,'ONE-THIRD OCTAVE',/,50X,'SOUND PRESSURE LEVELS'
     1       ////,5X,'                ','   PRESSURE    ',
     2                  '    SUCTION    ','  SEPARATION   '/,
     3             5X,' FREQUENCY(HZ) ','   SIDE TBL    ',
     4                 '   SIDE TBL    ','   SIDE TBL    ',
     5                 '    LAMINAR    ','  BLUNTNESS    ',
     6                 '      TIP      ','    TOTAL      ',
     7                 /,5X,8('-------------- '),/)

 7100 FORMAT(8F15.3)
 7200 FORMAT(' ')
 8000 FORMAT(I3)
 8002 FORMAT(4I10)


      STOP
      END
```

```
      SUBROUTINE LBLVS(ALPSTAR,C,U ,FRCEN,SPLLAM,THETA,PHI,L,R,
     1                 NFREQ,VISC,C0)

      PARAMETER (MAXFREQ = 27)



C             -------------------------------
C             ***** VARIABLE DEFINITIONS *****
C             -------------------------------

C       VARIABLE NAME                DEFINITION                  UNITS
C       -------------                ----------                  -----


C       ALPSTAR             ANGLE OF ATTACK                    DEGREES
C       C                   CHORD LENGTH                       METERS
C       C0                  SPEED OF SOUND                     METERS/SEC
C       D                   REYNOLDS NUMBER RATIO              ---
C       DBARH               HIGH FREQUENCY DIRECTIVITY         ---
C       DELTAP              PRESSURE SIDE BOUNDARY LAYER
C                             THICKNESS                        METERS
C       DSTRP               PRESSURE SIDE BOUNDARY LAYER
C                             DISPLACEMENT THICKNESS           METERS
C       DSTRS               SUCTION SIDE BOUNDARY LAYER
C                             DISPLACEMENT THICKNESS           METERS
C       E                   STROUHAL NUMBER RATIO              ---
C       FRCEN               1/3 OCTAVE FREQUENCIES             HERTZ
C       G1                  SOUND PRESSURE LEVEL FUNCTION      DB
C       G2                  OVERALL SOUND PRESSURE LEVEL
C                             FUNCTION                         DB
C       G3                  OVERALL SOUND PRESSURE LEVEL
C                             FUNCTION                         DB
C       ITRIP               FLAG TO TRIP BOUNDARY LAYER        ---
C       L                   SPAN                               METERS
C       M                   MACH NUMBER                        ---
C       NFREQ               NUMBER OF FREQUENCIES              ---
C       OASPL               OVERALL SOUND PRESSURE LEVEL       DB
C       PHI                 DIRECTIVITY ANGLE                  DEGREES
C       R                   OBSERVER DISTANCE FROM SEGMENT     METERS
C       RC                  REYNOLDS NUMBER BASED ON CHORD     ---
C       RC0                 REFERENCE REYNOLDS NUMBER          ---
C       SCALE               GEOMETRIC SCALING TERM
C       SPLLAM              SOUND PRESSURE LEVEL DUE TO
C                             LAMINAR MECHANISM                DB
C       STPRIM              STROUHAL NUMBER BASED ON PRESSURE
C                             SIDE BOUNDARY LAYER THICKNESS    ---
C       ST1PRIM             REFERENCE STROUHAL NUMBER          ---
C       STPKPRM             PEAK STROUHAL NUMBER               ---
C       THETA               DIRECTIVITY ANGLE                  DEGREES
C       U                   FREESTREAM VELOCITY                METERS/SEC
C       VISC                KINEMATIC VISCOSITY                M2/SEC



      DIMENSION STPRIM(MAXFREQ)  ,SPLLAM(MAXFREQ)    ,FRCEN(MAXFREQ)

      REAL      L                 ,M


C      COMPUTE REYNOLDS NUMBER AND MACH NUMBER
C      ---------------------------------------

      M         = U  / C0
      RC        = U  * C/VISC


C      COMPUTE BOUNDARY LAYER THICKNESSES
C      ----------------------------------

      CALL THICK(C,U ,ALPSTAR,ITRIP,DELTAP,DSTRS,DSTRP,C0,VISC)



C      COMPUTE DIRECTIVITY FUNCTION
```

```
C        ----------------------------

         CALL DIRECTH(M,THETA,PHI,DBARH)

C        COMPUTE REFERENCE STROUHAL NUMBER
C        ---------------------------------

         IF (RC .LE. 1.3E+05) ST1PRIM = .18
         IF((RC .GT. 1.3E+05).AND.(RC.LE.4.0E+05))ST1PRIM=.001756*RC**.3931
         IF (RC .GT. 4.0E+05) ST1PRIM = .28

         STPKPRM  = 10.**(-.04*ALPSTAR) * ST1PRIM

C        COMPUTE REFERENCE REYNOLDS NUMBER
C        ---------------------------------

         IF (ALPSTAR .LE. 3.0) RC0=10.**(.215*ALPSTAR+4.978)
         IF (ALPSTAR .GT. 3.0) RC0=10.**(.120*ALPSTAR+5.263)

C        COMPUTE PEAK SCALED SPECTRUM LEVEL
C        ----------------------------------

         D   = RC / RC0

         IF (D .LE. .3237) G2=77.852*ALOG10(D)+15.328
         IF ((D .GT. .3237).AND.(D .LE. .5689))
     1   G2 = 65.188*ALOG10(D) + 9.125
         IF ((D .GT. .5689).AND.(D .LE. 1.7579))
     1   G2 = -114.052 * ALOG10(D)**2.
         IF ((D .GT. 1.7579).AND.(D .LE. 3.0889))
     1   G2 = -65.188*ALOG10(D)+9.125
         IF (D .GT. 3.0889) G2 =-77.852*ALOG10(D)+15.328

         G3      = 171.04 - 3.03 * ALPSTAR

         SCALE   = 10. * ALOG10(DELTAP*M**5*DBARH*L/R**2)

C        COMPUTE SCALED SOUND PRESSURE LEVELS FOR EACH STROUHAL NUMBER
C        -------------------------------------------------------------

         DO 100 I=1,NFREQ

            STPRIM(I)  = FRCEN(I) * DELTAP / U

            E          = STPRIM(I) / STPKPRM

            IF (E .LT. .5974) G1=39.8*ALOG10(E)-11.12
            IF ((E .GE. .5974).AND.(E .LE. .8545))
     1         G1 = 98.409 * ALOG10(E) + 2.0
            IF ((E .GE. .8545).AND.(E .LT. 1.17))
     1         G1 = -5.076+SQRT(2.484-506.25*(ALOG10(E))**2.)
            IF ((E .GE. 1.17).AND.(E .LT. 1.674))
     1         G1 = -98.409 * ALOG10(E) + 2.0
            IF (E .GE. 1.674) G1=-39.80*ALOG10(E)-11.12

            SPLLAM(I) = G1 + G2 + G3 + SCALE

  100    CONTINUE

         RETURN
         END
```

```
      SUBROUTINE TBLTE(ALPSTAR,C,U ,FRCEN,ITRIP,SPLP,SPLS,
     1               SPLALPH,SPLTBL,THETA,PHI,L,R,NFREQ,VISC,C0)



C                  -------------------------------
C                  ***** VARIABLE DEFINITIONS *****
C                  -------------------------------



C        VARIABLE NAME                DEFINITION                UNITS
C        -------------                ----------                -----

C        A                  STROUHAL NUMBER RATIO                ---
C        A0                 FUNCTION USED IN 'A' CALCULATION     ---
C        A02                FUNCTION USED IN 'A' CALCULATION     ---
C        AA                 'A' SPECTRUM SHAPE EVALUATED AT
C                              STROUHAL NUMBER RATIO             DB
C        ALPSTAR            ANGLE OF ATTACK                    DEGREES
C        AMAXA              MAXIMUM 'A' CURVE EVALUATED AT
C                             STROUHAL NUMBER RATIO              DB
C        AMAXA0             MAXIMUM 'A' CURVE EVALUATED AT A0    DB
C        AMAXA02            MAXIMUM 'A' CURVE EVALUATED AT A02   DB
C        AMAXB              MAXIMUM 'A' CURVE EVALUATED AT B     DB
C        AMINA              MINIMUM 'A' CURVE EVALUATED AT
C                             STROUHAL NUMBER RATIO              DB
C        AMINA0             MINIMUM 'A' CURVE EVALUATED AT A0    DB
C        AMINA02            MINIMUM 'A' CURVE EVALUATED AT A02   DB
C        AMINB              MINIMUM 'A' CURVE EVALUATED AT B     DB
C        ARA0               INTERPOLATION FACTOR                 ---
C        ARA02              INTERPOLATION FACTOR                 ---
C        B                  STROUHAL NUMBER RATIO                ---
C        B0                 FUNCTION USED IN 'B' CALCULATION     ---
C        BB                 'B' SPECTRUM SHAPE EVALUATED AT
C                             STROUHAL NUMBER RATIO              DB
C        BETA               USED IN 'B' COMPUTATION              ---
C        BETA0              USED IN 'B' COMPUTATION              ---
C        BMAXB              MAXIMUM 'B' EVALUATED AT B           DB
C        BMAXB0             MAXIMUM 'B' EVALUATED AT B0          DB
C        BMINB              MINIMUM 'B' EVALUATED AT B           DB
C        BMINB0             MINIMUM 'B' EVALUATED AT B0          DB
C        BRB0               INTERPOLATION FACTOR                 DB
C        C                  CHORD LENGTH                         METERS
C        C0                 SPEED OF SOUND                     METERS/SEC
C        DBARH              HIGH FREQUENCY DIRECTIVITY           ---
C        DBARL              LOW FREQUENCY DIRECTIVITY            ---
C        DELK1              CORRECTION TO AMPLITUDE FUNCTION     DB
C        DELTAP             PRESSURE SIDE BOUNDARY LAYER THICKNESS METERS
C        DSTRP              PRESSURE SIDE DISPLACEMENT THICKNESS  METERS
C        DSTRS              SUCTION SIDE DISPLACEMENT THICKNESS   METERS
C        FRCEN              ARRAY OF CENTERED FREQUENCIES        HERTZ
C        GAMMA              USED IN 'B' COMPUTATION              ---
C        GAMMA0             USED IN 'B' COMPUTATION              ---
C        ITRIP              TRIGGER TO TRIP BOUNDARY LAYER       ---
C        K1                 AMPLITUDE FUNCTION                   DB
C        K2                 AMPLITUDE FUNCTION                   DB
C        L                  SPAN                                 METERS
C        M                  MACH NUMBER                          ---
C        NFREQ              NUMBER OF CENTERED FREQUENCIES       ---
C        PHI                DIRECTIVITY ANGLE                   DEGREES
C        P1                 PRESSURE SIDE PRESSURE              NT/M2
C        P2                 SUCTION SIDE PRESSURE               NT/M2
C        P4                 PRESSURE FROM ANGLE OF ATTACK
C                             CONTRIBUTION                      NT/M2
C        R                  SOURCE TO OBSERVER DISTANCE          METERS
C        RC                 REYNOLDS NUMBER BASED ON  CHORD      ---
C        RDSTRP             REYNOLDS NUMBER BASED ON PRESSURE
C                             SIDE DISPLACEMENT THICKNESS        ---
C        RDSTRS             REYNOLDS NUMBER BASED ON SUCTION
C                             SIDE DISPLACEMENT THICKNESS        ---
C        SPLALPH            SOUND PRESSURE LEVEL DUE TO ANGLE OF
C                             ATTACK CONTRIBUTION                DB
C        SPLP               SOUND PRESSURE LEVEL DUE TO PRESSURE
C                             SIDE OF AIRFOIL                    DB
```

```
C        SPLS                  SOUND PRESSURE LEVEL DUE TO SUCTION
C                                SIDE OF AIRFOIL                       DB
C        SPLTBL                TOTAL SOUND PRESSURE LEVEL DUE TO
C                                TBLTE MECHANISM                       DB
C        STP                   PRESSURE SIDE STROUHAL NUMBER           ---
C        STS                   SUCTION SIDE STROUHAL NUMBER            ---
C        ST1                   PEAK STROUHAL NUMBER                    ---
C        ST1PRIM               PEAK STROUHAL NUMBER                    ---
C        ST2                   PEAK STROUHAL NUMBER                    ---
C        STPEAK                PEAK STROUHAL NUMBER                    ---
C        SWITCH                LOGICAL FOR COMPUTATION OF ANGLE
C                                OF ATTACK CONTRIBUTION                ---
C        THETA                 DIRECTIVITY ANGLE                     DEGREES
C        U                     VELOCITY                             METERS/SEC
C        VISC                  KINEMATIC VISCOSITY                   M2/SEC
C        XCHECK                USED TO CHECK FOR ANGLE OF ATTACK
C                                CONTRIBUTION                          ---
C

      PARAMETER (MAXFREQ = 27)


      DIMENSION SPLTBL(MAXFREQ)  ,SPLP(MAXFREQ)     ,SPLS(MAXFREQ)  ,
     1          SPLALPH(MAXFREQ) ,STP(MAXFREQ)      ,
     1          STS(MAXFREQ)     ,FRCEN(MAXFREQ)

      LOGICAL SWITCH
      REAL    L,M,K1,K2

      RC        = U  * C / VISC
      M         = U  / C0


C      COMPUTE BOUNDARY LAYER THICKNESSES
C      ----------------------------------

      CALL THICK(C,U ,ALPSTAR,ITRIP,DELTAP,DSTRS,DSTRP,C0,VISC)

C     COMPUTE DIRECTIVITY FUNCTION
C     ----------------------------

      CALL DIRECTL(M,THETA,PHI,DBARL)
      CALL DIRECTH(M,THETA,PHI,DBARH)


C     CALCULATE THE REYNOLDS NUMBERS BASED ON PRESSURE AND
C     SUCTION DISPLACEMENT THICKNESS
C     ---------------------------------------------------

      RDSTRS = DSTRS * U  / VISC
      RDSTRP = DSTRP * U  / VISC

C      DETERMINE PEAK STROUHAL NUMBERS TO BE USED FOR
C      'A' AND 'B' CURVE CALCULATIONS
C      ----------------------------------------------

      ST1    = .02 * M ** (-.6)

      IF (ALPSTAR .LE. 1.333) ST2 = ST1
      IF ((ALPSTAR .GT. 1.333).AND.(ALPSTAR .LE. 12.5))
     1   ST2 = ST1*10.**(.0054*(ALPSTAR-1.333)**2.)
      IF (ALPSTAR .GT. 12.5) ST2 = 4.72 * ST1


      ST1PRIM = (ST1+ST2)/2.


      CALL A0COMP(RC,A0)
      CALL A0COMP(3.*RC,A02)

C      EVALUATE MINIMUM AND MAXIMUM 'A' CURVES AT A0
C      ---------------------------------------------

      CALL AMIN(A0,AMINA0)
      CALL AMAX(A0,AMAXA0)
```

```
      CALL AMIN(A02,AMINA02)
      CALL AMAX(A02,AMAXA02)

C       COMPUTE 'A' MAX/MIN RATIO
C       -------------------------

      ARA0  = (20. + AMINA0) / (AMINA0 - AMAXA0)
      ARA02 = (20. + AMINA02)/ (AMINA02- AMAXA02)

C       COMPUTE B0 TO BE USED IN 'B' CURVE CALCALCULATIONS
C       -------------------------------------------------

      IF (RC .LT. 9.52E+04) B0 = .30
      IF ((RC .GE. 9.52E+04).AND.(RC .LT. 8.57E+05))
     1    B0 = (-4.48E-13)*(RC-8.57E+05)**2. + .56
      IF (RC .GE. 8.57E+05) B0 = .56

C       EVALUATE MINIMUM AND MAXIMUM 'B' CURVES AT B0
C       ----------------------------------------------

      CALL BMIN(B0,BMINB0)
      CALL BMAX(B0,BMAXB0)

C       COMPUTE 'B' MAX/MIN RATIO
C       -------------------------

      BRB0  = (20. + BMINB0) / (BMINB0 - BMAXB0)

C       FOR EACH CENTER FREQUENCY, COMPUTE AN
C       'A' PREDICTION FOR THE PRESSURE SIDE
C       -------------------------------------

      STPEAK = ST1

      DO 100 I=1,NFREQ
        STP(I) = FRCEN(I) * DSTRP / U
        A      = ALOG10( STP(I) / STPEAK )
        CALL AMIN(A,AMINA)
        CALL AMAX(A,AMAXA)
        AA     = AMINA + ARA0 * (AMAXA - AMINA)

        IF (RC .LT. 2.47E+05) K1 = -4.31 * ALOG10(RC) + 156.3
        IF((RC .GE. 2.47E+05).AND.(RC .LT. 8.0E+05))
     1    K1 = -9.0 * ALOG10(RC) + 181.6
        IF (RC .GT. 8.0E+05) K1 = 128.5

        IF (RDSTRP .LE. 5000.) DELK1 = -ALPSTAR*(5.29-1.43*
     1    ALOG10(RDSTRP))
        IF (RDSTRP .GT. 5000.) DELK1 = 0.0

        SPLP(I)=AA+K1-3.+10.*ALOG10(DSTRP*M**5.*DBARH*L/R**2.)+DELK1



      GAMMA   = 27.094 * M +  3.31
      BETA    = 72.650 * M + 10.74
      GAMMA0  = 23.430 * M +  4.651
      BETA0   =-34.190 * M - 13.820

      IF (ALPSTAR .LE. (GAMMA0-GAMMA)) K2 = -1000.0
      IF ((ALPSTAR.GT.(GAMMA0-GAMMA)).AND.(ALPSTAR.LE.(GAMMA0+GAMMA)))
     1 K2=SQRT(BETA**2.-(BETA/GAMMA)**2.*(ALPSTAR-GAMMA0)**2.)+BETA0
      IF (ALPSTAR .GT. (GAMMA0+GAMMA)) K2 = -12.0

      K2 = K2 + K1



      STS(I) = FRCEN(I) * DSTRS / U

C       CHECK FOR 'A' COMPUTATION FOR SUCTION SIDE
C       ------------------------------------------

```

```
      XCHECK = GAMMA0
      SWITCH = .FALSE.
      IF ((ALPSTAR .GE. XCHECK).OR.(ALPSTAR .GT. 12.5))SWITCH=.TRUE.
      IF (.NOT. SWITCH) THEN
        A     = ALOG10( STS(I) / ST1PRIM )
        CALL AMIN(A,AMINA)
        CALL AMAX(A,AMAXA)
        AA = AMINA + ARA0 * (AMAXA - AMINA)

        SPLS(I) = AA+K1-3.+10.*ALOG10(DSTRS*M**5.*DBARH*
     1            L/R**2.)

C      'B' CURVE COMPUTATION
C       -------------------

        B = ABS(ALOG10(STS(I) / ST2))
        CALL BMIN(B,BMINB)
        CALL BMAX(B,BMAXB)
        BB = BMINB + BRB0 * (BMAXB-BMINB)
        SPLALPH(I)=BB+K2+10.*ALOG10(DSTRS*M**5.*DBARH*L/R**2.)

      ELSE

C       THE 'A' COMPUTATION IS DROPPED IF 'SWITCH' IS TRUE
C       --------------------------------------------------


        SPLS(I) = 0.0 + 10.*ALOG10(DSTRS*M**5.*DBARL*
     1              L/R**2.)
        SPLP(I) = 0.0 + 10.*ALOG10(DSTRS*M**5.*DBARL*
     1              L/R**2.)
        B = ABS(ALOG10(STS(I) / ST2))
        CALL AMIN(B,AMINB)
        CALL AMAX(B,AMAXB)
        BB = AMINB + ARA02 * (AMAXB-AMINB)
        SPLALPH(I)=BB+K2+10.*ALOG10(DSTRS*M**5.*DBARL*
     1           L/R**2.)
      ENDIF


C      SUM ALL CONTRIBUTIONS FROM 'A' AND 'B' ON BOTH
C      PRESSURE AND SUCTION SIDE ON A MEAN-SQUARE PRESSURE
C      BASIS
C      ---------------------------------------------------

      IF (SPLP(I)    .LT. -100.) SPLP(I)    = -100.
      IF (SPLS(I)    .LT. -100.) SPLS(I)    = -100.
      IF (SPLALPH(I) .LT. -100.) SPLALPH(I) = -100.

      P1  = 10.**(SPLP(I) / 10.)
      P2  = 10.**(SPLS(I) / 10.)
      P4  = 10.**(SPLALPH(I) / 10.)

      SPLTBL(I) = 10. * ALOG10(P1 + P2 + P4)

  100 CONTINUE

      RETURN
      END
```

```
      SUBROUTINE AMIN(A,AMINA)

C     THIS SUBROUTINE DEFINES THE CURVE FIT CORRESPONDING
C     TO THE A-CURVE FOR THE MINIMUM ALLOWED REYNOLDS NUMBER.
C

      X1 = ABS(A)

      IF (X1 .LE. .204) AMINA=SQRT(67.552-886.788*X1**2.)-8.219
      IF((X1 .GT. .204).AND.(X1 .LE. .244))AMINA=-32.665*X1+3.981
      IF (X1 .GT. .244)AMINA=-142.795*X1**3.+103.656*X1**2.-57.757*X1+6.006

      RETURN
      END
```

```
      SUBROUTINE AMAX(A,AMAXA)

C     THIS SUBROUTINE DEFINES THE CURVE FIT CORRESPONDING
C     TO THE A-CURVE FOR THE MAXIMUM ALLOWED REYNOLDS NUMBER.

      X1 = ABS(A)

      IF (X1 .LE. .13)AMAXA=SQRT(67.552-886.788*X1**2.)-8.219
      IF((X1 .GT. .13).AND.(X1 .LE. .321))AMAXA=-15.901*X1+1.098
      IF (X1 .GT. .321)AMAXA=-4.669*X1**3.+3.491*X1**2.-16.699*X1+1.149

      RETURN
      END
```

```
      SUBROUTINE BMIN(B,BMINB)

C     THIS SUBROUTINE DEFINES THE CURVE FIT CORRESPONDING
C     TO THE B-CURVE FOR THE MINIMUM ALLOWED REYNOLDS NUMBER.

      X1 = ABS(B)

      IF (X1 .LE. .13)BMINB=SQRT(16.888-886.788*X1**2.)-4.109
      IF((X1 .GT. .13).AND.(X1 .LE. .145))BMINB=-83.607*X1+8.138
      IF (X1.GT..145)BMINB=-817.81*X1**3.+355.21*X1**2.-135.024*X1+10.619

      RETURN
      END
```

```
      SUBROUTINE BMAX(B,BMAXB)

C     THIS SUBROUTINE DEFINES THE CURVE FIT CORRESPONDING
C     TO THE B-CURVE FOR THE MAXIMUM ALLOWED REYNOLDS NUMBER.

      X1 = ABS(B)

      IF (X1 .LE. .1) BMAXB=SQRT(16.888-886.788*X1**2.)-4.109
      IF((X1 .GT. .1).AND.(X1 .LE. .187))BMAXB=-31.313*X1+1.854
      IF (X1.GT..187)BMAXB=-80.541*X1**3.+44.174*X1**2.-39.381*X1+2.344

      RETURN
      END
```

```
      SUBROUTINE A0COMP(RC,A0)

C     THIS SUBROUTINE DETERMINES WHERE THE A-CURVE
C     TAKES ON A VALUE OF -20 dB.

      IF (RC .LT. 9.52E+04) A0 = .57
      IF ((RC .GE. 9.52E+04).AND.(RC .LT. 8.57E+05))
     1   A0 = (-9.57E-13)*(RC-8.57E+05)**2. + 1.13
      IF (RC .GE. 8.57E+05) A0 = 1.13
      RETURN
      END
```

```
      SUBROUTINE DIRECTH(M,THETA,PHI,DBAR)

C     THIS SUBROUTINE COMPUTES THE HIGH FREQUENCY
C     DIRECTIVITY FUNCTION FOR THE INPUT OBSERVER LOCATION

      REAL M,MC

      DEGRAD  = .017453

      MC     = .8 * M
      THETAR = THETA * DEGRAD
      PHIR   = PHI * DEGRAD

      DBAR=2.*SIN(THETAR/2.)**2.*SIN(PHIR)**2./((1.+M*COS(THETAR))*
     1      (1.+(M-MC)*COS(THETAR))**2.)
      RETURN
      END
```

```
      SUBROUTINE DIRECTL(M,THETA,PHI,DBAR)

C     THIS SUBROUTINE COMPUTES THE LOW FREQUENCY
C     DIRECTIVITY FUNCTION FOR THE INPUT OBSERVER LOCATION

      REAL M,MC

      DEGRAD  = .017453

      MC     = .8 * M
      THETAR = THETA * DEGRAD
      PHIR   = PHI * DEGRAD

      DBAR = (SIN(THETAR)*SIN(PHIR))**2/(1.+M*COS(THETAR))**4

      RETURN
      END
```

```
      SUBROUTINE BLUNT(ALPSTAR,C,U ,FRCEN,ITRIP,SPLBLNT,THETA,PHI,
     1                 L,R,H,PSI,NFREQ,VISC,C0)


C                  -------------------------------
C                  ***** VARIABLE DEFINITIONS *****
C                  -------------------------------

C       VARIABLE NAME                DEFINITION                  UNITS
C       -------------                ----------                  -----

C       ALPSTAR           ANGLE OF ATTACK                       DEGREES
C       ATERM             USED TO COMPUTE PEAK STROUHAL NO.      ---
C       C                 CHORD LENGTH                          METERS
C       C0                SPEED OF SOUND                        METERS/SEC
C       DBARH             HIGH FREQUENCY DIRECTIVITY             ---
C       DELTAP            PRESSURE SIDE BOUNDARY LAYER
C                           THICKNESS                            METERS
C       DSTARH            AVERAGE DISPLACEMENT THICKNESS
C                           OVER TRAILING EDGE BLUNTNESS         ---
C       DSTRAVG           AVERAGE DISPLACEMENT THICKNESS         METERS
C       DSTRP             PRESSURE SIDE DISPLACEMENT THICKNESS METERS
C       DSTRS             SUCTION SIDE DISPLACEMENT THICKNESS  METERS
C       ETA               RATIO OF STROUHAL NUMBERS              ---
C       FRCEN             ARRAY OF 1/3 OCTAVE CENTERED FREQ.   HERTZ
C       F4TEMP            G5 EVALUATED AT MINIMUM HDSTARP       DB
C       G4                SCALED SPECTRUM LEVEL                 DB
C       G5                SPECTRUM SHAPE FUNCTION               DB
C       G50               G5 EVALUATED AT PSI=0.0               DB
C       G514              G5 EVALUATED AT PSI=14.0              DB
C       H                 TRAILING EDGE BLUNTNESS              METERS
C       HDSTAR            BLUNTNESS OVER AVERAGE DISPLACEMENT
C                           THICKNESS                           ---
C       HDSTARL           MINIMUM ALLOWED VALUE OF HDSTAR       ---
C       HDSTARP           MODIFIED VALUE OF HDSTAR              ---
C       ITRIP             TRIGGER FOR BOUNDARY LAYER TRIPPING    ---
C       L                 SPAN                                  METERS
C       M                 MACH NUMBER                           ---
C       NFREQ             NUMBER OF CENTERED FREQUENCIES        ---
C       PHI               DIRECTIVITY ANGLE                    DEGREES
C       PSI               TRAILING EDGE ANGLE                  DEGREES
C       R                 SOURCE TO OBSERVER DISTANCE           METERS
C       RC                REYNOLDS NUMBER BASED ON CHORD        ---
C       SCALE             SCALING FACTOR                        ---
C       SPLBLNT           SOUND PRESSURE LEVELS DUE TO
C                           BLUNTNESS                            DB
C       STPEAK            PEAK STROUHAL NUMBER                  ---
C       STPPP             STROUHAL NUMBER                       ---
C       THETA             DIRECTIVITY ANGLE                     ---
C       U                 FREESTREAM VELOCITY                  METERS/SEC
C       VISC              KINEMATIC VISCOSITY                  M2/SEC


      PARAMETER (MAXFREQ = 27)

      DIMENSION SPLBLNT(MAXFREQ)  ,FRCEN(MAXFREQ)   ,STPPP(MAXFREQ)

      REAL M,L

C      COMPUTE NECESSARY QUANTITIES
C      ----------------------------

      M  = U /C0
      RC = U  * C / VISC


C      COMPUTE BOUNDARY LAYER THICKNESSES
C      ----------------------------------

      CALL THICK(C,U ,ALPSTAR,ITRIP,DELTAP,DSTRS,DSTRP,C0,VISC)

C      COMPUTE AVERAGE DISPLACEMENT THICKNESS
C      --------------------------------------

      DSTRAVG = (DSTRS + DSTRP) / 2.
```

```
      HDSTAR  = H / DSTRAVG

      DSTARH = 1. /HDSTAR

C      COMPUTE DIRECTIVITY FUNCTION
C      ----------------------------

      CALL DIRECTH(M,THETA,PHI,DBARH)


C      COMPUTE PEAK STROUHAL NUMBER
C      ----------------------------

      ATERM  = .212 - .0045 * PSI

      IF (HDSTAR .GE. .2)
     1   STPEAK    = ATERM / (1.+.235*DSTARH-.0132*DSTARH**2.)
      IF (HDSTAR .LT. .2)
     1   STPEAK    = .1 * HDSTAR + .095 - .00243 * PSI

C      COMPUTE SCALED SPECTRUM LEVEL
C      -----------------------------

      IF (HDSTAR .LE. 5.) G4=17.5*ALOG10(HDSTAR)+157.5-1.114*PSI
      IF (HDSTAR .GT. 5.) G4=169.7 - 1.114 * PSI


C      FOR EACH FREQUENCY, COMPUTE SPECTRUM SHAPE REFERENCED TO 0 DB
C      -------------------------------------------------------------

      DO 1000 I=1,NFREQ

        STPPP(I) = FRCEN(I) * H / U
        ETA      = ALOG10(STPPP(I)/STPEAK)

        HDSTARL = HDSTAR

        CALL G5COMP(HDSTARL,ETA,G514)

        HDSTARP = 6.724 * HDSTAR **2.-4.019*HDSTAR+1.107

        CALL G5COMP(HDSTARP,ETA,G50)


        G5 = G50 + .0714 * PSI * (G514-G50)
        IF (G5 .GT. 0.) G5 = 0.
        CALL G5COMP(.25,ETA,F4TEMP)
        IF (G5 .GT. F4TEMP) G5 = F4TEMP


        SCALE = 10. * ALOG10(M**5.5*H*DBARH*L/R**2.)

        SPLBLNT(I) = G4 + G5 + SCALE


 1000 CONTINUE

      RETURN
      END
```

```
      SUBROUTINE G5COMP(HDSTAR,ETA,G5)


      REAL M,K,MU


      IF (HDSTAR .LT. .25) MU = .1211
      IF ((HDSTAR .GT. .25).AND.(HDSTAR .LE. .62))
     1     MU=-.2175*HDSTAR + .1755
      IF ((HDSTAR .GT. .62).AND.(HDSTAR .LT. 1.15))
     1 MU = -.0308 * HDSTAR + .0596
      IF (HDSTAR .GE. 1.15)MU = .0242

      IF (HDSTAR .LE. .02) M = 0.0
      IF ((HDSTAR .GE. .02).AND.(HDSTAR .LT. .5))
     1    M=68.724*HDSTAR - 1.35
      IF ((HDSTAR .GT. .5).AND.(HDSTAR .LE. .62))
     1  M = 308.475 * HDSTAR - 121.23
      IF ((HDSTAR .GT. .62).AND.(HDSTAR .LE. 1.15))
     1  M = 224.811 * HDSTAR - 69.354
      IF ((HDSTAR .GT. 1.15) .AND. (HDSTAR .LT. 1.2))
     1  M = 1583.28 * HDSTAR - 1631.592
      IF (HDSTAR .GT. 1.2) M = 268.344
      IF (M .LT. 0.0) M = 0.0

      ETA0 = -SQRT((M*M*MU**4)/(6.25+M*M*MU*MU))

      K    = 2.5*SQRT(1.-(ETA0/MU)**2.)-2.5-M*ETA0

      IF (ETA .LE. ETA0) G5 = M * ETA + K
      IF ((ETA .GT. ETA0).AND.(ETA .LE. 0.))G5=2.5*SQRT(1.-(ETA/MU)**2.)-2.5
      IF((ETA.GT.0.).AND.(ETA.LE..03616))G5=SQRT(1.5625-1194.99*ETA**2.)-1.25
      IF (ETA .GT. .03616) G5=-155.543 * ETA + 4.375

      RETURN
      END
```

```
      SUBROUTINE TIPNOIS(ALPHTIP,ALPRAT,C,U ,FRCEN,SPLTIP,THETA,PHI,
     1                    R,NFREQ,VISC,C0,ROUND)

C                    ------------------------------
C                    ***** VARIABLE DEFINITIONS *****
C                    ------------------------------

C      VARIABLE NAME              DEFINITION                  UNITS
C      -------------              ----------                  -----

C      ALPHTIP          TIP ANGLE OF ATTACK                 DEGREES
C      ALPRAT           TIP LIFT CURVE SLOPE                  ---
C      ALPTIPP          CORRECTED TIP ANGLE OF ATTACK       DEGREES
C      C                CHORD LENGTH                          METERS
C      C0               SPEED OF SOUND                      METERS/SEC
C      DBARH            DIRECTIVITY                           ---
C      FRCEN            CENTERED FREQUENCIES                HERTZ
C      L                CHARACTERISTIC LENGTH FOR TIP       METERS
C      M                MACH NUMBER                           ---
C      MM               MAXIMUM MACH NUMBER                   ---
C      NFREQ            NUMBER OF CENTERED FREQUENCIES        ---
C      PHI              DIRECTIVITY ANGLE                   DEGREES
C      R                SOURCE TO OBSERVER DISTANCE         METERS
C      ROUND            LOGICAL SET TRUE IF TIP IS ROUNDED    ---
C      SCALE            SCALING TERM                          ---
C      SPLTIP           SOUND PRESSURE LEVEL DUE TO TIP
C                         MECHANISM                           DB
C      STPP             STROUHAL NUMBER                       ---
C      TERM             SCALING TERM                          ---
C      THETA            DIRECTIVITY ANGLE                   DEGREES
C      U                FREESTREAM VELOCITY                 METERS/SEC
C      UM               MAXIMUM VELOCITY                    METERS/SEC
C      VISC             KINEMATIC VISCOSITY                 M2/SEC

      PARAMETER (MAXFREQ =27)

      DIMENSION SPLTIP(MAXFREQ),FRCEN(MAXFREQ)
      REAL L,M,MM
      LOGICAL ROUND


      ALPTIPP = ALPHTIP * ALPRAT
      M       = U  / C0

      CALL DIRECTH(M,THETA,PHI,DBARH)

      IF (ROUND) THEN
        L = .008 * ALPTIPP * C
      ELSE
        IF (ABS(ALPTIPP) .LE. 2.) THEN
          L = (.023 + .0169*ALPTIPP) * C
        ELSE
          L = (.0378 + .0095*ALPTIPP) * C
        ENDIF
      ENDIF


      MM     = (1. + .036*ALPTIPP) * M

      UM     = MM * C0

      TERM  = M*M*MM**3.*L**2.*DBARH/R**2.
      IF (TERM .NE. 0.0) THEN
        SCALE = 10.*ALOG10(TERM)
      ELSE
        SCALE = 0.0
      ENDIF

      DO 100 I=1,NFREQ
        STPP      = FRCEN(I) * L / UM
        SPLTIP(I) = 126.-30.5*(ALOG10(STPP)+.3)**2. + SCALE
  100 CONTINUE
      RETURN
      END
```

```
      SUBROUTINE THICK(C,U ,ALPSTAR,ITRIP,DELTAP,DSTRS,DSTRP,C0,VISC)

C                   -------------------------------
C                   ***** VARIABLE DEFINITIONS *****
C                   -------------------------------

C       VARIABLE NAME               DEFINITION                  UNITS
C       -------------               ----------                  -----

C       ALPSTAR           ANGLE OF ATTACK                      DEGREES
C       C                 CHORD LENGTH                          METERS
C       C0                SPEED OF SOUND                      METERS/SEC
C       DELTA0            BOUNDARY LAYER THICKNESS AT
C                           ZERO ANGLE OF ATTACK                METERS
C       DELTAP            PRESSURE SIDE BOUNDARY LAYER
C                           THICKNESS                           METERS
C       DSTR0             DISPLACEMENT THICKNESS AT ZERO
C                           ANGLE OF ATTACK                     METERS
C       DSTRP             PRESSURE SIDE DISPLACEMENT
C                           THICKNESS                           METERS
C       DSTRS             SUCTION SIDE DISPLACEMENT
C                           THICKNESS                           METERS
C       ITRIP             TRIGGER FOR BOUNDARY LAYER TRIPPING  ---
C       M                 MACH NUMBER                           ---
C       RC                REYNOLDS NUMBER BASED ON CHORD        ---
C       U                 FREESTREAM VELOCITY                  METERS/SEC
C       VISC              KINEMATIC VISCOSITY                  M2/SEC


C      COMPUTE ZERO ANGLE OF ATTACK BOUNDARY LAYER
C      THICKNESS (METERS) AND REYNOLDS NUMBER
C      -------------------------------------------

      M         = U  / C0

      RC        = U  * C/VISC

      DELTA0    = 10.**(1.6569-.9045*ALOG10(RC)+
     1             .0596*ALOG10(RC)**2.)*C
      IF (ITRIP .EQ. 2) DELTA0 = .6 * DELTA0


C      COMPUTE PRESSURE SIDE BOUNDARY LAYER THICKNESS
C      ----------------------------------------------

      DELTAP    = 10.**(-.04175*ALPSTAR+.00106*ALPSTAR**2.)*DELTA0


C      COMPUTE ZERO ANGLE OF ATTACK DISPLACEMENT THICKNESS
C      ---------------------------------------------------

      IF ((ITRIP .EQ. 1) .OR. (ITRIP .EQ. 2)) THEN
        IF (RC .LE. .3E+06) DSTR0 = .0601 * RC **(-.114)*C
        IF (RC .GT. .3E+06)
     1    DSTR0=10.**(3.411-1.5397*ALOG10(RC)+.1059*ALOG10(RC)**2.)*C
        IF (ITRIP .EQ. 2) DSTR0 = DSTR0 * .6
      ELSE
        DSTR0=10.**(3.0187-1.5397*ALOG10(RC)+.1059*ALOG10(RC)**2.)*C
      ENDIF

C      PRESSURE SIDE DISPLACEMENT THICKNESS
C      ------------------------------------

      DSTRP    = 10.**(-.0432*ALPSTAR+.00113*ALPSTAR**2.)*DSTR0
      IF (ITRIP .EQ. 3) DSTRP = DSTRP * 1.48

C      SUCTION SIDE DISPLACEMENT THICKNESS
C      -----------------------------------

      IF (ITRIP .EQ. 1) THEN
        IF (ALPSTAR .LE. 5.) DSTRS=10.**(.0679*ALPSTAR)*DSTR0
        IF((ALPSTAR .GT. 5.).AND.(ALPSTAR .LE. 12.5))
     1   DSTRS = .381*10.**(.1516*ALPSTAR)*DSTR0
        IF (ALPSTAR .GT. 12.5)DSTRS=14.296*10.**(.0258*ALPSTAR)*DSTR0
      ELSE
```

```
        IF (ALPSTAR .LE. 7.5)DSTRS =10.**(.0679*ALPSTAR)*DSTRO
        IF((ALPSTAR .GT. 7.5).AND.(ALPSTAR .LE. 12.5))
     1   DSTRS = .0162*10.**(.3066*ALPSTAR)*DSTRO
        IF (ALPSTAR .GT. 12.5) DSTRS = 52.42*10.**(.0258*ALPSTAR)*DSTRO
      ENDIF

      RETURN
      END
```

References

1. Brooks, Thomas F.; and Schlinker, Robert H.: Progress in Rotor Broadband Noise Research. *Vertica*, vol. 7, no. 4, 1983, pp. 287–307.
2. Brooks, T. F.; and Hodgson, T. H.: Trailing Edge Noise Prediction From Measured Surface Pressures. *J. Sound & Vibration*, vol. 78, no. 1, Sept. 8, 1981, pp. 69–117.
3. Schlinker, Robert H.; and Amiet, Roy K.: *Helicopter Rotor Trailing Edge Noise*. NASA CR-3470, 1981. (See also AIAA Paper 81-2001.)
4. Liu, N. S.; and Shamroth, S. J.: *On the Application of a Hairpin Vortex Model of Wall Turbulence to Trailing Edge Noise Prediction*. NASA CR-177938, 1985.
5. Ffowcs Williams, J. E.; and Hall, L. H.: Aerodynamic Sound Generation by Turbulent Flow in the Vicinity of a Scattering Half Plane. *J. Fluid Mech.*, vol. 40, pt. 4, Mar. 1970, pp. 657-670.
6. Brooks, Thomas F.; and Marcolini, Michael A.: Scaling of Airfoil Self-Noise Using Measured Flow Parameters. *AIAA J.*, vol. 23, no. 2, Feb. 1985, pp. 207-213.
7. Chou, S.-T.; and George, A. R.: Effect of Angle of Attack on Rotor Trailing-Edge Noise. *AIAA J.*, vol. 22, no. 12, Dec. 1984, pp. 1821–1823.
8. George, Albert R.; and Chou, Shau-Tak: *Broadband Rotor Noise Analyses*. NASA CR-3797, 1984.
9. Grosveld, Ferdinand W.: Prediction of Broadband Noise From Horizontal Axis Wind Turbines. *AIAA J. Propuls. & Power*, vol. 1, no. 4, July–Aug. 1985, pp. 292–299.
10. Glegg, S. A. L.; Baxter, S. M.; and Glendinning, A. G.: The Prediction of Broadband Noise From Wind Turbines. *J. Sound & Vibration*, vol. 118, no. 2, Oct. 22, 1987, pp. 217–239.
11. Fink, M. R.; and Bailey, D. A.: *Airframe Noise Reduction Studies and Clean-Airframe Noise Investigation*. NASA CR-159311, 1980.
12. Paterson, Robert W.; Amiet, Roy K.; and Munch, C. Lee: Isolated Airfoil-Tip Vortex Interaction Noise. AIAA Paper No. 74-194, Jan.–Feb. 1974.
13. Tam, Christopher K. W.: Discrete Tones of Isolated Airfoils. *J. Acoust. Soc. America*, vol. 55, no. 6, June 1974, pp. 1173–1177.
14. Wright, S. E.: The Acoustic Spectrum of Axial Flow Machines. *J. Sound & Vibration*, vol. 45, no. 2, Mar. 22, 1976, pp. 165–223.
15. Fink, M. R.: *Fine Structure of Airfoil Tone Frequency*. UTRC78-10, United Technologies Research Center, Jan. 1978.
16. Paterson, Robert W.; Vogt, Paul G.; Fink, Martin R.; and Munch, C. Lee: Vortex Noise of Isolated Airfoils. *J. Aircr.*, vol. 10, no. 5, May 1973, pp. 296–302.
17. George, A. R.; Najjar, F. E.; and Kim, Y. N.: Noise Due to Tip Vortex Formation on Lifting Rotors. AIAA-80-1010, June 1980.
18. Brooks, Thomas F.; and Marcolini, Michael A.: Airfoil Tip Vortex Formation Noise. *AIAA J.*, vol. 24, no. 2, Feb. 1986, pp. 246–252.
19. Blake, William K.: *Aero-Hydroacoustics for Ships, Volume II*. Rep. No. DTNSRDC-84/010, U.S. Navy, June 1984.
20. Chou, S.-T.; and George, A. R.: Effect of Blunt Trailing Edge on Rotor Broadband Noise. *AIAA J.*, vol. 24, no. 8, Aug. 1986, pp. 1380–1382.
21. Brooks, Thomas F.; Marcolini, Michael A.; and Pope, Dennis S.: Airfoil Trailing-Edge Flow Measurements. *AIAA J.*, vol. 24, no. 8, Aug. 1986, pp. 1245–1251.
22. Amiet, R. K.: Refraction of Sound by a Shear Layer. *J. Sound & Vibration*, vol. 58, no. 4, June 1978, pp. 467–482.
23. Schlinker, R. H.; and Amiet, R. K.: Refraction of Sound by a Shear Layer—Experimental Assessment. AIAA Paper 79-0628, Mar. 1979.
24. Paterson, Robert W.; and Amiet, Roy K.: *Acoustic Radiation and Surface Pressure Characteristics of an Airfoil Due to Incident Turbulence*. NASA CR-2733, 1976. (See also AIAA Paper 76-571.)
25. Fink, Martin R.: Noise Component Method for Airframe Noise. AIAA Paper 77-1271, Oct. 1977.
26. Schlinker, R. H.: Airfoil Trailing Edge Noise Measurements With a Directional Microphone. AIAA Paper 77-1269, Oct. 1977.
27. Fink, M. R.; Schlinker, R. H.; and Amiet, R. K.: *Prediction of Rotating-Blade Vortex Noise From Noise of Nonrotating Blades*. NASA CR-2611, 1976.
28. Bendat, Julius S.; and Piersol, Allan G.: *Random Data: Analysis and Measurement Procedures*. John Wiley & Sons, Inc., c.1971.
29. Dowling, A. P.; and Ffowcs Williams, J. E.: *Sound and Sources of Sound*. John Wiley & Sons, c.1983.
30. Brooks, Thomas F.; Marcolini, Michael A.; and Pope, D. Stuart: Main Rotor Broadband Noise Study in the DNW. J. American Helicopter Soc., vol. 34, no. 2, Apr. 1989, pp. 3-12.
31. Golub, R. A.; Weir, D. S.; and Tracy, M. B.: Application of the Baseline Rotonet System to the Prediction of Helicopter Tone Noise. AIAA-86-1904, July 1986.

Table 1. Test and Data Processing Conditions for Tripped Boundary-Layer Airfoil Cases of Figures 11 to 43

Fig. no.	Run no.	Chord, c, cm	Tunnel angle, α_t, deg	Effective angle, α_*, deg	Tunnel velocity, U, m/s	Reynolds number, $R_c \times 10^{-6}$	Calculated ratio, δ_s^*/c	Peak Strouhal no., St_{peak} (fig. 76)	TBL-TE peak scaled $SPL_{1/3}$, dB (fig. 77)	Data processing (app. A) Microphones		No. sep.	Fold
11(a)	101	30.48	0.0	0.0	71.3	1.497	0.0087	0.046	128.5	4x5	4x8	0	F
11(b)	102	30.48	0.0	0.0	55.5	1.164	0.0093	0.056	128.0	4x5	4x8	0	F
11(c)	103	30.48	0.0	0.0	39.6	0.831	0.0102	0.065	128.5	4x5	4x8	0	F
11(d)	104	30.48	0.0	0.0	31.7	0.665	0.0109	0.082	128.5	4x5	4x8	0	F
12(a)	105	30.48	5.4	1.5	71.3	1.497	0.0111	0.050	128.5	4x5	4x8	0	F
12(b)	106	30.48	5.4	1.5	39.6	0.831	0.0129	0.076	128.0	4x5	4x8	0	F
13(a)	107	30.48	10.8	3.0	71.3	1.497	0.0140	0.050	129.0	4x5	4x8	0	F
13(b)	108	30.48	10.8	3.0	55.5	1.164	0.0149	0.069	129.0	4x5	4x8	0	F
13(c)	109	30.48	10.8	3.0	39.6	0.831	0.0163	0.101	129.0	4x5	4x8	0	F
13(d)	110	30.48	10.8	3.0	31.7	0.665	0.0174	0.125	128.0	4x5	4x8	0	F
14(a)	111	30.48	14.4	4.0	71.3	1.497	0.0164	0.057	131.5	4x5	4x2	0	F
14(b)	112	30.48	14.4	4.0	39.6	0.831	0.0191	0.103	130.5	4x5	4x2	0	F
15(a)	251	22.86	0.0	0.0	71.3	1.122	0.0094	0.061	128.5	4x5	4x8	0	NF
15(b)	252	22.86	0.0	0.0	55.5	0.873	0.0100	0.069	127.5	4x5	4x8	0	F
15(c)	253	22.86	0.0	0.0	39.6	0.624	0.0111	0.073	130.0	4x5	4x8	0	F
15(d)	254	22.86	0.0	0.0	31.7	0.499	0.0119	0.086	130.0	4x5	4x8	0	F
16(a)	255	22.86	5.4	2.0	71.3	1.122	0.0128	0.067	128.0	4x5	4x8	0	F
16(b)	256	22.86	5.4	2.0	55.5	0.873	0.0137	0.061	128.5	4x5	4x8	0	F
16(c)	257	22.86	5.4	2.0	39.6	0.624	0.0152	0.083	128.0	4x5	4x8	0	F
16(d)	258	22.86	5.4	2.0	31.7	0.499	0.0163	0.110	124.5	4x5	4x8	0	F
17(a)	259	22.86	10.8	4.0	71.3	1.122	0.0175	0.068	131.0	4x5	4x8	0	F
17(b)	260	22.86	10.8	4.0	55.5	0.873	0.0187	0.075	131.5	4x5	4x8	0	F
17(c)	261	22.86	10.8	4.0	39.6	0.624	0.0207	0.099	129.5	4x5	4x8	0	F
17(d)	262	22.86	10.8	4.0	31.7	0.499	0.0223	0.138	125.5	4x5	4x8	0	F
18(a)	263	22.86	14.4	5.3	71.3	1.122	0.0229	0.081	133.0	4x5	4x2	0	F
18(b)	264	22.86	14.4	5.3	39.6	0.624	0.0271	0.085	131.5	4x5	4x2	0	NF
19(a)	265	22.86	19.8	7.3	71.3	1.122	0.0461	0.050	140.0	4x5	4x2	0	NF
19(b)	266	22.86	19.8	7.3	55.5	0.873	0.0493	0.071	135.5	4x5	4x2	0	NF
19(c)	267	22.86	19.8	7.3	39.6	0.624	0.0545	0.120	131.5	4x5	4x2	0	NF
19(d)	268	22.86	19.8	7.3	31.7	0.499	0.0586	0.157	129.5	4x5	4x2	0	NF
20(a)	133	15.24	0.0	0.0	71.3	0.748	0.0105	0.058	128.0	4x5	4x8	0	F
20(b)	134	15.24	0.0	0.0	55.5	0.582	0.0113	0.065	128.5	4x5	4x8	0	F
20(c)	135	15.24	0.0	0.0	39.6	0.416	0.0127	0.070	130.0	4x5	4x8	0	F
20(d)	136	15.24	0.0	0.0	31.7	0.333	0.0137	0.087	130.5	4x5	4x8	0	F
21(a)	137	15.24	5.4	2.7	71.3	0.748	0.0160	0.057	129.5	4x5	4x8	0	F
21(b)	138	15.24	5.4	2.7	39.6	0.416	0.0193	0.094	129.5	4x5	4x8	0	F
22(a)	139	15.24	10.8	5.4	71.3	0.748	0.0263	0.075	132.5	4x5	4x2	0	F
22(b)	140	15.24	10.8	5.4	55.5	0.582	0.0284	0.081	132.0	4x5	4x8	0	NF
22(c)	141	15.24	10.8	5.4	39.6	0.416	0.0318	0.091	131.0	4x5	4x8	0	NF
22(d)	142	15.24	10.8	5.4	31.7	0.333	0.0345	0.109	130.0	4x5	4x8	0	NF
23(a)	143	15.24	14.4	7.2	71.3	0.748	0.0493	0.086	134.5	4x5	4x2	0	NF
23(b)	144	15.24	14.4	7.2	39.6	0.416	0.0596	0.130	132.5	4x5	4x2	0	NF
24(a)	145	15.24	19.8	9.9	71.3	0.748	0.1266	0.084	134.0	4x5	4x2	0	NF
24(b)	146	15.24	19.8	9.9	55.5	0.582	0.1368	0.105	131.5	4x5	4x2	0	NF
24(c)	147	15.24	19.8	9.9	39.6	0.416	0.1531	0.205	128.0	4x5	4x2	0	NF
24(d)	148	15.24	19.8	9.9	31.7	0.333	0.1659	0.301	129.5	4x5	4x2	0	NF
25(a)	149	15.24	25.2	12.6	71.3	0.748	0.3170	0.170	128.5	4x5	4x2	0	NF
25(b)	150	15.24	25.2	12.6	39.6	0.416	0.3832	1.131	116.5	4x5	4x2	0	NF
26(a)	293	10.16	0.0	0.0	71.3	0.499	0.0119	0.045	132.0	4x5	4x8	1	F
26(b)	294	10.16	0.0	0.0	55.5	0.388	0.0130	0.057	132.5	4x5	4x8	2	F
26(c)	295	10.16	0.0	0.0	39.6	0.277	0.0144	0.071	132.5	4x5	4x8	2	F
26(d)	296	10.16	0.0	0.0	31.7	0.222	0.0148	0.077	133.0	4x5	4x8	2	F
27(a)	297	10.16	5.4	3.3	71.3	0.499	0.0201	0.060	133.0	4x5	4x8	2	F
27(b)	298	10.16	5.4	3.3	55.5	0.388	0.0219	0.074	132.5	4x5	4x8	2	F
27(c)	299	10.16	5.4	3.3	39.6	0.277	0.0243	0.092	132.0	4x5	4x8	2	F
27(d)	300	10.16	5.4	3.3	31.7	0.222	0.0249	0.120	127.5	4x5	4x8	2	F
28(a)	301	10.16	10.8	6.7	71.3	0.499	0.0470	0.086	136.5	4x5	4x8	0	F

Table 1. Concluded

Fig. no.	Run no.	Chord, c, cm	Tunnel angle, α_t, deg	Effective angle, α_*, deg	Tunnel velocity, U, m/s	Reynolds number $R_c \times 10^{-6}$	Calculated ratio, δ_s^*/c	Peak Strouhal no., St_{peak} (fig. 76)	TBL-TE peak scaled $SPL_{1/3}$, dB (fig. 77)	Data processing (app. A) Microphones		No. sep.	Fold
28(b)	302	10.16	10.8	6.7	55.5	0.388	0.0513	0.102	136.0	4x5	4x8	0	F
28(c)	303	10.16	10.8	6.7	39.6	0.277	0.0568	0.125	133.5	4x5	4x8	0	F
28(d)	304	10.16	10.8	6.7	31.7	0.222	0.0583	0.156	131.5	4x5	4x8	0	F
29(a)	305	10.16	14.4	8.9	71.3	0.499	0.1024	0.085	138.0	4x5	4x2	0	NF
29(b)	306	10.16	14.4	8.9	39.6	0.277	0.1238	0.130	134.5	4x5	4x2	0	NF
30(a)	307	10.16	19.8	12.3	71.3	0.499	0.3296	0.209	138.5	4x5	4x2	0	NF
30(b)	309	10.16	19.8	12.3	55.5	0.388	0.3594	0.220	135.0	4x5	4x2	0	NF
30(c)	308	10.16	19.8	12.3	39.6	0.277	0.3984	0.265	129.0	4x5	4x2	0	NF
30(d)	310	10.16	19.8	12.3	31.7	0.222	0.4087	0.341	125.0	4x5	4x2	0	NF
31(a)	311	10.16	25.2	15.6	71.3	0.499	0.4309	0.192	132.5	4x5	4x2	0	NF
31(b)	312	10.16	25.2	15.6	39.6	0.277	0.5209	0.330	123.5	4x5	4x2	0	NF
32(a)	179	5.08	0.0	0.0	71.3	0.249	0.0146	0.044	133.5	4x5	4x8	2	F
32(b)	180	5.08	0.0	0.0	55.5	0.194	0.0150	0.057	134.0	4x5	4x8	2	F
32(c)	181	5.08	0.0	0.0	39.6	0.139	0.0156	0.068	134.5	4x5	4x8	2	F
32(d)	182	5.08	0.0	0.0	31.7	0.111	0.0160	0.077	134.5	4x5	4x8	2	F
33(a)	183	5.08	5.4	4.2	71.3	0.249	0.0282	0.076	133.0	4x5	4x8	0	F
33(b)	184	5.08	5.4	4.2	39.6	0.139	0.0301	0.109	133.0	4x5	4x8	0	F
34(a)	185	5.08	10.8	8.4	71.3	0.249	0.1051	0.156	134.0	4x5	4x8	0	F
34(b)	186	5.08	10.8	8.4	55.5	0.194	0.1082	0.164	132.0	4x5	4x8	0	F
34(c)	187	5.08	10.8	8.4	39.6	0.139	0.1124	0.205	130.0	4x5	4x8	0	F
34(d)	188	5.08	10.8	8.4	31.7	0.111	0.1153	0.236	129.5	4x5	4x8	0	F
35(a)	189	5.08	14.4	11.2	71.3	0.249	0.2801	0.220	135.5	4x5	4x2	0	F
35(b)	190	5.08	14.4	11.2	39.6	0.139	0.2995	0.303	132.0	4x5	4x2	0	F
36(a)	191	5.08	19.8	15.4	71.3	0.249	0.5215	0.412	131.5	4x5	4x2	0	F
36(b)	192	5.08	19.8	15.4	55.5	0.194	0.5367	0.483	129.5	4x5	4x2	0	F
36(c)	193	5.08	19.8	15.4	39.6	0.139	0.5577	0.621	128.0	4x5	4x2	0	F
36(d)	194	5.08	19.8	15.4	31.7	0.111	0.5721	0.741	125.0	4x5	4x2	0	F
37(a)	195	5.08	25.2	19.7	71.3	0.249	0.6698	0.294	127.0	4x5	4x2	0	NF
37(b)	196	5.08	25.2	19.7	39.6	0.139	0.7162	0.318	129.5	4x5	4x2	0	NF
38(a)	213	2.54	0.0	0.0	71.3	0.125	0.0158			4x5	4x8	2	F
38(b)	214	2.54	0.0	0.0	55.5	0.097	0.0162	0.051	133.0	4x5	4x8	2	F
38(c)	215	2.54	0.0	0.0	39.6	0.069	0.0169	0.072	135.5	4x5	4x8	0	F
38(d)	216	2.54	0.0	0.0	31.7	0.055	0.0173	0.083	137.5	4x5	4x8	0	F
39(a)	217	2.54	5.4	4.8	71.3	0.125	0.0332	0.060	134.0	4x5	4x8	2	F
39(b)	218	2.54	5.4	4.8	55.5	0.097	0.0341	0.087	134.5	4x5	4x8	0	F
39(c)	219	2.54	5.4	4.8	39.6	0.069	0.0355	0.116	134.0	4x5	4x8	0	F
39(d)	220	2.54	5.4	4.8	31.7	0.055	0.0364	0.131	134.5	4x5	4x8	0	F
40(a)	221	2.54	10.8	9.5	71.3	0.125	0.1658	0.164	135.0	4x5	4x8	0	F
40(b)	222	2.54	10.8	9.5	55.5	0.097	0.1707	0.190	133.5	4x5	4x8	0	F
40(c)	223	2.54	10.8	9.5	39.6	0.069	0.1773	0.218	130.5	4x5	4x8	0	F
40(d)	224	2.54	10.8	9.5	31.7	0.055	0.1819	0.209	130.5	4x5	4x8	0	F
41(a)	225	2.54	14.4	12.7	71.3	0.125	0.4787	0.356	133.5	4x5	4x2	0	F
41(b)	226	2.54	14.4	12.7	39.6	0.069	0.5119	0.501	129.0	4x5	4x2	0	F
42(a)	227	2.54	19.8	17.4	71.3	0.125	0.6349	0.493	126.0	4x5	4x2	0	F
42(b)	228	2.54	19.8	17.4	55.5	0.097	0.6533	0.518	126.5	4x5	4x2	0	NF
42(c)	229	2.54	19.8	17.4	39.6	0.069	0.6789	0.413	135.0	4x5	4x2	0	F
42(d)	230	2.54	19.8	17.4	31.7	0.055	0.6964	0.402	136.5	4x5	4x2	0	F
43(a)	231	2.54	25.2	22.2	71.3	0.125	0.8420	0.356	136.0	4x5	4x2	0	F
43(b)	232	2.54	25.2	22.2	39.6	0.069	0.9003	0.413	135.0	4x5	4x2	0	F

Table 2. Test and Data Processing Conditions for Untripped Boundary-Layer Airfoil Cases of Figures 44 to 74

Fig. no.	Run no.	Chord, c, cm	Tunnel angle, α_t, deg	Effective angle, α_*, deg	Tunnel velocity, U, m/s	Reynolds number $R_c \times 10^{-6}$	Calculated ratio, δ_p/c	Peak Strouhal no., St'_{peak} (fig. 86)	LBL-VS peak scaled level, dB (fig. 88)	Data processing (app. A) Microphones		No. sep.	Fold
44(a)	113	30.48	0.0	0.0	71.3	1.497	0.0221			4x5	4x8	0	F
44(b)	114	30.48	0.0	0.0	55.5	1.164	0.0231			4x5	4x8	0	F
44(c)	115	30.48	0.0	0.0	39.6	0.831	0.0246			4x5	4x8	0	F
44(d)	116	30.48	0.0	0.0	31.7	0.665	0.0258			4x5	4x8	0	F
45(a)	117	30.48	5.4	1.5	71.3	1.497	0.0192			4x5	4x8	0	NF
45(b)	118	30.48	5.4	1.5	39.6	0.831	0.0214	0.235	136.5	4x5	4x8	0	NF
46(a)	119	30.48	10.8	3.0	71.3	1.497	0.0169	0.225	138.0	4x5	4x2	0	NF
46(b)	120	30.48	10.8	3.0	55.5	1.164	0.0176	0.210	147.5	4x5	4x8	0	NF
46(c)	121	30.48	10.8	3.0	39.6	0.831	0.0188	0.210	152.0	4x5	4x8	0	NF
46(d)	122	30.48	10.8	3.0	31.7	0.665	0.0197	0.205	154.5	4x5	4x8	0	NF
47(a)	123	30.48	14.4	4.0	71.3	1.497	0.0156	0.210	148.0	4x5	4x2	0	NF
47(b)	124	30.48	14.4	4.0	39.6	0.831	0.0174	0.200	154.0	4x5	4x2	0	NF
48(a)	269	22.86	0.0	0.0	71.3	1.122	0.0232			4x5	4x8	0	F
48(b)	270	22.86	0.0	0.0	55.5	0.873	0.0244			4x5	4x8	0	NF
48(c)	271	22.86	0.0	0.0	39.6	0.624	0.0261			4x5	4x8	0	NF
48(d)	272	22.86	0.0	0.0	31.7	0.499	0.0274	0.310	126.5	4x5	4x8	0	F
49(a)	273	22.86	5.4	2.0	71.3	1.122	0.0194			4x5	4x8	0	NF
49(b)	274	22.86	5.4	2.0	55.5	0.873	0.0203	0.220	135.0	4x5	4x8	0	NF
49(c)	275	22.86	5.4	2.0	39.6	0.624	0.0218	0.205	145.5	4x5	4x8	0	NF
49(d)	276	22.86	5.4	2.0	31.7	0.499	0.0229	0.215	150.5	4x5	4x8	0	NF
50(a)	277	22.86	10.8	4.0	71.3	1.122	0.0165	0.185	148.5	4x5	4x2	0	NF
50(b)	278	22.86	10.8	4.0	55.5	0.873	0.0173	0.200	152.0	4x5	4x8	0	NF
50(c)	279	22.86	10.8	4.0	39.6	0.624	0.0185	0.190	152.5	4x5	4x8	0	NF
50(d)	280	22.86	10.8	4.0	31.7	0.499	0.0194	0.200	154.5	4x5	4x8	0	NF
51(a)	281	22.86	14.4	5.3	71.3	1.122	0.0149	0.165	154.5	4x5	4x2	0	NF
51(b)	282	22.86	14.4	5.3	39.6	0.624	0.0168	0.185	150.5	4x5	4x2	0	NF
52(a)	283	22.86	19.8	7.3	71.3	1.122	0.0131			4x5	4x2	0	NF
52(b)	284	22.86	19.8	7.3	39.6	0.624	0.0147			4x5	4x2	0	NF
53(a)	151	15.24	0.0	0.0	71.3	0.748	0.0251			4x5	4x8	0	F
53(b)	152	15.24	0.0	0.0	55.5	0.582	0.0265			4x5	4x8	0	F
53(c)	153	15.24	0.0	0.0	39.6	0.416	0.0286	0.265	136.0	4x5	4x8	0	F
53(d)	154	15.24	0.0	0.0	31.7	0.333	0.0302	0.265	144.0	4x5	4x8	0	F
54(a)	155	15.24	5.4	2.7	71.3	0.748	0.0197	0.205	147.0	4x5	4x8	0	F
54(b)	156	15.24	5.4	2.7	39.6	0.416	0.0225	0.190	159.0	4x5	4x8	0	F
55(a)	157	15.24	10.8	5.4	71.3	0.748	0.0161	0.160	155.0	4x5	4x2	0	NF
55(b)	158	15.24	10.8	5.4	55.5	0.582	0.0169	0.170	153.0	4x5	4x8	0	F
55(c)	159	15.24	10.8	5.4	39.6	0.416	0.0183	0.180	142.5	4x5	4x8	0	F
55(d)	160	15.24	10.8	5.4	31.7	0.333	0.0193			4x5	4x8	0	F
56(a)	161	15.24	14.4	7.2	71.3	0.748	0.0143			4x5	4x2	0	F
56(b)	162	15.24	14.4	7.2	39.6	0.416	0.0162			4x5	4x2	0	F
57(a)	163	15.24	19.8	9.9	71.3	0.748	0.0123			4x5	4x2	0	NF
57(b)	164	15.24	19.8	9.9	39.6	0.416	0.0140			4x5	4x2	0	NF
58(a)	165	15.24	25.2	12.6	71.3	0.748	0.0110			4x5	4x2	0	NF
58(b)	166	15.24	25.2	12.6	39.6	0.416	0.0125			4x5	4x2	0	NF
59(a)	313	10.16	0.0	0.0	71.3	0.499	0.0274	0.290	132.0	4x5	4x8	1	F
59(b)	314	10.16	0.0	0.0	55.5	0.388	0.0291	0.300	138.5	4x5	4x8	0	F
59(c)	315	10.16	0.0	0.0	39.6	0.277	0.0316	0.240	151.0	4x5	4x8	0	F
59(d)	316	10.16	0.0	0.0	31.7	0.222	0.0335	0.210	159.5	4x5	4x8	0	F
60(a)	317	10.16	5.4	3.3	71.3	0.499	0.0204	0.180	161.5	4x5	4x8	0	NF
60(b)	318	10.16	5.4	3.3	55.5	0.388	0.0217	0.185	159.5	4x5	4x8	0	NF
60(c)	319	10.16	5.4	3.3	39.6	0.277	0.0235	0.190	157.0	4x5	4x8	2	F
60(d)	320	10.16	5.4	3.3	31.7	0.222	0.0249	0.220	147.0	4x5	4x8	2	F
61(a)	321	10.16	10.8	6.7	71.3	0.499	0.0161			4x5	4x8	2	NF
61(b)	322	10.16	10.8	6.7	55.5	0.388	0.0170			4x5	4x8	2	F
61(c)	323	10.16	10.8	6.7	39.6	0.277	0.0185			4x5	4x8	2	F
61(d)	324	10.16	10.8	6.7	31.7	0.222	0.0196			4x5	4x8	2	F
62(a)	325	10.16	14.4	8.9	71.3	0.499	0.0141			4x5	4x2	2	F

Table 2. Concluded

Fig. no.	Run no.	Chord, c, cm	Tunnel angle, α_t, deg	Effective angle, α_*, deg	Tunnel velocity, U, m/s	Reynolds number, $R_c \times 10^{-6}$	Calculated ratio, δ_p/c	Peak Strouhal no., St'_{peak} (fig. 86)	LBL-VS peak scaled level, dB (fig. 88)	Data processing (app. A) Microphones		No. sep.	Fold
62(b)	326	10.16	14.4	8.9	39.6	0.277	0.0163			4x5	4x2	2	F
63(a)	327	10.16	19.8	12.3	71.3	0.499	0.0122			4x5	4x2	0	NF
63(b)	328	10.16	19.8	12.3	39.6	0.277	0.0140			4x5	4x2	0	NF
64(a)	329	10.16	25.2	15.6	71.3	0.499	0.0111			4x5	4x2	0	NF
64(b)	330	10.16	25.2	15.6	39.6	0.277	0.0128			4x5	4x2	0	NF
65(a)	197	5.08	0.0	0.0	71.3	0.249	0.0325	0.230	153.0	4x5	4x8	0	F
65(b)	198	5.08	0.0	0.0	55.5	0.194	0.0347	0.210	160.5	4x5	4x8	0	NF
65(c)	199	5.08	0.0	0.0	39.6	0.139	0.0382	0.210	166.0	4x5	4x8	0	NF
65(d)	200	5.08	0.0	0.0	31.7	0.111	0.0408	0.190	172.5	4x5	4x8	0	NF
66(a)	201	5.08	5.4	4.2	71.3	0.249	0.0226	0.157	164.0	4x5	4x8	0	NF
66(b)	202	5.08	5.4	4.2	39.6	0.139	0.0266	0.190	148.0	4x5	4x8	0	NF
67(a)	203	5.08	10.8	8.4	71.3	0.249	0.0172			4x5	4x8	2	F
67(b)	204	5.08	10.8	8.4	55.5	0.194	0.0184			4x5	4x8	2	F
67(c)	205	5.08	10.8	8.4	39.6	0.139	0.0202			4x5	4x8	2	F
67(d)	206	5.08	10.8	8.4	31.7	0.111	0.0216			4x5	4x8	2	F
68(a)	207	5.08	14.4	11.2	71.3	0.249	0.0150			4x5	4x2	0	F
68(b)	208	5.08	14.4	11.2	39.6	0.139	0.0176			4x5	4x2	0	F
69(a)	209	5.08	19.8	15.4	71.3	0.249	0.0132			4x5	4x2	0	F
69(b)	210	5.08	19.8	15.4	39.6	0.139	0.0155			4x5	4x2	0	F
70(a)	211	5.08	25.2	19.7	71.3	0.249	0.0126			4x5	4x2	0	NF
70(b)	212	5.08	25.2	19.7	39.6	0.139	0.0148			4x5	4x2	0	NF
71(a)	233	2.54	0.0	0.0	71.3	0.125	0.0394	0.170	169.0	4x5	4x8	0	NF
71(b)	234	2.54	0.0	0.0	55.5	0.097	0.0425	0.180	170.0	4x5	4x8	0	NF
71(c)	235	2.54	0.0	0.0	39.6	0.069	0.0473	0.180	170.0	4x5	4x8	0	NF
71(d)	236	2.54	0.0	0.0	31.7	0.055	0.0510	0.210	164.5	4x5	4x8	0	NF
72(a)	237	2.54	5.4	4.8	71.3	0.125	0.0264			4x5	4x8	0	F
72(b)	238	2.54	5.4	4.8	55.5	0.097	0.0284			4x5	4x8	2	F
72(c)	239	2.54	5.4	4.8	39.6	0.069	0.0317			4x5	4x8	0	F
72(d)	240	2.54	5.4	4.8	31.7	0.055	0.0341			4x5	4x8	0	F
73(a)	241	2.54	10.8	9.5	71.3	0.125	0.0197			4x5	4x8	0	F
73(b)	242	2.54	10.8	9.5	55.5	0.097	0.0213			4x5	4x8	0	F
73(c)	243	2.54	10.8	9.5	39.6	0.069	0.0237			4x5	4x8	0	F
73(d)	244	2.54	10.8	9.5	31.7	0.055	0.0255			4x5	4x8	0	F
74(a)	245	2.54	14.4	12.7	71.3	0.125	0.0172			4x5	4x2	0	F
74(b)	246	2.54	14.4	12.7	39.6	0.069	0.0207			4x5	4x2	0	F

NASA
National Aeronautics and Space Administration

Report Documentation Page

1. Report No.	2. Government Accession No.	3. Recipient's Catalog No.
NASA RP-1218		

4. Title and Subtitle	5. Report Date
Airfoil Self-Noise and Prediction	July 1989
	6. Performing Organization Code
7. Author(s)	8. Performing Organization Report No.
Thomas F. Brooks, D. Stuart Pope, and Michael A. Marcolini	L-16528
9. Performing Organization Name and Address	10. Work Unit No.
NASA Langley Research Center Hampton, VA 23665-5225	505-63-51-06
	11. Contract or Grant No.
12. Sponsoring Agency Name and Address	13. Type of Report and Period Covered
National Aeronautics and Space Administration Washington, DC 20546-0001	Reference Publication
	14. Sponsoring Agency Code

15. Supplementary Notes

Thomas F. Brooks and Michael A. Marcolini: Langley Research Center, Hampton, Virginia.
D. Stuart Pope: PRC Kentron, Inc., Aerospace Technologies Division, Hampton, Virginia.

16. Abstract

A prediction method is developed for the self-generated noise of an airfoil blade encountering smooth flow. The prediction methods for the individual self-noise mechanisms are semiempirical and are based on previous theoretical studies and data obtained from tests of two- and three-dimensional airfoil blade sections. The self-noise mechanisms are due to specific boundary-layer phenomena, that is, the boundary-layer turbulence passing the trailing edge, separated-boundary-layer and stalled flow over an airfoil, vortex shedding due to laminar-boundary-layer instabilities, vortex shedding from blunt trailing edges, and the turbulent vortex flow existing near the tip of lifting blades. The predictions are compared successfully with published data from three self-noise studies of different airfoil shapes. An application of the prediction method is reported for a large-scale-model helicopter rotor, and the predictions compared well with experimental broadband noise measurements. A computer code of the method is given.

17. Key Words (Suggested by Authors(s))	18. Distribution Statement
Airframe noise Helicopter rotor acoustics Rotor broadband noise Propeller noise Wind turbine noise Trailing-edge noise Vortex-shedding noise	Unclassified—Unlimited Subject Category 71

19. Security Classif. (of this report)	20. Security Classif. (of this page)	21. No. of Pages	22. Price
Unclassified	Unclassified	142	A07

NASA FORM 1626 OCT 86

NASA-Langley, 1989

For sale by the National Technical Information Service, Springfield, Virginia 22161-2171